
Magnetization dependent effects in superconducting nanowires influenced by the ferromagnetic proximity effect

Thomas Wren

Supervisors: Prof. Victor Petrashov, Dr. Olga Kazakova



Thesis submitted in part fulfilment of the requirement for the degree of Doctor of
Philosophy from Royal Holloway, University of London

Declaration of Authorship

I, Thomas Wren, hereby declare that this thesis and the work presented in it is entirely my own. Where I have consulted the work of others this is always clearly stated.

signed:_____

date:_____

Abstract

This thesis presents the experimental study of superconducting nanowires under the influence of ferromagnetic nano-structures. Placing superconducting and ferromagnetic materials in contact with one another causes their long range orders to compete. This manifests as the leakage of superconducting properties into the ferromagnet and the suppression of superconductivity in the superconductor near the interface, known as the proximity and inverse proximity effects, respectively. The experiments presented in this thesis aim to show that the inverse proximity effect is sensitive to the magnetization of the ferromagnet, specifically that the suppression is weaker if the ferromagnet has an inhomogeneous magnetization. To do this, the magnetic vortex state in sub-micron nickel disks and L-shape domain wall traps were used as the inhomogeneous magnetizations. The magnetization in the nickel disks and L-shape domain wall traps were investigated using magnetic force microscopy (MFM), in situ MFM, magnetotransport, and modelling. Aluminium nanowires were deposited over the ferromagnets and low temperature transport measurements of the hybrid structures were performed. It is found that the superconductivity in the nanowire above the disks is suppressed, creating an SNS junction. The critical current is shown to be sensitive to the magnetic history of the disks. The critical current of the entire nanowire is found to be dependent on the properties of the hybrid junction. This long-range influence has a thermal origin due to Joule heating in the hybrid junction as demonstrated by use of heat sink structures and Andreev loop interferometers. Replacing the disk with L-shape domain wall traps shows that the suppression of superconductivity is weakest when a domain wall is placed beneath the nanowire. Lastly, comparison to theory indicates the junction length is proportional to temperature. The results presented demonstrate previously unknown complexity in the behaviour of so-called proximity junctions and a step toward magnetically controlled superconducting circuitry.

Acknowledgements

First and foremost I wish to thank my supervisors, Dr. Olga Kazakova at NPL and Prof. Victor Petrashov at Royal Holloway for providing me the opportunity of this PhD project. Without the unwavering support of both of you this thesis would never have been possible. I must also thank Dr. James Wells, Dr. Connor Shelly and Dr. Richard Marsh for their assistance as fellow students and more importantly mentors. A special thanks to Dr. Rais Shaikhaidarov for his efficient running of the Royal Holloway clean room and his helpful discussions. I would also like to thank the Royal Holloway administration staff.

This thesis being a piece of experimental work I owe a huge debt of gratitude to the technical staff at Royal Holloway. I'd especially like to thank Mr Mass Venti, Mr Andy Alway, Mr Ian Murray for their technical assistance and Mr Harpal Sandhu and Mr Francis Greenough for their smooth running of the cryogenic facilities at Royal Holloway. I would also like to thank my moderator Prof. Pedro Texia-Dias for his helpful discussions in end of year reviews and my advisor Prof. Phil Meeson for equally helpful discussion and his invaluable assistance in the repair of the cryostat. Thanks must also be made to Dr. Boris Gribkov for all the help provided in his short time at NPL.

A PhD is an exceedingly difficult endeavour and not one that can be completed in isolation. The support of other students at both Royal holloway and NPL has been endearing and humbling. I would like to make a special thanks in no particular order to, Dr. Dave Voneshan, Dr. Kristian Kent, Dr. George Nichols, Dr. Terence Giles, Dr. Will Shields, Toby Willis, Alex Waterworth, James Poulten, Dave Bowman, Rupert Mellor, Katie Porche, George Long, Jacob Dunstan, Harriet Van der Vilet, Pardis Sahafi, Eugene Ergov, Eugene Balkind, Lorenzo Frantino, Teresa Honigl, Tim Lehner, Viktoria Eless, Dr. Vishal Panchal, Dr. Ravish Rajakumar, Ilana Wisby, Hector Corte-Leon, and Christos Melios. I would like to thank my family for putting up with me over the past four years and supporting me throughout.

Lastly I must thank my partner, Siobhan. You have been an unwavering pillar of support for the past two years, without you I'd never have made it this far.

Contents

1	Introduction	11
2	Theory and Background	16
2.1	Mesoscopic Ferromagnetism	16
2.1.1	Magnetic interactions	18
2.1.2	Domain structure	24
2.1.3	Anisotropic Magneto resistance - AMR	33
2.2	Superconductivity	35
2.2.1	Proximity effects	42
2.2.2	Ferromagnetic proximity effect	51
3	Experimental Techniques	71
3.1	Nanoscale fabrication	71
3.1.1	Main principle of fabrication	71
3.1.2	Substrate preparation	73
3.1.3	Electron beam lithography	74
3.1.4	Thin film deposition	76
3.2	Cryogenic measurement systems	77
3.2.1	He-3 Cryostat	77
3.2.2	Magnetic properties measurement system MPMS	81
3.3	Room temperature magnetoresistance measurements	82
3.4	Magnetic force microscopy	84

4	Magnetic characterization	88
4.1	Remnant MFM measurements of nickel disks	89
4.1.1	Standard moment probes	89
4.1.2	Low moment probes	96
4.1.3	Simulations and Analytical fits	102
4.2	Magnetization reversal of vortices in nickel disks	119
4.2.1	<i>In situ</i> MFM	120
4.2.2	Electrical measurement	123
4.3	L-shape domain wall traps	129
4.3.1	Nickel L-shape device	131
4.3.2	Permalloy L-shape device	135
5	Hybrid SF junctions	140
5.1	Initial experiments: 800 nm and 1000 nm disks	142
5.2	Long range suppression due to spin polarised current injection: distance dependence	153
5.3	Heat sinks sample	156
5.4	Interferometer devices - Phase coherent oscillations	166
5.5	Hybrid junctions using L-shape domain wall traps	178
5.5.1	Nickel L-shape hybrid junction	179
5.5.2	Permalloy L-shape hybrid junction	181
5.6	Comparison of experimental results to existing theoretical models	189
5.6.1	Theory of critical current in long SNS junctions	190
5.6.2	Comparison to theory of self heating hotspots	199
6	Summary and conclusions	204

List of Figures

2.1	Illustration of the reduction of stray field achieved by formation of magnetic domains	25
2.2	Illustration of Néel and Bloch domain walls	26
2.3	Diagram of a magnetic vortex state and single domain state in a sub micron disk	27
2.4	Vortex images observed via MFM by Pokhil et al. and Shinjo et al.	29
2.5	MFM images of nickel cylinders by Skidmore et al.	31
2.6	MFM images asymmetric permalloy disks by Schrider et al.	33
2.7	Illustration of the Meissner effect	36
2.8	Illustration of the principle of flux quantization	40
2.9	Diagram demonstrating the penetration of superconducting electrons into a normal metal	44
2.10	Illustration of the Andreev reflection process	46
2.11	Sketch of the experimental set up of Petrashov et al. used to observed resistance oscillations in a Ag/Al SNS junction	47
2.12	Tunelling measurements by Le Sueur et al. showing the destruction of the minigap in an Al/Au SNS junction by increasing phase change across the junction	48
2.13	Diagram of the triplet condensate generated via the ferromagnetic proximity effect	53

2.14	Observed oscillations in the critical temperature and critical current of SF multilayers with increasing F layer thickness by Jiang et al. and Kontos et al.	54
2.15	Diagram of the long range triplet condensate components generated via the ferromagnetic proximity effect in the presence of an inhomogeneous magnetization	56
2.16	Long range triplet supercurrent observation by Keizer et al.	58
2.17	Long range triplet supercurrent observation by Khaire et al.	59
2.18	Inverse proximity effect of a superconductor in contact with a ferromagnetic insulator discussed by Rainer et al.	61
2.19	Tunnelling spectroscopy of Al in contact with Ni by Sillanpaa et al.	62
2.20	Measurement by Kinsey et al. and Rusanov et al. of the effect of multi-domain structures on T_c and I_c	63
2.21	Results of the calculations by Champel and Escriu of the superconducting pair amplitudes in an SF bilayer with and without a domain wall	64
2.22	Induced magnetization in a superconductor by inverse proximity effect measured by MOKE and muon spin rotation by Xia et al. and Flokstra et al.	66
2.23	SEM image and data by Vávra et al. of a PdFe/Nb proximity junction	68
2.24	SEM image and data by Vávra et al. of a Fe/Nb proximity junction with additional injection through the Fe	69
3.1	Diagram of the principle of nanoscale fabrication	72
3.2	Photograph of the sample substrates with gold contacts	73
3.3	simulated e-beam scatter at 10 and 20 kV by Kyser et al.	75
3.4	Diagram of the Edwards thermal evaporator	77
3.5	Diagram of the ^3He cryostat	78
3.6	Schematic of the current biased measurement set-up	80
3.7	Schematic of the MPMS magnetometer	82
3.8	Picture of the rotating sample holder and room temperature magnet used for AMR measurements	83

3.9	SEM micrograph of an MFM tip	84
3.10	Diagram illustrating magnetic force microscopy	85
3.11	Diagram of the assumption used to calculate the force between MFM probe and sample	87
4.1	SEM micrograph of a disk array	90
4.2	MFM images of nickel disks obtained using standard moment probes	92
4.3	Phase diagram of magnetic states in nickel disks obtained using standard moment probes	93
4.4	Line profile of a nickel disk possessing a vortex state measured with a stan- dard moment MESP probe	94
4.5	Illustrations of in-plane and 'canted' vortex	95
4.6	MFM images of a single nickel disk imaged with standard and low moment probes	97
4.7	MFM images of magnetic states in nickel disks obtained using low moment probes	98
4.8	Line profile of a disk possessing a vortex state measured with a Low moment probe	100
4.9	Phase diagram of magnetic states in nickel disks obtained using low moment probes	101
4.10	Still images of a simulated nickel disk relaxing from a random distribution into a vortex state	103
4.11	Simulated magnetic phase diagram using cubic anisotropy	104
4.12	Simulated magnetic states in nickel disks using an effective out-of-plane anisotropy	106
4.13	Simulated magnetic phase diagram using a constant effective out-of-plane anisotropy	108
4.14	Hysteresis curves of reference nickel thin films 15, 30, 50 nm thick for in- plane and out-of-plane configurations	110

4.15 Simulated magnetic phase diagram using a thickness dependent effective out-of-plane anisotropy	111
4.16 Analytical single domain to vortex phase boundary fit to the experimental phase diagram	118
4.17 <i>In situ</i> MFM images of a nickel disk possessing a vortex state	120
4.18 SEM micrograph of a nickel disk with additional gold contacts used to measure the disk magnetoresistance	123
4.19 AMR response of an 800 nm diameter disk	124
4.20 The AMR response of the 800 nm diameter disk in the 90° orientation with additional <i>in situ</i> MFM images and simulations, explaining the effect of inhomogeneous current distribution	126
4.21 AMR response of 800 nm diameter disk for field applied at all angles from $0 - 180^\circ$	128
4.22 MFM images of permalloy L-shape domain wall trap by Corte-leon et al.	129
4.23 AFM image of nickel L-shape hybrid junction	130
4.24 Magnetoresistance of the Nickel L-shape	133
4.25 <i>In-situ</i> MFM images of the nickel L-shape	134
4.26 SEM image of permalloy L-shape hybrid junction	136
4.27 Magnetoresistance of the Permalloy L-shape	137
4.28 <i>In situ</i> MFM of permalloy L-shape hybrid junction	138
5.1 SEM micrograph of 800 nm diameter 30 nm thickness SF proximity junction & AFM topography image of a 1000 nm disk junction	142
5.2 Temperature dependence of the differential resistance of an 800 nm diameter 25 nm thickness disk junction	143
5.3 $I_c(T)$ plot for a 800 nm diameter hybrid junction and aluminium nanowire without ferromagnetic proximity	145
5.4 $I_c(T)$ plot for an aluminium nanowire when current is passed through an 800 nm diameter hybrid junction and when the current bypasses the junction	148

5.5	$I_c(T)$ plot for a 800 & 1000 nm diameter hybrid junctions in disk sample 2 before and after field	150
5.6	SEM micrograph of the sample used to investigate the range of the long range suppression of I_c	154
5.7	differential resistance of the sample used to investigate the range of the long range suppression of I_c	155
5.8	$I_c(T)$ data for the sample used to investigate the range of the long range suppression of I_c	157
5.9	Fitting of the current at wich $T_e = T_c$ to the SNS to normal state transtion of disk sample 1	158
5.10	SEM micrograph of the heat sink samples used to test for suppression of superconductivity by local heating	160
5.11	$I_c(T)$ for the hybrid junctions with and without heat sinks	161
5.12	SEM image of the Au SNS junctions with and without heatsinks used as a control experiment to test the suppression superconductivity by local heating	163
5.13	differential resistance at 0.3 K for Au SNS junctions	164
5.14	$I_c(T)$ data for the adjacent Al nanowire with current injection through Au SNS junctions	165
5.15	SEM image of a Hybrid junction loop interferometer	166
5.16	$I_c(T)$ for 800 nm disk junction interferometer before and after field	167
5.17	$I_c(T)$ for 1000 nm disk junction interferometerd	168
5.18	800 nm disk junction phase depednent oscillations before and after field at 0.85 K	169
5.19	800 nm disk junction phase depednent oscillations before and after field at 0.3 K	171
5.20	1000 nm disk junction phase depednent oscillations before and after field at 0.3 K	172
5.21	1000 nm disk junction Al phase depednent oscillations before field at 0.85 K	173

5.22 Fits of the peak 800 nm disk interferometer I_c decay to a Fraunhofer inter- ferce model	176
5.23 Fits of the peak 1000 nm disk interferometer I_c decay to a Fraunhofer in- terferce model	177
5.24 AFM image of nickel L-shape hybrid junction	180
5.25 The temperature dependence of the differential resistance of the nickel L- shape hybrid junction	181
5.26 The magnetic field dependence of the critical current of the nickel L-shape hybrid junction	182
5.27 SEM image of permalloy L-shape hybrid junction	183
5.28 Temperature dependence of dV/dI for the permalloy L-shape hybrid junction	184
5.29 Temperature dependence of I_c for the permalloy L-shape hybrid junction .	185
5.30 The anisotropic magnetoresistance of the permalloy L-shape domain wall trap at and the magnetic field dependence of the critical current of the Permalloy L-shape hybrid junction at 0.3 K	186
5.31 The dV/dI of the permalloy L-shape hybrid junction in the collinear and domain wall states	187
5.32 Fitting of the $I_c(T)$ for disk sample 2 to low temperature limit of long SNS junctions theory	192
5.33 Fitting of the $I_c(T)$ for disk sample 2 to high temperature limit of long SNS junctions theory	194
5.34 Fitting of the $I_c(T)$ for disk sample 2 to high temperature limit of long SNS junctions theory for arbitrary junction length	196
5.35 Fitting of the $I_c(T)$ for disk sample 1 to the theories of local hot spot heating	201

List of Tables

5.1	Table of the I_c properties of 800 and 1000 nm disk interferometer devices . .	174
-----	--	-----

Chapter 1

Introduction

The aim of this research was to investigate the role of magnetization in proximity effects between nanoscale superconductors and ferromagnets. The focus of this project was specifically directed towards how the ferromagnetic suppression of superconductivity is altered by changing magnetization. The proximity effect can refer to the leakage of superconducting electrons into an adjacent normal metal, first observed in 1932 by Holm and Meissner [1]. Similarly however, the proximity effect can refer to the inverse situation, i.e. the suppression of superconductivity in a superconductor by proximity to a non superconducting material. In normal metals this effect is mostly negligible. However, the long-range spin ordering of superconductivity and ferromagnetism are antagonistic: while superconductivity seeks to pair electrons with anti-parallel spin, ferromagnetism seeks the alignment of adjacent spins. This antagonism induces a strong suppression of superconductivity near the interface between superconducting and ferromagnetic materials. This project aims to investigate if this suppression is sensitive to the magnetization of the ferromagnetic element, and if such effects can be controlled.

Research in hybrid superconducting-ferromagnetic (SF) structures has been an area of interest for approximately 20 years, since the advent of thin film technologies made the observation of proximity effects possible. This is because the characteristic length for changes to occur in a superconductor is the so-called coherence length, $\xi_s = \sqrt{\hbar D / 2\pi \Delta(0)}$, where D is the materials diffusion constant and $\Delta(0)$ is the superconducting gap energy at

zero temperature. Similarly the distance of penetration of superconducting electrons into a ferromagnet is the ferromagnetic coherence length, $\xi_f = \sqrt{\hbar D / 2\pi k_B T_{curie}}$, where T_{curie} is the Curie temperature of the ferromagnet. ξ_s is on the order of hundreds of nanometres in aluminium, whereas ξ_f is on the order of nanometers due to the pair breaking effect of the ferromagnetic exchange interaction. Therefore, to observe the effects that occur between superconducting and ferromagnetic materials, structures on lengths scale ξ_f to ξ_s must be fabricated, something only possible with thin film technologies.

Early experiments into SF nano-structures in the 1980s concerned the discovery of the π phase in SF multi-layers. The π phase was found to be one of the first consequences of the antagonism of superconductivity and ferromagnetism. The exchange interaction in the ferromagnet was found to generate a zero spin triplet Cooper pair and cause both the singlet and triplet superconducting pair wavefunction to oscillate in space. By correct engineering of the SF layer thickness, this meant that a state could be made in which the phase of the superconducting electrons would be opposite in adjacent layers. Thus, the long ago theorised Fulde–Ferrell–Larkin–Ovchinnikov (FFLO) state of a supposed ferromagnetic superconductor [2] was realised at the SF interface [3, 4, 5]. This discovery encouraged research into how the superconducting electrons penetrate into adjacent ferromagnets and the question was raised, was it possible to create a spin-polarised Cooper pair that could survive in a ferromagnet at distance greater than ξ_f ? The search for this so-called long range triplet superconductivity was the focus of much of SF research from the 1990s to 2000s. It was found both theoretically [6, 7, 8, 9] and experimentally [10, 11, 12, 13] that the key to creating spin polarised Cooper pairs was to create a changing inhomogeneous magnetic structure in the adjacent ferromagnet. This change in the magnetic structure rotated the axis of spin quantisation of the triplet Cooper pair and converted the zero spin pair into a spin polarised pair, immune to the pair breaking exchange field, thus surviving for long distances in the ferromagnet.

Simultaneously with the search for the long-range triplet was the investigation into how a ferromagnet suppressed the superconductivity of an adjacent superconductor, often referred to as the inverse proximity effect. The original question of inverse proximity was

raised in 1988 by Rainer et al. [14]. In this theoretical work it was shown that the exchange field of the ferromagnet leaked into the superconductor, suppressing the pairing of electrons. Experimental work showed that superconductivity, at a distance ξ_s from an SF interface, was indeed suppressed [15]. With the discovery of the need for an inhomogeneous magnetization to create the long-range triplet, research in inverse proximity effects began to question if the similar magnetization dependent effects could be observed on the superconducting side. The earliest confirmation of this came from investigations of micron scale and macroscopic SF bilayers [16, 17]. When the coercive field of the ferromagnetic bilayer was applied and the domains of the bilayer began to rotate, the critical current of the bilayer increased. However, no such effect was observable in nano-structured samples. The problem was approached theoretically by Champel and Escrig [18], who found that a superconducting thin film adjacent to a ferromagnetic domain wall would have stronger superconducting correlations than if placed in contact with a collinear/single domain magnetic structure.

Very recently, a new class of inverse proximity structures has appeared commonly referred to as proximity junctions. Thin film superconducting nanowires are deposited with a small section of the nanowire on the order of ξ_s overlying a ferromagnetic element. Experiments by Marsh [19], Wells [20], Vávra et al. [21, 22] and Lin et al. [23] have shown that the inverse proximity of the ferromagnet suppresses the superconductivity in the nanowire and creates a novel superconducting-normal-superconducting (SNS) junction. Such a structure provides the ideal environment to study the effect of the varying magnetic structure on the inverse proximity effect on the nanoscale. This is possible by careful choice and engineering of the ferromagnetic element used in the junction. This naturally means that any research into ferromagnetic proximity effects in these systems goes hand in hand with the detailed understanding of the magnetic properties of nano-structures.

Thin film nanomagnetism concerns the investigation of new ferromagnetic structures for the purposes of fundamental physics [24, 25], sensing applications [26, 27], and the next generation of memory devices in data storage [28]. The early investigations of proximity junctions by Marsh and Wells [19, 20] utilised the ferromagnetic vortex state in nickel

sub-micron disks. This state consists of an in-plane magnetization that rotates around an out-of-plane core, positioned in the centre. The vortex state has been an intense area of research for the last decade, identifying both the dimensions required to observe it [25, 29] and its dynamic behaviour [30, 31]. This inhomogeneous magnetic state is ideal for the manipulation of the proximity junctions under inhomogeneous magnetization.

In this project, the disciplines of SF hybrid systems and thin film nanomagnetism were combined to investigate the influence of changing magnetization on the behaviour of the new class of proximity junctions. This was done by first performing extensive magnetic force microscopy (MFM) studies of nickel disks to ensure that the desired magnetic vortex state could be reliably fabricated and manipulated. The MFM studies were supported by micro-magnetic simulations of the disks, and a new treatment of simulations in sub-micron nickel disks is presented, demonstrating that, to simulate all the magnetic states observed experimentally in the disks, the model must include an effective out-of-plane crystalline anisotropy. The magnetization reversal of the disks was investigated using *in situ* MFM techniques and electrical measurements. Concurrently with the magnetic characterisation of the disks, magnetotransport and *in situ* MFM studies were performed on nickel and permalloy L-shape domain wall traps, with an aim to use these structures as an alternative to the disks. The L-shape domain wall traps consist of two thin magnetic nanowires placed at a right angle to each other such that the direction of magnetization lies along each arm and the corner where they meet acts as a pinning site for a domain wall. The domain wall can be placed and removed in the corner by application of an in-plane field [27, 32, 33].

The disks were then incorporated into hybrid SF junctions. Low temperature measurements of the junctions were performed that show the unique three phase behaviour, fully superconducting state, normal state and an intermediary SNS like state. It has also been demonstrated that the junctions exhibit a long range influence on the adjacent superconducting nanowires, limiting the critical current of the nanowires. The properties of the hybrid junctions are shown to be dependent on the disk magnetic history, with a reduced critical current after the application of large out-of-plane magnetic fields. The magnetization dependence was then confirmed by use of the L-shape domain wall traps in place

of the disks in the junctions. In these experiments, it is shown that large increases in the critical current of the junction can be strongly correlated with the existence of a domain wall in the adjacent magnetic element.

It has then been demonstrated, via comparison to theoretical models of critical current in SNS junctions, that the junctions do not possess a rigid and well defined junction length, but a length that is proportional to the temperature, i.e. the junction length decreases with decreasing temperature. The dependence of the junction critical current upon changing magnetization is shown to most likely be an extension of this changing junction size, with the length decreasing in the presence of the inhomogeneous vortex and domain wall magnetizations. The anomalous behaviour of the junctions observed by previous works [21, 19, 20, 23, 22], i.e. the existence of two critical current behaviours at high and low temperature and the SNS phase, are shown to be due to thermal effects. Specifically, it is demonstrated that the existence of the SNS phase at high temperature, and subsequent disappearance at low temperature, is due to Joule heating of the hybrid junction in its normal state. The Joule heating is also responsible for the long range limiting of the critical current in the nanowire. This is demonstrated by the addition of heat sinks to the junctions to reduce the joule heating and by using the junctions as the weak link in hybrid Andreev loop interferometers. By comparison with theoretical models of superconducting hot spots, it is discussed that the suppression of superconductivity by joule heating can not be explained by hot spot models that consider only a simply heat transfer from the film to the substrate.

In summary, the results presented in thesis demonstrate that this new class of proximity junctions are more complex than originally assumed, provide a new knowledge base for the continued research of SNS junctions induced by the ferromagnetic proximity effect, and are a step toward new types of magnetically controlled superconducting circuits.

Chapter 2

Theory and Background

This chapter gives an overview to the theoretical concepts concerned in the thesis. First an overview of ferromagnetism in mesoscopic structures is given, describing the behaviour of ferromagnetic materials and the theory used to predict the magnetization structures of mesoscopic ferromagnets. The magnetic structure of the ferromagnetic vortex is introduced and a brief overview of the recent research efforts concerning ferromagnetic vortices is presented. The second section of this chapter provides an overview of the physics of superconductivity, including a brief explanation of the cause of superconductivity in metals. Proximity effects are then discussed, explaining the phenomenon that can be observed when a superconductor is brought into contact with a normal metal. This is then extended to the case where the normal metal is replaced with a ferromagnet. The proximity effects between superconducting and ferromagnetic (SF) thin film systems are then discussed in the context of the past few decades of SF research.

2.1 Mesoscopic Ferromagnetism

Ferromagnetism is a well known effect of long range order of magnetic moments, or spins. Ferromagnetism has been studied intensively for many years, great advances include the development of the Ising[34] and Stoner[35] theories of ferromagnetism. The Ising model solved the problem of how a population of quantum mechanical spins in a lattice interacts

to produce long range order. The Stoner model went further and predicted how a population of moments with long range order acting as one large moment, or single domain, behave in an external magnetic field. This correctly described the observed hysteresis of ferromagnetic samples. The famous Curie-Weiss law describes the temperature dependence of the ferromagnetic phase, $\chi = C/(T - T_c)$, where χ is the susceptibility of a ferromagnet above the critical Curie temperature T_c , where the Curie constant C is material dependent. At temperatures below the Curie temperature ferromagnetic materials show a spontaneous magnetization, above the Curie temperature they behave as paramagnetic materials. The most common ferromagnetic materials are the transition metals iron, nickel and cobalt. These are the itinerant ferromagnets in which the Curie temperature is much higher than room temperature.

Following from these fundamental works, modern day research in ferromagnetism is focused in two areas. The first is discovery of new ferromagnetic materials and exotic ferromagnetism. The second is due to advancements in modern fabrication techniques and entails the investigation of mesoscopic magnetic structures for use in novel devices, data storage and biomedical applications. In this dimensional range a careful balance is achieved between the alignment of spins governed by the exchange interaction and the formation of domains to lower the magnetic energy of the spins. Because of this, mesoscopic magnetism is home to a wealth of rich physics and possible applications. Research in mesoscopic magnetism has been aided in recent decades with the advent of numerical simulations, such as the OOMMF code developed by NIST [36] as well as nmag and magpar [37, 38] codes. This section of the thesis will discuss the theory of ferromagnetism, mesoscopic magnetic structures and the OOMMF software used to perform micromagnetic simulations in the project.

2.1.1 Magnetic interactions

Dipolar interaction

The first magnetic interaction to consider is that of the dipole-dipole interaction, in which two magnetic dipoles interact via their respective magnetic fields. The force between the two moments will induce a torque that will act to align the two moments in opposite directions. The potential energy P associated with two magnetic moments of magnetization m_1 and m_2 at a distance \hat{r} from each other is:

$$P = -\frac{\mu_0}{4\pi|\hat{r}|^3}(3(\mathbf{m}_1 \cdot \hat{r})(\mathbf{m}_2 \cdot \hat{r}) - \mathbf{m}_1 \cdot \mathbf{m}_2) \quad (2.1)$$

If one considers the typical magnetic moment of electron spins, on the order of the Bohr magneton $\mu_B = e\hbar/2m_e$ at a distance on the order of inter atomic distance $\sim 1 \text{ \AA}$ then the energy of the interaction is $P \sim 9 \times 10^{-24} \text{ J}$ or a temperature of $\sim 0.7 \text{ K}$. As ferromagnetic materials exhibit spontaneous alignment of their magnetization at temperatures hundreds of times this, coupled with the fact that the dipolar interaction seeks to place the moments anti-aligned, it is clear that the dipole-dipole interaction cannot be the source of spontaneous magnetization.

Exchange interaction

In 1926 both Werner Heisenberg and Paul Dirac independently solved the problem of spontaneous magnetization in the context of quantum mechanics, proving that the alignment of spins in ferromagnetic materials cannot be described classically. The result is famously known as the exchange interaction. The exchange interaction is a consequence of both the indistinguishable nature of electrons and the Pauli exclusion principle. The following discussion is a condensed summary of the exchange interaction based on the description found in ref [39]. If one considers two electrons, 1 & 2, in two similar potentials, V , with no electron-electron interaction then they can be described by the following Schroedinger equation (eqn 2.2) and trivial answers (eqn 2.3):

$$\left[-\frac{\hbar^2}{2m}(\nabla_1^2 + \nabla_2^2) + V(q_1) + V(q_2) \right] \psi = E\psi \quad (2.2)$$

$$\psi_a(1)\psi_b(2) \quad \& \quad \psi_a(2)\psi_b(1) \quad (2.3)$$

where $\psi_a(1)$ is the one electron wavefunction for electron 1 in state a . However, this assumes that the electrons are distinguishable, which they are not. Because the electrons are indistinguishable the two electron wave functions must be equal such that $|\psi(1,2)|^2 dq_1 dq_2 = |\psi(2,1)|^2 dq_1 dq_2$ [39], where $\psi(1,2)$ is the 2 electron wavefunction that describes both systems. The only wavefunctions that satisfy these conditions are the symmetric and anti-symmetric linear combination of eqn 2.3:

$$\psi(1,2)_{sym} = \frac{1}{\sqrt{2}}[\psi_a(1)\psi_b(2) + \psi_a(2)\psi_b(1)] \quad (2.4)$$

$$\psi(1,2)_{anti} = \frac{1}{\sqrt{2}}[\psi_a(1)\psi_b(2) - \psi_a(2)\psi_b(1)] \quad (2.5)$$

Due to the Pauli exclusion principle the wavefunctions of electrons must be antisymmetric, thus it would suggest that the wavefunction of the two electrons is simply eqn 2.5. However, this neglects the electron spin. If one considers the above two wave functions as solutions for electrons with no spin, Φ_{sym} and Φ_{anti} , and that the spin states are independent of these solutions, then one can introduce additional wavefunctions that describe the symmetrical and antisymmetrical arrangement of the electrons spins, χ_{sym} and χ_{anti} respectively. χ_{sym} is the state in which the electron spins are aligned and χ_{anti} is the state in which the spins are opposite. Because the electrons must have antisymmetric wavefunctions this leaves two possibilities:

$$\Phi_{sym}(1,2)\chi_{anti}(1,2) \quad \& \quad \Phi_{anti}(1,2)\chi_{sym}(1,2) \quad (2.6)$$

One can then consider these two wavefunctions in their single electron form, $\psi_I = \Phi_{sym}(1,2)\chi_{anti}(1,2)$ and $\psi_{II} = \Phi_{anti}(1,2)\chi_{sym}(1,2)$ respectively. The interaction between electrons

can then be introduced as the simple interaction Hamiltonian between two hydrogen atoms. $H_{1,2}$, with nuclei a and b:

$$H_{1,2} = \frac{e^2}{r_{a,b}} + \frac{e^2}{r_{1,2}} - \frac{e^2}{r_{1,b}} - \frac{e^2}{r_{2,a}} \quad (2.7)$$

where $r_{a,b}$ is the distance between nuclei, $r_{1,2}$ is the distance between the electrons and $r_{1,b}$ and $r_{2,a}$ are the distances from each electron to the nucleus of the other atom, where this expression is given in CGS units. By solving for the energies of states ψ_I and ψ_{II} using this Hamiltonian one is left with the energies;

$$E_I = A^2(K_{1,2} + J_{1,2}) \quad (2.8)$$

$$E_{II} = B^2(K_{1,2} - J_{1,2}) \quad (2.9)$$

where $K_{1,2}$ is the Coulomb interaction energy integral, $J_{1,2}$ is the exchange integral and A and B are normalisation constants. The existence of the integral $J_{1,2}$ is the source of ferromagnetism. When J is positive, then ψ_{II} is the ground state and the electron spins are aligned. This is the case in the ferromagnetic materials. The above equations can be simplified for use by considering the two electrons as coupled by their spins only, which is valid as the orbital symmetry and spin alignment are correlated. The coupling is proportional to the scalar product of the electron spins, \mathbf{s}_1 and \mathbf{s}_2 such that the energy is now:

$$E = K_{1,2} - \frac{1}{2}J_{1,2} - 2J_{1,2} \mathbf{s}_1 \cdot \mathbf{s}_2 \quad (2.10)$$

In this equation, only the last term is important for most applications. This leads to the more commonly used exchange Hamiltonian:

$$H = -2J \sum_{i,j} \mathbf{S}_i \cdot \mathbf{S}_j \quad (2.11)$$

Where additional simplification has been made; \mathbf{J} has been assumed to be isotropic within a given crystal lattice and \mathbf{S}_1 and \mathbf{S}_2 are the total spins of the atoms i and j . The sum is over all atoms in the lattice, j , with their nearest neighbours, i . This describes the basis of the exchange interaction.

Micromagnetics

While the derivation of the exchange Hamiltonian (eqn 2.11) allows for the calculation of the energy of a given lattice of spins, it is not simple to solve for a particular distribution of spins in a ferromagnetic material. The problem of mesoscopic distributions of spins was solved by Landau, Lifshitz and Gilbert [40]. The equation is named after it's discoverers and known as the LLG equation:

$$\frac{\partial \mathbf{M}}{\partial t} = -\gamma(\mathbf{M} \times \mathbf{H}_{eff}) - \frac{\gamma d}{M_s}[\mathbf{M} \times (\mathbf{M} \times \mathbf{H}_{eff})] \quad (2.12)$$

where \mathbf{M} is the magnetization, M_s the saturation magnetization, γ the gyromagnetic ratio, d is a dimensionless dampening constant and H_{eff} is an effective field, which will be discussed in detail below. Rather than consider the spins of every atom in the lattice, the LLG equation simplifies the problem to a collection of classical magnetic moments where each moment is the effective average of the atomic spins in a given volume. This approximation is valid as long as the distance between each of these moments is within the so called exchange length $L_{ex} = \sqrt{2A/(\mu_0 M_s^2)}$ [41] where A is the exchange energy constant in units J m^{-1} and M_s the saturation magnetization in units A m^{-1} . The assumption is that the spins within the L_{ex} distance of each other are approximately aligned and act as one large moment and that changes in the direction of magnetization are only possible over distances larger than this length scale.

The effective field term H_{eff} is a collective term that contains the effect of all the individual forces that exert a torque on the magnetic moments. To derive this effective field term one must first consider all the energy contributions to the total energy of the distribution of moments. The total energy is a sum of the individual energy terms:

$$E_{Total} = E_{Exchange} + E_{Magnetostatic} + E_{Anisotropy} + E_{Zeeman} \quad (2.13)$$

These four energy terms will now be discussed separately, beginning with the exchange energy.

A simplified way to calculate the exchange energy per unit volume of a distribution of magnetic moments is to Taylor expand equation 2.11 to [42]:

$$\frac{E_{Exchange}}{V} = A[(\nabla \mathbf{m}_x)^2 + (\nabla \mathbf{m}_y)^2 + (\nabla \mathbf{m}_z)^2] \quad (2.14)$$

where \mathbf{m}_i are the magnetic moment components in the x, y z axes and A is the exchange constant. The strength of this interaction has great weighting on the size of micro magnetic domains. The exchange energy is lowest when all moments in the magnetic body are collinear, correspondingly it has a minimum when the vector gradient of magnetisation unit vector $\mathbf{m} = \mathbf{M}/\mathbf{M}_s$ is a minimum. While it would still be possible to calculate the exchange energy of each moment by using equation 2.11 directly, equation 2.14 allows for a simpler calculation for a very large collection of magnetic moments. It is worth stating though that if possible, 4-neighbour or in 3D calculations, 6-neighbour exchange calculations are more accurate.

The magnetostatic or demagnetization energy concerns the energy cost of stray magnetic fields caused by the alignment of magnetic moments caused by the exchange interaction and is the manifestation of the dipolar interaction (eqn. 2.1). In a simplified model, the alignment of magnetic moments induces magnetic charges at the surface of the body, these charges cause a field, known as the demagnetising field, \mathbf{H}_d . The energy due to this for an arbitrary magnetic body is [42],

$$E_{Magnetostatic} = - \int_{\tau} \frac{1}{2} \mu_0 \mathbf{M} \cdot \mathbf{H}_d dV \quad (2.15)$$

where μ_0 is the permeability of vacuum and τ is the volume enclosed by the magnetic material. Clearly it can be seen from eqn 2.15 that the magnetostatic energy will be minimum when either \mathbf{M} or \mathbf{H}_d is a minimum, the former is a trivial solution. Therefore,

the formation of domains which minimise the stray field, \mathbf{H}_d , are energetically favourable. This leads to shape anisotropy in magnetic elements; if a particular axis of a magnetic element exists such that magnetisation along this axis induces the lowest magnetic surface charges in comparison to other axes then this will be a preferred axis of magnetisation. An example of this shape anisotropy is a thin film magnetic wire. When magnetised along the axis of the wire there is only stray field at the ends of the wire, whereas if magnetised perpendicular to the axis of the wire there is a much greater stray field, the same is true for an out-of-plane magnetisation. The demagnetizing field is often calculated by using some demagnetizing factor NM_s , where M_s is the saturation magnetization and N is a unit-less parameter that describes the demagnetizing field for an object of given geometry. The anisotropy energy term is concerned with crystalline anisotropy. Crystalline anisotropy occurs due to symmetries in the crystal lattice and spin orbit coupling. Crystalline anisotropy has two common forms; uniaxial and cubic, depending on the lattice. In spherical polar coordinates, where the anisotropy axis is taken as the z axis, the energy density of the uniaxial anisotropy can be taken as the expansion in z [42]:

$$\frac{E_{uniaxial}}{V} = K_0 + K_1 \sin^2 \theta + K_2 \sin^4 \theta + \dots \quad (2.16)$$

where K_i are the anisotropy constants, which are material dependent. Often this is truncated to the second term, thus the sign of K_1 controls the direction of anisotropy, i.e. with $K_1 > 0$ giving energy minima along the z axis and $K_1 < 0$ giving an energy minima in the x - y plane. Similarly the expansion in Cartesian coordinates for the cubic anisotropy energy density is [42],

$$\frac{E_{cubic}}{V} = K_0 + K_1(m_x^2 m_y^2 + m_y^2 m_z^2 + m_z^2 m_x^2) + K_2 m_x^2 m_y^2 m_z^2 \dots \quad (2.17)$$

again if truncated to the second term it can be seen that with $K_1 > 0$ the energy minima exist along the Cartesian axes and with $K_1 < 0$ the minima at the corners of the cube.

Lastly the Zeeman energy simply describes the energy of a magnetic dipole in a magnetic field and thus takes into account the effect of applied fields on the magnetic element in

question and is given by [42],

$$E_{zeeman} = - \int_{\tau} \mathbf{M} \cdot \mathbf{H}_a dV \quad (2.18)$$

where the energy is taken across the entire volume τ and \mathbf{H}_a are the externally applied fields. Via first order variation theory these energy expressions can be combined to find the energy equilibrium conditions and one can write a term for the effective field \mathbf{H}_{eff} , as was done by Brown [43], as,

$$\mathbf{H}_{\text{eff}} = \frac{2}{\mu_0 M_s} \nabla \cdot (A \nabla \mathbf{m}) - \frac{1}{\mu_0 M_s} \frac{\partial f_{anis}}{\partial \mathbf{m}} + \mathbf{H}_d + \mathbf{H}_a \quad (2.19)$$

where f_{anis} refers to the applicable anisotropy energy function (eqns. 2.16 and 2.17), uniaxial or cubic, depending on the material in question. It can be seen that when using eqn 2.19 for the effective field in eqn 2.12 one is solving a non linear equation, and as such analytical solutions will either be for trivial cases or will make use of simplifications. Because of this, solutions to problems of interest are often solved numerically. Micromagnetic simulation software is commonly used for such numerical calculations. One of the most commonly used is known as OOMMF or the *Object Oriented Micro Magnetic Framework* developed by NIST [36], which has been used in the work presented in the thesis.

2.1.2 Domain structure

Domains

With no external influence, a ferromagnetic material appears to have no spontaneous magnetization. This seems counter-intuitive when considering that the alignment of spins caused by exchange interaction should create a total magnetization in the material. However, when one considers the energy contributions (eqns 2.15 - 2.17) that compete with the exchange interaction it can be seen that an equilibrium must be struck between the exchange interaction and the magnetostatic energy of such a large collection of magnetic moments. This equilibrium is achieved by the formation of magnetic domains. Each domain has a typical size of 10^{-7} m to 10^{-5} m within which the moments are aligned along

the same direction, however the magnetization of each domain will be along different directions such that the stray field of each domain averages out with the other domains to zero. This principle is illustrated in figure 2.1. When the magnetic material consists of a single large domain the stray field is large (fig 2.1a), yet by splitting into two domains the stray field is reduced (fig 2.1b) or even effectively eliminated by splitting into more domains (fig 2.1c). The size and number of domains depends on the strength of the exchange interaction, the shape of the ferromagnet and the energy associated with the boundary between the domains. This boundary is known as a domain wall.

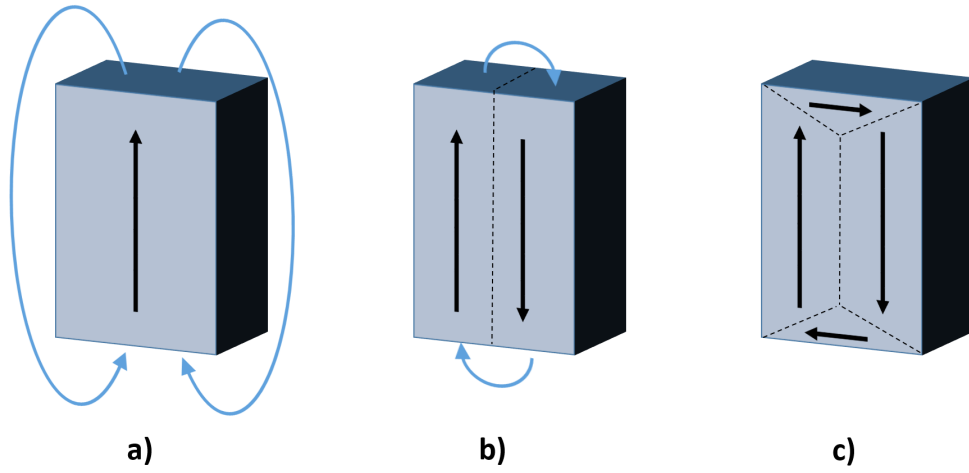


Figure 2.1: Illustration of the domain principle. a) the magnetic material is magnetized as a single large moment. The stray field is large and extends far from the sample. b) By splitting the magnetization into two oppositely magnetized domains the stray field is reduced. c) by splitting into 4 domains that rotate around the materials edge, the stray field is effectively eliminated reducing the total energy of the ferromagnet.

Domain walls form naturally in bulk ferromagnetic materials to reduce the overall magnetic energy of the system. However, the domain wall structure is highly dependent on the material properties and dimensions and comes with it's own energy cost. Domain walls can be generally split into two types, Néel and Bloch walls. Néel walls rotate the local spins within the plane of the the domain alignment as shown in fig 2.2 top image. This is most common in magnetic materials with strong uniaxial anisotropy, such as magnetic thin films, where the short range misalignment of spins has a lower energy cost than

aligning the moments out of plane with the film against the thin film shape anisotropy, as illustrated in fig. 2.2 bottom image. Bloch walls rotate the spins perpendicular to the domain alignment. This arrangement allows for much smaller domain walls on the order of the exchange length, however this has a large magnetostatic energy cost in typical thin films with anisotropy aligned along the plane of the film. Because of this, Bloch domain walls are typical of thin films in which the crystalline anisotropy is out-of-plane with the film.

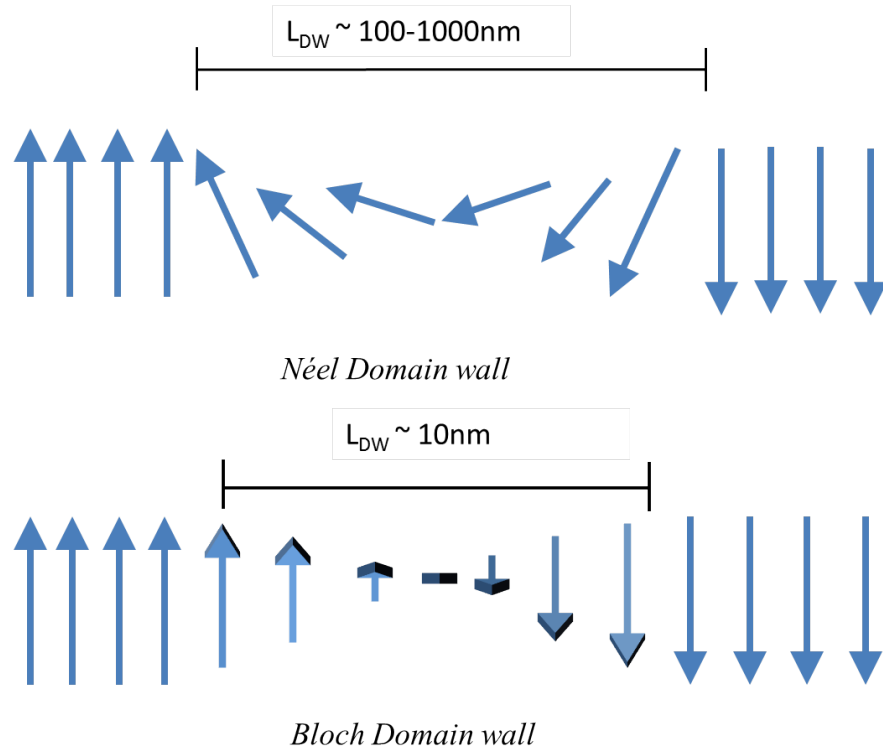


Figure 2.2: Top: the Néel wall rotates the magnetization within the plane of the domains magnetization direction. This creates quite large domain walls on the order of hundreds of nanometres Bottom: The Bloch wall rotates the magnetization out-of-plane relative to the domains direction of magnetization. This allows the domain wall to be smaller than the Néel wall, but is limited by both crystalline and shape anisotropy and often is not plausible in thin films due to the large energy cost of directing the magnetization out-of-plane with the film.

The magnetic vortex

Advances in microfabrication technology have allowed the creation of nano engineered structures on the order of tens to hundreds of nanometres. This allows for the control of magnetic structure by manipulation of the magnetostatic energy via geometry. For example, this has been leveraged to control the position of domain walls in lithographically patterned ferromagnetic wires for sensing applications [26, 27] by controlling the width and length of the wire. This can be taken further by controlling all the dimensions of the structure and shrinking the size from large multi-domain structures to structures so small that the exchange energy dominates and the magnetic structure behaves as a large single domain. At dimensions between these two extremes, the magnetization structure is very sensitive to the geometry, this can be seen most prominently in the ferromagnetic vortex. This short overview of the magnetic vortex state serves to highlight the importance and ongoing interest in magnetic vortices. The ferromagnetic vortex, herein referred to

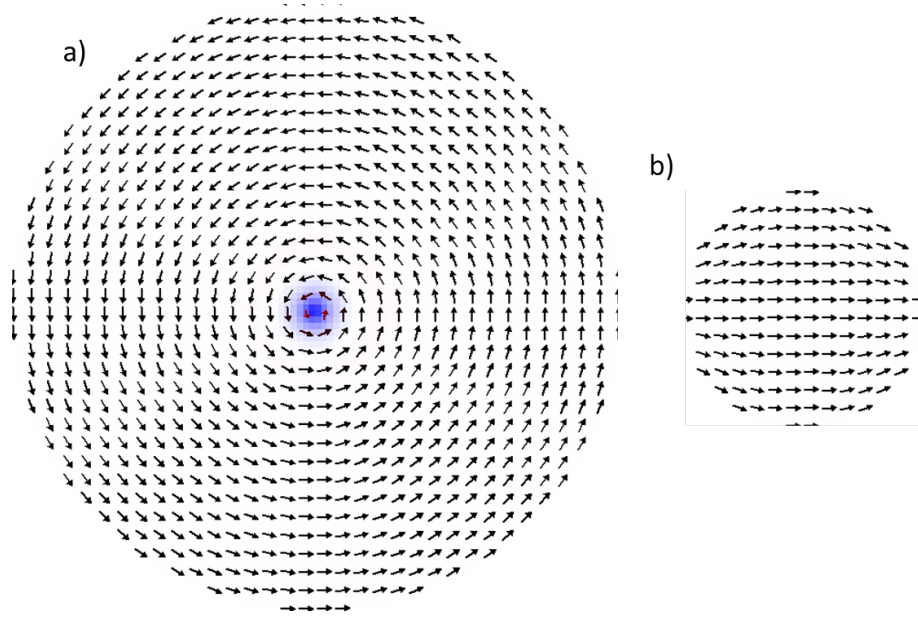


Figure 2.3: a) A simulated nickel disk of thickness 20 nm and diameter 800 nm, the disk has a vortex structure with out-of-plane central vortex core seen as the blue dot. b) A simulated nickel disk 15 nm thick and 300 nm in diameter. As the disks dimensions have shrunk the exchange energy begins to dominate and the disk is in the single domain state.

as simply the vortex, exists in small magnetic thin films with square, triangular or most often circular geometry. The vortex is defined as a flux closure domain structure, as the magnetization remains within the plane of the thin film, rotating such that the local magnetization vector is approximately parallel with the disk edge. At the centre of the disk the magnetization is forced out of plane, perpendicular to the thin film, this is known as the vortex core. The vortex structure is illustrated in fig 2.3a, as a micromagnetic simulation using the OOMMF code [36]. The arrows indicate the direction of local magnetization and colour indicates out of plane components of magnetization. Figure 2.3b demonstrates that as the size of the disk is shrunk the exchange energy dominates and the disk becomes a single domain.

One of the earliest observations of magnetic flux closure domains was performed by Dunnin-Borkowski et al. in 1998[24] in which the authors used off axis electron holography and Lorentz microscopy to image cobalt rectangular elements 30 nm thick and 275 nm by 220 – 800 nm laterally. Their imaging indicated that at remenence the magnetization structure was closed, such that no magnetic moment could be detected.

Cowburn et al. [25] performed hysteresis measurements of superpermalloy ($\text{Ni}_{80}\text{Fe}_{14}\text{Mo}_5$) disks of diameters 55 – 500 nm and thickness 6 – 15 nm using magneto-optical methods. Analysis of the hysteresis loops indicated that the geometrical crossover from single domain to vortex states was dependent on both the thickness and diameter of the disks. They found that the extremes of this boundary exists at ~ 200 nm diameter and ~ 5 nm thickness and ~ 100 nm diameter and ~ 15 nm thickness. This work was then extended to the geometry of rectangles and triangles [44].

At a similar time, the internal structure of the vortex was probed by MFM by two groups independently. First, Pokhil et al.[30] performed MFM measurements of the internal structure of permalloy disks in applied in-plane magnetic fields. The images, fig 2.4a, showed no obvious vortex core and a chaotic arrangement of domain walls. yet the domain structure resembled that of the rotating flux closure of a vortex. Furthermore, in applied in-plane magnetic field, the domain structure evolved as expected for a vortex structure, with the vortex core moving perpendicular to the direction of applied field.

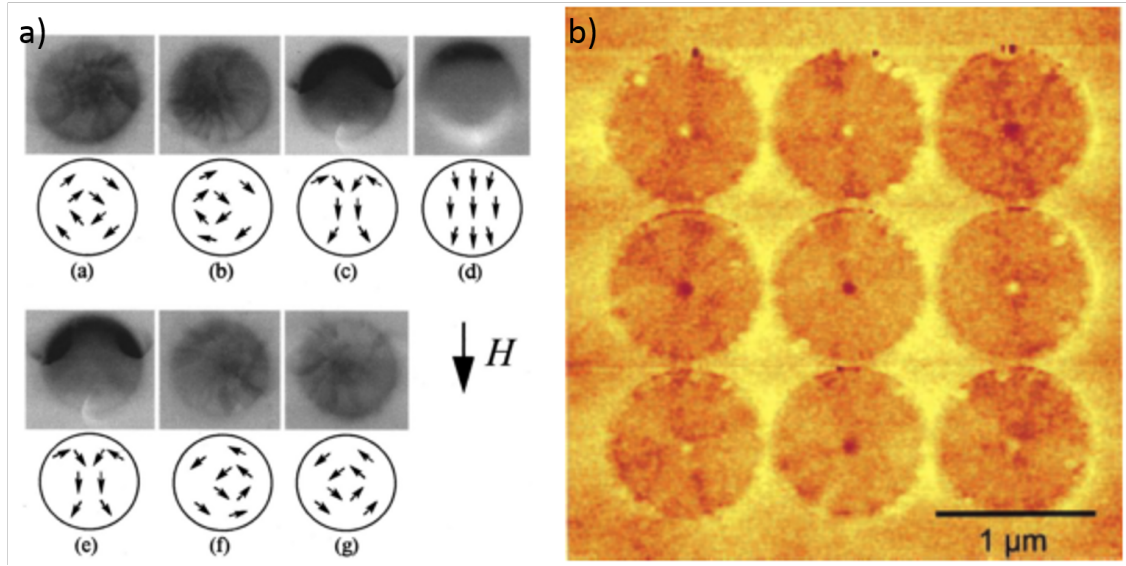


Figure 2.4: a) Early MFM measurements by Pokhil et al. of flux closure in permalloy disks of diameter 800 nm and thickness 20 nm[30]. The ideal vortex image was not obtained but the flux closure behaviour was observed. b) MFM images obtained by Shinjo et al. [45] in permalloy disks of diameter 1000 nm and thickness 50 nm. The MFM images confirmed the vortex structure and were the first to directly observe the characteristic out-of-plane core using MFM.

This was improved upon later by Shinjo et al. [45] who observed the first MFM images of the ideal vortex in permalloy disks 50 nm thick and 300 – 1000 nm in diameter. In these MFM images, fig 2.4b, the vortex core was clearly visible and the magnetic response from the plane of the disks was comparable with the background response, as was expected from the MFM measurements which are sensitive only to fields directed perpendicular to the film. This experiment helped prove the practicality of MFM for use in measurements of such small magnetic structures as the vortex core. The core structure in iron ellipsoids was later measured in high resolution using spin polarised Scanning Tunnelling microscopy (STM) by Wachowiak et al. [46]. Since these experiments the domain evolution has been shown to align with the hysteresis features like those measured by Cowburn et al., as expected[47, 31, 48] and the cross over between single domain and vortex states measured by Cowburn et al. was calculated by Hoffman et al. using a 2D magnetization approximation [49], giving the critical disk thickness for the phase boundary between single domain

and vortex states in short circular cylinders with in-plane uniaxial anisotropy as:

$$t_{crit} = \frac{R}{3.37} \left\{ \exp \left[\frac{4A}{2.4M^2R^2} \left(\ln \left(\frac{R}{a} + 1 \right) + \gamma \right) + \frac{K_u}{2.4M^2} \right] - 1 \right\}^{1.15} \quad (2.20)$$

where A is the exchange constant, R is the disk radius, a is the lattice constant of the material, M is the saturation magnetization, K_u is the uniaxial anisotropy constant and $\gamma \approx 0.5772$ is the Euler constant.

Micromagnetic simulations of permalloy sub-micron disks by Ha et al. [50] predicated a much richer variety of magnetic states than those observed previously, for example the so called C-state and buckling S-state that were predicted earlier by Rave and Hubert [51]. These states were observed later by Kazakova et al. [52] in FeCo sub-micron disks. Recent micromagnetic simulations have included the effects of the chosen material anisotropy to more accurately simulate the magnetic structure [53].

The majority of research into sub micron structures exhibiting vortex states was performed in permalloy, this being the ideal material for investigating shape anisotropy based effects due to it's mostly negligible uniaxial crystalline anisotropy. However, because of this there is sparse literature on the domain structure in nickel sub micron disks, which are of interest to the work presented here. Evidence that the variety of domain structures for nickel disks was more complicated than that of permalloy was first presented by Skidmore et al. [29] in 2004. This work showed a detailed study of nickel cylinders 100 nm thick and 40 – 1700 nm in diameter. In these cylinders a 2D approximation is no longer valid. Using MFM imaging, Skidmore et al identified the so called "bullseye state" similar to a vortex structure but with a much large core diameter and observed stripe domain states in the thickest and largest cylinders. MFM images of the states observed by Skidmore et al. are presented in fig. 2.5 left image, with the percentage of states observed at each diameter shown in fig. 2.5 right image. Within recent years however, interest in nickel elements has increased, for example the work by Samardak et al. [54] in which vortex states were observed in 3D hemispherical granular nickel elements formed by electro-deposition and the observation by Nasirpouri et al. [55] of single domain and vortex states in closely

packed nickel nano dots. As well as disk and dot structures, there has also been increasing attention toward nickel nanowires [56] and planar thin film wires [57].

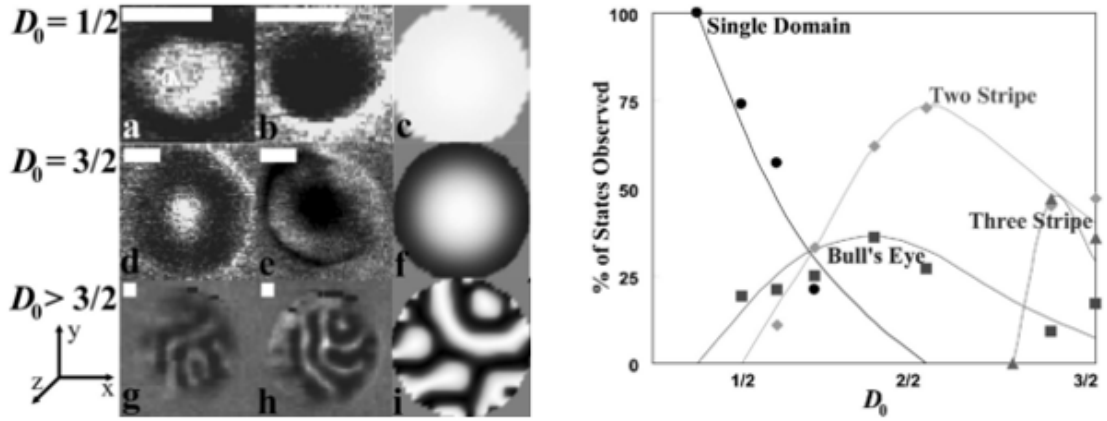


Figure 2.5: Left: MFM images of nickel cylinders by Skidmore et al. [29]. D_0 is the ratio of the cylinders diameter to the stripe domain period of the film, measured to be 200 nm. Therefore the cylinder diameters are 100 nm, 300 nm and > 300 nm from top to bottom. The thickness of all cylinders is 100 nm. The smallest diameter cylinders were seen to be single domain particles. Larger diameter cylinders showed a bulls eye like state similar to that of the vortex but with a much increased core size. At $D_0 > 3/2$ the cylinders showed a stripe domain state. Right: the distribution of magnetic states in cylinders with increasing diameter observed by Skidmore et al.. At small diameters the single domain dominates. As the diameter increases the bullseye state appears, followed by the stripe domain states at $D_0 > 3/2$.

From the mid 2000s interest in vortex states shifted towards how the vortices could be manipulated and used for functional purposes such as magnetic memory storage. Towards this end, much work was focused on electrical measurements of disks to determine their magnetic state. The magnetoresistance of multiple permalloy disks were measured by depositing the disks on top of an Au strip, such that four point resistance measurements can be made of the disk/strip bilayer [58, 59] and subsequently using Kirchoffs current laws to extrapolate the response to a single disk, showing hysteric magnetoresistance. Measurements of the magnetoresistance of a single permalloy disks were performed by Vavassori et al. [60] using a four probe geometry of gold probes deposited on top of the disk. This allowed for much more accurate electrical measurement of the vortex nucleation and

annihilation. These being the applied fields at which the vortex core structure nucleates as the disk transitions from a saturated single domain structure and the field at which the vortex core is annihilated as the disk transitions from the vortex state to the saturated single domain state. A similar geometry was used by Goto et al. [61], however with two of the contacts deliberately asymmetric, such that as a field is applied, the vortex core will travel under the contacts differently. This meant that the chirality of magnetization could be determined from the electrical response.

Once electrical measurement of the vortex dynamics was shown possible new research aimed to control the vortex properties, such as core direction and magnetization chirality, via electrical methods. Ishida et al. [62] measured the vortex magnetoresistance in a permalloy disk using the planar hall effect (PHE) whilst simultaneously injecting a DC current. It was found that the DC current displaced the vortex in the disk, and with an applied field annihilated the vortex. This indicated that electrical control was possible. Similarly, Kasai et al. [63] showed that an AC current applied to a disk creates a resonant excitation of the vortex core. The vortex core direction has proved more difficult to control. It has been shown that pulses of AC magnetic field can switch the core direction in permalloy disks [64] and theoretically suggested that magnetic field pulses can facilitate ultra fast switching of the vortex core [65]. Electrical control of the core has been shown via the application of high frequency AC current [66] and nanosecond current pulses [67]. These techniques, along with tunnelling magnetoresistance, have been used by Nakano et al. [28] to create an all electrical vortex memory cell that uses the cores direction as a binary data bit. In another work towards the control of vortex state properties, Garicia et al. [68] showed that in Co/Pt multilayer disks the size of the vortex core can be increased by increasing the perpendicular anisotropy due to the inter-facial interaction between the cobalt and platinum. The anisotropy can be controlled simply by changing the cobalt thickness.

Control of the vortex chirality has been shown to be possible by introducing asymmetry into the disk geometry in the form of a flat edge to the disk, as in fig. 2.6. This has been shown to reliably nucleate a vortex when going from saturation to remenence that

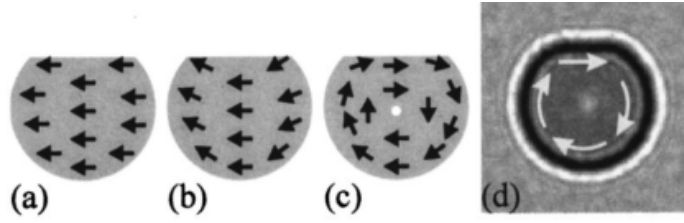


Figure 2.6: a)-c) Modelled magnetization direction of asymmetric permalloy disks by Schrider et al. showing control of the vortex formation with controlled chirality d) Under focused Fresnel image of a permalloy disk with superimposed magnetization direction. Images adapted from [69]

has chirality such that the magnetization along the straight edge is anti-parallel to the direction of the saturating field [69, 70]. Further work by Im et al. [71] has revealed that such asymmetric effects actually take place in disks designed to be symmetric and that the four possible vortex states are not degenerate, due to asymmetries in the surface roughness of the disks and an intrinsic Dzyaloshinskii–Moriya interaction.

2.1.3 Anisotropic Magneto resistance - AMR

Measuring the magnetic properties of thin film nano-structures is a difficult task due to the inherently small magnetic moments involved. The magnetic moment from a single nano-structure is far too small to be measured by SQUID or vibrating sample magnetometers which have sensitivities typically on the order of 10^{-8} emu. Magneto-optical Kerr effect microscopy (MOKE) allows the measurement of hysteresis loops of a nano-structure but requires laser apparatus adding complexity to the measurement apparatus. However, electrical measurement of the magnetic properties of magnetic thin films is possible through the anisotropic magnetoresistance effect (AMR), originally discovered by Lord Kelvin in 1857 [72]. AMR is a consequence of the spin-orbit interaction and as such the exact mechanism and strength of the effect differs between materials. In general, the resistance of a magnetic material is lower when the magnetization \vec{M} is perpendicular to the direction of current \vec{j} . The resistance can be described by equation 2.21, where ρ is the measured resistance, ρ_{\perp} is the resistance when \vec{M} is perpendicular to \vec{j} , ρ_{\parallel} is the resistance when

\vec{M} and \vec{j} are parallel, and α is the angle between \vec{M} and \vec{j} [60]:

$$\rho = \rho_{\perp} + (\rho_{\parallel} - \rho_{\perp})\cos^2\alpha \quad (2.21)$$

The difference in resistance between ρ_{\perp} and ρ_{\parallel} is typically on the order of 1–2 %. Although it is not a direct measure of the magnetization, AMR allows the electrical measurement of the movement of domains and domain walls under field. For example, fast switching events such as the annihilation or nucleation of a magnetic vortex will be seen as jumps in the resistance of the magnetic material, making this effect usefully for the measurement of these switching fields.

2.2 Superconductivity

The term superconductivity refers to a low temperature phase of metals and some more complicated compounds in which the electrical resistivity of the material is exactly zero and the current in the material dissipates no energy to the crystal lattice. At the turn of the 20th century, physicists were at odds as to what would happen to electrical resistivity at low temperatures. Some believed the resistivity would slowly fall to zero at a temperature of absolute zero, others believed there would be a base minimum resistance or that the electron movement would freeze at low temperatures and the resistance would become infinite. However, none of these theories were correct, instead it was discovered that the resistance of some metals sharply decreased to zero at some finite temperature that was material dependent. This drop to zero resistance was originally discovered by Kamerlingh Onnes when he submerged solid mercury into liquid helium in 1911 and observed that the electrical resistance of the mercury was exactly zero, he declare this new state to be a superconductor.

This new phenomenon lead to much immediate interest in the area in the years after the original discovery. One of the most important and famous of such works is the discovery of the Meissner effect. It was clear that the sharp transition from the resistive state to the zero resistance state meant that there was some fundamental phase change in the material. In 1933 Meissner and Ochsenfeld sought to measure how superconductors behaved in magnetic fields to investigate this phase change. In their experiment [73] tin and lead samples were placed in a magnetic field and then cooled beneath their critical temperature, T_c , the temperature at which the metals become superconducting. By measuring the magnetic flux outside of the samples as they cooled it was observed that the magnetic flux permeated the samples above T_c as expected, yet below T_c the flux was completely expelled, as illustrated in fig. 2.7. Thus, the superconductors were found to possess perfect diamagnetism. This effect is seen for magnetic field strengths up to a critical field strength H_c at which point the material transitions into the normal state. This discovery reinforced the understanding that superconductivity was a new phase and provided a second criteria

to determine if a material was superconducting alongside zero electrical resistance; for a material to be superconducting it must exhibit the Meissner effect.

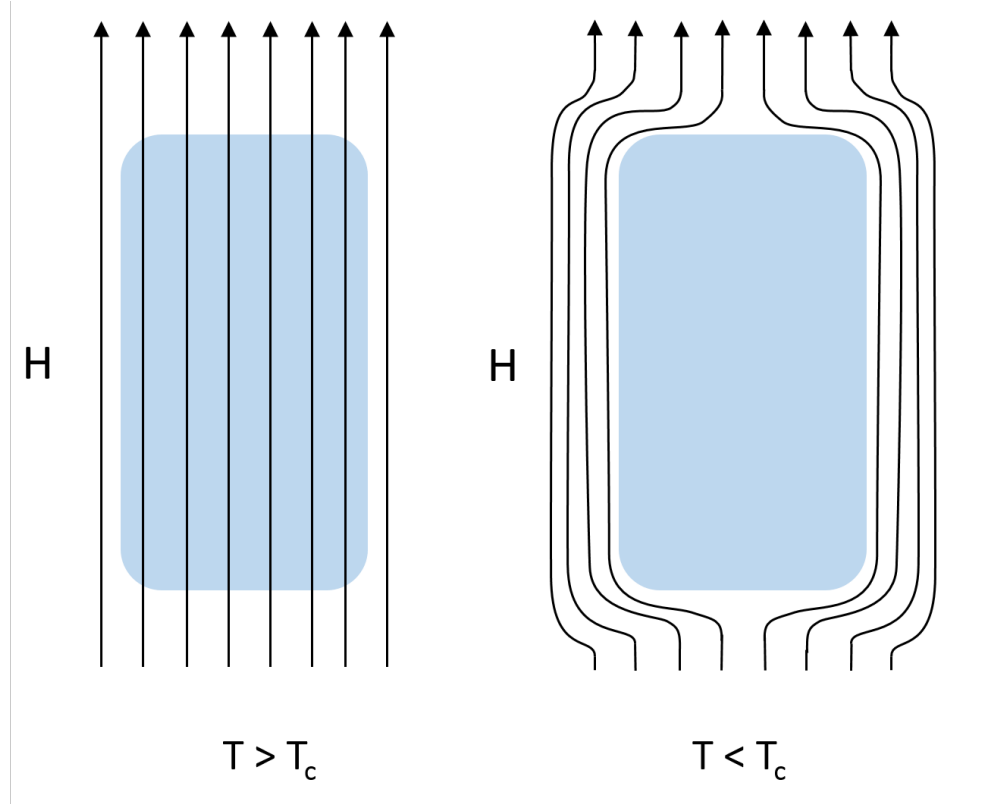


Figure 2.7: This illustration demonstrates the Meissner effect. When above the critical temperature, T_c the magnetic flux passes through the material (left). When cooled below T_c the magnetic flux is expelled from the superconducting material (right).

The mechanism for superconductivity however remained a mystery for the better half of a century. Phenomenological theories arose to describe the experimental observations of superconductivity. The first such theory was developed by the London brothers in 1935 [74]. This theory explained the observation of the Meissner effect by relating the super-current density \mathbf{J}_s , that is the density of superconducting electrons, to the electromagnetic fields. Later in 1950, Ginzburg and Landau derived their famous Ginzburg-Landau theory of superconductivity. This theory described the transition from the normal to superconducting states in the context of Landaus earlier theory of second order phase transitions. The

theory postulated that the superconducting transition could be described in the context of the free energy combined with a complex order parameter, ψ which is zero above T_c and non zero below T_c .

Even with the advances in phenomenological theories, a base principles microscopic theory was not developed until 1957 [75], more than 40 years after the discovery of superconductivity. The theory was developed by Bardeen, Cooper and Schrieffer and named BCS theory after its developers. The theory arose from Cooper's earlier work [76]. Cooper showed that even a weak attractive interaction between electrons is enough for electrons above the Fermi sea to form bound pairs. The source of the attraction was determined concurrently with the development of BCS theory. In 1950 Maxwell and Reynolds observed the *isotope effect* [77, 78] in which the critical temperature of mercury increased by using heavier isotopes of mercury. This observation indicated that the interaction was linked to the phonon vibrations in the crystal lattice. The work of Fröhlich [79] and Pines [80, 81] showed that the interaction was indeed mediated by phonons as a combination of the screened Coulomb repulsion and the phonon mediated interaction [74]. However, for Cooper's problem and for the formation of the full BCS theory, the source of the interaction was inconsequential, all that was required was to assume an attractive interaction.

Cooper derived a wavefunction for two electrons of momenta and spin $\mathbf{k} \uparrow$ and $-\mathbf{k} \downarrow$ above the Fermi surface that only interacted with the electrons in the Fermi sea via the exclusion principle. However, the two electrons above the Fermi surface interacted with each other with interaction potential $V_{\mathbf{k}\mathbf{k}'}$, which describes the scattering of a pair of electrons from the states $(\mathbf{k}' \uparrow, -\mathbf{k}' \downarrow)$ to the states $(\mathbf{k} \uparrow, -\mathbf{k} \downarrow)$. Cooper made the assumption that the potential $V_{\mathbf{k}\mathbf{k}'}$ is a constant, V , for energies from the Fermi surface E_F up to a cut-off energy $\hbar\omega_c$ [74]. With this assumption and the valid approximation that the product of the density of states at the Fermi level, $N(0)$, with the interaction potential is small ($N(0)V < 0.3$) in classical superconductors the energy of the bound pair can be expressed as [74]:

$$E \approx 2E_F - 2\hbar\omega_c e^{-2/N(0)V} \quad (2.22)$$

Thus, a state exists in which a pair of bound electrons above the Fermi surface has energy less than the Fermi energy, these bound pairs are known as Cooper pairs. It was then clear that as the Cooper pairs are similar to bosons, electrons near the Fermi surface will condense into pairs that all share the same ground state until an equilibrium is reached when the Fermi surface differs greatly from that of the normal state, this means that the entire superconducting condensate can be described as a super-fluid of electron pairs with a single macroscopic wavefunction with a defined phase:

$$\psi(r, t)e^{i\phi(r, t)} \quad (2.23)$$

The further work of Bardeen, Cooper and Schriber determined the BCS ground state wavefunction as a phase coherent superposition of many-body states in which Bloch state pairs $(\mathbf{k} \uparrow, -\mathbf{k} \downarrow)$ are occupied or unoccupied exactly[75]. To do this they made two leaps: firstly they used the formation of second quantization where the operators $c_{\mathbf{k}\sigma}^*$ and $c_{\mathbf{k}\sigma}$ create and destroy an electron in state \mathbf{k} with spin $\sigma = \uparrow, \downarrow$. Secondly, as the number of electrons in the system are too large for calculation, they used a mean field approximation in which total electron number is not conserved, only the average number of electrons is fixed, and the probability that a \mathbf{k} state is occupied depends only of the average occupancy of the other \mathbf{k}' states. Thus, the occupancy of pairs of Bloch states, or Cooper pairs, can be described in terms of coefficients $v_{\mathbf{k}}$ and $u_{\mathbf{k}}$, where $|v_{\mathbf{k}}|^2 + |u_{\mathbf{k}}|^2 = 1$ and $|v_{\mathbf{k}}|^2$ is the probability that a state $(\mathbf{k} \uparrow, -\mathbf{k} \downarrow)$ is occupied and $|u_{\mathbf{k}}|^2$ is the probability that it is unoccupied. For simplicity, $v_{\mathbf{k}}$ and $u_{\mathbf{k}}$ were taken to be real but in reality they differ by phase $e^{i\phi}$ in which ϕ is the coherent phase of the condensate wavefunction. By determination of these coefficients this lead to the self consistent BCS gap function [74]:

$$\Delta_{\mathbf{k}} = -\frac{1}{2} \sum_{\mathbf{k}'} \frac{\Delta_{\mathbf{k}'}}{(\Delta_{\mathbf{k}'}^2 + \xi_{\mathbf{k}'}^2)^{1/2}} V_{\mathbf{k}\mathbf{k}'} \quad (2.24)$$

where $\xi_{\mathbf{k}}$ measures the electron energy, $\epsilon_{\mathbf{k}} = \hbar^2 k^2 / 2m$, from the Fermi surface such that $\xi_{\mathbf{k}} = \epsilon_{\mathbf{k}} - E_F$ and $\Delta_{\mathbf{k}}$ is the energy gap for unpaired electrons, otherwise known as quasiparticles, in the superconducting state. Following Cooper's assumption that the

interaction $V_{kk'}$ is constant from the Fermi surface up to the cut-off frequency, then same is true of the gap energy $\Delta_{\mathbf{k}}$ and thus the gap is equal to [74]:

$$\Delta = \frac{\hbar\omega_c}{\sinh[1/N(0)V]} \approx 2\hbar\omega_c e^{-1/N(0)V} \quad (2.25)$$

The existence of the superconducting gap can be understood intuitively as a consequence of the coherent phase of the Cooper pairs in the condensate. Each pair state interacts with the other pair states such that the change in one pair state effects the others and therefore the energy of the entire condensate. Thus, the minimum energy required to break a pair is the minimum energy required to change the condensate wavefunction, which is Δ . Because of this coherence between Cooper pairs, there is a characteristic distance over which the superconducting properties can change, known as the coherence length. In the "dirty" or diffusive limit at zero temperature [82] this is:

$$\xi_0 = \sqrt{\frac{\hbar D}{2\pi\Delta}} \quad (2.26)$$

where D is the diffusion constant in the normal state. whereas in the "clean" or pure limit the coherence length is:

$$\xi_0 = \frac{\hbar v_f}{2\pi\Delta} \quad (2.27)$$

where v_f is the fermi velocity of the superconductor and Δ is the superconducting gap energy. This distance can be considered to be the approximate size of a Cooper pair and is of the order of 100 – 200 nm. Considering the size of the Cooper pairs it is now clear why each pair is coupled with each other through the condensate; the Cooper pair wave functions heavily overlap, making each pair strongly correlated to it's neighbours.

This theory has stood the test of time and still stands as the best explanation of the origin of superconductivity. However, in the light of the new high temperature superconductors, the phonon mediated interaction is insufficient to explain the high critical temperature of these materials, therefore it is clear that there is still more work to be done in the theory of superconductivity.

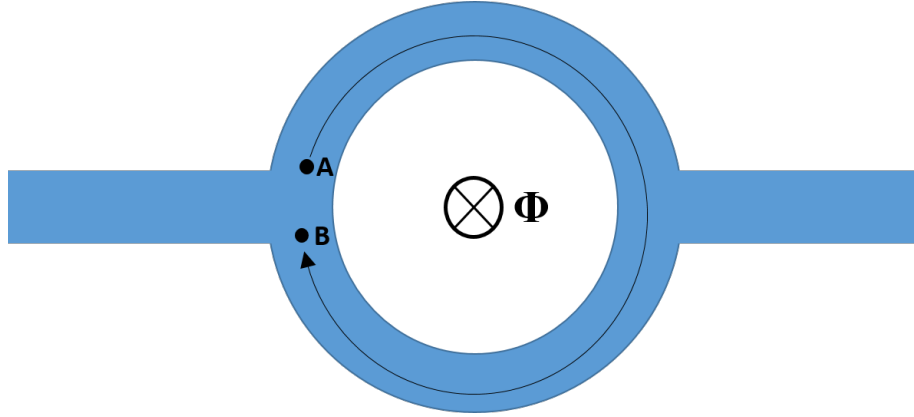
flux quantization

Figure 2.8: A superconducting loop threaded by a magnetic flux Φ . The wavefunction phase must be single valued at all points in the loop. The flux through the loop alters the momentum of superconducting electrons, which in turns is related to the phase of the condensate. The requirement that the phase be single valued means when points A and B are brought to the same point in the loop, the total change in phase around to loop from point A to B must be integer units of 2π . This means that the flux through the loop must be quantised.

A consequence of the macroscopic wavefunction of the superconducting condensate is that the phase at every point must be single valued. In the correct geometries this naturally leads to quantization. This can be demonstrated by considering a closed loop of superconducting material with two points A and B . By describing the superconducting electron pairs as plane wave states with mass $2m$, charge $2e$ and momentum \mathbf{P} equal to the centre of mass momentum of the pair the phase coherent macroscopic wavefunction becomes [83];

$$\psi(r, t)e^{i\phi(r, t)} = \psi(r, t)e^{i(\mathbf{P} \cdot \mathbf{r})/\hbar} \quad (2.28)$$

if there is no supercurrent flow, then \mathbf{p} is zero and the phase in the superconductor is constant and equal at points A and B. If a supercurrent now flows, then \mathbf{p} is non zero and a phase difference $\Delta\phi$ exists between points A and B that is constant in time. The phase difference between A and B in one dimension is:

$$\Delta\phi = \phi_A - \phi_B = 2\pi \int_A^B \frac{\mathbf{x}}{\lambda} \cdot d\mathbf{l} \quad (2.29)$$

where the displacement vector \mathbf{r} has been reduced to the one dimension vector \mathbf{x} , the momentum has been replaced by the electron pair de Broglie wavelength, $\lambda = P/h$ and $d\mathbf{l}$ is the line element in the direction of the wave propagation from A to B. As $\lambda = P/h$ and $P = 2mv$ where v is the pair velocity one can calculate the phase difference due to current using the relation between supercurrent velocity and current density $J_s = (1/2)n_s 2ev$ where n_s is the density of superconducting electrons. Thus because the supercurrent J_s must be parallel to \mathbf{x} , the wavelength and subsequent phase difference due to current is:

$$\lambda = \frac{hn_s e}{2mJ_s} \quad (2.30)$$

$$\Delta\phi = \frac{4\pi m}{hn_s e} \int_A^B \mathbf{J}_s \cdot d\mathbf{l} \quad (2.31)$$

If a magnetic field is now applied perpendicular to the loop the momentum of the superconducting electrons is modified by the magnetic vector potential, \mathbf{A} , such that $\mathbf{P} = 2mv + 2e\mathbf{A}$ and the phase difference between A and B becomes:

$$\Delta\phi = \frac{4\pi m}{hn_s e} \int_A^B \mathbf{J}_s \cdot d\mathbf{l} + \frac{4\pi e}{h} \int_A^B \mathbf{A} \cdot d\mathbf{l} \quad (2.32)$$

In the case when the points A and B form a closed path, as in fig. 2.8, the phase must be single valued at all points around the loop, which is only satisfied if the phase change around the full loop is $n2\pi$ where n is an integer. By use of Stokes theorem the line integral $\int_A^B \mathbf{A} \cdot d\mathbf{l}$ in eqn. 2.32 can be transformed to the surface integral $\int \int_S \mathbf{B} \cdot d\mathbf{S}$ and the phase difference around the loop is now constrained such that:

$$\Delta\phi = \frac{4\pi m}{hn_s e} \oint \mathbf{J}_s \cdot d\mathbf{l} + \frac{4\pi e}{h} \int \int_S \mathbf{B} \cdot d\mathbf{S} = 2\pi n \quad (2.33)$$

$$\Delta\phi = \frac{m}{n_s e^2} \oint \mathbf{J}_s \cdot d\mathbf{l} + \int \int_S \mathbf{B} \cdot d\mathbf{S} = n \frac{h}{2e} \quad (2.34)$$

This implies that, the total flux threading a superconducting loop due to both supercurrent and applied magnetic field, which is the left side of eqn. 2.34, must be in integer values of $h/2e$. This quantity is known as the flux quantum and is equal to $\Phi_0 = 2.06 \times 10^{-15}$ Wb. This phenomena is the basis of the commonly used superconducting quantum interference devices, or SQUIDS, which allow exceptionally precise measurements of magnetic field by measuring the number of flux quanta enclosed by a superconducting loop.

2.2.1 Proximity effects

Proximity effects is a term that concerns the physical phenomenon that occur when a superconducting material is brought into contact with a non superconducting material. This manifests in many ways, for example the induction of superconductivity in an otherwise non superconducting material, the tunnelling of superconducting electrons from one superconductor to another across an insulating barrier or the suppression of superconductivity due to proximity to a material that is intricately unable to form the superconducting phase. This section will give a brief overview of the physics behind these effects and a review of research in the field of superconducting proximity effects.

Josephson effect

The first and most well known superconducting proximity effect to be considered is that of the Josephson effect. This effect was predicted in 1962 by Brian Josephson [84]. He predicted that, if two superconductors were separated by a thin insulating boundary a supercurrent, I_s should flow between the two electrodes at zero applied voltage with the form [74]:

$$I_s = I_c \sin \Delta\phi \quad (2.35)$$

where $\Delta\phi$ is the difference in phase between the two superconducting electrodes and I_c is

the maximum current that can flow between the electrodes, otherwise known as the critical current. Such a geometry is known as a Josephson junction. Furthermore, Josephson predicted that the time dependence of phase between the two electrodes was dependent on the voltage between them [74]:

$$\frac{d(\Delta\phi)}{dt} = \frac{2eV}{\hbar} \quad (2.36)$$

such that a constant DC voltage applied to the Josephson junction creates an AC current with amplitude I_c and frequency $f = 2eV/h$. If one considered the energy of such an AC current, $E = hf = 2eV$, it is obvious that the energy is that of one Cooper pair carried across the junction from one superconducting electrode to the other. From this result it is clear that Cooper pairs can tunnel across small distances. There has been much research in the field of Josephson junctions and it has been found that the two superconducting electrodes need not be separated by an insulator but simply a 'weak link'. This weak link can be an insulator as in the original prediction (SIS), a constriction of the superconducting material (ScS), or a normal metal in contact with the superconducting electrodes (SNS). It is this last situation, SNS junctions, which is of the most importance to the work described here.

SN boundary

In 1932 Holms and Meissner[1] observed zero resistance in a normal metal that was sandwiched between two superconducting metal films. This effect became known as the proximity effect. The characteristic properties of the proximity effect at the interface between a superconducting metal, S, and a normal metal, N, are the weakening of superconductivity on the S side of the interface and the leak of superconducting properties into the N side. If one is considering "dirty" metals where the motion of electrons is diffusive, an appropriate assumption to be made in mesoscopic systems, then the probability amplitude of a Cooper pair, P , existing in the normal metal at some distance x from the S-N interface is[85]:

$$P = \phi(x)e^{-x/\xi_N} \quad (2.37)$$

where $\phi(x)$ is some slowly varying function of x and ξ_N is the normal state coherence length in the dirty normal metal,

$$\xi_N = \sqrt{\frac{\hbar D}{2\pi k_B T}} \quad (2.38)$$

where D is the diffusion constant in the normal metal and T is the temperature. It is clear that at low temperatures and in relatively clean metals such as silver and copper the normal state coherence length can be long, on the order of microns, such that superconducting properties are observed in the normal metal up to this distance from the interface. Fig 2.9 illustrates how the superconducting pair amplitude in the superconductor leaks into the normal metal and decays exponentially there.

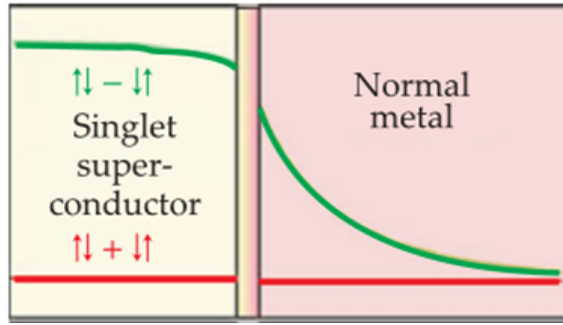


Figure 2.9: At the interface between a normal metal and superconducting metal the Cooper pair amplitude in the superconducting metal decays slightly and leaks in the normal metal exponentially. The pair amplitude remains non zero up to microns away from the interface, inducing superconducting properties in the normal metal. Image adapted from [86]

Andreev Reflection and SNS junctions

While it is clear that at an S-N boundary the superconducting properties leak into the N metal and that it can be easily described qualitatively in terms of the Cooper pair amplitudes leaking into the normal metal, it remains to be seen how the coherent nature of the superconducting state is passed to the normal metal or, more importantly, how

electrons with energy less than the gap, Δ can pass the boundary from N to S.

If one considers a current flowing across an SN boundary from the N electrode to the S electrode electrons of energy less than Δ should not be able to cross the boundary into the S metal as there are no available quasiparticle states at energies within the energy gap. One would expect then that current would not flow until a voltage difference $eV \sim \Delta$ exists between the S and N metals. However, with the observation of both the proximity effect and the Josephson effect it is known that this is not the case. The problem of how current is passed across the S-N boundary was solved by Andreev [87] and is known as Andreev reflection. In this process an incoming electron with energy $E < \Delta$ incident on a SN boundary with state (\mathbf{k}, \uparrow) is reflected as a hole with state $(-\mathbf{k}, \downarrow)$ and a Cooper pair is injected into the superconductor, such that a charge $2e$ crosses the boundary from N to S and a Cooper pair is effectively created from the incoming electron and time reversed hole. During this process, the reflected hole gains the phase of the superconductor. As the reflected hole can be considered as the time reversed state of the incoming electron and they have coherent phase, much like that of the Cooper pairs in the superconductor, the electron - hole pair will remain correlated until the phase coherence is lost at the phase breaking length L_ϕ . It can now be seen that the superconducting properties are carried into the normal metal by the correlated electron-hole pairs generated by the Andreev reflection process.

When the normal metal is sandwiched between two superconducting electrodes, the system becomes what is known as an SNS junction. The flow of supercurrent across the SNS junction can now be considered in terms of Andreev reflection. The supercurrent is carried across the SNS junction by correlated electron-hole pairs as previously discussed, thus only electron-hole pairs that have the correct energy to remain correlated across the junction will contribute to the flow of supercurrent. This energy is defined as the Thouless energy:

$$E_{Th} = \frac{\hbar D}{L^2} \quad (2.39)$$

where D is the diffusion constant and L is the length of the normal metal section. This

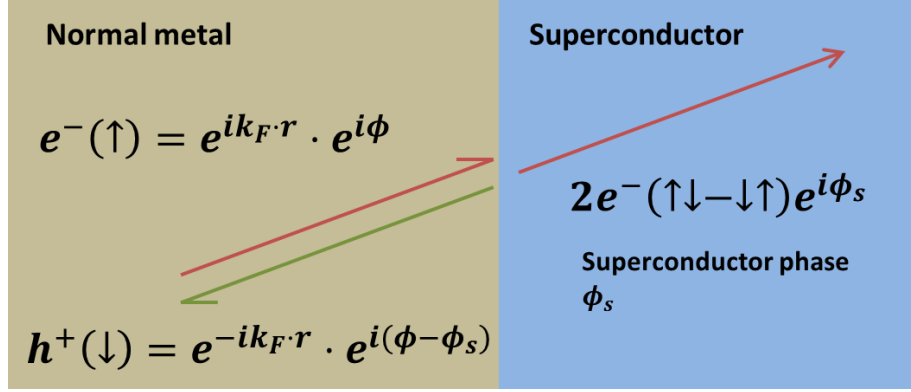


Figure 2.10: A spin up electron at the Fermi momentum with $E < \Delta$ and phase ϕ is reflected back along it's incident path as a hole with phase $\phi - \phi_s$ and two electrons propagate as a Cooper pair into the superconductor. This allows a current to flow from the normal metal to the superconductor, and causes phase coherence in the reflected holes and electrons, carrying the superconducting correlations into the normal metal.

correlation creates an energy gap in the normal metal equal to the Thouless energy but less than the superconducting gap. This energy gap is commonly referred to as a minigap. Because the minigap is dependent on the phase coherence of the reflected electron-hole pairs, it is sensitive to differences in phase between the two superconducting electrodes. If the phase difference between the S electrodes is $\Delta\phi = n2\pi$, where n is an integer, then there is maximum correlation between electron hole pairs and the minigap is at a maximum, if $\Delta\phi = n\pi$ then the correlation is at a minimum as is the minigap, due to the destructive interference of the electron hole pairs coming from both interfaces. This phase controlled coherence was observed by Petrashov et al. [88] by creating a superconducting loop that is closed by a mesoscopic silver loop as in fig 2.11. The resistance of the silver cross was measured between points A and B and the phase difference across the SNS junction was controlled either by application of a sub critical current or by applied flux through the loop. The resistance of the silver element was shown to oscillate with a flux period $h/2e$, the period of flux quantisation of a superconducting loop, linking the resistance oscillations to the phase oscillation around the loop due to applied field or supercurrent. This device is now known as an flux biased Andreev interferometer, as it allows the probing of phase dependent interference of Andreev reflected electrons much like that of an optical

interferometer.

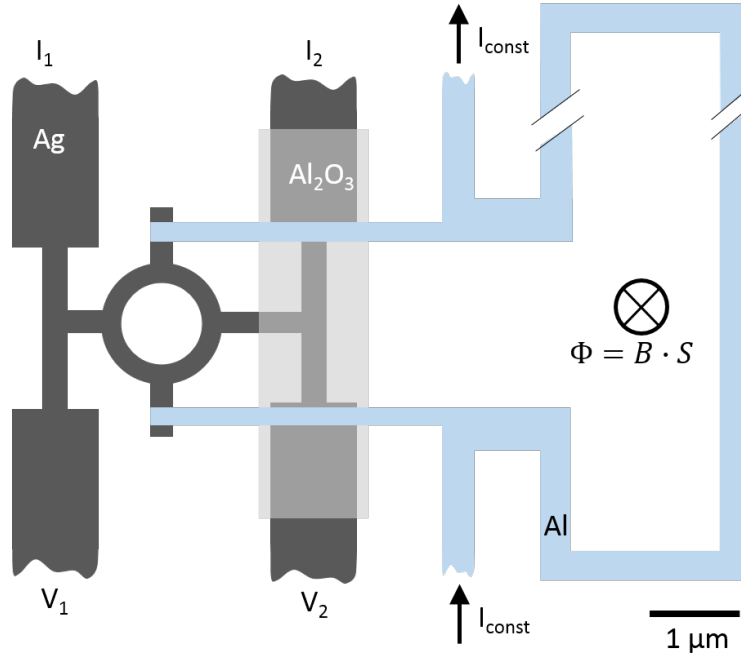


Figure 2.11: A sketch of the experimental set-up of Petrashov et al. [88]. The Silver loop element forms the normal metal part of an SNS junction, where the superconductor is aluminium. The Al electrodes then close to form a loop. The resistance of the silver loop can be independently measured using the silver wires $V_{1,2}$ and $I_{1,2}$, that are electrically isolated from the Al loop by a layer of Al_2O_3 , as a four point resistance measurement. This can be measured while a flux $\Phi = B \cdot S$ where S is the loop area and B is the external field, threads the loop and thus controls the phase difference across the Ag ring. Similarly, by passing a constant current I_{const} Through the Al loop, the effect of current induced phase difference on the Ag ring could be measured. Sketch based on images from [88].

Le Sueur et al. [89] showed the evolution of the minigap directly in an aluminium - gold SNS junction in which the aluminium formed a half loop that was connected by the gold bridge. By use of a cryogenic dual function atomic force - scanning tunnelling microscope (AFM-STM) Le Sueur et al. could directly measure the minigap in the gold by tunnelling conductance and thus its spatial dependence from the SN interface, as demonstrated in fig. 2.12 top image. Furthermore, because of the ring geometry, the phase difference across the SNS junction could be controlled by use of the flux quantization phenomena via the application of a magnetic field perpendicular to the sample plane like the Andreev inter-

ferometer measured by Petrashov et al. They showed that, as the phase difference across the junction was swept from 0 to 2π , the minigap did indeed shrink and disappear at a phase difference of π and then reappear at 2π .

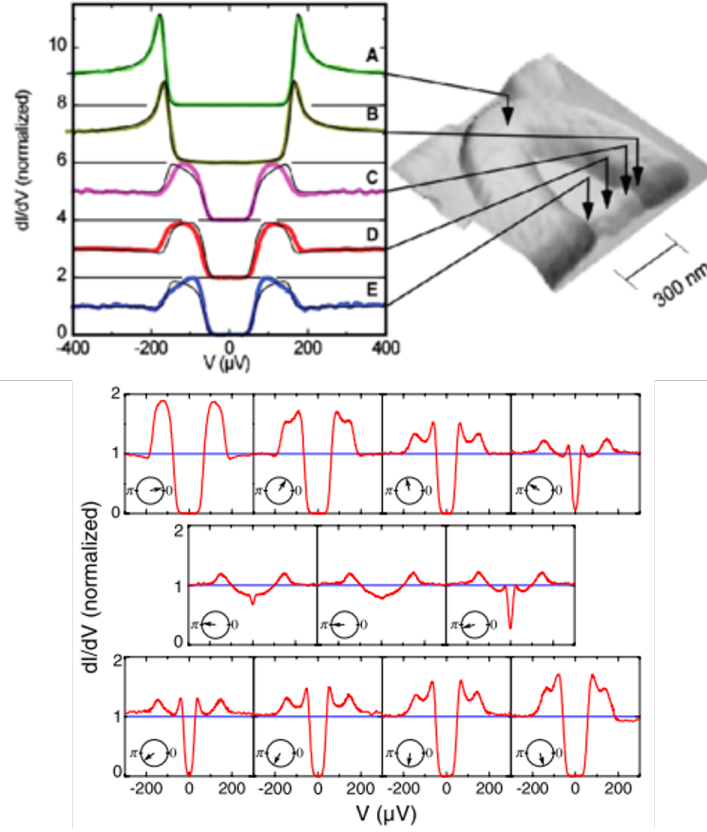


Figure 2.12: STM measurements observed by Le Seur et al. [89] Top: the superconducting gap can be observed as a zero tunnelling conductance in the Al loop (A). The conductance is zero as there are no states available for the electrons in the STM tip to tunnel within the gap energy and Andreev reflection is inhibited by the insulating nature of the STM method. In the Au the minigap is less than the Al gap energy and decreasing as a function of distance from the interface, (B-E). Bottom: When the phase difference across the Au is controlled by applying a magnetic field through the loop, the minigap shrinks and disappears at a phase difference of π , reappearing at a phase difference of 2π . Image adapted from [89].

Critical current in SNS junctions

Theoretical calculation of the observable properties in SNS junctions is a complicated endeavour. One such observable is that of the critical current, that is the current applied at which the SNS junction transitions into the normal resistive state. In pure superconducting materials, this current is either due to the current itself generating a magnetic field that is equal to the superconductors critical field, forcing a transition into the normal state, or due to depairing of Cooper pairs when the kinetic energy due to the current flow of the individual electrons in the pair is larger than the binding energy of the pair. In SNS junctions the critical current is more complex and concerns the properties of the adjacent superconductor, the normal metal and the interface between them.

The critical current of SNS junctions was studied first by De Gennes in the early 1960s [90] in the context of 'thick' junctions, and later extensively studied both experimentally and theoretically by Dubos et al. [91] in the context of long diffusive junctions. The treatment by Dubos is followed in this project. In this context a "long junction" is one in which the length of the normal metal is larger than the mean free path but shorter than the phase breaking length, dimensions typically achievable with lithography techniques. In the experiment Dubos et al. used Nb-Cu-Nb junctions with high interface transparency. The results are shown to be in excellent agreement with the accompanying theory, formulated using the Usadel equations for quasi classical diffusive systems. At high temperature, $k_B T \gg E_{Th}$, the $R_N I_c$ product is found to be [91]:

$$e R_N I_c = 64 \pi k_B T \sum_{n=0}^{\infty} \frac{L}{L \omega_n} \frac{\Delta^2 e^{-L/L \omega_n}}{(\omega_n + \Omega_n + \sqrt{2(\Omega_n^2 + \omega_n^2)})^2} \quad (2.40)$$

where R_N is the resistance of the normal metal, L is the length of the normal metal, $\omega_n = (2n+1)\pi k_B T$ is the Matsubara frequency, $\Omega_n = \sqrt{\Delta^2 + \omega_n^2}$ and $L \omega_n = \sqrt{\hbar D / 2 \omega_n}$. When the junction is very long, i.e. $\Delta / E_{th} \rightarrow \infty$, this simplifies to:

$$e R_N I_c = \frac{32}{3 + 2\sqrt{2}} E_{Th} \left(\frac{L}{L_T} \right)^3 e^{-L/L_T} \quad (2.41)$$

where $L_T = \sqrt{\hbar D / 2\pi k_B T}$, the thermal coherence length in the normal metal. Thus this equation can be simplified further to give $I_c(T)$:

$$I_c(T) = AT^{3/2}e^{-B\sqrt{T}} \quad (2.42)$$

$$A = \frac{32}{3 + 3\sqrt{2}} \frac{L^3}{eR_N} E_{Th} \left(\frac{2\pi k_B}{\hbar D} \right)^{3/2} \quad (2.43)$$

$$B = L \sqrt{\frac{2\pi k_B}{\hbar D}} \quad (2.44)$$

In the low temperature limit, the full Usadel equations must be solved numerically. Although the numerical solution can be approximated by

$$I_c(T) = \frac{E_{Th}a}{eR_N} (1 - be^{-aE_{Th}/3.2k_BT}) \quad (2.45)$$

where $a = 10.82$ and $b = 1.3$ are numerical fitting coefficients. In the very low temperature and long junction limits, it is found that at zero temperature the critical current is a constant value and dependent on the Thouless energy,

$$I_c(T = 0) = \frac{10.82E_{Th}}{eR_N} \quad (2.46)$$

whereas in the short junction limit, where $\Delta \ll E_{Th}$, the zero temperature critical current is found by numerical calculation, to be

$$I_c(T = 0) \approx \frac{1.326\pi\Delta}{eR_N} \quad (2.47)$$

This formalism is of use in this thesis to describe the behaviour of the SNS like junctions presented in chapter 5 within the limits presented.

2.2.2 Ferromagnetic proximity effect

The phenomena of superconductivity and ferromagnetism both exist due to long range ordering of electrons. However, both of these two long range orders are antagonistic. Whereas the superconducting order creates pairs of electrons with opposite spin, the ferromagnetic order seeks to align the spin of the electrons. Thus, if a superconducting metal and ferromagnetic metal are brought into contact, these two long range orders will compete at the interface. This can be referred to as the ferromagnetic proximity effect.

If the normal metal in an SN structure is replaced with a ferromagnetic metal, the proximity effect is modified such that the distance at which the superconducting correlations penetrates into the ferromagnet is very small compared to that of a normal metal, typically only a few nanometers. This is because the exchange field in the ferromagnet attempts to align the spins of the electrons in the Cooper pair. Thus the influence of the exchange field will be much greater than the influence of the temperature on the electron coherence and one can define a coherence length in the ferromagnetic metal[92]:

$$\xi_F = \sqrt{\frac{\hbar D}{2\pi k_B T_{curie}}} \quad (2.48)$$

where T_{curie} is the curie temperature of the ferromagnet. T_{curie} is typically on the order of several hundred degrees, therefore $\xi_F \approx 1 - 2$ nm. The influence of the ferromagnetic order is also seen in the S metal, where the superconducting properties are weakened within typically a coherence length, ξ_s from the SF interface, this is known as the inverse proximity effect.

The antagonistic nature of superconducting and ferromagnetic orders, coupled with the short coherence length in a ferromagnet would instinctively suggest that SF systems produce effects of little interest. However, it is the competition of the two ordering mechanisms that produces unique physics in these systems. In 1964 Larkin and Ovchinnikov, and Fulde and Ferrell [2] simultaneously showed that in a weak exchange field of a theoretical ferromagnetic superconductor, electrons would form pairs of opposite spin yet due to the exchange energy splitting these Cooper pairs would have a non zero centre of mass

momentum Q . This is commonly referred to as the FFLO state, named after its discoverers. While this state is theoretically possible in a bulk superconductor, in practice it has been difficult to identify experimentally, except for experiments on nano scale SF systems, where the ferromagnetic and superconducting orders can coexist at the interface of SF structures.

The existence of the FFLO state at an SF boundary can be discussed by considering a Cooper pair as Bloch states at the Fermi energy $(\mathbf{k}_f, \uparrow, -\mathbf{k}_f, \downarrow)$ in the S metal. When the pair penetrates an adjacent ferromagnet, each electron is then exposed to the ferromagnetic exchange field, h and gains/loses energy $\mu_B h/v_F$, where μ_B is the Bohr magneton, v_F the Fermi velocity, and the pair state becomes $(\mathbf{k}_f - \mu_B h/v_F, \uparrow, -\mathbf{k}_f + \mu_B h/v_F, \downarrow)$. It can now be seen that inside the superconductor the total momentum of the Cooper pair is $|k_f - k_f| = 0$. Whereas, in the ferromagnet the total momentum of the Cooper pair is now $|(k_f - \mu_B h/v_F) - (k_f + \mu_B h/v_F)| = 2\mu_B h/v_F = Q$, where Q is the new centre of mass momentum of the Cooper pair which now oscillates in space within the ferromagnet. A consequence of the oscillation is that the singlet Cooper pair state, $(\uparrow\downarrow - \downarrow\uparrow)$, mixes into the anti-parallel spin triplet Cooper pair state $(\uparrow\downarrow + \downarrow\uparrow)$ [86],

$$(\uparrow\downarrow - \downarrow\uparrow) \rightarrow (\uparrow\downarrow e^{i(\mathbf{Q} \cdot \mathbf{R})} - \downarrow\uparrow e^{-i(\mathbf{Q} \cdot \mathbf{R})}) = \cos(\mathbf{Q} \cdot \mathbf{R})(\uparrow\downarrow - \downarrow\uparrow) + i \sin(\mathbf{Q} \cdot \mathbf{R})(\uparrow\downarrow + \downarrow\uparrow) \quad (2.49)$$

In this case the singlet state refers to the state in which the orbital quantum number of the pair is, $l = 0$, whereas the triplet state has orbital quantum number of the pair, $l = 1$. Thus, in the singlet state there is only one possible projection of the spins $(\uparrow\downarrow - \downarrow\uparrow)$. Whereas, in the triplet state, there are three possible projections: $(\uparrow\downarrow + \downarrow\uparrow)$, $(\uparrow\uparrow)$, and $(\downarrow\downarrow)$. The process of converting the singlet state into anti-parallel triplet state described by eqn. 2.49 is known as spin mixing. The oscillatory behaviour of the singlet and triplet Cooper pairs is demonstrated in fig. 2.13. In a normal metal, no triplet pairs are produced as there is no spin mixing. In a weakly spin polarised ferromagnet, the triplet pairs are produced and both triplet and singlet pairs oscillate in the ferromagnet while decaying

exponentially due to the pair breaking effect of the ferromagnet. In a strongly polarised ferromagnet the oscillation is rapid and the decay length is much shorter. The triplet state is one of the most interesting phenomena that arises in SF systems, and has been the focus of a vast amount of SF research. The following section will discuss the proximity effect in ferromagnet the context of the SF research of the past several decades.

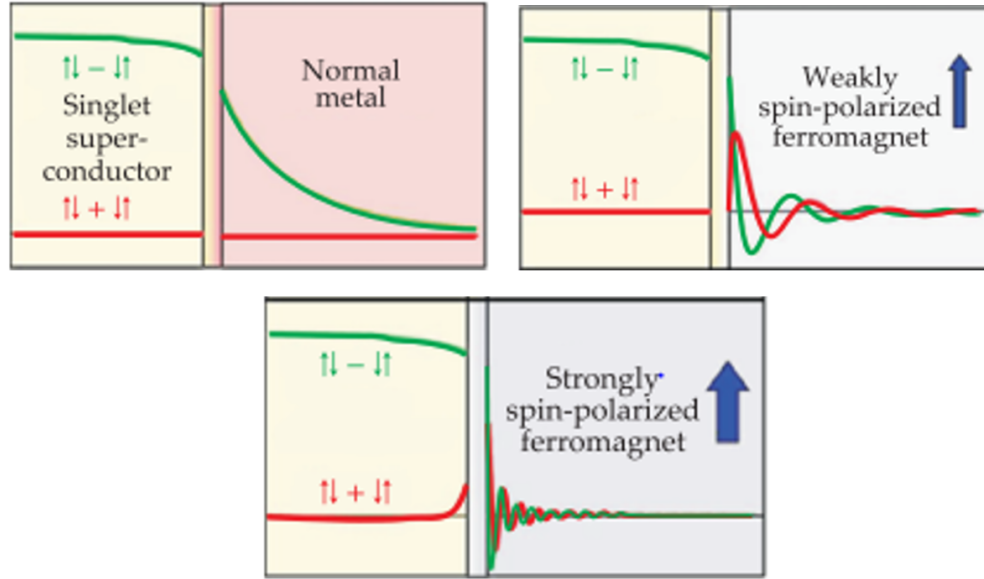


Figure 2.13: The singlet and triplet components at an SF boundary for the case of a normal metal, weak ferromagnet and strong ferromagnet. In the SF system case both the singlet and triplet anti-parallel pairs are generated at the boundary, oscillate with opposite phase and decay. [86]

SFS multi layers and π junctions

The advent of new thin film technologies in the late 80s and early 90s allowed the investigation of films thin enough to show the predicted effects in SF structures. The oscillatory behaviour of the FFLO state was predicted to be observable in SF multilayer structures as an oscillation of the critical temperature with increasing F layer thickness [93, 94]. This prediction was later confirmed in several experiments that varied the ferromagnetic thickness in an F/S multilayer [3, 4, 5], bilayer [95] or trilayer [96, 97, 98, 99]. This ob-

servation of oscillating critical temperature is due to the oscillatory dependence of the superconducting condensate in the F layers. In a multilayer SFS film, with a thin F layer the superconducting condensate wavefunction penetrates into the ferromagnet and does not become negative. As the thickness of the F layer increases the oscillation of the wavefunction in the F layer crosses zero, the wavefunction becomes negative, and the phase difference between adjacent S layers is now π , as such this is known as the π phase. The T_c oscillations correspond to the multilayer switching between 0 and π phases at the cross over points when the T_c in the 0 phase becomes less than T_c^* in the π phase and vice versa.

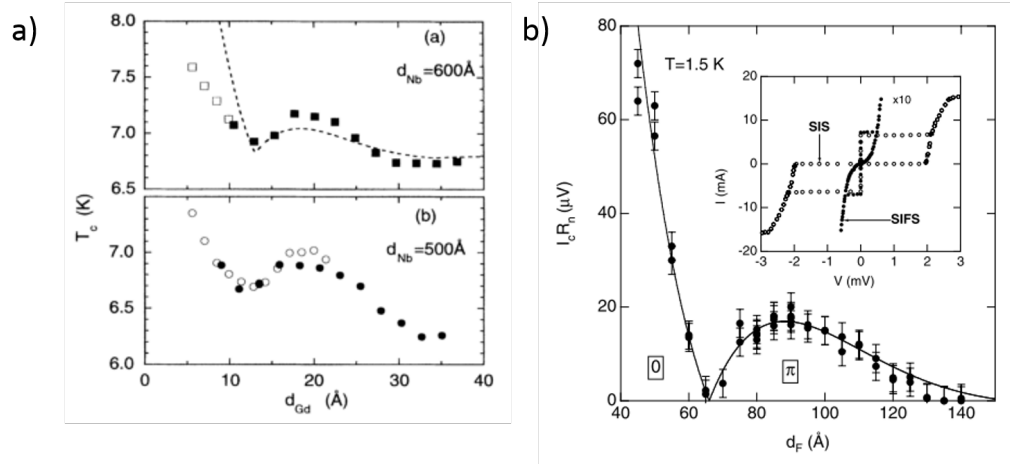


Figure 2.14: a) Oscillatory behaviour of the critical temperature of Nb/Gd multilayer with increasing Gd thickness, image adapted from [3]. b) Oscillations of the critical current in Nb/Al/Al₂O₃/PdNi/Nb junctions with increasing PdNi thickness, image adapted from [100].

The effect of this π phase shift with increasing F layer thickness is also evident in the critical current of SFS Josephson junctions. As was discussed earlier, the Josephson current is due to the phase difference between two superconductors separated by some barrier. Thus, if one were to create an SFS junction with an F thickness such that the SFS system were in the π phase, the Josephson current would be negative. This was shown to be true theoretically by Buzdin et al. in ballistic [101] and later diffusive junctions [102]. Due to the requirements of very thin ferromagnetic films however, the oscillations in critical

current were not observed until much later by Ryazanov et al. [103] in SFS junctions made of Nb/CuNi. These measurements showed the critical current decay with increasing F layer thickness, reaching zero and then reappearing. This reappearance of the critical current indicates the cross over into the π phase, where the critical current is negative, however it is measured positive as it is only possible to measure the current magnitude. The observation was later improved upon several times, including showing that at the correct F thickness, the $0-\pi$ transition occurs with decreasing temperature [100, 104, 105]. Figure 2.14a shows the oscillation of T_c in Nb/Gd multilayers by Jiang et al. [3]. With increasing F layer thickness, T_c decreases until a critical thickness at which T_c increases as predicted. Similarly, Fig. 2.14b shows the oscillation in critical current with increasing F layer thickness in Nb/Al/Al₂O₃/PdNi/Nb observed by Kontos et al. [100].

Magnetization dependence and long range triplet pairs

The first interest in the magnetization dependent effects in SF systems began with FSF spin valves. An SFS spin valve consists of a superconducting layer sandwiched between two ferromagnetic layers, similar to the SF multilayers, yet the magnetization direction of the F layers can be independently controlled. In the simplest case this means that the magnetization in the F layers can be either parallel (P) or anti-parallel (AP), with the magnetization direction along the plane of the thin film. It was predicted that the superconductivity in the parallel orientation would be suppressed compared to the anti-parallel orientation due to the the superconducting layer feeling a greater average exchange field in the parallel orientation, this would be observed as a reduction of T_c in the P orientation. FSF spin valves were extensively studied theoretically, showing this to be the case for the simple P-AP orientation [106, 107] and for arbitrary angle between F layers [108, 109, 110] as well as being experimentally observed [111, 112].

This work on spin valves lead to an increased interest in the triplet copper pairing at SFS interfaces and the possibility of a long range component of the condensate that would penetrate into the ferromagnet over distances greater than ξ_f . This was driven by earlier anomalous experimental observations of proximity effects that appeared to extend further

than the ferromagnetic coherence length [113, 114, 115]. The origin of the long range effects was sourced to the triplet component of the superconducting condensate. The key theoretical prediction presented by Bergeret et al. and Kadigrobov et al. [6, 7, 8, 9] was that, when the magnetization of F layers in an FSF spin valve system are non-collinear, an even spin triplet pairing, $(\uparrow\uparrow + \downarrow\downarrow)$, is generated. As this pairing state is constructed of electrons with aligned spins, such a pairing state would survive in a ferromagnetic material unhindered by the exchange field, at distances equal to that of the thermal coherence length ξ_T . This long range triplet would only appear in the non collinear magnetizations because a changing exchange field vector was required to transform the anti-parallel triplet pair into the equal spin pair in the new magnetization basis created by the changing magnetization direction, i.e. $(\uparrow\downarrow + \downarrow\uparrow)_y = i(\uparrow\uparrow + \downarrow\downarrow)_z$.

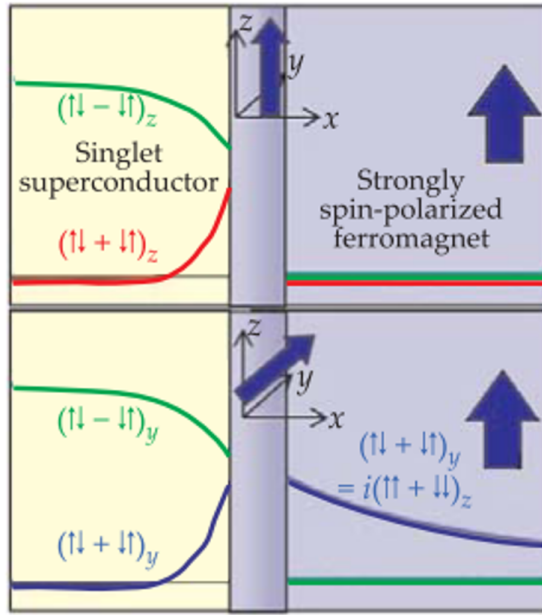


Figure 2.15: Illustration of spin polarised triplet pair generation. For an SF'F system, when the F' and F layers are collinear (top) then the singlet and anti-parallel triplet decay in the F' layer and no superconductivity extends into the F layer. If F' and F are non-collinear (bottom) then the singlet still decays in F' but the changing exchange field direction transforms the anti-parallel triplet into the parallel spin triplet, which survives over long distance in the F layer. Image adapted from [86]

The truly astonishing property of this spin polarized Cooper pair is its wavefunction asymmetry. As the spins in the pair are aligned, the pair wave function is even in parity with respect to exchange of spin and position coordinates. Thus, to obey the Pauli principle the frequency (time) component of the wavefunction must be of odd parity. As such, the long range spin polarised triplet Cooper pairing is often referred to as odd frequency superconductivity. Such a pairing state is not seen in other natural systems and thus makes SF systems of great interest.

The first unarguable experimental evidence of the long range triplet supercurrent was shown by Keizer et al. [11]. A planar Josephson junction was made by depositing NbTiN electrodes on top of a CrO₂ film, which is a half metallic ferromagnet, that is to say that the band structure is such that the up spin band is metallic and the down spin band is insulating. The distance between the superconducting electrodes was made to be much greater than the ξ_f and on the order of ξ_N , thus any super current that flows between the electrodes must be due to long range triplet components. A supercurrent was inferred to flow between the electrodes, as a characteristic Fraunhofer pattern was observed in the I_c when a magnetic field was applied, as shown in fig. 2.16 bottom image. While no magnetic inhomogeneity (changing in magnetization direction) was engineered in this device, it was theorised that the inhomogeneity that generated the long range triplet was due to the crystallographic anisotropy of the CrO₂.

The need for changing magnetization was demonstrated further by the observation of phase coherent resistance oscillations in a flux biased superconducting loop interferometer that used Holmium as a weak link by Sosin et al. [10]. Again the distance of the junction was greater than ξ_f . While no Josephson current could be measured, the phase difference of the junction was controlled through application of flux through the interferometer loop, showing resistance oscillations in the holmium. This was inferred to be due to triplet superconducting correlations in the holmium created by its helical ferromagnetic ordering. The need for magnetic non-collinearity was unequivocally proven by the work of Khairi et al. in 2010 [12]. In this work, a complex magnetic multilayer was sandwiched between two niobium films, fig 2.17a, in which two Co layers in the centre were separated by a thin layer

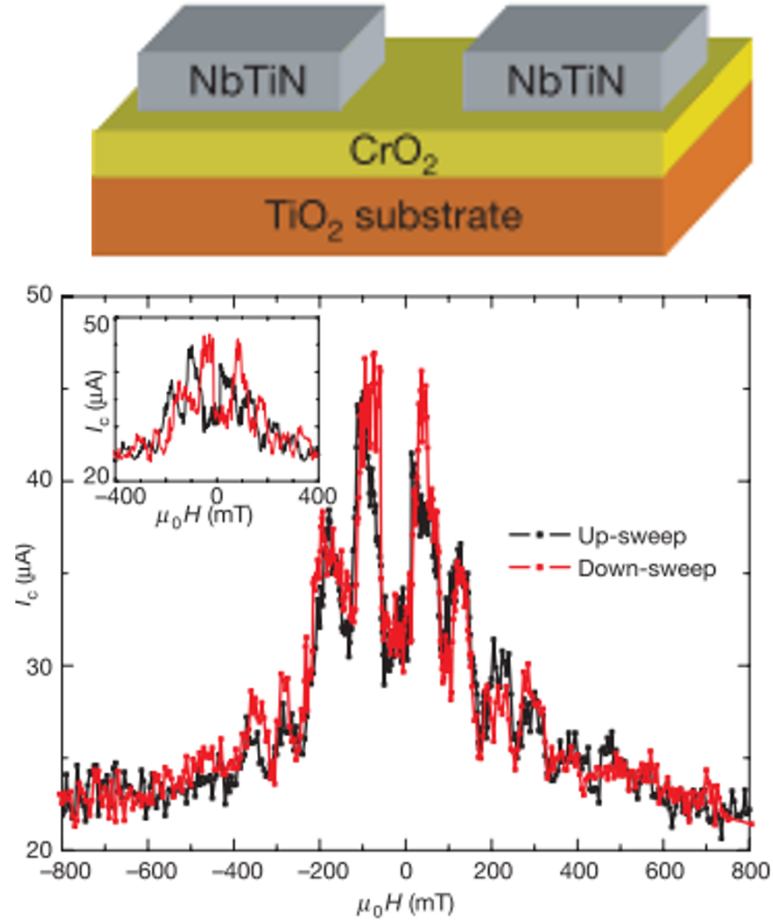


Figure 2.16: Top: a schematic of the junction measured by Keizer et al.. The superconducting electrodes (grey) were separated at a distance much greater than ξ_f on top of a half metallic film of CrO_2 (yellow). Bottom: The critical current of the SFS junction as a function of applied field. The critical current exhibits Fraunhofer oscillations that are characteristic of Josephson junctions, indicating that a supercurrent flows between the electrodes and through the CrO_2 . As the distance between the electrodes is greater than ξ_f , this supercurrent must be due to long range spin polarised triplet Cooper pairs. Image adapted from [11]

of Ru, causing the Co layers to have an anti-parallel alignment. An extra ferromagnetic layer of either PdNi or CuNi alloy, called the X layer, was deposited with a Cu spacing layer between the Co and X layer, fig 2.17b. It was shown that if the X layer was omitted, the critical current rapidly decreased with increasing cobalt thickness. Whereas, with the X

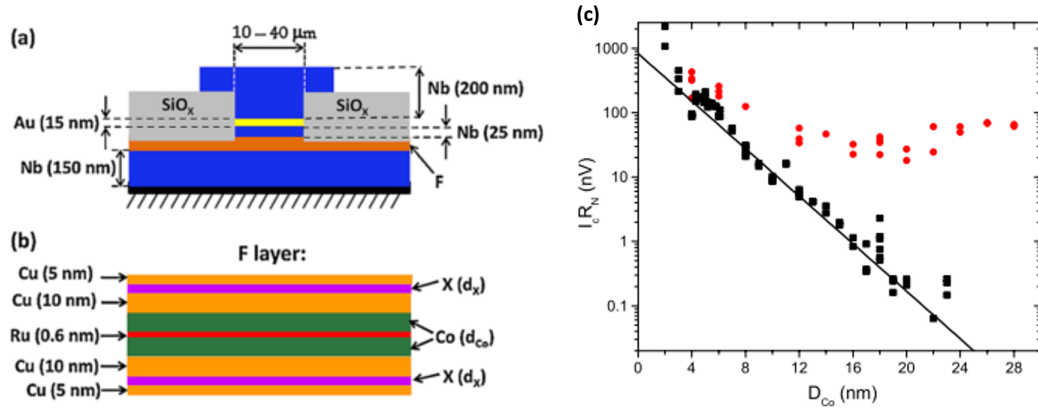


Figure 2.17: a) The stacked SFS junction design used by Khaire et al.[12] The complex structure of the F layer is shown in b). The F layer consists of a central Ru film sandwiched between two anti-parallel Co layers, followed by Cu spacers and the X layer of either PdNi or CuNi alloy and finally a Cu layer. The X layer was either included or excluded. c) The critical current of the junction with (red symbols) or without (black symbols) the X layer. Without the X layer the I_c of the junction decays exponentially with increasing Co layer thickness, with the X layer the I_c does not decay strongly with increasing Co thickness. Image adapted from [12].

layer the critical current decayed orders of magnitude slower than without it, surviving at Co thickness's where previously the critical current was not observed, fig 2.17c. The need for the PdNi/CuNi layer was explained as the competition of thin film shape anisotropy and out-of-plane crystalline anisotropy in these films likely resulted in stripe domains. These stripe domains were the inhomogeneity required to transform the anti-parallel spin triplet into the long range spin polarised triplet. This effect was observed again soon after by Robinson et al. [13] in a Nb/Ho/Co/Ho/Nb junction. This experiment again utilised the spiral magnetization of Holmium and demonstrated that the critical current decayed slowly with increasing Co layer thickness if the Ho layer thickness was equal to a non-integer value of the holmium magnetization spiral wavelength. This further indicated that the surviving critical current was due to long range spin polarised Cooper pairs induced by the non-collinear holmium magnetization.

The discovery of odd frequency spin triplet superconductivity was a huge leap forward in

the field of SF hybrid structures and propelled the research into the search for controllable spin polarised supercurrents that would allow for low power spintronic devices. Since the early observations, new devices that observe spin triplets have been proposed and created that use nano-engineered magnetic structures such as exchange spring like junctions [116, 117, 118, 119, 120] and possibly magnetic vortices [121].

What the discovery of odd frequency spin triplet superconductivity made clear was that in SF systems, the magnetization state of the ferromagnet is of great importance and can be used to alter the superconducting properties of the system.

Inverse proximity effects

The proximity effect often refers to the influence of a superconducting material on an adjacent material that is not superconducting; a normal or ferromagnetic metal, insulator or semiconductor. This is usually the effect of interest as the penetration of superconducting properties into the adjacent material is the largest measurable effect at work. However, the effect of the non-superconducting material on the superconductor can be of interest and is known as the inverse proximity effect. In the case of a normal metal, the inverse proximity effect is small, with only mild reduction in superconducting properties within a distance ξ_s in the superconductor. However, in an SF system the influence of the ferromagnet across the same distance can be profound due to the pair breaking effect of the ferromagnet exchange field.

In 1988 Rainer et al. [14] considered the case of a superconducting thin film in contact with a ferromagnetic insulator. By treating the interaction with the ferromagnetic domain wall as perfect specular reflection they showed that with increasing spin mixing angle, the gap is reduced within a distance on the order of ξ_s from the magnetic interface with the gap reduced to zero at a spin mixing angle of π , as illustrated in fig 2.18.

This calculation was in response to the experiment by Tedrow et al. [122] in which the density of states (DOS) of an aluminium film backed by the ferromagnetic insulator EuO was measured by tunnelling spectroscopy. The authors observed that in an applied in-plane magnetic field the Zeeman splitting of the DOS of states deviated from the expected

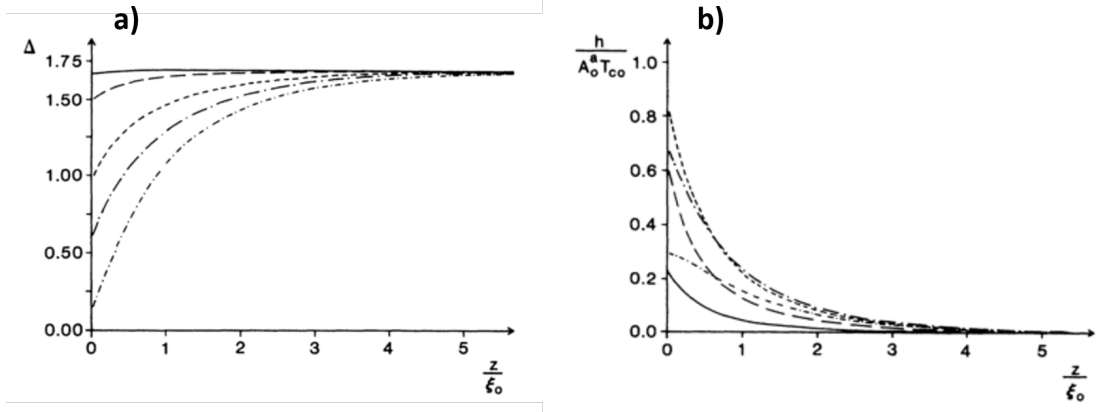


Figure 2.18: a) Superconducting gap energy (relative to T_c) of a superconductor in contact with a ferromagnetic insulator with increasing spin angle in order from top to bottom: 0.2, 0.6, 1.2, $\pi/2$, $3\pi/4$. b) Induced exchange field in the superconductor for the same increasing spin angles. Images adapted from [14]

splitting such that: $E_{Zeeman} = 2\mu_e H \rightarrow 2\mu_e(B^* + H)$. The additional field B^* was accounted for as the exchange field induced in the superconductor by proximity with the ferromagnet, this was supported by the calculations performed by Rainer et al.

Inverse proximity effects were given comparatively less attention in light of the search for the proximity induced superconductivity on the ferromagnetic side. However, in 2001 Sillanpaa et al. [15] investigated the inverse phenomena directly via further tunnelling spectroscopy.

The authors observed a smearing of the density of states (DOS) in the Al that could not be accounted for by stray magnetic field from the ferromagnet. Figure 2.19a shows the geometry used to measure the DOS of an aluminium wire in contact with a Ni wire. The DOS of the aluminium at a distance of $1.2\xi_s$ and $10\mu\text{m}$ from the Ni-Al interface is shown in fig. 2.19b. The DOS near the Ni is smeared due to the inverse proximity influence of the ferromagnet on the superconducting aluminium. In addition, measurements of the DOS at increasing external field showed only a reduction of the gap energy that was of the same character in the proximity influenced thin film Al and the thin film Al far from the interface, with no change in the zero bias conductance. This indicated that superconducting thin films were indeed influenced by adjacent ferromagnet and that the

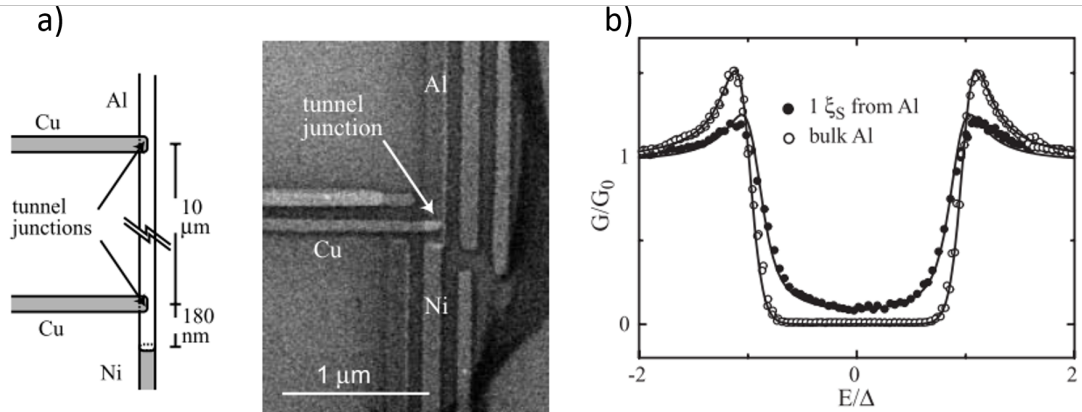


Figure 2.19: a) The thin film geometry used to measure the inverse proximity effect in an Al thin film in contact with a Ni thin film. b) The DOS measured by tunnelling spectroscopy in the Al film $L = 1.2\xi_s$ (solid symbols) and $L \sim 66\xi_s$ (open symbols) where L is the distance between the tunnel junction and the nickel-aluminium interface. image adapted from [15]

proximity effect is a phenomenon felt on both sides of the SF interface.

Theoretical discussions of the properties of the inverse proximity effect considered its mechanism as a leakage of ferromagnetic order into the superconductor, inducing a magnetization in the superconductor near the interface [123, 124, 125]. The induced magnetization is opposite to that of the ferromagnet. This can be explained in a simple model by considering a Cooper pair travelling near the interface such that one electron in the pair resides in the superconductor and one in the ferromagnet. The electron in the ferromagnet feels the exchange field and aligns with the direction of magnetization. The paired electron in the superconductor feels no exchange field, yet as the singlet pair has anti-parallel spin, the electron in the superconductor must have opposite spin to that in the ferromagnet. Thus, when considering many such pairs, a magnetization arises in the superconductor that is opposite to that of the ferromagnet and decays on the distance ξ_s as paired electrons are no longer shared across the interface.

Simultaneously, measurements by Kinsey et al. [16] and in Nb/Co indicated that the presence of multi-domain structures in the ferromagnet had a large effect on the properties of the bilayer. The authors fabricated mesoscopic tracks of Co deposited on top of Nb

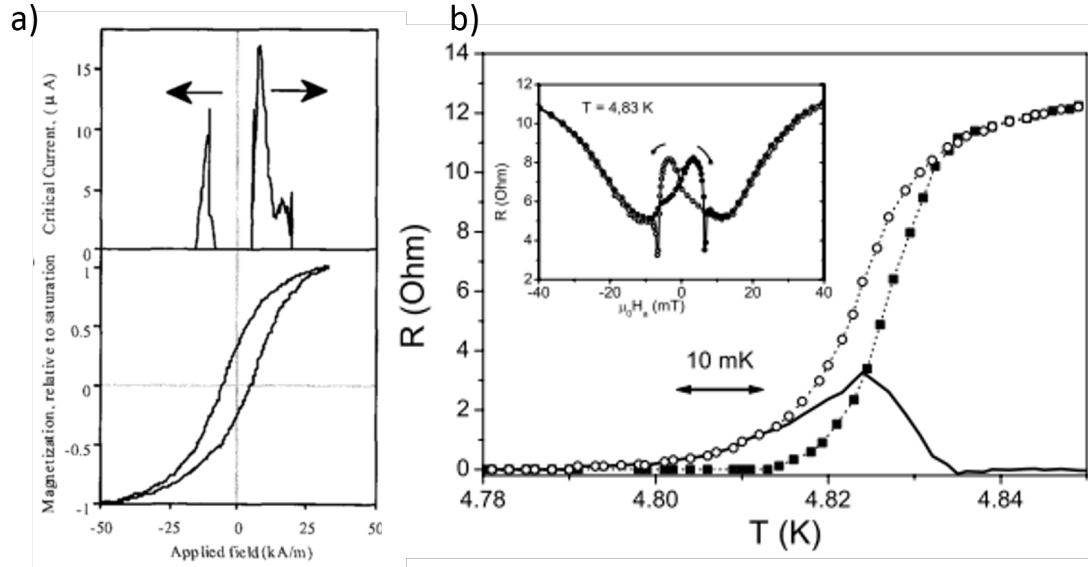


Figure 2.20: a) The critical current of Nb/Co bilayer in an applied in-plane magnetic field (top), the hysteric double peak aligns with the coercive field of the Co film (bottom) b) The resistive transition of a Nb/Py bilayer at zero applied field (open symbols) and 6.3 mT applied field (closed symbols). Images adapted from [16, 17]

with lateral dimensions $1 \mu\text{m} \times 10 \mu\text{m}$. It was observed that in an applied in-plane field the critical current of the track showed a hysteric two peak structure that could be aligned with the coercive field of the cobalt film, shown in fig 2.20a. The behaviour was explained as a reduction in the total exchange field felt by the Cooper pairs when the magnetization of the Co formed multi-domain structures near the coercive field. Similar behaviour was observed by Rusanov et al. in 2004 [17] in large Nb/Py bilayers of lateral dimensions $0.5 \text{ mm} \times 4 \text{ mm}$. In this work the authors observed a 10 mK shift in T_c between measurements at zero applied in-plane field and at 6.3 mT field such that T_c was lower at 6.3 mT, as in fig 2.20b. The lower T_c could again be aligned with the coercive field of the Py layer at which multi-domain structures were present. However, the same behaviour was not observed in micro-structured samples of lateral dimensions $1.3 \mu\text{m} \times 20 \mu\text{m}$, where the authors attributed this to the lack of stable multi-domain structures in these samples due to the magnetization process being dominated by coherent reversal along the wire length rather than a transition into multiple domains.

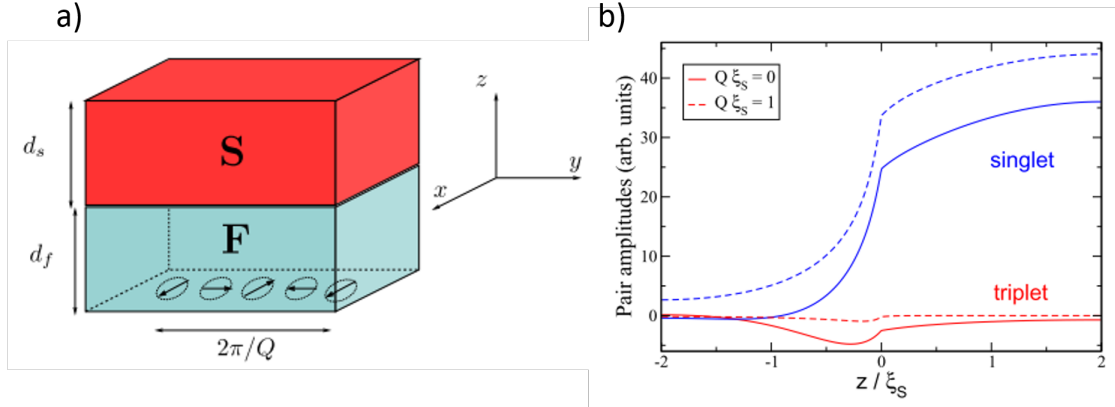


Figure 2.21: a) The geometry considered by Champel and Eschrig. b) The calculated singlet and triplet pair amplitudes at the SF boundary. $z > 0$ is the superconductor and $z < 0$ is the ferromagnet. $Q\xi_s = 0$ corresponds to no domain wall, whereas $Q\xi_s = 1$ is a domain wall with one complete rotation over the distance of one superconducting coherence length. With the domain wall present, the singlet correlations are increased and triplet correlations decreased in comparison with the case of no domain wall. Images adapted from [18]

This magnetization dependent effect was investigated theoretically soon after by Champel and Eschrig [18] in the formalism of the quasi-classical theory of superconductivity based upon the Usadel transport equation. The authors considered a superconducting thin film on top of a magnetic thin film. The magnetic film could have a magnetization that is collinear and directed in-plane with the film or with a domain wall that rotates in the plane of the film, a n el wall, with wave vector of rotation Q such that the period of spin rotation is $2\pi/Q$ as illustrated in fig 2.21a. These calculations showed that the singlet and triplet superconducting components were always present at the SF interface. The majority of triplet components were shown to be of anti-parallel spin pairs and an induced magnetization was shown to exist in the superconductor that followed the magnetization of the domain wall. Most importantly, the authors showed that the presence of a domain wall reduces the triplet pair correlations and increases the singlet pair correlations, as shown in fig 2.21b. In this calculation the non-monotonic behaviour of T_c seen in SFS multi layers was reproduced and it was shown that the overall suppression effect of the ferromagnet on the superconductor was reduced when a domain wall was present due to the

overall smaller exchange field felt by the Cooper pairs, in agreement with experimental observations. Similar calculations by Houzet et al. [126] were also in agreement with Champel and Eschrig [18].

These experiments and calculations indicate that the effect of magnetization states in SF systems can be considered as a weakening of the exchange field felt by the Cooper pairs in the superconductor. However, more recent work by Zhu et al. [127] suggests that the answer is more complex. In this work the authors fabricated an SF bilayer in which the F layer was an exchange spring made of Sm-Co/Py and the S layer was Nb. The Sm-Co/Py structure creates an exchange coupling between the hard magnetic Sm-Co and soft Py such that the Py magnetization at the interface is held fixed to the magnetization of the Sm-Co. Thus, when a field is applied in-plane with the sample at an angle with the saturated magnetization of the Sm-Co layer, the magnetization of the Py rotates at the Py surface but remains fixed at the interface and a spiral magnetization structure is created in the Py layer. Using this geometry the authors measured the resistive transition and critical current of the SF bilayer and found a non-monotonic enhancement of T_c and I_c on the rotation angle. Their results could not be explained by either the theory of reduced average exchange field or the production of triplet pairing, indicating that more complex effect are at play.

Some recent experimental work concerning the inverse proximity effect has focused on observing the induced magnetization in the superconducting layer. Measurements by Xia et al. [128] utilised the magneto optical Kerr effect (MOKE) to investigate the induced magnetization in Ni/Pb and (Co-Pd)/Al bilayers. MOKE allows the measurement of local magnetization by using a polarised laser beam incident on the surface of the film of interest. The interaction between the light and magnetization causes a rotation of the light polarisation known as the Kerr angle. Thus, this method allows for relatively localised lateral measurements of magnetization, limited by the width of the beam. Xia et al. used this method to measure the Kerr angle when the beam was incident on the Nb or Al film and observed a shift in the Kerr angle with the onset of superconductivity as illustrated in fig 2.22a, indicating that a magnetization was induced in the superconducting film due

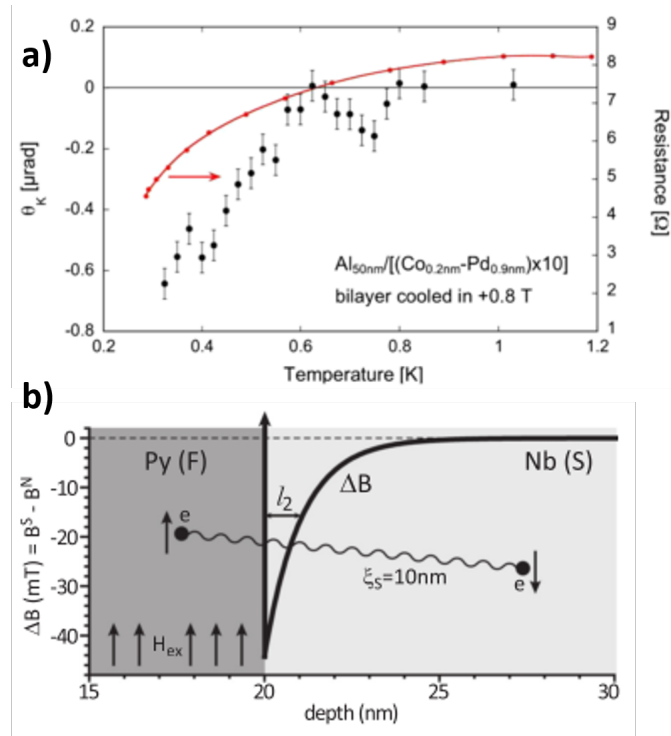


Figure 2.22: a) the measured Kerr angle (black points) and resistance (red points) with decreasing temperature of an Al/(Co-Pd) bilayer. The changing Kerr angle on transition into the superconducting state infers a magnetization induced in the superconductor. b) The spatial change in local flux density of part of a Py/Nb/Py tri-layer at 9.7 mT, measured using low energy spin polarised muon rotation. Again, the reduction in flux in the Nb near the SF interface indicates an induced magnetization in the superconducting state. Images adapted from [128, 129]

to proximity with the Ni or Co-Pd film.

Similarly Flokstra et al. [129] took the principle further by using low energy spin polarised muon rotation. This technique uses muons of controllable energy to probe a thin film with a controllable depth profile. The depth profile is controlled by increasing the muon energy, as the muon energy is increased the muons penetrate further into the film, with a broadening range of the muons penetration depth. The sample, a Py/Nb/Py spin SFS valve, is placed in a magnetic field of 9.7 mT in plane with the film and the muons are incident with the film normal. When the muons enter the sample, their spin processes around the local magnetic flux with frequency $\omega = \gamma_\mu B$, where γ_μ is the muon gyromagnetic ratio. When

a muon decays, it emits a positron with an angle relative to the spin direction at the point of decay. Thus, by spin-polarising the muons, controlling their energy, and measuring the angle and time of emitted positrons the local magnetic flux can be calculated. Because of the spread in muon penetration depths for a given energy, many counts must be taken to accurately measure the field at a given penetration depth. The main result from these measurements is shown in fig 2.22b, as a change in field $\Delta B = B_S - B_N$, where B_S and B_N are the measured flux in the superconducting and normal states, respectively. This data indicates a reduction in flux near the SF interface in the superconducting state that would agree with the explanation that a magnetization opposite to the magnetization in the permalloy is induced in the Nb. However, this magnetization decays over a ~ 1 nm, much shorter than the coherence length in the Nb. Measurements such as these are still in their infancy but appear to indicate that the idea of an induced magnetization in the superconductor is true.

Building on top of this work, research in the last few years has begun to investigate the use of the inverse proximity effect to create so called *proximity-junctions*. The group of Vávra et al. published the first research on such a system [21]. The proximity junction was fabricated by depositing a weakly ferromagnetic PdFe wire 20 nm thick and 400 nm wide on top of a Nb wire 820 nm wide and 30 nm thick, as illustrated in fig 2.23ii. Measurements of the resistive transition into the superconducting state, fig 2.23ia, indicated two superconducting transitions, first the Nb leads not influenced by the PdFe at 6.15 K and then a gradual decrease in resistance of the Nb in which the superconductivity is suppressed by proximity with the PdFe. Differential resistance measurements with decreasing temperature, fig 2.23ic-b, showed a fine structure above 5.7 K with three peaks. The authors attributed peak 1 to the transition of the majority of the junction, S'' (see fig 2.23ii b) and peaks 2 and 3 to the transition of the two parts S' on the junction edge. The edge sections were considered under a different proximity induced suppression due to irregularities at the edges of the PdFe film. Measurements of differential resistance with decreasing temperature showed that this fine structure reduced into a single transition into the resistive state when below 5.7 K. The authors attributed this to the development of

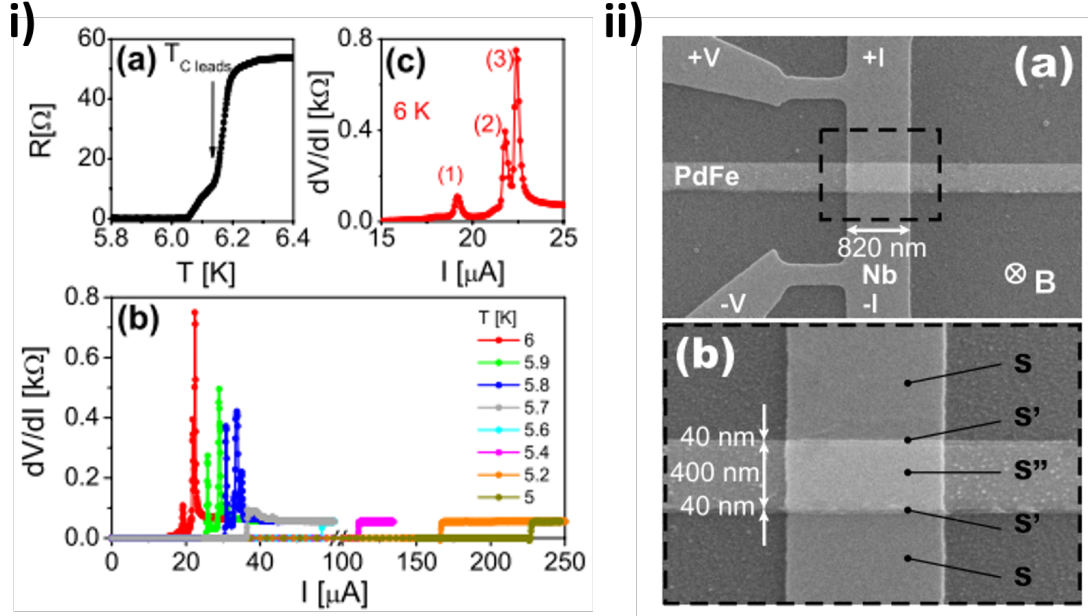


Figure 2.23: Results published by Vávra et al. of a proximity junction. The junction consists of a Nb wire overlying a PdFe wire (iia-b). The transition into the superconducting state at T_c shows two transitions for the leads and junction respectively (ia). Differential resistance measurements of the junction at varying temperatures show three transitions at $T > 5.7$ K attributed again to the junction and the leads separately. Below 5.7 K, the three transitions merge into a single transition. Images adapted from [21]

the superconducting condensate in the Nb beneath the PdFe reaching a point in which the super current in the Nb overlying the PdFe dominates over the Josephson effect. The authors observed the expected Fraunhofer interference pattern in the critical current when a magnetic field is applied perpendicular to the plane of the junction with two different periods at 5.9 K and 6 K corresponding to the two effective junction areas S'' and S' . When irradiated with radio frequency radiation the authors observed Shapiro steps in the differential resistance. Both of these observations confirm that the proximity junction does indeed exhibit the Josephson effect.

These observations were reproduced by Lin et al. [23] in a proximity junction consisting of 100 nm thick 1.5 μ m wide Nb wire deposited on top of a 50 nm thick 700 nm wide permalloy (NiFe) wire. In this work however, because Py has a larger exchange field than PdFe, the

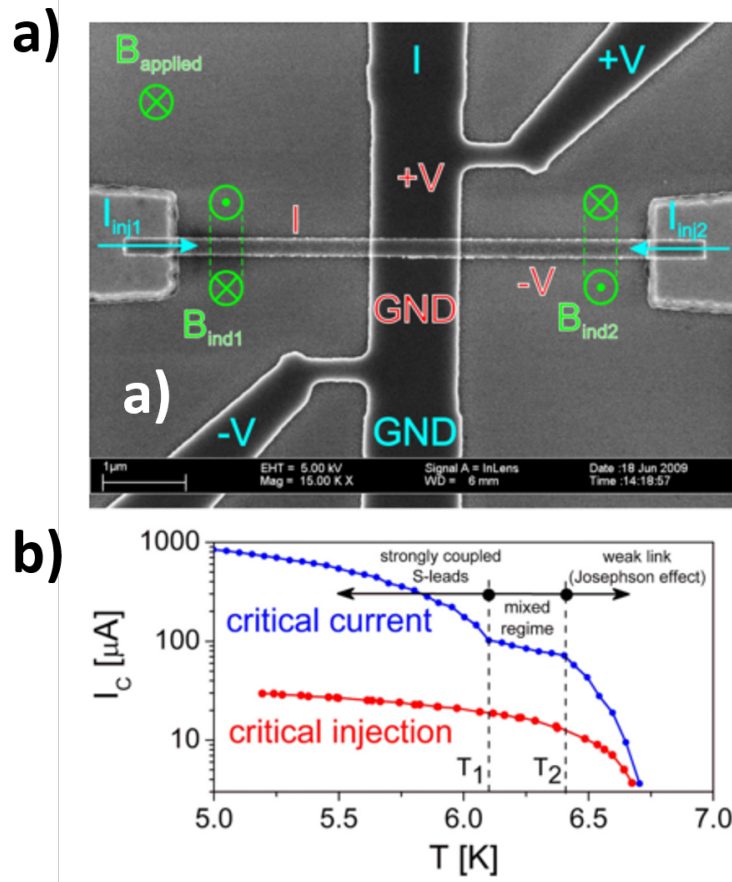


Figure 2.24: More recent results published by Vávra et al. of a proximity junction. The junction consists of a Nb wire overlying a Fe wire (a). The junction behaved like that of the previous experiment by Vávra et al. (fig. 2.23). The authors now defined three regimes of the critical current behaviour (b, blue line); the weak link behaviour where the junction is dominated by the Josephson effect, the strongly coupled regime where the I_c is dominated by the supercurrent and the mixed regime between the two extremes. Injection of current through the Fe wire (red line, b) showed only a single transition behaviour with critical current less than the SNS measurement arrangement (blue line)[22].

Fraunhofer interference could be observed down to 2K. However, the transition into the superconducting state was a single step, suggesting a reduced influence of the ferromagnet compared to the work of Vávra et al.. Most recently Vávra repeated their experiment from 2009 with the addition of current injection through the now Fe ferromagnetic wire, as illustrated in fig 2.24a. Again, the authors observed suppression of the critical current

with two resistive transitions in the differential resistance above 6.1 K. The authors defined three regimes of the junction behaviour based on the critical current evolution with decreasing temperature, fig 2.24b blue curve; the weak link regime when $6.4\text{ K} < T < 6.8\text{ K}$, the mixed regime when $6.1\text{ K} < T < 6.4\text{ K}$ and strongly superconducting regime when $T < 6.1\text{ K}$. The authors also repeated their observation of the Fraunhofer pattern as before. The extension of this work was to the injection of current through the ferromagnetic leads, as indicated by the I_{inj} geometry in fig. 2.24a. When injecting current through both ends of the ferromagnetic leads the authors observed a the critical current behaviour shown by the red curve in fig 2.24b, exhibiting no mixed behaviour. Furthermore, the interference patterns in an applied magnetic field now resembled fresnel like interference, with a skewed character that the authors attributed to the inhomogeneous magnetic field generated by their injection scheme. This work however, demonstrated active control of the critical current in such a junction, an important step towards novel superconducting electronics.

To the authors knowledge, these are the only published works concerning proximity junctions to date. These experiments demonstrate that such a system creates a Josephson effect, however questions remain. In all of the experiments, a simple ferromagnetic wire geometry was used, meaning that the magnetization distribution in the ferromagnet would be collinear and directed along the wires length. It stands to question then, knowing that the inverse proximity effect is influenced by varying magnetization structure, how these proximity junctions would behave when in contact with more complex inhomogeneous magnetic structures. Further more, why does the junction prepared by Lin et al. [23] show only a single transition into the superconducting state compared to the two step transition observed by Vávra et al. [21] when Lin et al. [23] used a much stronger ferromagnetic material. Lastly, it has yet to be confirmed that the three regimes seen by Vávra et al. [22] are indeed due to their explanation of increasing superconductivity in the Nb dominating over the Josephson effects. This thesis aims to answer these questions.

Chapter 3

Experimental Techniques

This chapter of the thesis introduces the experimental techniques used. The fabrication of samples is discussed, introducing the principle of fabrication of thin film nano scale samples and the specific techniques used to fabricate the hybrid Ni-Al structures in this project. The cryogenic system used for measurement is presented, giving a brief explanation of the operation of both the ^3He cryostat and magnetic properties measurement system (MPMS), including the electrical measurement techniques used. The room temperature apparatus used for magnetoresistance measurements is introduced and finally the principle of magnetic force microscopy is explained.

3.1 Nanoscale fabrication

3.1.1 Main principle of fabrication

Nano-fabrication is performed via a process of layered resists and lithography procedures. Particular techniques exist for differing designs, for example photolithography is often used for structures on the order of tens of microns, whereas electron beam lithography is necessary for designs involving features of just a few hundred nanometres. This is because photolithography uses light with wavelengths on the order of hundreds of nanometres and electron beam lithography uses electrons with wavelengths on the order of tens of nanometres. This is of importance as the limit of the resolution of the lithography is the

wavelength of the light or e-beam used. The principle of nano fabrication is illustrated in fig. 3.1. First one or two resist layers are spun and baked on the surface of the substrate (fig. 3.1a), commonly Si or SiO. The desired pattern is then exposed via photo or, in the case of this project, e-beam lithography (fig. 3.1b) which weakens the bonds of the polymer resist in the exposed areas, allowing the resist to be removed by a chemical developer. The exposed resist is then developed in a development solution of 7 % water to 93 % IPA (fig. 3.1c). The patterned resist is then mounted inside a vacuum chamber deposition system and the desired material is deposited, forming a thin film across the resist and on the substrate revealed by the patterning (fig. 3.1d). The unwanted film and resist is then removed via lift-off using solvent such as acetone (fig. 3.1e) and the desired patterned structure is obtained (fig. 3.1f). The following sections will discuss each of these steps in the sample fabrication in more detail.

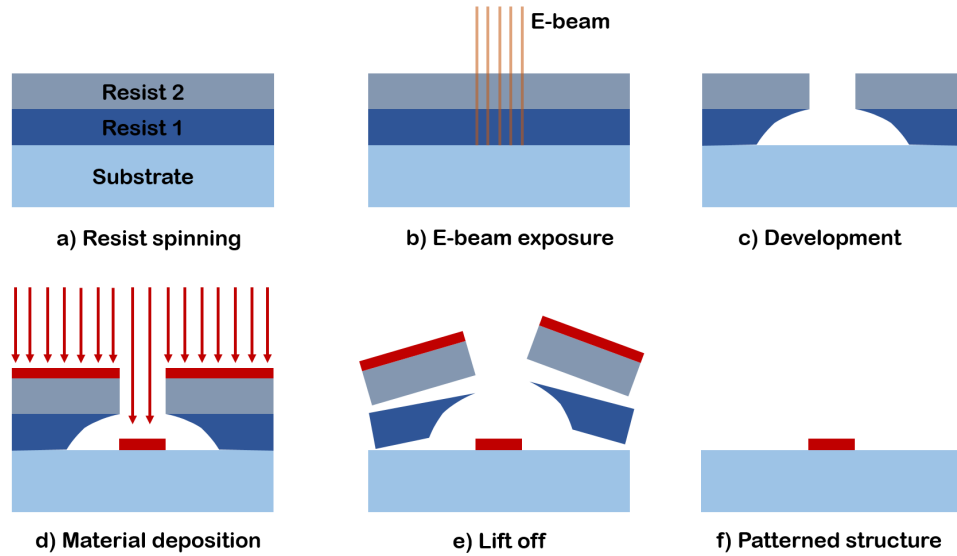


Figure 3.1: The principle of nanofabrication used in the present work. Polymer resists are deposited on a substrate by spinning and then baking (a). Part of the resist is then exposed to either light or an electron beam weakening the polymer bonds (b). The weakened polymer is then removed with a chemical developer (c). The substrate is then coated with the desired material (d). The unwanted resist is then removed with a solvent (e). The desired patterned thin film structure then remains on the substrate (f)

3.1.2 Substrate preparation

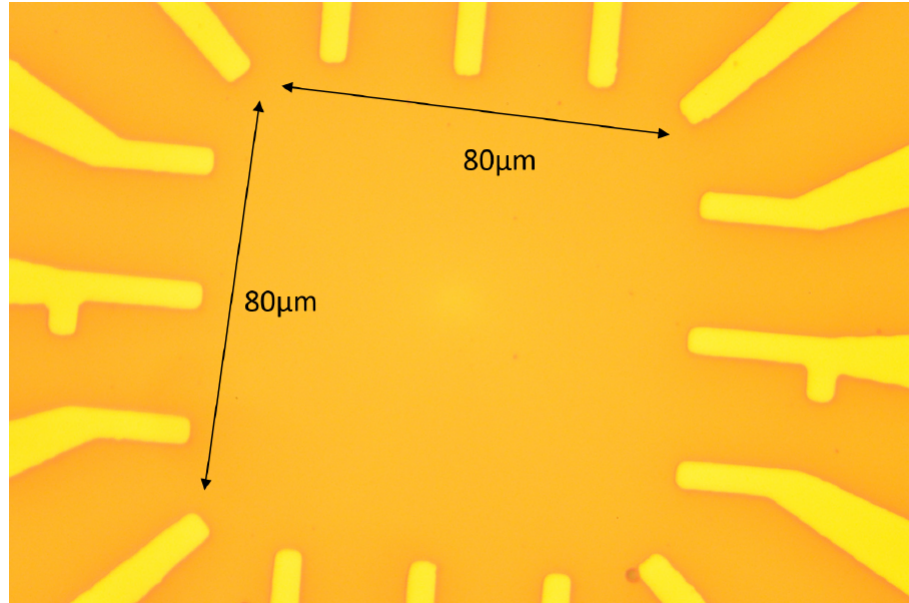


Figure 3.2: Optical photograph of a sample substrate with gold contacts that had been deposited by photo lithography techniques. The central substrate area is $80\text{ }\mu\text{m} \times 80\text{ }\mu\text{m}$, within this area nano structures are deposited.

Substrates were fabricated on silicon wafers with a native silicon oxide. The wafers were cleaned with a five minute oxygen plasma etch to remove contamination. Approximately $70\text{ }7\text{ mm} \times 7\text{ mm}$ chips with Sixteen gold contact leads were patterned on to the wafers. This leaves an $80\text{ }\mu\text{m} \times 80\text{ }\mu\text{m}$ area in the centre of each of the chips for the deposition of the nano structures as seen in fig 3.2, such that the nano structure can be electrically connected to the measurement apparatus via the gold contacts. A two layer photo sensitive resist profile was used such that the bottom layer of resist develops faster than the top creating an undercut as demonstrated in fig 3.1c. The use of this undercut avoids unwanted material deposition on the walls of the patterned resist. Photo resist was used as it is ideal for the the large area needed to be exposed at once, however this limits the resolution of the exposure to at best a few microns, limited by the diffraction of the UV light. The 80 nm thick gold contacts were deposited via thermal evaporation of 99.999% gold in a vacuum of $1 - 5 \times 10^{-6}$ torr after the evaporation of $5 - 10\text{ nm}$ of NiCr to assist the adhesion of

the gold film. Lift off was performed and the $7\text{ mm} \times 7\text{ mm}$ chips were scribed and cut into individual chips for use as sample substrates.

3.1.3 Electron beam lithography

As the all the structures investigated in this project are smaller than the resolution of the UV photolithography described above the samples were patterned using electron beam lithography. The electron beam lithography process again uses two layers of resist to avoid the deposition of the desired film on the walls of the resist. The electron sensitive resists used are typically Copolymer and PMMA with thickness's dependent on the structure to be fabricated. However, it is generally good practice for the resist layer to be three times the thickness of the desired structure. The resist is scratched away from the central sample space for focusing and substrate is then mounted in the vacuum chamber of the Scanning electron microscope (SEM) along with an additional focus sample. The focus sample has well defined gold rings in the sample space which are useful for the focusing of the beam. Once the sample is inside the SEM chamber at an acceptable vacuum the beam current is set to 15 pA by focusing on a Faraday cup in the centre of the sample holder that is connected to a nearby ammeter. Once the correct beam current set by changing the beam spot size, the beam is focused on the focusing chip. This stage is important to ensure that the beam is correctly focused and that the astigmatism of the beam is minimized, both of these factors can be detrimental to the lithography. The beam is then moved to the sample and the beam is again focused on the scratch in the resist to ensure the focus is as accurate as possible near the sample space in the centre of the chip. The beam is quickly centred on the sample space, turned off to avoid unwanted exposure of the resist and beam control passed to the lithography software. The location of the gold contacts is used to align the sample space for the first layer of lithography and eight crosses are patterned for fine alignment of following lithography layers, a crucial step in this project as samples were fabricating using two lithography steps. Without the fine alignment markers, the second film could not be aligned accurately with the first. The lithography pattern is designed first in AutoCad software and then passed to the nanomaker software for the lithography.

The e-beam dose is carefully selected for each part of the pattern, if the dose is too low then the resist will not develop at all, if the dose differs across the pattern then some structures will develop faster than others and the fine detail of the pattern will be lost. If the dose is too high, then the opposite of the desired effect can occur, the polymer bonds can be strengthened and become irremovable by the developer.

The scattering of the incident electrons as they pass through the resist and substrate is called the proximity effect. For small structures on the order of a micron, the scattering is not dominant enough to effect the exposure, however for larger structures, the dose of the beam must be adjusted across the structure. Figure 3.3 demonstrates that the scatter in the resist layer can be reduced using higher accelerating voltages. At low accelerating voltages (10 kV) the electrons scatter inside the PMMA resist layer and the effectively exposed area is much larger than the beam width. At higher accelerating voltages, 20 – 30 kV, the beam penetrates through the PMMA layer first and then scatters in the silicon substrate. The exposed area of PMMA is now on the order of the beam width.

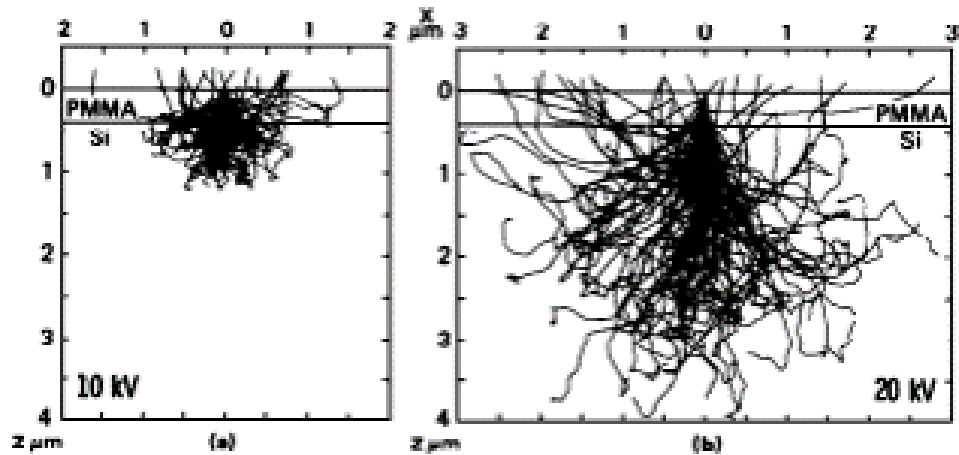


Figure 3.3: A simulation of the electron beam scattering through PMMA on top of a silicon substrate at 10 kV (left) and 20 kV. At lower accelerating voltages the electrons from the beam mostly scatter inside the PMMA, increasing the effective area of PMMA exposed to larger than the beam width. At higher voltages, the beam penetrates the PMMA and scatters mostly in the Si substrate, restricting the exposed area of PMMA to the beam width as desired. Image adapted from [130].

3.1.4 Thin film deposition

The samples in this project were fabricated using metals thermally evaporated on to the substrates. For this thin film deposition the Edwards evaporator illustrated in fig. 3.4 was used. This chamber pumps down to pressures as low as 10^{-6} Torr using a rotary pump and a diffusion pump. Samples are placed in a stage that can rotate freely such that the samples can be faced down towards the metal source or up towards a plasma etch chamber. Before pumping the chamber, a tungsten boat is placed between the two electrodes with the desired metal placed in the boat. Once the chamber is pumped down, samples are first cleaned with a non reactive argon plasma etch to remove excess resist and contamination. A large current is then passed between the electrodes and through the tungsten boat to heat the metal creating a metal vapour that coats the sample above. The material thickness is measured using a vibrating thickness monitor crystal positioned at the same distance from the source as the sample, with nominal error in the thickness of ± 0.1 nm. The freely rotating sample stage allows material to be deposited at different angles, an extremely useful addition that facilitates the shadow evaporation techniques. After deposition of the thin film, the resist and excess film is removed using acetone at 60°C . The addition of the *in situ* non-reactive argon plasma etch in the Edwards evaporator was key to this project, as to observed proximity effects between ferromagnetic and superconducting aluminium films the interface between films must be of good quality. Ferromagnetic films were always deposited first in this project, therefore before the deposition of the aluminium films the ferromagnetic film was always etched with the argon plasma, cleaning any oxide layer on the ferromagnet and ensuring a good interface between the films.

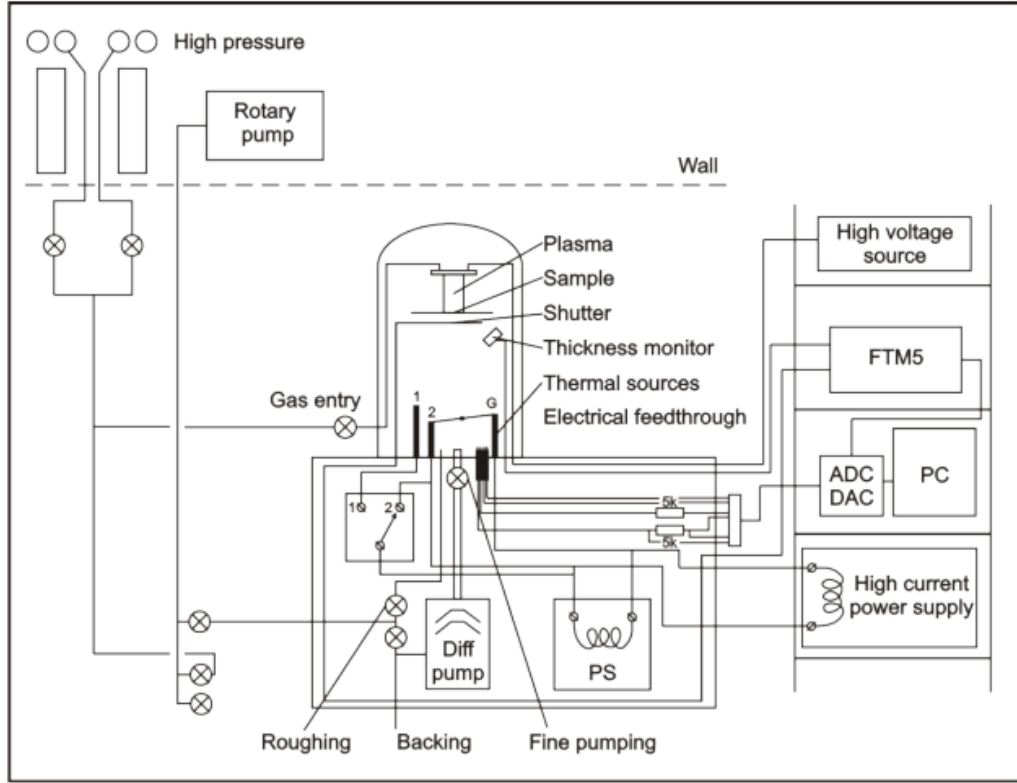


Figure 3.4: A schematic of the Edwards evaporator used for the deposition of metallic thin films. [131]

3.2 Cryogenic measurement systems

3.2.1 He-3 Cryostat

As aluminium has been used as the superconductor in this project, the samples had to be measured at temperatures less than 1.2 K, the critical temperature of aluminium. Thus, samples were cooled using a top loading one-shot ^3He cryostat. This cryostat has a base temperature of $\sim 240 - 300$ mK depending on the heat load. This temperature is not as low as that of the more commonly used dilution cryostats that can reach temperatures as low as 10 mK. However, samples are mounted to the end of an electrical probe that can be inserted and removed from the cryostat while it is still at liquid ^4He temperatures. This top loading probe used means that samples can be changed in as fast as 12 hours, compared to the several days needed to mount a sample to the mixing chamber of a

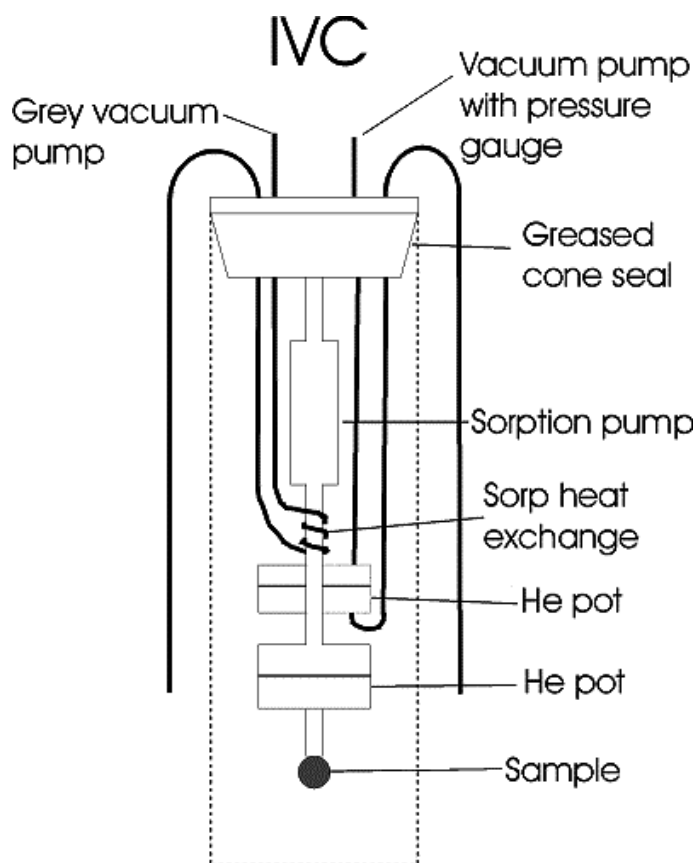


Figure 3.5: Schematic of the ^3He cryostat IVC assembly. The entire IVC assembly (inside the dotted line) is submerged in liquid ^4He . The inside of the IVC is a vacuum, thermally isolating the internals from the ^4He . The sample probe is inserted through the middle hollow section, which is surrounded by the charcoal absorption pump and then 1 K pot. The sample, at the end of the probe, then hangs just above the bottom of the hollow sample space, where it can be submerged in liquefied ^3He [132].

dilution cryostat, suitably prepare the seals, and then cool down the system. As such, the speed of use of this cryostat was ideal for this project.

The cryostat is referred to as a one-shot cryostat because of its method of operation, which is relatively simple to that of other cryostats. The main operating parts of the cryostat are situated inside the inner vacuum chamber (IVC) as seen in fig 3.5. The IVC assembly is submerged inside a liquid ^4He dewar. Everything inside the IVC is thermally isolated from the liquid ^4He by the vacuum apart from the pick up tubes from the 1 K pot and sorb heat exchanger to the ^4He bath and the top plate of the IVC. A volume of ^3He is

kept within a sealed dump vessel attached to the sample space within the IVC. Once the cryostat has been cooled down to liquid ^4He temperature, the ^3He is released from the dump vessel and is absorbed by the charcoal sorbtion pump. The 1 K pot is cooled down to 1.2 K by allowing a small flow of liquid ^4He in through the pick up line into the pot whilst simultaneously pumping on the pot using a rotary pump. This lowering of the vapour pressure of the ^4He in the pot reduces the temperature. To bring the cryostat down to base temperature the charcoal sorb is heated to 45 K and kept at this temperature for ~ 45 minutes. This causes the ^3He to desorb from the charcoal and condense to a liquid on the cold surface of the 1 K pot inside the sample chamber. The ^3He liquid collects as a pool at the bottom of the sample chamber such that the sample at the end of the probe sits in the liquid ^3He . At this point the sample temperature is in equilibrium with the 1 K pot. The heater for the sorbtion pump is then turned off and the sorb cools, by both the cooling power of the 1 K pot and heat exchanger. Once the sorb temperature is below 30 K the charcoal becomes absorbing again and begins to pump on the liquid ^3He , lowering its vapour pressure. The enthalpy change of the evaporating ^3He absorbs heat from the sample, lowering the temperature of the sample to 240 – 300 mK within approximately 2 hours. Depending on the heat load and probe used the sample will stay at base temperature for 8 - 36 hours, hence the term one-shot cryostat. After all the ^3He has evaporated the condensation of the ^3He must be repeated.

Current-biased measurement

Samples mounted in the ^3He cryostat were measured using a current-biased electronics set-up. A schematic of the electronics can be seen in fig. 3.6. The current bias set-up is designed to measure the differential resistance, or dV/dI , of the samples. The dV/dI measurement is used because it is easier to measure small features in the I-V properties of structures compared to simple I-V curves. Two voltage sources are used: a DC voltage is supplied from a Yokogawa multisource and a small AC voltage, typically 10 mV, is supplied from the internal oscillator of a DSP lock-in amplifier. The small AC voltage is then added to the DC voltage as a modulation by the summing amplifier, which has a

gain of 1. A constant current bias is then ensured by adding a $10\text{ k}\Omega$ resistor in series with the output of the summing amplifier. Because the samples measured have small resistance relative to the bias resistor, on the order of a ohms to tens of ohms, the voltage drop across the bias resistor is much greater than that across the sample. Thus, the current is effectively limited by the resistor and the current through the sample is simply calculated using ohms law, $I_{bias} = V_{in}/10\text{ k}\Omega$. The resistor is then connected in series to the cryostat wiring and passed through the device under test (DUT) which is then grounded outside the cryostat.

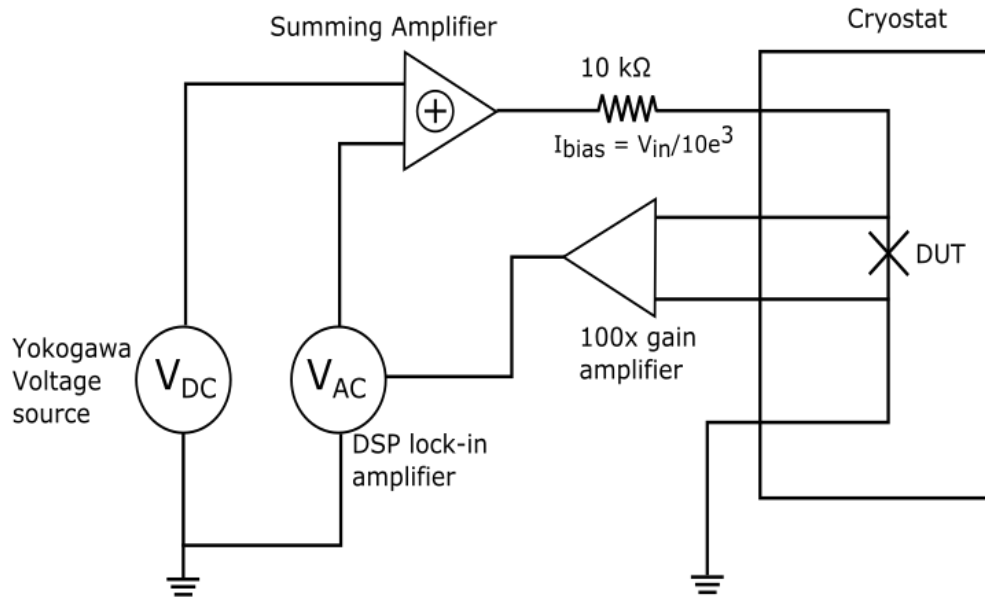


Figure 3.6: A schematic of the current bias set-up used to measure samples in the ^3He cryostat. The samples measured have small resistance, on the order of an ohm to tens of ohms. Thus the $10\text{ k}\Omega$ bias resistor is much larger than the sample resistance and the current is limited by the size of this resistor.

Two independent voltage probes are used to measure the AC voltage drop across the DUT, as the signal is small the voltage is amplified using a differential amplifier with $100\times$ gain. The signal from the amplifier is then connected to the lock-in input. To measure the

sample the AC oscillation is set to less than 100 Hz so that the measured AC voltage drop can be reasonably extrapolated to the DC response. To measure the dV/dI the AC voltage is set to a constant value and the DC voltage is swept usually from -3 to $+3$ V, thus a current of -300 to $+300$ μ A. Thus as the DC voltage is swept the AC voltage across the sample corresponds to the resistance of the sample at the DC bias current applied, the dV/dI . The dV/dI in ohms can be calculated from the input voltages by the equation,

$$\frac{dV}{dI} = \left(\frac{V_{measured}}{100} \right) / \left(\frac{V_{AC}}{10\,000\,\Omega} \right) \quad (3.1)$$

3.2.2 Magnetic properties measurement system MPMS

To aid in magnetic characterisation of samples, hysteresis curves were measured using a magnetic properties measurement system (MPMS). The MPMS measures the magnetic moment of samples from 2–380 K with a field up to 7 T. The MPMS uses a superconducting solenoid mounted inside a liquid 4 He dewar. Inside the solenoid is a superconducting wire round into three pick up coils that are wound from top to bottom; counter-clockwise once, clockwise twice and then counter-clockwise once again. This forms a second order gradiometer, that increases the sensitivity and reduces the background noise of the measurement. A field is then applied using the solenoid and the sample is moved through the gradiometer coils such that the moment of the sample creates an EMF in the coils. The coils are then inductively coupled to a SQUID below the magnet. As the coils, the SQUID, and the wires connecting them are all superconducting they form a closed loop and the current induced from the movement of the samples magnetic moment through the coils is converted to a voltage in the SQUID. Thus, the magnetic moment of the sample is directly converted to a voltage in the SQUID, which acts as the sensitive magnetometer in the system. A schematic of the MPMS magnet and gradiometer coils is shown in fig. 3.7.

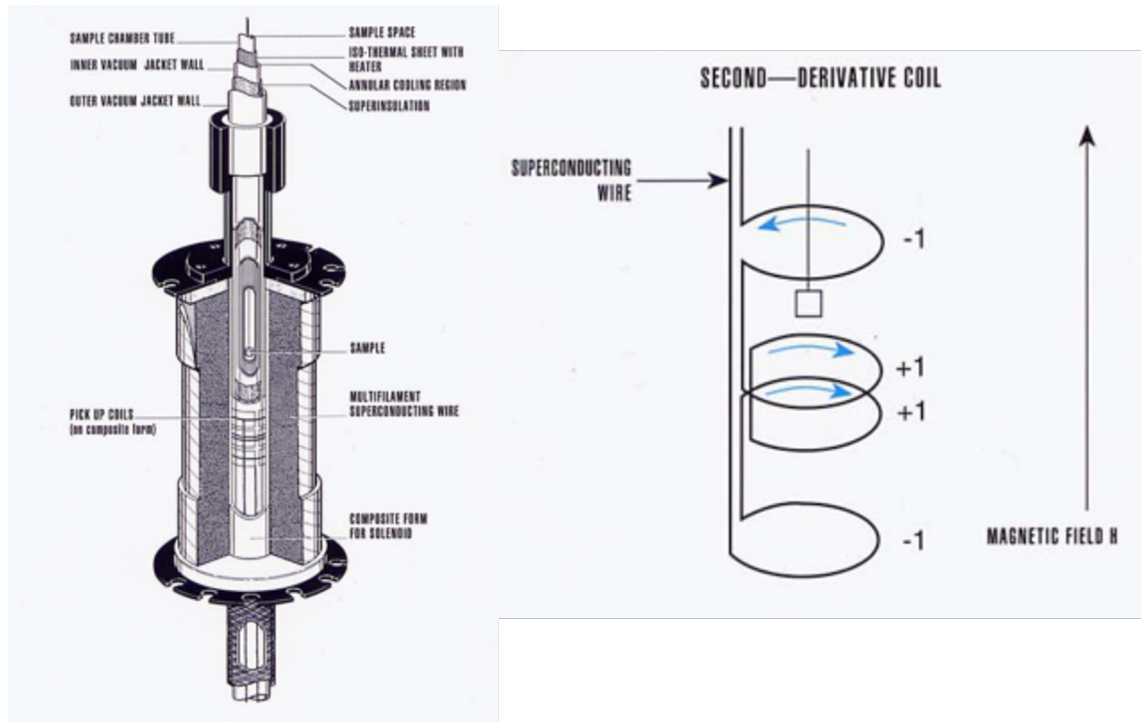


Figure 3.7: The MPMS magnet and coil assembly (left) and a schematic of the pick-up coil windings (right). The sample (square) is moved through the counter-wound pick up coils inducing a surface current in the superconducting coil due to the samples moment. This surface current is inductively transferred to an RF SQUID away from the applied magnetic field, precisely measuring the magnetic moment of the sample.[133]

3.3 Room temperature magnetoresistance measurements

The anisotropic magneto resistance effect (AMR), discussed in chapter 2, was used as part of the magnetic characterisation of samples. The magnetoresistance of samples at cryogenic temperatures in the ^3He cryostat were measured using standard 4-point geometry and a DSP lock-in amplifier. At room temperature the AMR of samples was measured using a rotating stage mounted in the magnet shown in fig. 3.8. Samples were measured with four point geometry with a DC current bias where the voltage drop across the sample was measured using an Agilent nano-voltmeter. The rotating stage allows the measurement of the magneto resistance within a full 360° rotation in 0.9° increments. This allows the investigation of the magnetisation reversal in samples when the magnetic field is ap-

plied in different directions relative to the sample geometry, introducing an extra degree of control of the magnetic elements.

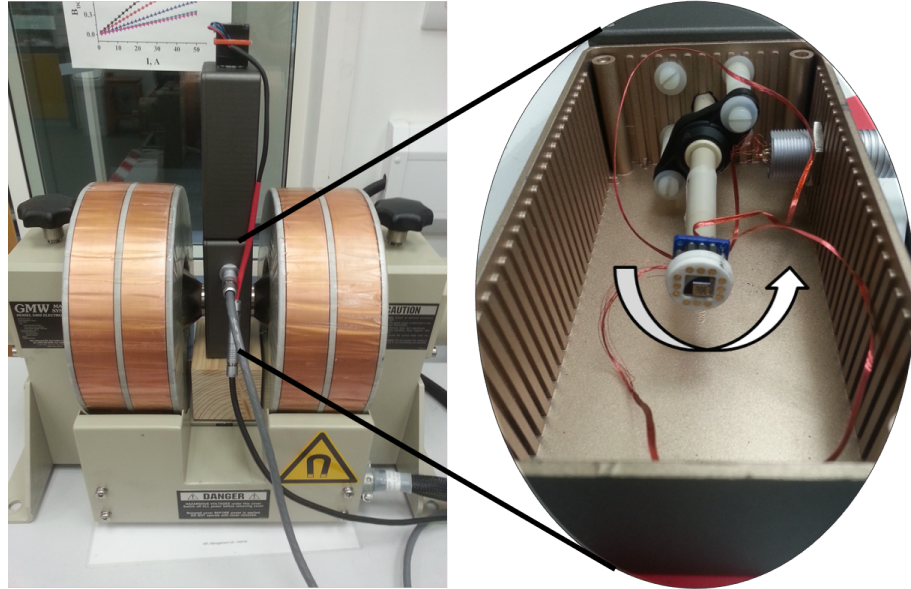


Figure 3.8: Picture of the room temperature magnet and rotating sample holder used for AMR measurements.

3.4 Magnetic force microscopy

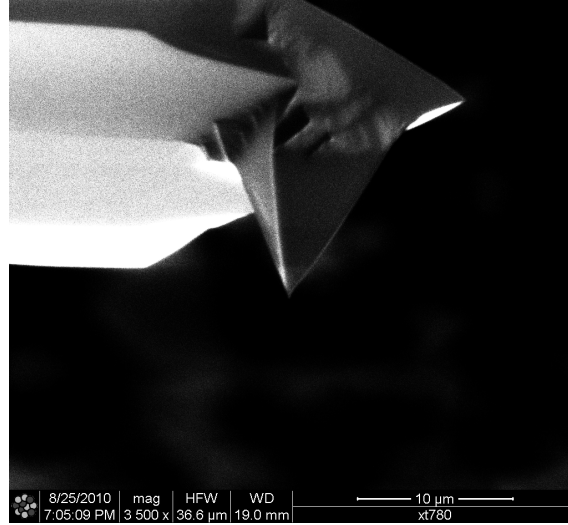


Figure 3.9: An SEM image of an MFM probe tip showing the pyramid tip structure. Image taken by Dr. Ravish Rajakumar.

Magnetic force microscopy (MFM) is a form of scanning probe microscopy. A micron scale probe that ends in a pyramid tip (fig. 3.9), with a ferromagnetic coating, attached to a cantilever arm is mechanically oscillated at its resonance frequency by use of piezoelectric motors. The principle of the MFM technique is illustrated in fig. 3.10. The probe is moved across the sample in a raster pattern in tapping mode operating as an atomic force microscope (AFM). As the probe moves across the sample, the resonant frequency and phase of the probe oscillation are shifted due to the probe interaction with the sample surface. By using a feedback loop the height of the probe is changed to keep the frequency of the oscillation constant. By recording the change in height a detailed image of the surface topography is acquired. The probe is then raised to a user defined lift height, (20 – 150 nm), and the measured topography is retraced. At this increased distance the interaction between the probe and sample is no longer due to atomic forces but magnetic forces between the magnetic probe coating and any magnetic materials on the sample surface. The shape of the probe tip is designed as to have perpendicular magnetic anisotropy with respect to the sample plane, therefore when operated in lift mode, the MFM measures

qualitatively the perpendicular field from the sample. The measurements are qualitative because only the probe oscillation phase difference is measured, to directly measure the field strength from the sample, one would need to know the exact magnetisation magnitude and distribution in the tip, a non trivial task.

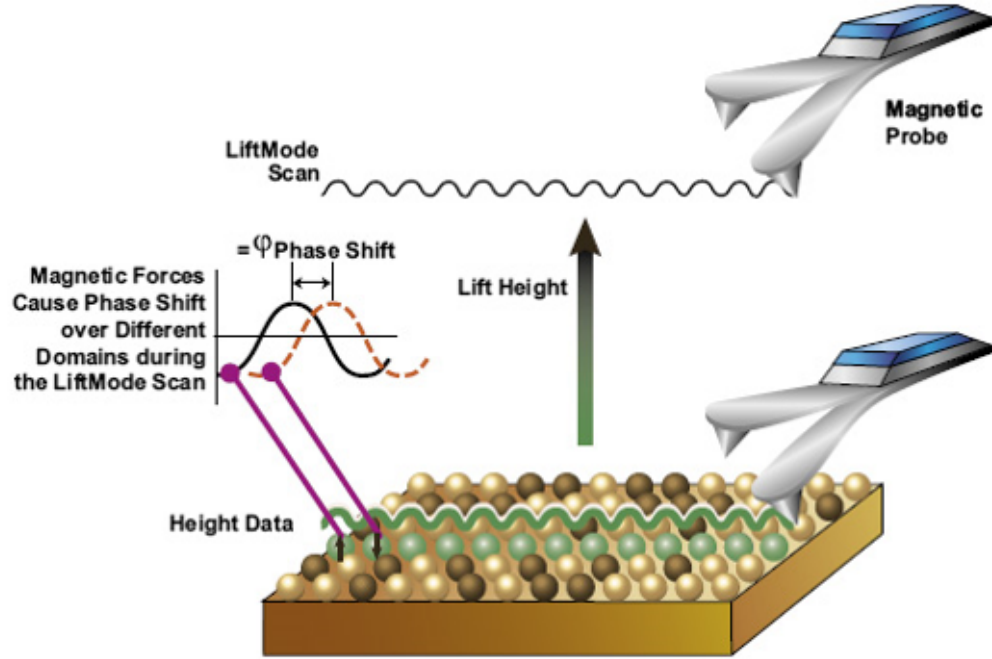


Figure 3.10: The principle of the MFM technique. First the probe is swept across the sample in tapping mode to acquire the sample topography (green curve). The probe is then lifted to a predetermined lift height above the sample so that the only interaction between probe and sample is due to magnetic forces. The measured topography is then retraced at this lift height and the shift in oscillation phase due to the magnetic interaction between the probe and sample is measured and an image of the magnetic field emanating from the sample is acquired. Image adapted from [134]

To see how the magnetic forces from the sample are detected by the magnetic probe, one can consider the magnetic probe tip as a collection of dipoles of the form [135]:

$$\vec{M}(\vec{r})dV \quad (3.2)$$

where \vec{M} is the magnetization of the probe magnetic coating and dV is a unit volume of

the coating. Therefore, the energy of the interaction between the probe and the sample is the integral across the entire magnetic coating of the probe and the magnetic field:

$$W = - \int (\vec{M}(\vec{r}) \cdot \vec{H}(\vec{r} + \vec{r}')) dV' \quad (3.3)$$

and the force of this interaction is the gradient of the energy:

$$\vec{F} = \int \nabla(\vec{M} \cdot \vec{H}) dV' \quad (3.4)$$

where \vec{H} is the field from the magnetic sample at position $\vec{r} + \vec{r}'$, where \vec{r} and \vec{r}' are defined as positions along the probe tip as illustrated in fig. 3.11 and $\vec{M}(\vec{r})$ is the magnetization of the infinitesimal volume element dV' at position \vec{r} . These integrals describe the sum of energy and the subsequent force that each infinitesimal magnetization volume feels from the field at all points along the probe coating. The cantilever oscillation is only sensitive to the out-of-plane field component from the sample because the tip magnetization is directed in the z direction. Thus, the z component of the force on the probe is most important and is given by:

$$F_z = - \frac{\partial W}{\partial z} = \int \left(M_x \frac{\partial H_x}{\partial z} + M_y \frac{\partial H_y}{\partial z} + M_z \frac{\partial H_z}{\partial z} \right) dV' \quad (3.5)$$

where $H_{x,y,z}$ and $M_{x,y,z}$ are the field and probe magnetization components in the x , y and z directions. By operating the cantilever in the oscillating mode, the sensitivity of the measurement is greatly increased. This is because the presence of a force gradient, such as that in a magnetic field, causes changes to the resonant frequency and phase of the cantilever oscillation that are simple to measure in comparison to small forces. Therefore, the force gradient of concern is in the z direction and given by

$$F'_z = \frac{\partial F_z}{\partial z} = \int \left(M_x \frac{\partial^2 H_x}{\partial z^2} + M_y \frac{\partial^2 H_y}{\partial z^2} + M_z \frac{\partial^2 H_z}{\partial z^2} \right) dV' \quad (3.6)$$

It occurs that the phase change of the oscillation is the most sensitive to the magnetic interaction. Therefore the phase change of the oscillation is measured. The phase change,

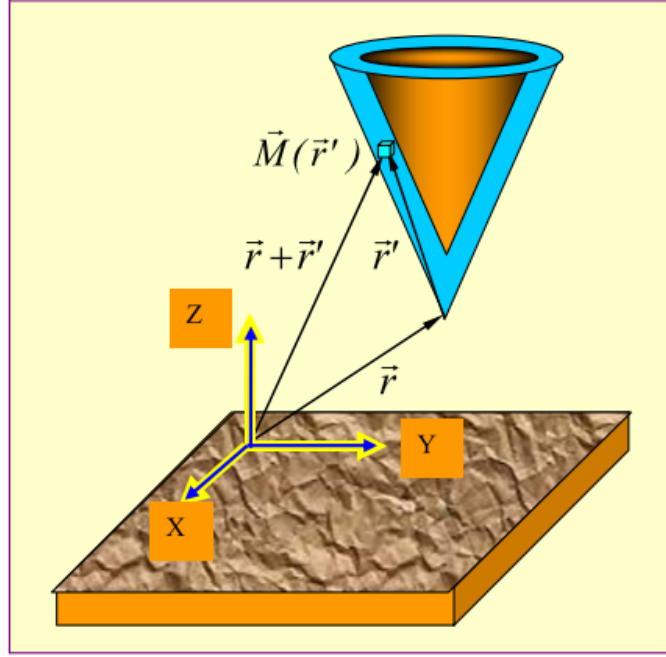


Figure 3.11: Diagram explaining the vectors \vec{r} and \vec{r}' . The force on the probe due to the field \vec{H} is a sum of all the force components between the field \vec{H} and the infinitesimal volume elements of the probe dV' [135]

$\Delta\phi$ for the difference in force gradient between points z and z_0 is

$$\Delta\phi = \phi(F'_z) - \phi(F'_{z_0}) = \phi'(F'_z)|_{F'_{z_0}} \Delta F'_z \quad (3.7)$$

and it can be seen that the change in oscillation phase is linked to the change in force gradient $\Delta F'_z$ and thus the magnetic field from the sample.

Equations 3.3 - 3.7 illustrate the difficulty of quantitative MFM. If one wishes to calculate the field components from a sample M_x, M_y, M_z from the measured phase change one would need to know the exact magnetization components H_x, H_y, H_z of the MFM probe. As all MFM probes are slightly different, this is an extremely difficult task that is the focus of much of the contemporary scanning probe research. Nevertheless, by using MFM as a qualitative imaging technique one can interpret the detailed domain structure of magnetic elements that are in the sub-micrometer range, even so far as to be able to image individual domain walls on the order of tens of nanometres in size.

Chapter 4

Magnetic characterization

The initial aim of the project was to gather a complete understanding of magnetic states in sub-micron nickel disks. This was motivated by previous work in the group [19, 20] related to the search for long range triplet super currents generated in the rotating magnetization of a ferromagnetic vortex within SFS junctions, in which the magnetic disk represented the F component. For this experiment, the mean free path needed to be as long as possible to ensure phase coherence over long distances, $\sim 500 - 1000$ nm. The alloy nature of permalloy, while favourable for the purposes of magnetic engineering, was considered detrimental to the requirement of phase coherence. As such, nickel was chosen as a pure magnetic metal, as in comparison to cobalt and iron it has the weakest exchange field, a property beneficial to the observation of superconducting proximity effects within ferromagnetic materials. In the work of Marsh [19] and Wells [20], they found the reliable formation of vortices in nickel to be challenging. Therefore, the first task in the project was to use the scanning probe facilities at NPL to determine the correct dimensions of disk required to reliably create a magnetic vortex, such that they could be used as part of the hybrid nickel disk - aluminium nanowire experiments that will be presented in chapter 5. While at the time this was considered a simple task, this section will discuss how it was in fact much more complicated, and also introduces an alternative to using the disks in the form of L-shape domain wall traps.

This chapter discusses the experiments performed to characterize the magnetic states in

sub micron nickel disks and L-shape domain wall traps. The evolution of MFM studies of the disks is presented first in section 4.1, discussing the initial use of standard moment probes in section 4.1.1. The need for low moment probes and the remnant states obtained using them are presented in section 4.1.2. Section 4.1.3 presents simulations of the magnetic states and analytical fits to the magnetic state phase boundaries, which are compared with the results of the MFM studies. In this section, the changes made to the simulations to reproduce the states observed by MFM, i.e. the inclusion of an effective out-of-plane anisotropy, is discussed. The magnetization dynamics of the vortex state investigated via *in situ* MFM and electrical measurements, conducted by employing the anisotropic magnetoresistance effect, is presented in section 4.2. After discussing the magnetic states of the nickel disks, section 5.5 introduces L-shape domain wall traps as an alternative magnetic element to the nickel disks. Magnetotransport and *in situ* MFM studies are presented for L-shape domain wall traps made of nickel and permalloy. Together these experiments allowed one to determine the magnetic state of a nickel disk based on the knowledge of its dimensions only, and present the magnetization dynamics of the L-shape devices, providing an understanding of their magnetic structures when including either into SF hybrid structures.

4.1 Remnant MFM measurements of nickel disks

4.1.1 Standard moment probes

Arrays of nickel disks were fabricated using the standard two layer resist and thermal evaporation method described previously. Nickel with a purity of 99.999 % was used. An SEM image of a typical array can be seen in fig 4.1. The distance between disks was kept to at least the radius of the disks to reduce magnetostatic interaction between disks. Arrays were made with a multitude of sizes, with diameters between 200 and 1000 nm and thickness 15 to 55 nm. Multiple samples were imaged with MFM techniques using standard moment commercial Bruker MESP probes with a magnetic coating of CoCr. Samples were imaged using two pass lift mode MFM with a lift height of 35 – 50 nm depending on the

probe and sample used. Samples were imaged as fabricated, i.e. not being exposed to magnetic fields prior to the measurements, thus the magnetic states imaged are remnant states and should be dependent only on the dimensions of the disks.

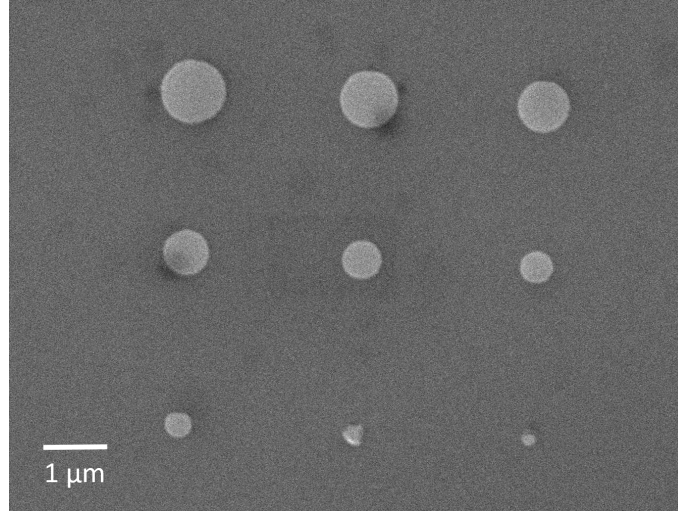


Figure 4.1: SEM image of a disk array showing disks of diameter 1000 (top left) to 300 nm (bottom right) in decreasing steps of 100 nm.

By investigation of the disks across the full range of dimensions using MFM techniques four states were observed. Figure 4.2 shows typical MFM images of each of these observed states. In the smallest disks a single domain state is observed (fig 4.2a). This state is identified by the dark to light contrast in the phase image, indicating that the disk is magnetized from left to right as a single domain. As the diameter and thickness of the disks is increased, two vortex like states are observed. The first of these states clearly exhibits radially distributed domain structure (fig 4.2b). This is evident by the sharp domain wall like features that stretch outward from the disk centre to the edge and is somewhat similar to the magnetization state observed by Pokhil et al. [30] in permalloy disks. The second vortex structure (fig 4.2c) is much more like those observed previously in permalloy disks [45] and similar to the bullseye state observed in nickel cylinders [29]. It exhibits a clear vortex core in the centre seen as a dark spot. However, the vortex core has a diameter of ~ 130 nm, i.e. much larger than the core diameter expected. Typically the core is expected to be on the order of exchange length, which can be calculated as [41] $l_{ex} = \sqrt{A/(\mu_0 M_s^2/2)}$.

Using typical values for nickel ($M_s = 490 \text{ kA m}^{-1}$, $A = 9 \times 10^{-12} \text{ J m}^{-1}$), $l_{ex} \approx 7 \text{ nm}$, much smaller than the observed vortex core. Furthermore, there is a clear domain wall like structure passing vertically through the disk. Such additional domain wall like features were typical of these smooth vortex states that were observed. When the thickness of the disks was increased, an unexpected state was observed, the stripe domain state (fig 4.2d). This state exhibits alternating domains that are directed out of the plane of the film and was only observed previously in nickel disk structures by Skidmore et al. in cylinders 100 nm thick, i.e. at least twice as thick as the disks presented here.

The magnetic states of all the disks imaged are collated in a magnetic state phase diagram based on the the diameter and thickness of the disks, fig. 4.3. The diameter and thickness of each disk was measured using the topography mode of the MFM scan. Diameter was measured parallel and perpendicular to the scan direction, these values were then averaged and the error was estimated as half the difference in the two measurements. This procedure was performed as although the disks are certainly circular, as seen in the SEM image (fig 4.1), drift of the SPM technique can skew the image, making the disk appear elliptical in the AFM typography. Similarly, the thickness was estimated as the average thickness of the disk, where the error was $\pm(T_{max} - T_{min})$, rounded to the nearest nanometre. The magnetic state of each disk is presented by the colour of the symbols: red for single domain states, dark blue for smooth vortex states, light blue for radial domain vortex states, and green for stripe domain states. Dotted lines are shown as guides to the eye separating the magnetic states phases.

At first inspection, the phase diagram is qualitatively similar to that presented by Cowburn et al. in permalloy disks [25], with a cross over from single domain states to vortex states with increasing thickness and diameter. This is to be expected as the dominant energy contribution in the disks shifts from exchange energy to magnetostatic energy as the size of the disks increases. This crossing point is approximately 400 nm in diameter at 10 nm thickness, dropping to 300 nm diameter when the thickness is increased to 40 nm. However, contrary to the observation in Py, at a thickness of 40 – 45 nm the disks are completely dominated by stripe domain states, with no vortex states observed above 45 nm thickness.

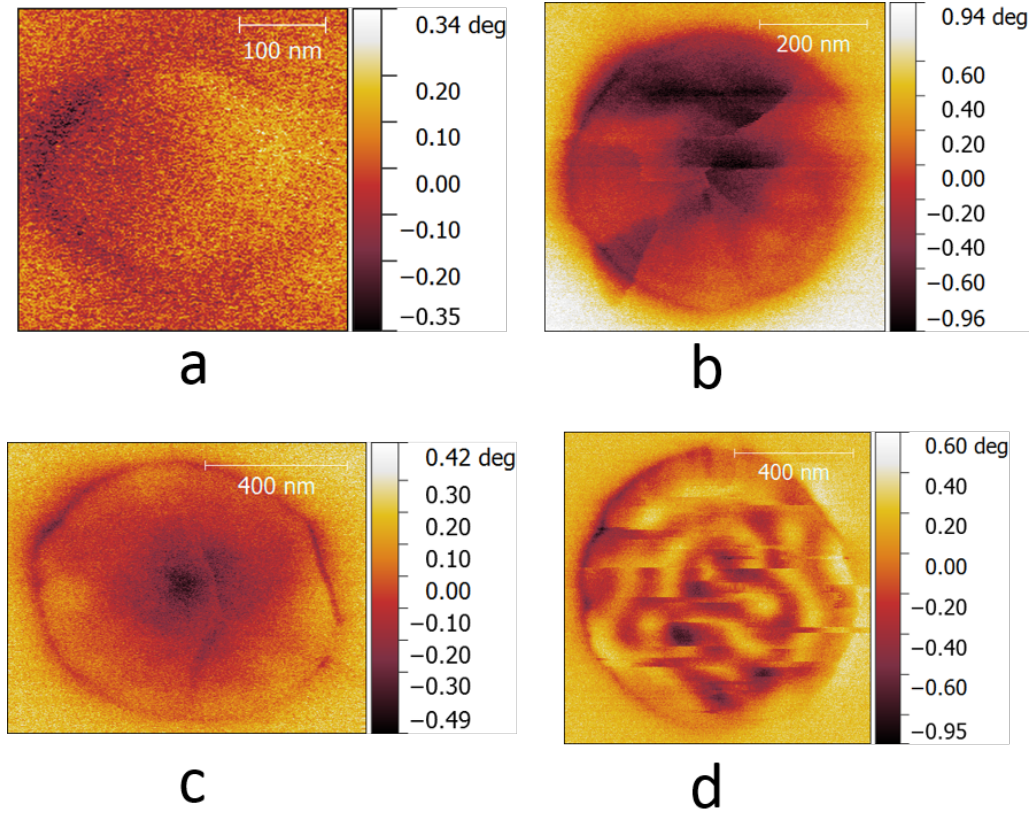


Figure 4.2: MFM images of the 4 magnetic states observed using standard moment MESP probes. a) A single domain state disk ($T = 30$ nm ; $\varnothing = 250$ nm). b) a vortex like state with a radially distributed domain structure ($T = 30$ nm ; $\varnothing = 500$ nm). c) a smoother vortex state than the radial domain state, with a large vortex core in the center (dark spot) as well as some domain walls in the plane of the disk ($T = 35$ nm ; $\varnothing = 800$ nm). d) a stripe domain state, with horizontal lines in the image typical of probe-sample induced magnetization switching ($T = 55$ nm ; $\varnothing = 900$ nm)

This is in contrast with permalloy disks, which exhibit vortex states in disks as thick as 50 nm [45]. Furthermore, there is a distinct mixing of vortex and single domain states in the diameter and thickness range 400 – 600 nm and 10 – 30 nm, respectively. These two features suggest that the dimensional range, in which the vortex state is stable, is relatively narrow, sandwiched between single domain states and stripe domain states. This itself may explain the previous difficulty in reliably fabricating disks in remnant vortex states. While the diagram in shown in fig 4.3 reflects the same general trend of geometrical

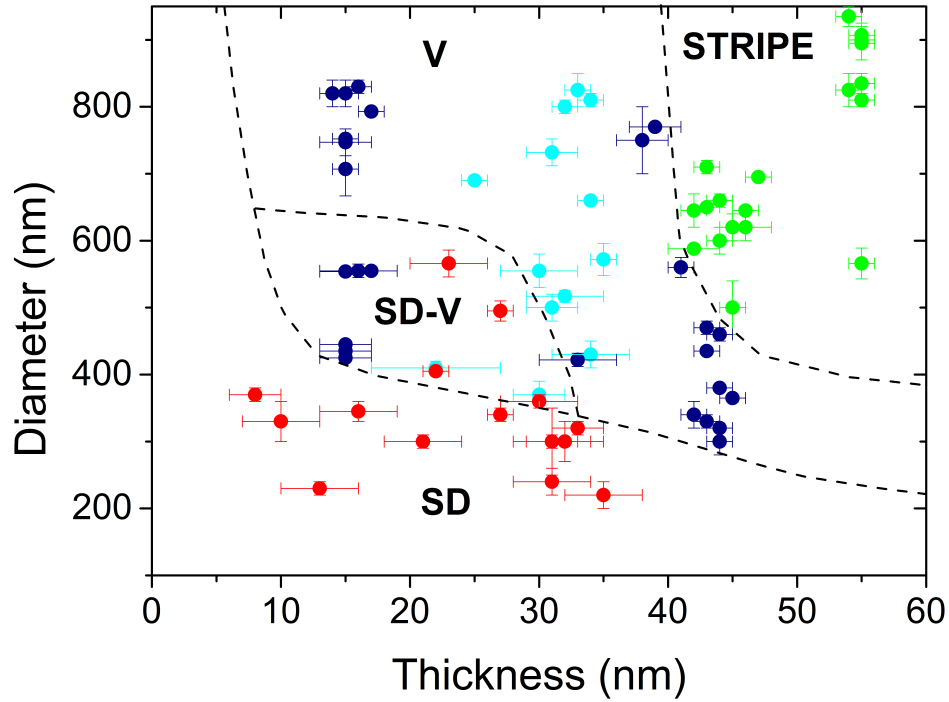


Figure 4.3: The phase diagram of disks imaged using standard moment MESP tips. Colour indicates the state of the disk: red for single domain states, light blue for radial domain vortex states, dark blue for smooth vortex states and green for stripe domain states. The dotted lines are guides to the eye showing the separate magnetic state phases. These phases are labelled: SD- single domain, SD-V- cross over between SD and V, V- vortex, STRIPE- stripe domain states.

dependence of magnetic states as that observed in Py disks, certain features of the MFM images presented in fig. 4.2 indicate that a more detailed analysis is required. Firstly, the radial domain like structure in fig. 4.2b is counter intuitive of domain wall formation, domain walls like the ones seen in this image would surely increase the energy of a disk this size, also there is a general negative phase change across the top part of the disk disk implying an out-of-plane component of magnetization. There is a similar consistent negative phase change in fig. 4.2c. Fig. 4.4 demonstrates this further. In this figure, the line profile is take horizontally (blue line) and vertically (red line) through smooth vortex MFM image. The phase change along these line profiles is then presented in the

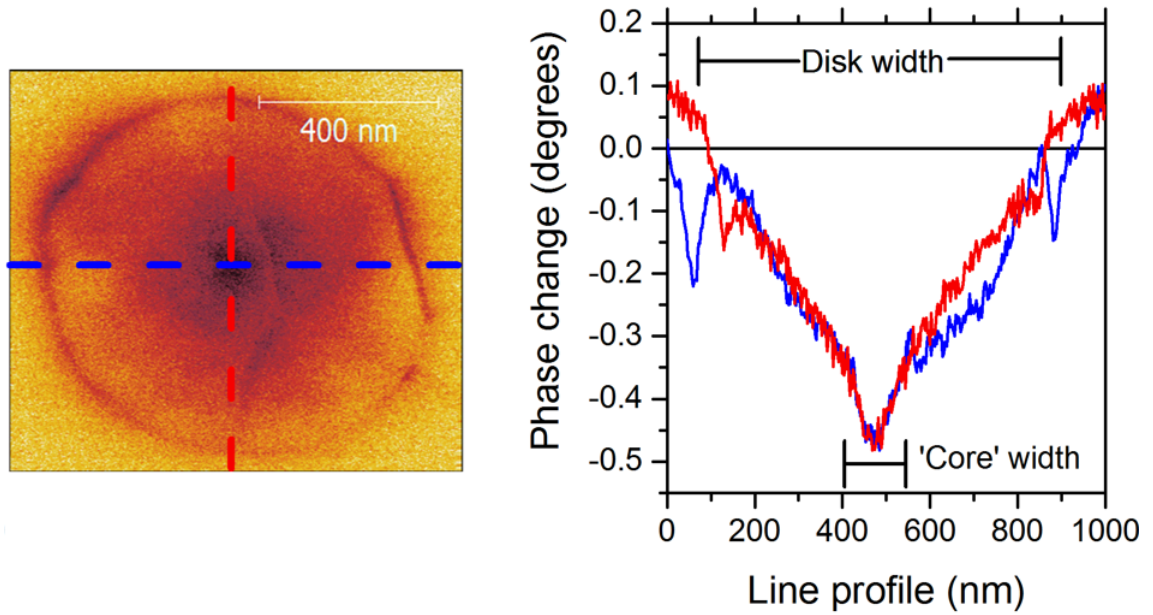


Figure 4.4: vertical and horizontal line profiles of the smooth vortex state measured using a MESP tip. There is a distinct overall negative phase change across the entire disk, reaching a maximum at the centre where the vortex core resides.

adjacent graph. Upon inspection of the phase change, it can be seen that the substrate outside the disk has approximately zero phase change. The disk edge can be seen in the horizontal line profile as two sharp troughs at ~ 50 nm and ~ 900 nm. Within the confines of the disk, between these troughs, the phase change has a linear decrease towards the vortex core, where the phase change is a minimum of $\sim 0.5^\circ$. When considering how the MFM phase change is related to the magnetic force gradient (eqn. 3.7), a negative phase change corresponds to an attractive force. This signifies that in figures 4.2b-c there is a constant attractive force between the probe and disk. This is counter intuitive, as the magnetization in the body of the disk should be in the plane of the film with no out-of-plane field component to interact with the probe except in the vortex core. To add to this, no vortices imaged with standard moment MESP probes were ever observed with cores that induced a positive phase change, i.e. with a magnetization opposite to the probe

magnetization. Statistically there should be an equal distribution of core directions across all the samples measured. Lastly, fig. 4.2d shows a considerable amount of horizontal lines in the image, this is due to either the probe or sample magnetization switching as the probe passes over the sample. This is caused by a strong interaction between sample and probe, so strong that the measurement can no longer be considered non-invasive.

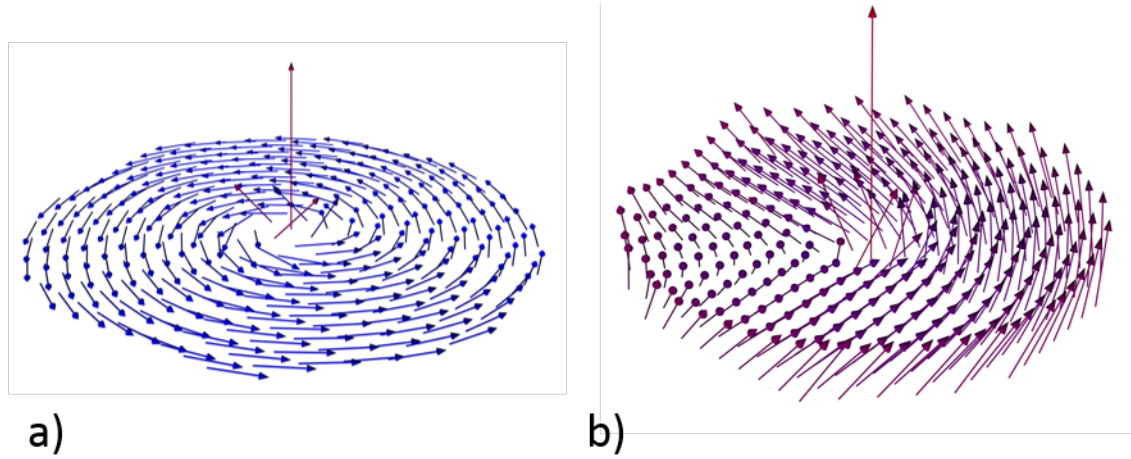


Figure 4.5: An illustration of the effective magnetic state imaged using standard moment MESP probes. The expected vortex configuration should be as seen in image a, in plane throughout the disk with an out of plane core. However, the strong interaction between the probe and the sample magnetization pulls the magnetization out of plane, creating the appearance of a 'canted' vortex structure as illustrated in image b. Colour indicates the out-of-plane component of the magnetization, blue in plane and red out of plane.

When all these features are taken into account, it becomes apparent that the images acquired with standard moment MESP probes suffer from a strong probe sample interaction that is influencing the magnetization of the disks by pulling the magnetization out-of-plane as the probe passes over the sample. This is shown in fig 4.5, where the expected in-plane vortex state is illustrated in fig. 4.5a and the vortex has been canted out of plane by application of a magnetic field in the positive z direction in fig. 4.5b. This canted vortex is the most likely state imaged in fig. 4.2c and is somewhat similar to the structure of a magnetic skyrmion. The radial domain like vortices of the type shown in fig. 4.2b likely exhibit induced domain wall like features as these features were created by the interaction

with the probe. As yet, there is no reliable explanation why some vortices show a smooth response, whereas others show a fractured domain structure. It may be due to the grain size and surface roughness of individual samples.

4.1.2 Low moment probes

To confirm this strong probe-sample interaction caused by the MESP probes, an image of the same disk was acquired using both a standard moment (SM) MESP probe and a low moment probe (LM). Low moment probes are coated with a much thinner layer of magnetic material. This means that they weakly interact with magnetic samples, avoiding the undesirable strong probe-sample interaction, but at the cost of the magnitude of the phase response. Both probes were carefully prepared so that they were magnetised in the same direction and the sample was not exposed to any external fields between measurements. The relevant images can be seen in fig. 4.6. It is immediately clear that the low moment probe (fig. 4.6a) and standard moment probe (fig. 4.6b) show drastically different responses from the disk. While the LM probe shows a much reduced sensitivity in comparison with the SM probe, i.e. approximately ten times less phase change, it also shows an opposite sign of overall phase change to the SM probe (positive, rather than negative) and no fractured domain structures that are seen in the image acquired with the SM probe. While difficult to discern in the MFM image, upon closer analysis of the line profile through the centre of the disk (fig. 4.6c black line) there is a core structure approximately 100 nm in diameter observed with the LM probe, in the same position as the fractured core structure seen in the line profile obtained with the SM probe (fig. 4.6c blue line).

It is obvious from the comparison of these images that using the SM probes does introduce an undesirable strong probe-sample interaction and that standard moment MESP probes were not suitable for the measurement of the nickel disks. Therefore, it was decided that the disks should be remeasured using low moment probes.

For the remeasurements with low moment probes, images were again taken using two pass lift mode MFM, with a lift height of 25 – 50 nm depending on the sample and probe used.

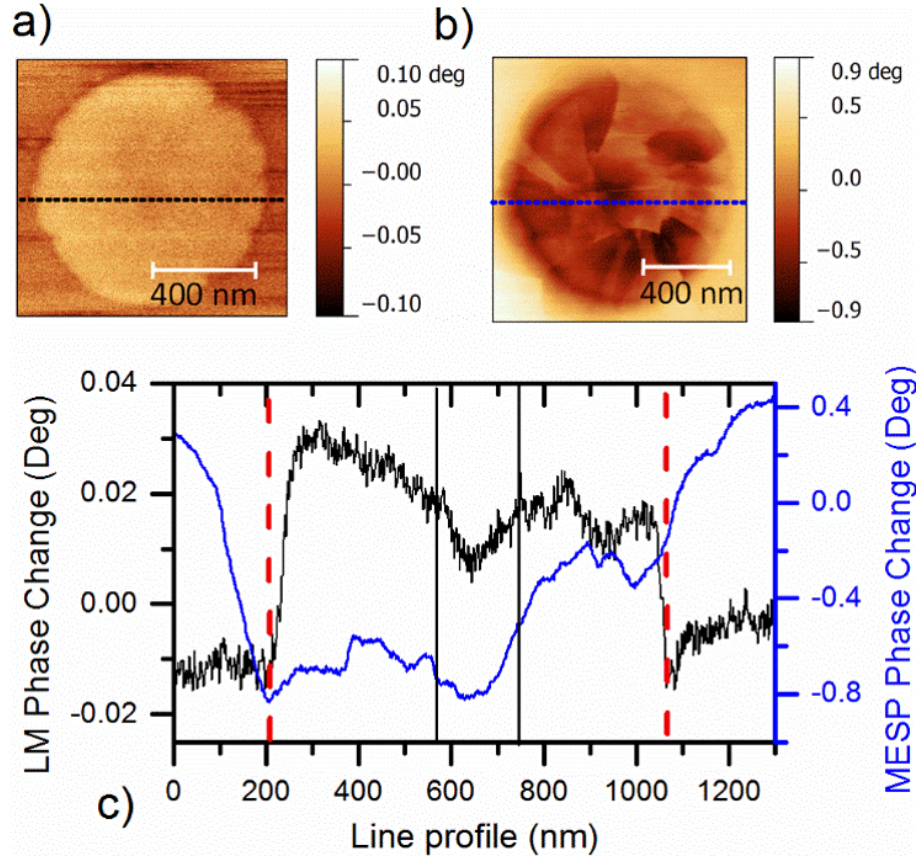


Figure 4.6: The same nickel disk imaged using low (a) and standard moment (b) probes ($T = 25$ nm ; $\varnothing = 800$ nm). There is a clear difference between probes visible in the images alone, with a fractured domain structure seen with the standard moment probe and a smooth vortex response seen with the low moment probe. The central line profiles (c) show that the phase change response from the low moment probe is ~ 10 times less than that of the standard moment probe. The red dotted lines indicate the disk edge and the vertical black lines indicate the core observed using the low moment probe. The line profile also shows that the response with the MESP probe is negative (attractive), whereas with the low moment probe the response is positive (repulsive).

The lift height was required to be smaller than the measurements using SM probes in most cases due to the reduced sensitivity of the LM probes.

An example image of each of the states observed with LM probes can be seen in fig. 4.7a-c. Figure 4.7a shows a small thin disk ($T = 15$ nm ; $\varnothing = 300$ nm) in a single domain state imaged with the LM probe. The features that indicate this disk is in a single domain state are the faint dark contrast in the top left of the disk and faint bright contrast in the

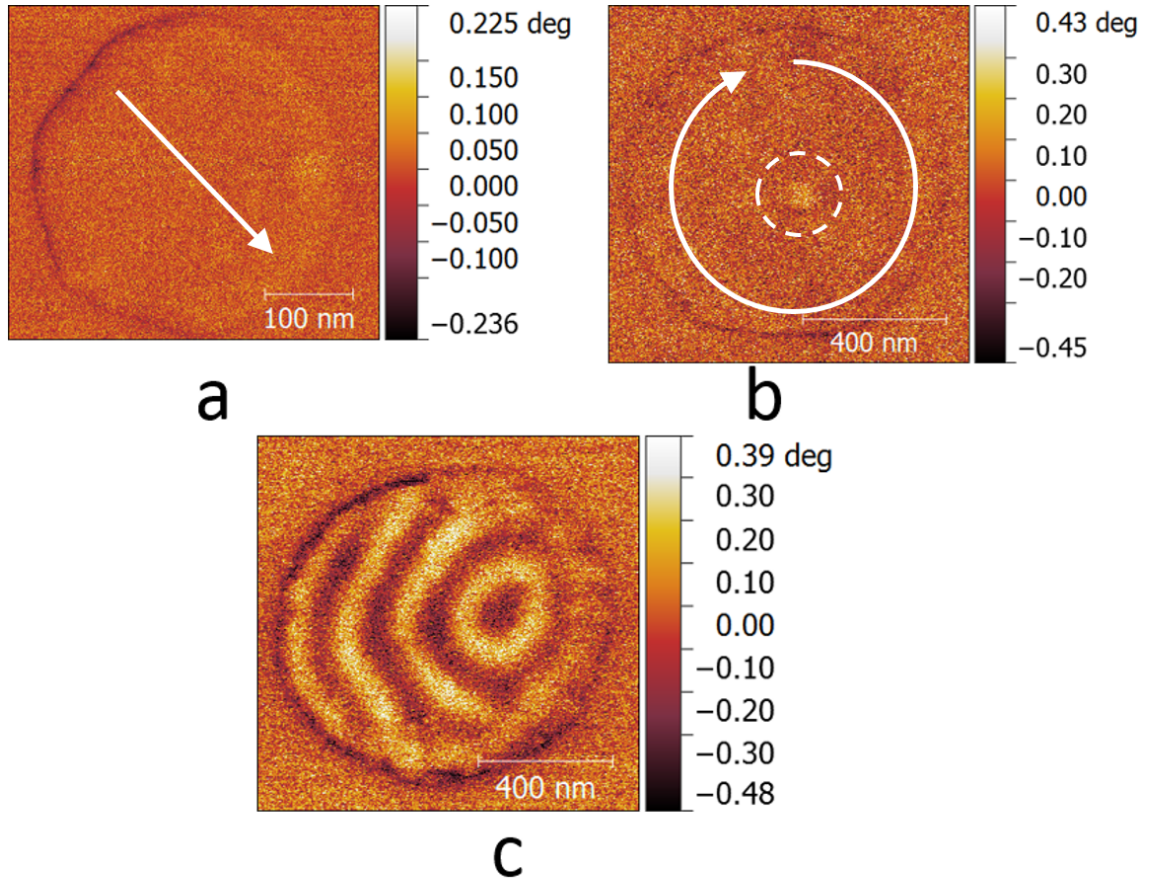


Figure 4.7: Typical images of the magnetic states imaged using low moment probes. a) a single domain state, which in this case is much more difficult to interpret than images obtained with standard moment probes. The magnetization is directed from the top left quadrant of the disk to the bottom right as indicated by the white arrow. This is signified by the faint dark contrast in the top left and brighter contrast in the bottom right ($T = 15 \text{ nm}$; $\varnothing = 300 \text{ nm}$). b) A vortex state disk, indicated by the clear vortex core as a bright spot in the disk centre, highlighted by the white dotted line, and no phase change in the body of the disk, signifying a curling in-plane magnetization as illustrated by the white arrow ($T = 30 \text{ nm}$; $\varnothing = 850 \text{ nm}$). c) ($T = 55 \text{ nm}$; $\varnothing = 850 \text{ nm}$) A stripe domain disk, with a clear dark bright repeating stripe pattern of $\sim 70 \text{ nm}$ period. No horizontal lines due to tip/sample magnetization can be seen, unlike the images acquired with SM probes. Image adapted from [136], a published work by the author.

bottom right of the disk. This infers that the magnetization is directed diagonally across the disk. The single domain state was exceedingly hard to image and interpret using the

LM probes. As expected from the earlier SM probe measurements, when the thickness and diameter of the disks is increased, the vortex state is observed. An example of the vortex state image is seen in Fig. 4.7b ($T = 30 \text{ nm}$; $\varnothing = 850 \text{ nm}$). The vortex state is now very clear in this image in comparison to the SM probe images with a clear core seen as bright spot in the disk centre and a phase change response in the body of the disk comparable with the background phase change signal. In all the images obtained with the LM probes, no fractured radial domain states were observed. This further supports that the radial domain states observed using the SM probes were observed solely due to the strong interaction between the probe and sample. When the thickness of the disks is further increased to $T > 35 - 40 \text{ nm}$, the stripe domain appears as in the case when using SM probes. The stripe domain state imaged with an LM probe is seen in fig. 4.7c ($T = 55 \text{ nm}$; $\varnothing = 850 \text{ nm}$), a clear repeating stripe pattern can be seen with a period of $\sim 70 \text{ nm}$, the same period as that imaged using the SM probes. However, unlike the stripe images obtained with the SM probes, there is no horizontal line scarring due to probe/sample magnetization switching.

The line profile of the vortex state image is shown in fig. 4.8. Here the vortex core is clearly seen as a peak in the phase change with a value of $\sim 0.3^\circ$ degrees. At the same time, the response in the main body of the disk is comparable with the background response. The core size is $\sim 100 \text{ nm}$, i.e. approximately the same size as that measured with SM probes. This suggests that the large core size is a feature of the vortex state in nickel, rather than induced by the probe-sample interaction caused by the SM probes as previously theorised. The magnetic state phase diagram collating the magnetic states of the disks imaged using LM probes is shown in figure 4.9. The dotted lines are guides to the eye separating the magnetic states phases, labelled SD (for single domain), vortex, and stripe. Qualitatively the low moment phase diagram is similar to the standard moment probe diagram, however more ordered. There is a clear crossover between single domain and vortex states, unlike the mixed single domain - vortex phase that was observed using the SM probes. This boundary is at approximately 400 nm diameter for 15 nm thickness extending to 250 nm diameter at 30 nm thickness. The boundary is extrapolated from here to be continuing at

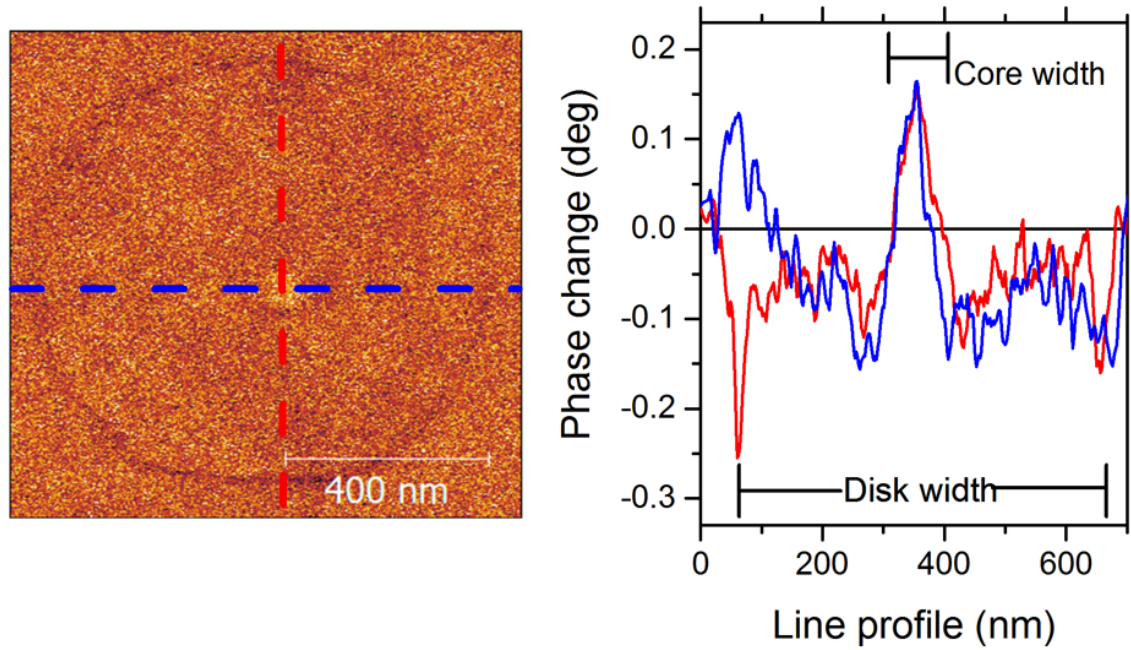


Figure 4.8: Vertical and horizontal line profiles of the vortex state measured using an LM probe. The vortex core is clearly seen as a peak in the phase change response of 0.3° , with a width of ~ 100 nm. Unlike the SM probe image, the phase change in the body of the disk is comparable with the background response.

250 nm diameter for thickness greater than 30 nm. The vortex state phase consists of only smooth vortex states and exists for thickness 15 – 30 nm for diameters 400 nm and greater and for diameters greater than 300 nm in the thickness range 20 – 35 nm, with the thickest disk observed to be in a vortex state seen at 45 nm thickness and 300 nm diameter. The stripe domain state appears to be dominant at thickness greater than 40 nm, however with a minimal diameter of ~ 400 nm. A new feature in comparison with the SM probe phase diagram is the mixing of vortex and stripe domain states in the range 30 – 40 nm thickness and greater than 400 nm diameter. This creates a somewhat wide boundary between the vortex and stripe domain states, suggesting that the magnetic energy of the vortex and stripe domain states in this range have a complex dependence on sample specific properties such as surface roughness and grain structure of the film.

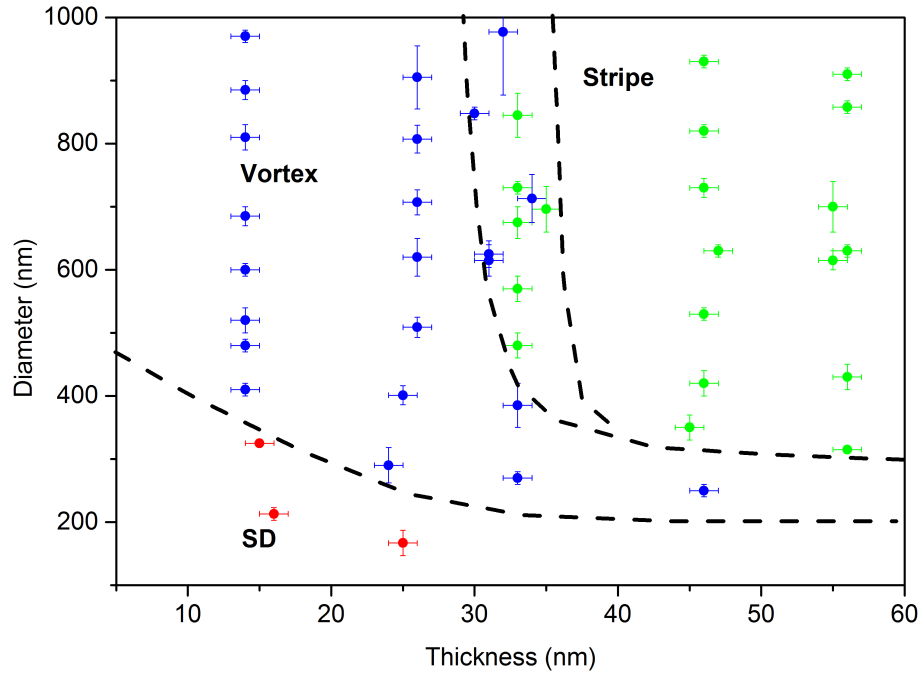


Figure 4.9: The phase diagram of disks imaged using low moment probes. Colour indicates the state of the disk; red for single domain states, blue for vortex states and green for stripe domain states. The dotted lines are guides to the eye showing the separate magnetic state phases. These phases are labelled; SD: single domain, SD-V: single domain vortex cross over, V: vortex, STRIPE: stripe domain states. Image adapted from [136], a published work by the author.

In comparison between the SM probe and LM probe phase diagrams, the LM probe phase diagram is a more accurate representation of the magnetic states in sub micron nickel disks. Therefore, all references to "the experimental phase diagram" from here onwards refers to the low moment probe diagram. This phase diagram serves as a map for fabricating a chosen magnetic structure, specifically vortices, for use in conjunction with aluminium nanowires to create hybrid SF devices with a well defined magnetic structure. However, the existence of the stripe domain state and large size of observed vortex core size are unique in nickel disks. Because of this, it was of interest to investigate the cause of these features. This was done by micromagnetic modelling.

4.1.3 Simulations and Analytical fits

This section will discuss the micromagnetic modelling that was performed concurrently with the MFM investigations as part of the aim to characterise the magnetic states in the disks. The *Object Oriented Micro-Magnetic Framework* (OOMMF) was used to simulate the magnetization in the disks in the range 100 – 1000 nm in diameter and 5 – 55 nm thickness. The OOMMF code was developed by researchers at NIST [36] and is a widely used open source software. The simulation divides a given sample geometry into a regular grid of classical magnetic moments, each moment belonging to a cell in the grid. For accuracy the cell size of the grid should be on the order of the exchange length of the material being modelled. The exchange length being the characteristic length of which the exchange interaction is dominant and all spins can be considered aligned and acting as a single large magnetic moment. As was previously discussed, the exchange length in nickel can be estimated to be, $L_{ex} \sim 7$ nm. Therefore, for simplicity of constructing grids, a 5×5 nm cell size is sufficient to accurately simulate the magnetization in nickel. Once the problem has been reduced from a complex quantum mechanical picture of electron spins to a simple classical array of magnetic moments, the direction of each moment in the grid can be calculated by using the LLG equation, eqn. 2.12, to calculate the torque on each moment due to all the cumulative factors: exchange interaction, magnetostatic energy due to stray fields, anisotropy energy and external fields. The key success achieved by the group at NIST was how to implement these factors, specifically the magnetostatic interaction, in an efficient way.

To simulate the remnant state of a disk of certain dimensions, a relaxation method was used. In this method a random distribution of magnetic moments in the grid was set and then the simulation was run with no external fields applied, allowing the distribution to relax into a final state. Snap shots of the relaxation method for a simulated disk relaxing into the vortex state are shown in fig. 4.10. The solution for a given external field, in the case zero, is considered solved when the value of $\mathbf{M} \times \mathbf{H}_{eff}$ is small, typically $\sim 1 \times 10^{-5} \text{ A}^2 \text{ m}^{-2}$. As the simulation begins with a random distribution, it is prudent to run several simulations for each set of disk dimensions and average the resulting end

states. Simulations can take a considerable amount of time, thus as a mid ground between time efficiency and statistically accuracy, 10 simulations were run for each dimension of disk. The relaxed magnetic state was then assigned a value, 0 for the single domain state, 1 for a vortex state and 2 for a stripe domain state. The results of all 10 simulations were then averaged to give an average remnant magnetic state value. The values were then plotted against the diameter and the thickness of the disks to give a simulated phase diagram.

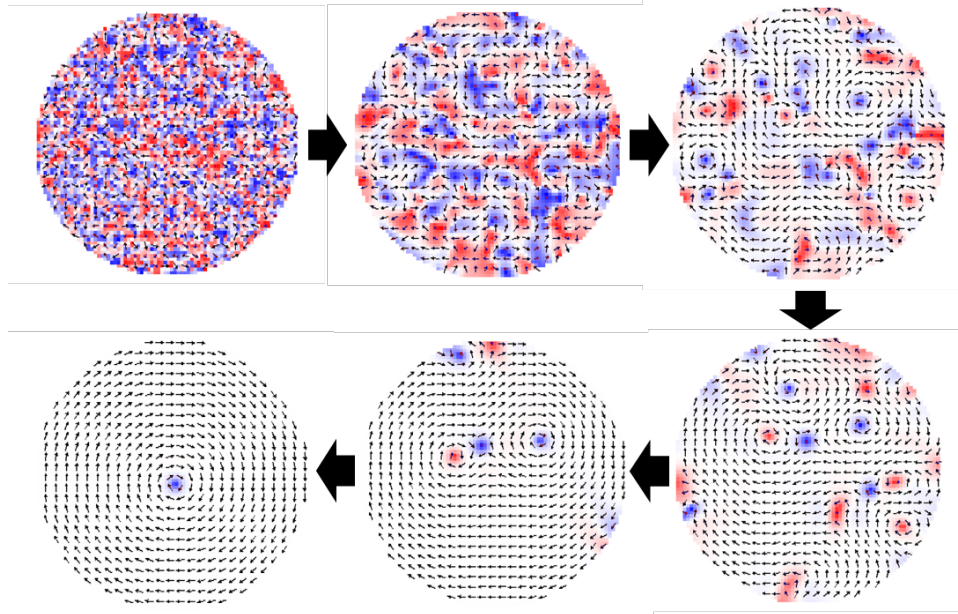


Figure 4.10: A simulated disk ($T = 20 \text{ nm}$; $\varnothing = 400 \text{ nm}$) during the relaxation process from a random distribution (top). Colour represents the out-of-plane component of magnetization, red out of the page and blue into the page.

The aim of simulating the disks was to reproduce the phase diagram obtained via MFM imaging. This would facilitate the understanding of what causes the unexpected observed features in the MFM investigation, specifically the existence of the stripe domain state. The following will discuss the simulations in the order they were performed and the reasoning behind the choice of properties used. The last section will calculate analytical boundaries between the observed magnetic states and compare these with both the experimental and simulated phase diagrams.

Cubic anisotropy

The first simulation of the disks was performed simultaneously with the MFM investigation using standard moment MESP tips and the simulations used the bulk properties for nickel found in the literature [36, 53, 137]: exchange constant $A = 1 \times 10^{-12} \text{ J m}^{-1}$, saturation magnetization $M_s = 490 \text{ kA m}^{-1}$ and cubic magnetocrystalline anisotropy with constant $K_1 = -5.7 \times 10^3 \text{ J m}^{-3}$. As the problem consisted of calculating what was assumed to be in-plane magnetization in thin films, the 2D solver was used. This solver is much faster than a full 3D solution because it treats the system as a 2D grid, taking the thickness into account in the calculation of the self demagnetization field of the element being solved.

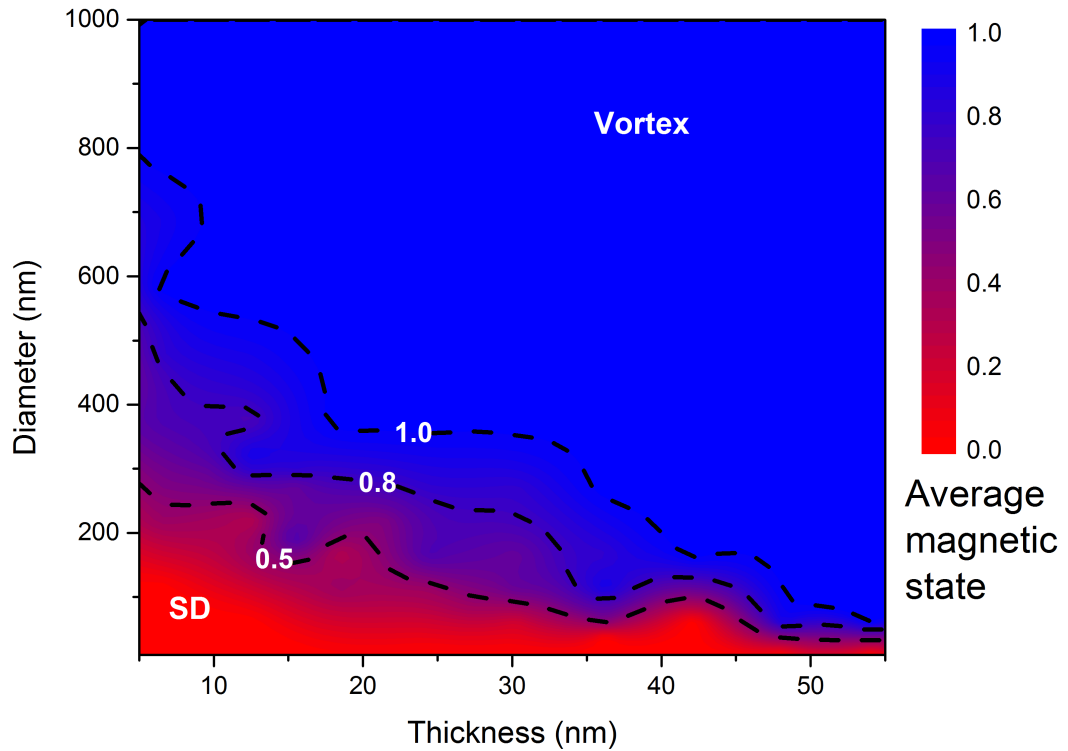


Figure 4.11: The simulated phase diagram using cubic anisotropy constant $K_1 = -5.7 \times 10^3 \text{ J m}^{-3}$ and the 2D solver. Colour represents the average magnetic state value which ranges in this case from 0 (single domain) to 1 (vortex state). The dashed lines are contours of constant average magnetic state value: 0.5, 0.8, and 1.0. Image adapted from [136], a published work by the author.

The simulated phase diagram using these properties is presented in fig. 4.11. The colour scale represents the average magnetic state value ranging from red for 0 (single domain) to blue for 1 (vortex state). The dashed lines show contours of constant value for average magnetic state values of 0.5, 0.8 and 1. The non-monotonic shape of the contour lines is most likely due to the chosen sampling of thickness and diameter as well as the choice of 10 repeated simulations per disk. By increasing the sampling of the dimensions and increasing the number of repetitions this boundary could be made smooth. The simulations show that as the disk diameter and thickness are increased, the probability of the disk forming a vortex state (where in this case $P(\text{vortex}) = \text{average magnetic state value}$ and $P(\text{single domain}) = 1 - P(\text{Vortex})$) smoothly increases. At a thickness of 10 nm and diameter of ~ 800 nm the formation of a remnant vortex state is guaranteed. As the thickness is increased to 20 nm the SD-Vortex boundary drops to 400 nm diameter, reaching as small as 100 nm diameter at 55 nm thickness. Beyond this boundary only the vortex state was observed. Qualitatively this single domain to vortex boundary is in good agreement with the experimental phase diagram, however without the observation of the stripe domain state the parameters used in this simulations cannot be considered to be accurate for nickel disks.

Effective out-of-plane anisotropy

As the nickel disks are thin film structures, it was a sensible assumption to make that the dominant anisotropy would be in-plane due to both the magnetostatic energy cost of directing the magnetization perpendicular to the film and the cubic crystalline anisotropy of nickel. However, the observation of the stripe domain state as the thickness of the disks increases indicates that an out-of-plane anisotropy component must become dominant. Similar simulations by Skidmore et al., which successfully simulated stripe domains in nickel cylinders used an out-of-plane crystalline anisotropy of $K = 6 \times 10^4 \text{ J m}^{-3}$ measured from films grown simultaneously with the arrays of cylinders. In the case of cylinders, the aspect ratio is large as the thickness is on the order of or greater than the diameter of the cylinder. Therefore, one would assume that the easy direction of magnetization in

a cylinder would be perpendicular to the substrate, along the cylinders length. Thus an out-of-plane anisotropy was a valid assumption. In the experiment by Skidmore et al. the stripe domain was similarly observed in the cylinders via MFM techniques. Therefore, simulations using an out-of-plane anisotropy should simulate the stripe domain as observed in the MFM measurements. However, in a physical sense the nickel disk presented here do not possess true out-of-plane anisotropy. Rather, the combination of the cubic anisotropy of nickel and the energetic gain of creating flux closure domains within the thickness of the film, results in an effective out of plane anisotropy. In reality, the axis of anisotropy is likely at some canted angle from both the film plane and normal. However, by using an effective out-of-plane anisotropy, it should be possible to simulate all the experimentally observed magnetic states in the disks.

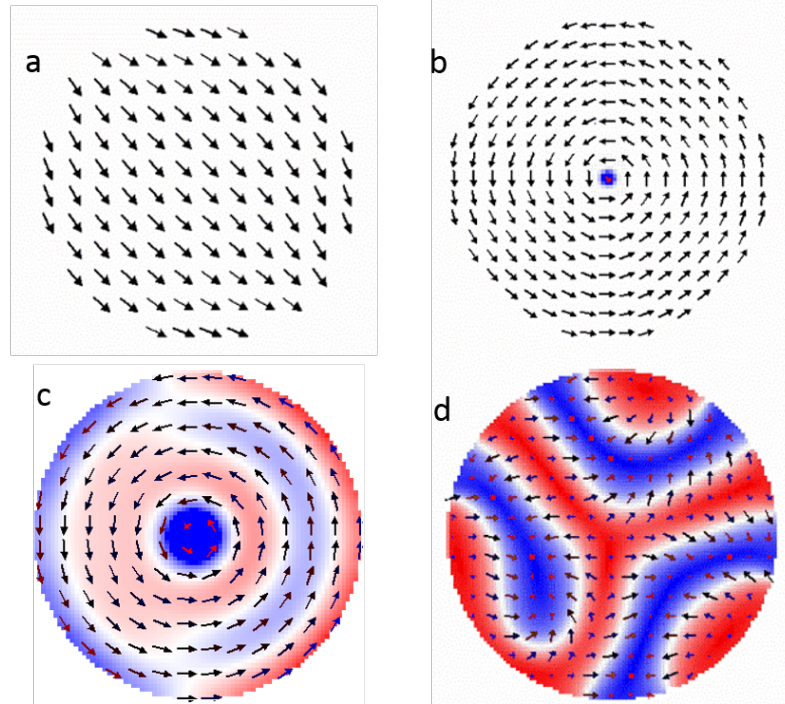


Figure 4.12: The magnetic states simulated using a constant out-of-plane anisotropy. Surprisingly, even with a strong out-of-plane anisotropy all the states are observed, the single domain (a), vortex (b), and stripe domain (d). Also observed is a mix of the vortex state with the the canted magnetization of the stripe domain (c), the colour scale in this simulation has been over saturated to show the weak out-of-plane components. Image adapted from [136], a published work by the author.

The first iteration of simulations using effective out of plane anisotropy followed the work of Skidmore et al. and used their quoted value of $K = 6 \times 10^4 \text{ J m}^{-3}$ as a uniaxial anisotropy directed in the z direction (out-of-plane) with all other parameters the same as in the simulations using cubic anisotropy. Test simulations of large thick disks, with dimensions the same as those in the experimentally observed stripe domain phase, using the 2D solver did not simulate stripe domains. However, simulations using the fully 3D solver available in the OOMMF code, called *oxiis*, did successfully reproduce remnant stripe domains. The requirement for the full 3D solver is due to the importance of the interaction between subsequent layers of magnetic moments. To ensure that the 3D solver alone was not responsible for the observation of the stripe domains, tests were made with the 3D solver of disks in the experimentally observed stripe phase that had the original cubic anisotropy ($K_1 = -5.7 \times 10^3 \text{ J m}^{-3}$). These simulations did not produce stripe domain states either. This indicates that both the full 3D solver and the out-of-plane anisotropy are required to simulate the stripe domain state. The three states observed in the simulations using out-of-plane anisotropy can be seen in fig 4.12. Surprisingly, all three experimentally observed states were simulated with these parameters: the single domain state (fig. 4.12a), vortex state (fig. 4.12b) and stripe domain state (fig. 4.12d). At a thickness of 45 nm a new state was observed that exhibits features of both the vortex and stripe domain states (fig. 4.12c). This state showed a clear vortex structure but with striped out-of-plane components. It was named the mixed state and given a magnetic state value of 1.5 to reflect that its attributes are between that of the vortex and stripe domain states. It is possible that this mixed state is the cause of the mixing of stripe and vortex states in the observed phase diagram at thickness 30 – 40 nm, as some stripe domain disk images did show circular stripe domain patterns as observed in the simulations.

The simulated phase diagram is presented in fig. 4.15. In comparison with the cubic anisotropy phase diagram, the immediate differences are the appearance of the stripe domain state at 45 – 50 nm and the extent of the single domain state at 10 nm thickness reaching to 800 nm diameter. The in-plane single domain state will only exist where the exchange energy is large in comparison to the magnetostatic energy of the single domain,

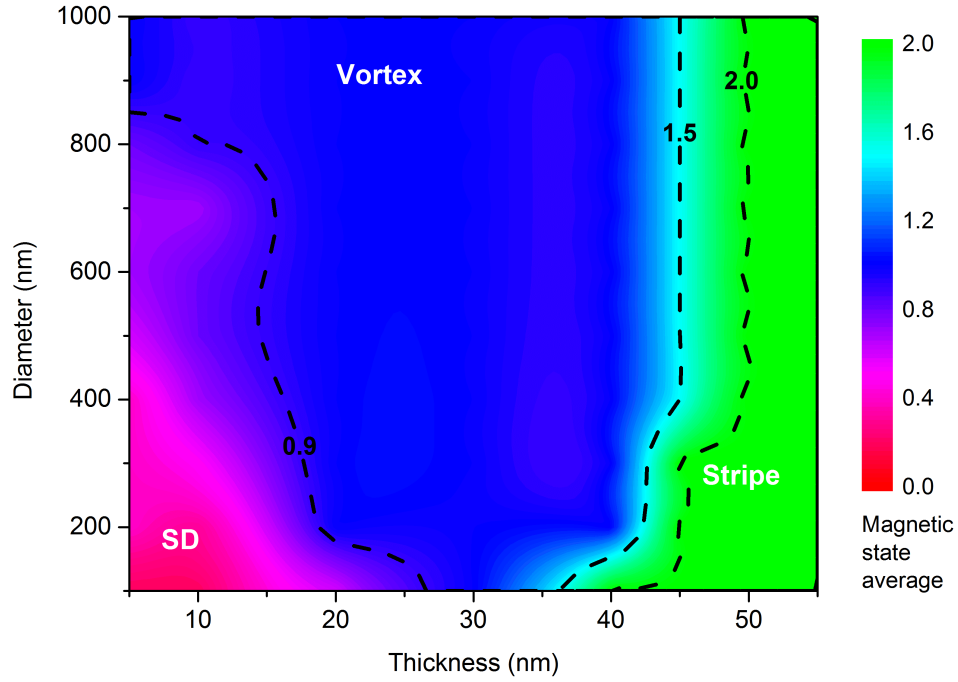


Figure 4.13: The simulated phase diagram using a constant out-of-plane anisotropy and full 3D solver. The single domain appears to exist at a much larger range of diameters in comparison to the cubic anisotropy simulation. Above 400 nm diameter the mixed vortex-stripe domain state appears at a thickness of ~ 45 nm, this state is given a magnetic state value of 1.5. At 50 nm thickness all diameters of disk exhibit the stripe domain state. Image adapted from [136], a published work by the author.

i.e. smaller disks, and where the magnetostatic energy of a single domain directed out-of-plane has a larger energy cost than that of directing the magnetization along the hard anisotropy axis (in-plane with the film). This changed competition of energies, relative to the cubic anisotropy case, changes the single domain phase eliminating it completely at thickness's greater than 25 nm as well as allowing it to exist at larger diameters below 15 nm thick. The transition into the vortex phase is now much more abrupt, likely due to the energetically favourable formation of the vortex core. The vortex phase is now sandwiched between the single domain and stripe domain phases, much like the experimental phase diagram. At a thickness of 40 – 45 nm, the mixed state is observed for all diameters of the disks, signalling the beginning of the transition into the stripe domain state. At 50 nm

thickness the stripe domain state is dominant for all diameters, similar to the experimental phase diagram.

While the inclusion of out-of-plane anisotropy in the simulations did correctly reflect all the experimentally observed magnetic states, the simulated phase diagram still does not accurately reproduce the experimentally observed one. Firstly, the stripe domain was observed at 35–40 nm thickness, rather than the 45–50 nm in the simulated data. Secondly, the simulated single domain to vortex state transition extends to 800 nm diameter at its maximum, whereas the experimental data implies that the maximum diameter for single domain states is approximately 400 nm. These difference are likely due to the choice of the out-of-plane anisotropy constant taken from the literature. To obtain accurate results from the simulations the anisotropy of the films used in the experiment should be measured.

Ideally, one would grow a reference film simultaneously with the patterned film. Hysteresis measurements of the reference film could then be used to calculate an effective out-of-plane anisotropy constant which should be identical for the patterned film. Unfortunately, simulations using effective out-of-plane anisotropy were performed after the experimental MFM investigation. Therefore, no reference films were grown simultaneously with the patterned films. However, it was decided that new films grown using the same source material and under the same conditions would be satisfactory. Three nickel films were deposited on to naturally oxidised SiO_x/Si substrates with area 3 mm^2 of thickness 15, 30, 50 nm. These thickness's were chosen to represent the three thickness regimes that showed each magnetic state, 15 nm for single domain states, 30 nm for vortex states and 50 nm for the stripe domain states. The effective out of plane anisotropy of each film was then determined by measurement of the magnetization curve of each film in both in-plane and out-of-plane orientations using the MPMS magnetometer at $T = 300\text{ K}$. The hysteresis curves for the films can be seen in fig. 4.14. The black lines are the $M(H)$ curves with field applied in-plane with the film and the red lines for the field out-of-plane with the film. The red curves have been corrected for the demagnetization of a thin film ($H = H_{ext} + H_d$ where $H_d = -NM$ and M is the magnetization, for thin films with field

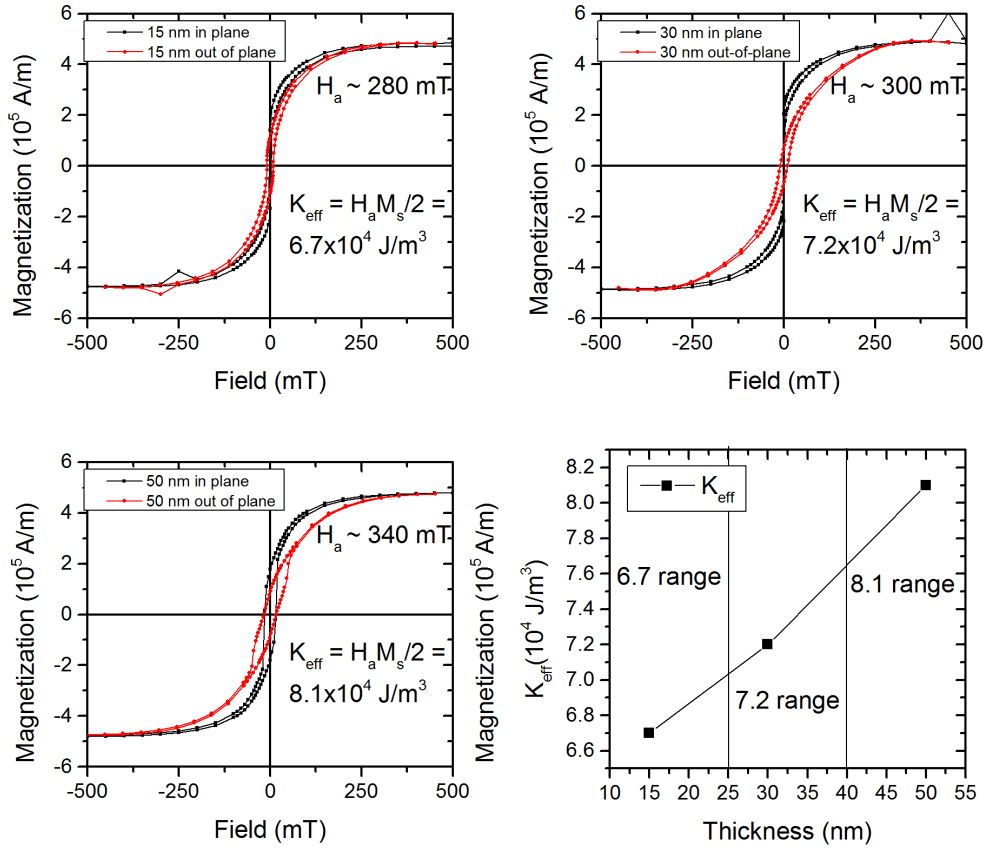


Figure 4.14: Hysteresis curves in-plane (black) and out of plane (red) for the nickel reference films 15, 30, 50 nm thick as well as the extracted anisotropy values for each thickness (bottom right).

applied out of plane $N = 1$). The squareness of the in-plane hysteresis curves indicates that this is an easy axis and the anisotropy is mainly in-plane with the film. Nevertheless, an effective anisotropy value can be calculated by extracting the anisotropy field, H_a , which is the field at which the in-plane and out-of-plane (black and red) curves meet. The effective anisotropy constant can then be calculated as $K_{eff} = H_a M_s / 2$ where M_s is the saturation magnetization. This gives effective anisotropy constants for each film to be $K_{15} = 6.7 \times 10^4 \text{ J m}^{-3}$, $K_{30} = 7.2 \times 10^4 \text{ J m}^{-3}$, $K_{50} = 8.1 \times 10^4 \text{ J m}^{-3}$, respectively. These values are in agreement with those used by Skidmore et al. and indicate that the effective anisotropy in the nickel films increases with thickness. This partially explains the

existence of the stripe domain state, as the anisotropy increases with thickness, at some critical thickness the out of plane component of the effective anisotropy will be larger than the thin film shape anisotropy and the stripe domain state becomes energetically favourable. As previously stated, the squareness of the in-plane hysteresis loops indicates that the true easy axis for the nickel films lies mostly in plane with the film and is most likely directed at a canted angle with the film plane. However, without knowing the exact direction of the anisotropy axis, these values can be used within simulations by directing the anisotropy axis out of plane to induce the observed stripe domain structures, creating an approximation of the true anisotropy axis.

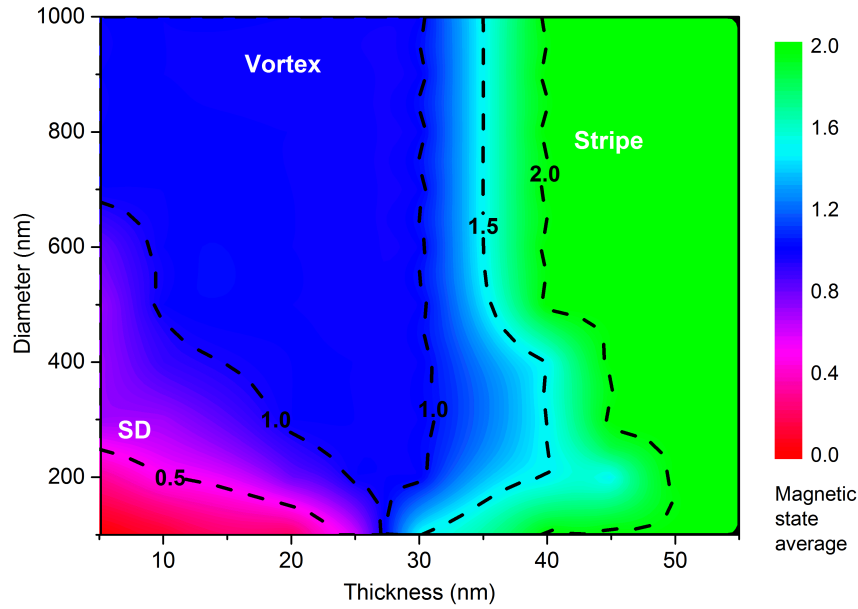


Figure 4.15: The simulated phase diagram using variable out-of-plane anisotropy. This phase diagram most accurately represents the experimentally observed one, exhibiting the same single domain to vortex and vortex to stripe domain state boundaries. The dashed lines are contours of constant average magnetic state value. Image adapted from [136], a published work by the author

The out of plane anisotropy simulations were repeated using the experimentally obtained values of thickness dependent effective anisotropy. Each anisotropy value is assigned to a thickness range: K_{15} is used in the range 10 – 25 nm, K_{30} in the range 25 – 45 nm and K_{50}

in the range 45 – 55 nm. The simulated phase diagram using these parameters can be seen in fig. 4.15. This simulated phase diagram is the closest replication of the experimental phase diagram. The single domain vortex state boundary again disappears at 35 nm thickness, yet only extends to 600 nm diameter at 5 nm thickness and 400 nm at 15 nm thickness, as observed experimentally. The mixed state now appears at 30 – 40 nm with the stripe domain state dominating in disks greater than 40 nm thick, also as observed experimentally. Furthermore, below 400 nm in diameter the mixed state exists up to 45 – 50 nm, this explains the MFM observation of vortex states in this dimension range as they exist as part of the mixed state. This simulation demonstrates that it is necessary to use not only an effective out-of-plane anisotropy to simulate the magnetic states in nickel sub-micron disks but more specifically an anisotropy that is thickness dependent.

Analytical fit

Further analysis of the accuracy of both the experimental and simulated phase diagrams was preformed by comparison to analytical solutions to the phase boundary between states. This can be done by the calculation of the magnetic energy of a given state. For each transition, single domain to vortex and then to stripe, it is expected that within a certain dimensional range the energy of one state will be lower than the others. For example, it is expected that the energy of the single domain state is smaller than that of the vortex state until a critical diameter and thickness, at this point the vortex state energy will be lower and thus the vortex state will be come the more favourable of the two. By deriving the energy of each state dependent on the diameter and thickness, the critical thickness denoting the boundary between states ($T(R)$ where T is the thickness and R is the radius of the disk) will be when the two energies are equal.

For the single domain state to vortex state phase boundary, the method presented by Hoffman et al. [49] has been followed using the appropriate corrections for the nickel FCC lattice and CGS units. First, one considers a single disk that is one atomic monolayer of lattice constant a and radius R . For an FCC lattice, there are $N = 2R/a$ circles of atoms within the radius r_i on which there are $n_i = 2\pi r_i/a$ spins, where i is an integer that counts

the circles outward from the middle such that the radius of a given circle is $r_i = ia/2$. The angle between two spins on the circle r_i is $\phi_i = 2\pi/n_i = a/r_i$. Therefore, the exchange energy between two spins on the circle, w_i , is:

$$w_i = -2JS^2 \cos \phi_i \approx -2JS^2 + JS^2 \phi_i = \text{constant} + JS^2 a^2 / r_i^2 \quad (4.1)$$

where J is the exchange coupling, and S is the spin angular momentum. Thus the change in exchange energy required for the spins to be at angle ϕ_i is:

$$\Delta w(r_i) = JS^2 a^2 / r_i^2 \quad (4.2)$$

which is now considered the exchange energy. Therefore, the total exchange energy for all spins on a circle with radius r_i is;

$$w(r_i) = n_i \Delta w(r_i) = \frac{2\pi r_i}{a} \frac{a^2}{r_i^2} S^2 J = 2\pi \frac{a}{r_i} S^2 J \quad (4.3)$$

For a single monolayer, neglecting the vortex core, the total exchange energy is thus the sum of all circles of radius r_i up to the total number of circles $N = 2R/a$

$$w_{ML} = \sum_{i=1}^N w(r_i) = 2\pi S^2 J \sum_{i=1}^N \frac{a}{r_i} \quad (4.4)$$

$$= 4\pi S^2 J \sum_{i=1}^N \frac{1}{i} \quad (4.5)$$

where the simplification of the sum uses the relation $r_i = ia/2$. This sum is the Digamma function $\Psi(x) = d/dx \ln \Gamma(x)$ plus Eulers constant, $\gamma = 0.5772$. The Digamma function can be approximated as $\ln(x)$ so that;

$$w_{ML} = 2\pi S^2 J \left[\Psi\left(\frac{2R}{a} + 1\right) + \gamma \right] \quad (4.6)$$

$$w_{ML} \approx 2\pi S^2 J \left[\ln\left(\frac{2R}{a} + 1\right) + \gamma \right] \quad (4.7)$$

A single disk of thickness t will contain $N_{ML} = 2T/a$ monolayers, so if one neglects the exchange interaction between monolayers, then the total exchange energy of the vortex state is simply:

$$E_{ex} = \frac{2T}{a} w_{ML} = 2\pi AT \left[\ln\left(\frac{2R}{a} + 1\right) + \gamma \right] \quad (4.8)$$

where $A = 4S^2 J/a$ is the exchange constant. This is the exchange energy of the vortex state and should be equated with the demagnetizing energy of the single domain state to acquire the critical thickness at which their energies are equal. The demagnetizing energy density per unit volume of a single domain particle is

$$\epsilon_d = \frac{1}{2} H_d M_s = \frac{1}{2} N M_s^2 \quad (4.9)$$

where H_d is the demagnetizing field, M_s is the saturation magnetization, and N is the demagnetizing factor that must be calculated for the required geometry. The demagnetizing factor for the disk in the single domain state can be calculated as an oblate spheroid ($R \gg t$, $m = 2R/t \gg 1$) [138, 49]:

$$N = \frac{\pi^2}{m} \left(1 - \frac{4}{\pi m} \right) \approx \frac{\pi^2}{m} \quad (4.10)$$

So that the total demagnetizing energy of a disk of volume $\pi R^2 T$ modelled as a oblate spheroid is

$$E_d = \frac{\pi^3}{4} T^2 M_s^2 R \quad (4.11)$$

In the original treatment by Hoffman, uniaxial anisotropy was included as an additional

constant energy to the vortex state $E_{Ku} = \pi R^2 T K_u / 2$, where K_u is the uniaxial anisotropy constant. In this calculation, a cubic anisotropy energy should be added to the vortex state energy to account for the magnetocrystalline anisotropy of nickel. This is coupled with the assumption that in the single domain state the magnetization will naturally fall along, or close enough to, the direction of minimum anisotropy energy, i.e. an easy axis, that the anisotropy energy contribution in the single domain state is zero or at most negligible. The cubic anisotropy energy for a disk of volume $\pi R^2 T$ in the vortex state was calculated by Jubert et al. [139] for a disk with finite core width β as:

$$E_{K_c} = \frac{K_c}{8} \pi T \left(\frac{R}{2} \right)^2 \left[1 + \frac{6}{\beta^2 R^2} (1 + e^{-\beta^2 R^2}) - \frac{7}{2\beta^2 R^2} (1 - e^{-2\beta^2 R^2}) \right] \quad (4.12)$$

While this equation is complex due to the inclusion of the vortex core, it can be greatly simplified by continuing with original the approximation in the treatment by Hoffman et al. [49] that the vortex core should be neglected. Thus, $\beta \rightarrow 0$ and the cubic anisotropy energy is now:

$$E_{K_c} = \frac{K_c}{8} \pi T \left(\frac{R}{2} \right)^2 \quad (4.13)$$

Therefore, the critical thickness as a function of radius, $T_{crit}(R)$, is when this demagnetization energy equals the vortex exchange energy plus the cubic anisotropy energy, which gives:

$$T_{crit} = \frac{4}{\pi^2 M_s^2 R} \left[2A \left[\ln \left(\frac{2R}{a} + 1 \right) + \gamma \right] + \frac{K_c}{8} \left(\frac{R}{2} \right)^2 \right] \quad (4.14)$$

Conversely, Hoffman et al. [49] also modelled the demagnetization coefficient of the signal domain state as flat circular cylinder based on the work of Joseph [140]. In this model the demagnetization coefficient is:

$$N = \frac{4}{m} \left[\ln(4m) - 0.5 \right] \quad (4.15)$$

So that the total demagnetizing energy of a disk is now:

$$E_d = \pi R^2 T \epsilon_d = \pi R T^2 \left[\ln\left(\frac{8R}{T}\right) - 0.5 \right] M_s^2 \quad (4.16)$$

And the critical thickness, with the inclusion of the cubic anisotropy for nickel in the vortex state, is:

$$\frac{2T_{crit}}{R} \left[\ln\left(\frac{8R}{T_{crit}}\right) - 0.5 \right] = \frac{4A}{M_s^2 R^2} \left[\ln\left(\frac{2R}{a} + 1\right) + \gamma \right] + \frac{K_c}{16M_s^2} \quad (4.17)$$

Eqn. 4.17 is presented in this form as the left hand side now equals the demagnetizing coefficient, N , which can be approximated further by $N = b \ln(1 + c/m^d)$ where b, c and d are numerical fitting parameters. The fitting has been solved by Hoffman et al. [49] leading to a critical thickness:

$$T_{crit} = \frac{R}{3.37} \left\{ \exp \left[\frac{4A}{2.4M_s^2 R^2} \left(\ln\left(\frac{2R}{a} + 1\right) + \gamma \right) + \frac{K_c}{38.4M_s^2} \right] - 1 \right\}^{1.15} \quad (4.18)$$

Furthermore, to calculate the critical thickness of the onset of the stripe domain state, the simpler theory of Kittel can be used to determine the critical thickness at which the stripe domains should appear. In this model the energy density of a thin film of thickness T with uniaxial perpendicular anisotropy K is [141]

$$\frac{E}{V} = 0.136 \mu_0 M_s^2 \frac{d}{T} + \frac{\sigma}{d} \quad (4.19)$$

where d is the stripe domain width and is σ the domain wall surface energy which can be expressed as $\sigma = 4\sqrt{AK}$. By minimising the energy with respect to the stripe domain width d and equating this minimum energy to the anisotropy energy K , the critical thickness for the onset of the stripe domains is

$$T_{stripe} = 8.7 \sqrt{A/K} \frac{K}{\mu_0 M_s^2} \quad (4.20)$$

This allows for a simple approximation of the onset of the stripe phase. A calculation similar to that of the single domain - vortex phase boundary (i.e. Hoffman et al. [49]) would be much more complex, as the exact domain structures of the stripe domain is not

known, i.e., is the magnetization in the stripe domains directed completely perpendicular to the plane of the film or canted at some angle? If canted at an angle, what is the magnitude of the angle? As the out of plane anisotropy used to simulate the stripe domain is on the order of the demagnetization energy density $K_d = \mu_0 M_s^2/2$, the stripe domain is likely to be a complex flux closure domain structure, not simply an alternating directly out of plane magnetization pattern. Such a flux closure domain structure would be very difficult to model, therefore this simple approximation of critical thickness is adequate for this discussion.

The calculated critical boundaries are shown in fig 4.16, superimposed on both the experimental (left) and simulated (right) phase diagrams, the simulations being that which used the changing out of plane anisotropy model. For simplicity, the phase labels have been removed and only the contour line for the single domain to vortex transition is shown in the simulated diagram as a white dashed line. The parameters used for the presented single domain to vortex phase boundaries are, $A = 9 \times 10^{-12} \text{ J m}^{-1}$, $a = 0.3 \text{ nm}$, $K_c = -5.7 \times 10^{-3} \text{ J m}^3$ for both the oblate spheroid and flat cylinder demagnetization models. For the oblate spheroid model (black curve), the bulk value of M_s , as used in simulations (490 kA m^{-1}), shows a good fit to the lower bound of the SD-vortex phase boundary. For the flat cylinder model (red curve), an M_s value of 340 kA m^{-1} is required to produce a best fit to the upper bound of the SD-Vortex phase boundary. If the bulk value of M_s is used in the flat cylinder model, the critical thickness underestimates the experimentally observed SD-vortex boundary significantly. The analytical curves are also in agreement with the simulated phase diagram. Again however, the oblate spheroid model is more accurate to the simulations than the flat cylinder model, as the former is in close agreement with the simulated SD-vortex phase boundary (white dashed line) whereas the latter overestimates the boundary above 20 nm thickness. Therefore, the oblate spheroid model is the more accurate approximation of the SD-vortex phase boundary in nickel disks.

To correctly replicate the observed critical thickness of the onset of the stripe phase using eqn. 4.20, the anisotropy value $K_{30} = 7.2 \times 10^4 \text{ J m}^3$ is used, and the saturation magnetization must be set to $M_s = 420 \text{ kA m}^{-1}$ for a good fit to the experimentally observed

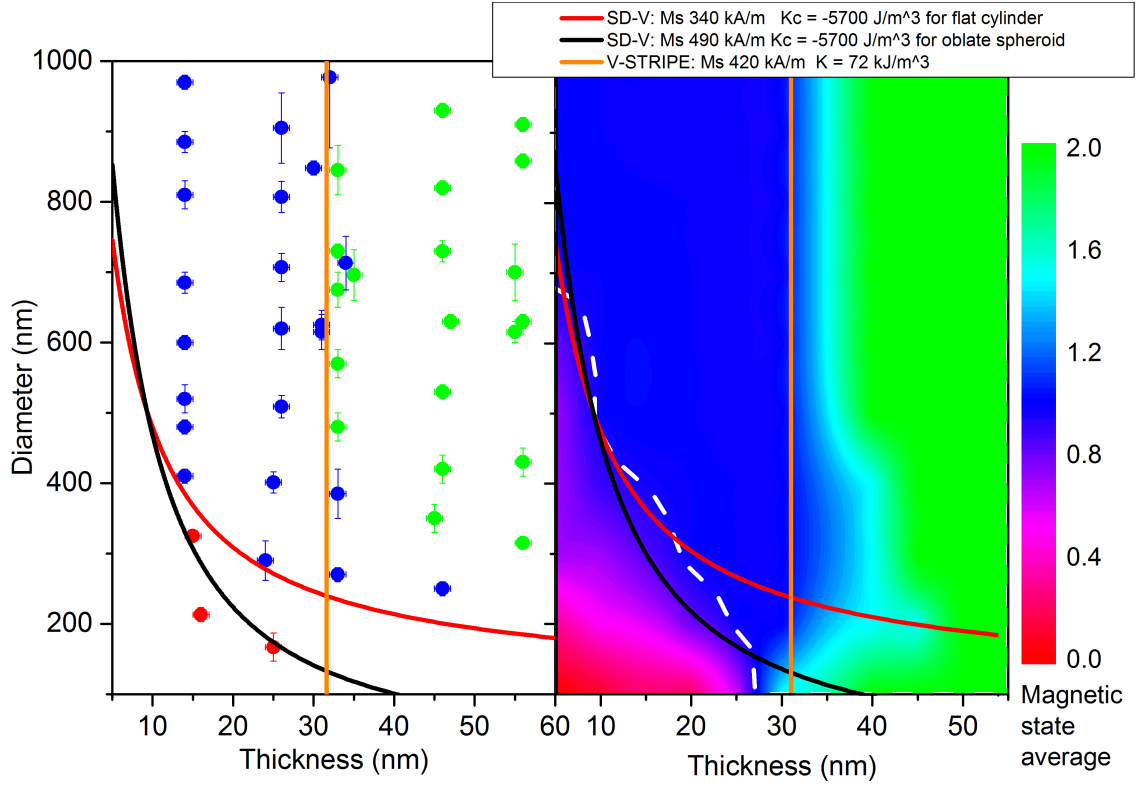


Figure 4.16: The analytical critical phase boundaries superimposed on the experimental (left) and the simulated, changing out of plane anisotropy, (right) phase diagrams, where the dashed white line is the simulated SD-vortex phase boundary. The SD-V curves were calculated using eqns. 4.14 and 4.18 (black and red lines respectively) for parameters $A = 9 \times 10^{-12} \text{ J m}^{-1}$, $a = 0.3 \text{ nm}$, $K_c = -5.7 \times 10^{-3} \text{ J m}^3$. For the oblate spheroid model of demagnetization (black curve) the value of M_s used in simulations, 490 kA m^{-1} , provides an accurate fit to the lower bound of the SD-V phase boundary. For the flat cylinders model (red curve), a best fit value of magnetization, 340 kA m^{-1} , is required to reproduce the upper bound of the SD-V phase boundary. The critical thickness for the stripe domain was calculated using eqn. 4.20 with 420 kA m^{-1} and $K_{eff} = 7.2 \times 10^4 \text{ J m}^3$.

onset of the stripe domain. This is likely due to the simplicity of the fit. However, this calculation accurately represents the observed data for the onset of the stripe domain being predominantly dependent on the thickness only.

These results provide a comprehensive mapping of the possible magnetic states in nickel sub micron disks. The requirement of out-of-plane anisotropy shows that disks made of nickel have a far more complex and rich behaviour than those made of permalloy.

Furthermore, these results allow for a much more accurate way to reliably fabricate vortex states in disk for the use in hybrid SF structures.

4.2 Magnetization reversal of vortices in nickel disks

With the completion of the magnetic state phase diagram and the ideal dimensions for fabricating vortex states being determined, it was of interest to investigate the magnetization dynamics of the vortex state under external field as a precursor to using external field to change the magnetic state of the disks in SF experiments. The simplest method would be to measure the hysteresis curve of a disk with remnant vortex state. Such a measurement should allow for the extraction of the field at which the vortex nucleates, H_{Nuc} , from a saturated single domain state and annihilates, H_{An} , when the disk transitions into the saturated single domain state, as observed by many other experiments [25, 142, 48, 31]. This was attempted using the magnetic properties measurement system (MPMS) at NPL. Large arrays of ~ 80000 disks of thickness 25 nm and diameters 300, 800, 1000 nm were fabricated on SiOx/Si substrates for measurement in the MPMS. Large numbers of disks were required to ensure a detectable magnetic moment. However, this was not successful for two reasons. Firstly, current nanofabrication limitations meant that the disks were not uniform, consequently the nucleation and annihilation fields of each disk were not identical and the resulting curve of averaged switching events showed simply a smooth magnetization reversal. Secondly, the maximum array that could be exposed at once was $300\text{ }\mu\text{m} \times 400\text{ }\mu\text{m}$. This array is not large enough to be detected by the MPMS. Therefore, multiple arrays were deposited. Without any way to deposit alignment markers however, the arrays had to be deposited randomly across the substrate. This meant that the disks were unevenly distributed across the substrate. Due to the assumption in the fitting for the MPMS that the magnetic moment measured is centred along the axis of the sample space, this creates artefacts in the magnetization measurement that resemble magnetization switching events [143]. Thus, other techniques were investigated.

4.2.1 *In situ* MFM

The obvious alternate method for investigation of the vortex under field was *in situ* MFM. MFM Measurements in external field were performed *in situ* using the NT-MDT Aura system available at NPL. This scanning probe microscope allows for the mounting of an in-plane electromagnet with maximum field ± 100 mT. Using this system, the motion of the vortex under in-plane field could be directly imaged.

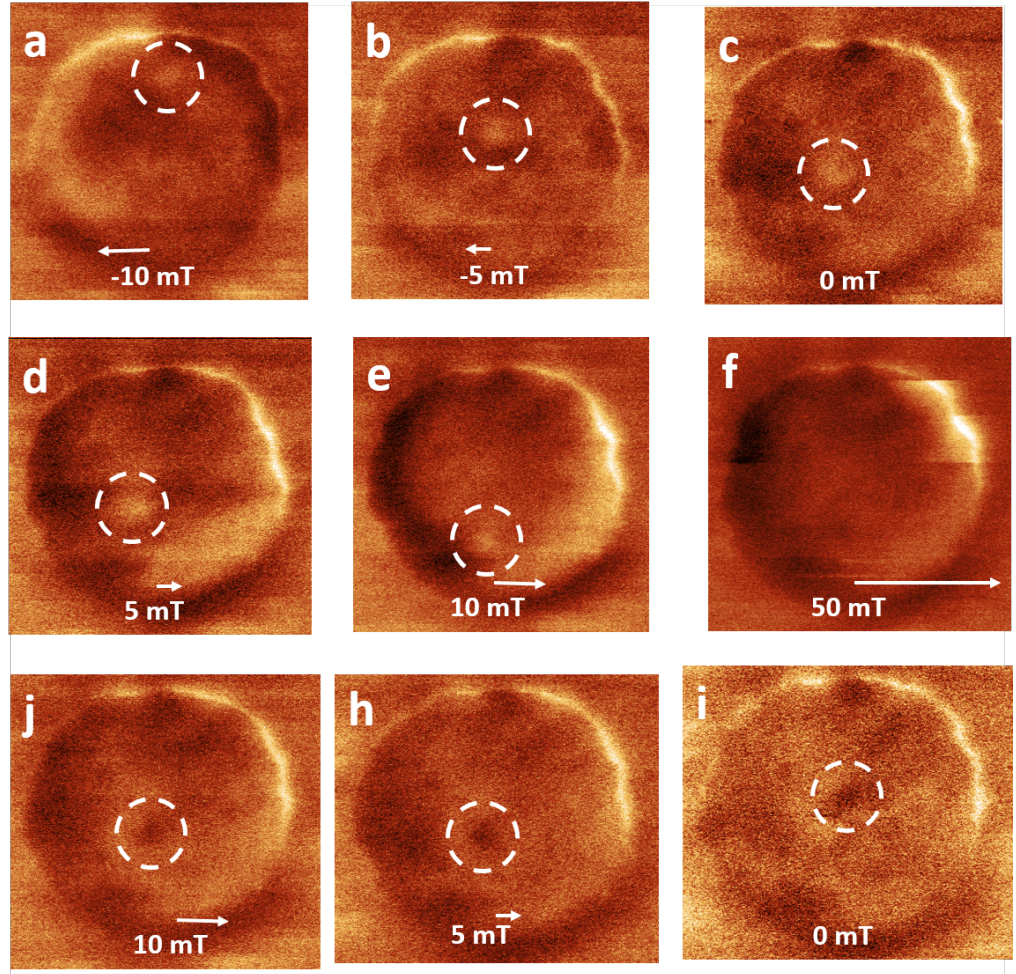


Figure 4.17: *In situ* MFM images of a nickel disk ($T = 25$ nm ; $\varnothing = 800$ nm) at varying applied in-plane magnetic fields. The fields are indicated and were applied in the order a-i. Full description of the images can be found in the text. Image adapted from [136], a published work by the author.

Building off what was learnt during measurements of the magnetic state phase diagram, it was decided that low moment probes were best for the *in situ* MFM measurements. At the time when *in situ* measurements were performed, the improvements in imaging using low moment tips were actually taken further by the use of a multi-layer magnetic probe available through collaboration with Dr. Boris Gribkov. The multilayer probe coating consists of two 15 nm layers of Co/Cr separated by a 10 nm Si spacer layer on one side of the probes pyramid. The interaction between magnetic layers is dominated by magneto-static interaction and two possible states are available with the layers magnetization either parallel (P) or anti-parallel (AP). In the P state, the probe behaves similar to a standard moment MESP probe, however in the AP state the alignment cancels the majority of the magnetization in the layers except for the probe apex where the magnetization behaves like a single dipole. In the AP state, the probe behaves very similar to the low moment probes used for previous measurements, with no influence to the magnetization of the sample, yet with an increased phase change response in comparison to the low moment probes. This made the multi layer probe in its AP state ideal for imaging the vortex *in situ*.

Figure 4.17a-i shows the *in situ* MFM images of a disk with a remnant vortex state ($T = 25 \text{ nm}$; $\varnothing = 800 \text{ nm}$). The field magnitude and direction are shown by the arrows in each image. At -10 mT the vortex core can be seen at the top edge of the disk as a bright spot defined as an upward core. At this field the vortex is on the edge of annihilation, annihilation being the point at which the core is expelled from the edge of the disk. This places the vortex annihilation field at $\sim -10 \text{ mT}$. As the field is lowered to -5 mT and then back to 0 mT , the vortex core moves down into the centre of the disk. This motion indicates that the vortex must have a clockwise chirality as the magnetization bottom half of the disk is aligned with the field direction. This is supported further as the field is increased to 5 mT and then 10 mT , the vortex core moves down towards the bottom edge of the disk and the top of the disk is magnetized along the field direction. When the field is increased to 50 mT the vortex has been annihilated and the disk is saturated shown by the dark to bright contrast from left to right in the disk. When the field is then reduced

to 10 mT the core is visible again, signifying that the vortex has nucleated. Now however, the core is seen as a dark spot meaning that the core direction is now downward upon this nucleation. With no out-of-plane field applied, this suggests that the core direction is random upon nucleation. As the field is lowered to 5 mT, the core hardly moves until the field is reduced to 0 mT and the core returns to the centre, slightly closer to the top of the disk than in the original state.

This data indicates two things; firstly the nucleation and annihilation fields are in the range of 10 mT. Obtaining the exact field value with this method is difficult, as each image takes considerable time, so a limited amount of field steps can be acquired. Secondly, The vortex state is the sole remnant state of the disk under application of in-plane field. This is important for SF experiments where the superconducting properties are to be investigated under the influence of different magnetic states. It would be of great advantage in the experiments if it were possible, via application of in-plane field, to set either a vortex state or single domain/ quasi-single domain state at remnance. Multiple remnance states would mean that the effect of different magnetic states upon a superconductor adjacent to the ferromagnet could be investigated without the addition of any external field that further effect the superconductor, i.e. magnetic state dependant effects could be isolated from applied field effects in SF devices. This measurement suggests that this is not likely in the disks using in-plane field.

It would have been advantageous to repeat the MFM measurements in out-of-plane field, however the out-of-plane fields available for *in situ* MFM were far too small to influence the thin film nickel disks.

4.2.2 Electrical measurement

A higher resolution method for measuring the magnetic state of a single disk would be via electrical measurements of the disks resistance utilizing the anisotropic magnetoresistance (AMR) effect described in section 2.1.3. As the AMR effect causes a decrease in resistance when the magnetization is perpendicular to the direction of current flow, the resistance of the disk under in-plane magnetic field will be heavily dependent on the direction of applied field relative to the current.

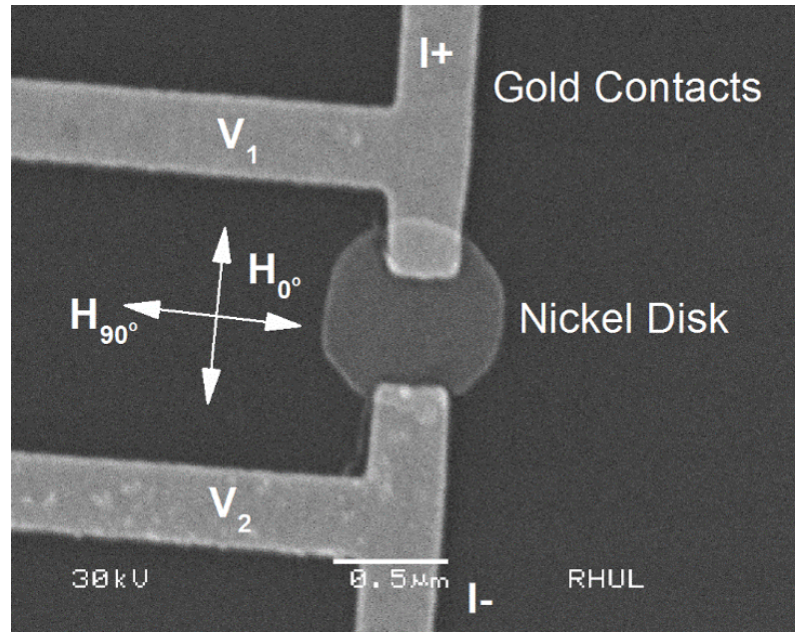


Figure 4.18: SEM image of a nickel disk ($T = 30 \text{ nm}$; $\varnothing = 800 \text{ nm}$) with attached 50 nm thick gold contacts. The measurement scheme and applied field directions have been added as annotations. Image adapted from [144], a published work by the author.

To measure the resistivity of a disk ($T = 30 \text{ nm}$; $\varnothing = 800 \text{ nm}$), 50 nm thick gold contacts were deposited on the disk edges in a 4-point geometry as shown in fig 4.18, in which the electrical contact arrangement is also labelled. The resistance of the disk is shown in fig 4.19 for the both the cases in which the field is aligned parallel (H_{0° , black line) and perpendicular (H_{90° , red line) to the current.

Under simple analysis, the magnetoresistance behaves as expected. In the 0° orientation,

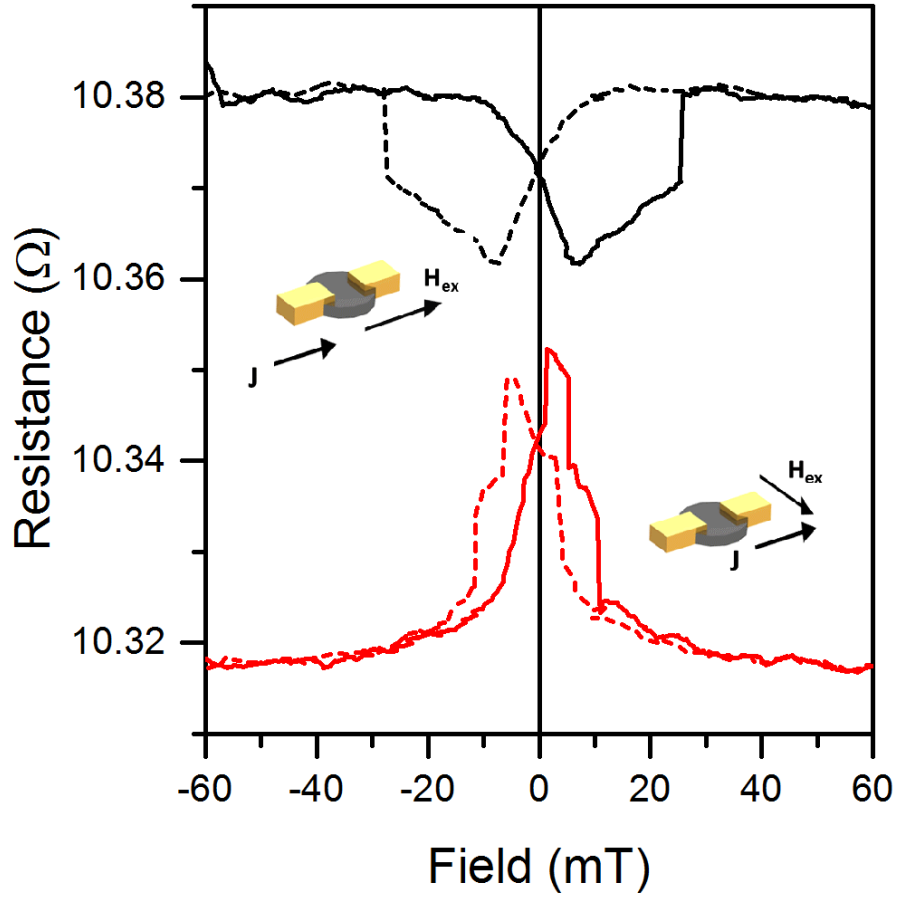


Figure 4.19: The AMR response of a nickel disk ($T = 30 \text{ nm}$; $\varnothing = 800 \text{ nm}$) with the field applied at 0° (black curve) and at 90° (red curve) to the current direction. In the 0° orientation, the vortex is observed to nucleate smoothly and annihilate in a single step transition. In the 90° , the vortex is observed to nucleate in two steps and then with a sharp change. The annihilation is a two step transition with a reduced annihilation field in comparison to the 0° orientation. Image adapted from [144], a published work by the author.

the resistance is at a maximum at saturation when the magnetization and field are completely parallel. As the field is lowered, the resistance gradually drops until a minimum at 7 mT. As the field is increased further, the resistance increases linearly until it suddenly jumps to the value of resistance at saturation at a field of 25 mT. This behaviour is symmetric about the zero field axis. This magnetoresistance behaviour suggests that the vortex nucleation, signified by the drop in resistance due to the increasing angle between

current and magnetization as the vortex forms, is a gradual process beginning at -10 mT with a full vortex formation at 7 mT. The vortex core then moves perpendicular to the current direction as the field increases, until it is annihilated at 25 mT. The annihilation field is in disagreement with the data acquired via MFM which indicated that the nucleation and annihilation fields were in the range of 10 mT and that the vortex nucleation occurred before zero applied field was reached.

When the field is applied in the 90° orientation, the minimum resistance is now at saturation when the magnetization is completely parallel to the current flow. As the field is lowered from -60 mT to zero, the resistance begins to gradually increase at -10 mT with a rapid increase at -7 mT. At 1 mT, there is a sudden jump in resistance that likely signifies the vortex nucleation. Similar to the 0° orientation, the resistance now decreases linearly until a sudden drop in resistance at 5 mT and a second drop at 10 mT, at which point the resistance returns to the non-vortex behaviour. As the disk is symmetrical there should be no preferred field direction for the vortex nucleation and annihilation. However, it appears that the vortex state has a higher annihilation field in the 0° orientation. Furthermore, the annihilation process in the 90° orientation has a characteristic two step behaviour, indicating that annihilation of the vortex occurs via two rapid changes in the sample magnetization.

Because of the symmetric nature of the disk, the asymmetric behaviour of the magnetoresistance must be due to the choice of the contact placement. Machado et al. [145] theoretically discussed the influence of current distribution in anisotropic magnetoresistance of magnetic vortices. In their work they bring attention to the fact that due to the reduction of resistance for magnetization perpendicular to the current direction, the current distribution in the vicinity of the vortex core will be inhomogeneous due to the local magnetization changes across the disk. Effectively this means that the vortex core acts as a path of least resistance (high current density). When the field is applied in the 0° orientation the vortex core moves perpendicular to current flow, as in the simulation by Machado et al., and the expected behaviour is observed. However, in the 90° orientation, the vortex core moves parallel with the current flow. In this direction the core travels be-

neath the electrical contacts. As the boundary conditions of the current flow through the disk must be such that the current flowing from the contacts into the disk is a constant, only the components of magnetization not overlapped by the contacts contribute to the magnetoresistance.

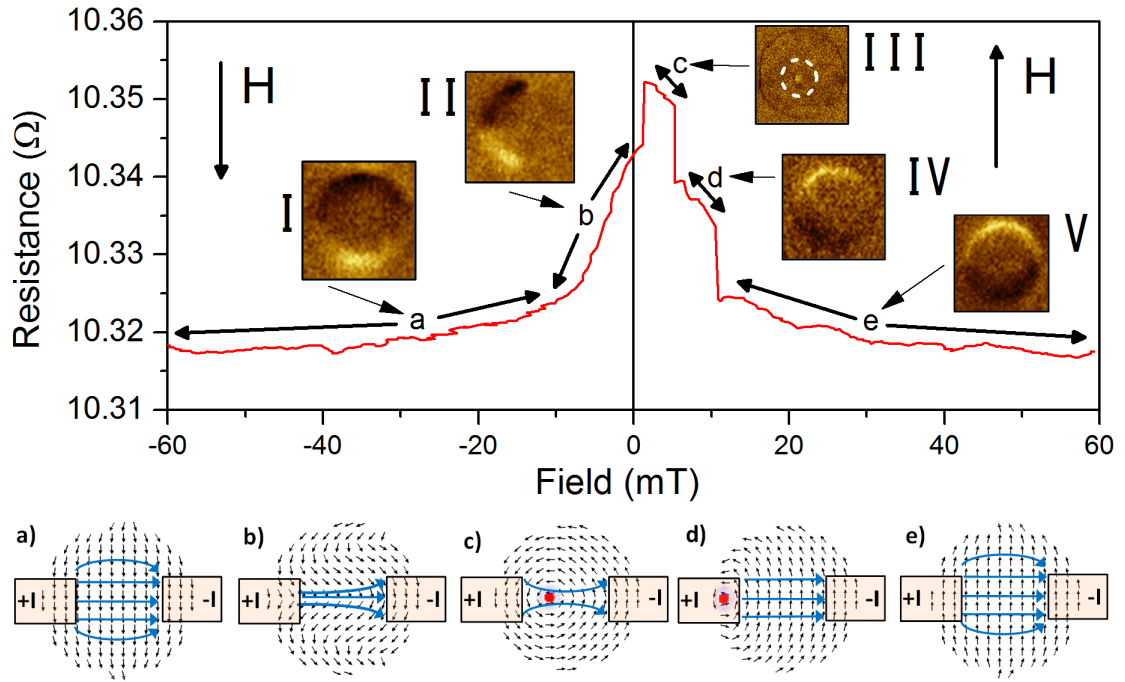


Figure 4.20: The 90° orientation negative to positive field sweep from fig. 4.19 used to explain the origin of the two step annihilation field. The *in situ* MFM images are taken from a disk of the same dimensions as that that was measured electrically and aide in the understanding of the AMR behaviour. The OOMMF simulations illustrate the path of highest current density at each magnetisation state a-e. Full description of the disk behaviour can be found in the text. Image adapted from [144], a published work by the author.

Fig 4.20 demonstrates how this motion explains the features of the magnetoresistance in the 90° orientation. Fig. 4.20 uses *in situ* MFM images of a disk of the same dimensions as the disk measured by AMR and OOMMF simulated vector fields for a disk of the same dimensions in an applied in-plane field to illustrate the process. In the simulated images the vortex core is represented by the red dot and the blue arrows are sketches of the likely current distribution taking into account the local magnetization. At -60 mT the magne-

tization is saturated along the field direction (Fig. 4.20I) and the current distribution is constant throughout the disk (Fig. 4.20a). As the field is lowered a c-like state forms in the disk (Fig. 4.20II) and the current distribution begins to be restricted (Fig. 4.20b). When the field reaches 1 mT the vortex spontaneously nucleates in the body of the disk rather than the edge (Fig. 4.20III & c) and the current distribution is restricted mostly to the core, maximising the resistance. The core then moves towards one of the contacts (depending on the vortex chirality) until it moves beneath the contact. At this point the core no longer contributes to the current distribution in the disk and the resistance drops (Fig. 4.20d) but the disk is still in a c-state as the vortex has not been annihilated (Fig. 4.20IV). Once the vortex is annihilated at 10 mT the current distribution and magnetization return to the saturation state (Fig. 4.20V & e) and the resistance drops again. This is similar to the effect observed by Goto et al. [146] in which the authors used asymmetric contacts on a permalloy disk. The asymmetry of the contacts meant that the electrical properties of the disk were dependent on the disk chirality; one chirality would move the vortex core under the contacts at lower fields than the other, changing the disk resistance. This is further supported by obtaining the angular-dependent magnetoresistance in the range $0 - 180^\circ$. This is shown as a pair of colour maps in fig 4.21. In this figure, the negative to positive field sweep is shown on the left and the opposite direction of the field sweep is shown on the right. This data was acquired by starting in the 0° orientation, sweeping the field from -60 mT to 60 mT and then back to -60 mT. The angle was then increased by 0.9° using a step motor and the field sweep repeated. This procedure was repeated to measure the magnetoresistance for all angles up to 180° .

The angular dependence of the magnetoresistance has many features which are not directly relevant to the vortex dynamics. However, it can be seen that at $\sim 40^\circ$ the annihilation field suddenly decreases. This behaviour continues until $\sim 145^\circ$ when the annihilation field suddenly increases back to its original value. The angle of switching, $\sim 40^\circ$ coincides with the angle at which the motion of the vortex core would begin to move beneath the contacts. Similarly, at $\sim 145^\circ$ the vortex core would no longer be moving beneath the contacts. This strongly supports the hypothesis that the direction of the core motion

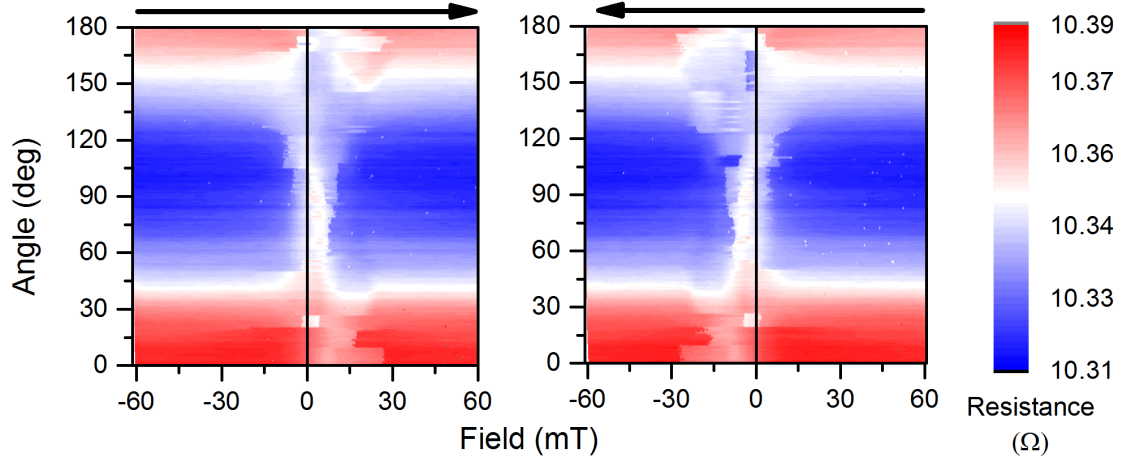


Figure 4.21: The full angular field dependence of the AMR of the nickel disk for field sweeping negative to positive (left) and positive to negative (right). Colour represents the resistance. It can be seen that as the angle between the applied field and current direction reaches approximately 40° , the annihilation field drops. When the angle then reaches 145° the annihilation field suddenly increases again. These angles align with the angles at which the vortex core begins to move beneath the contacts. Image adapted from [144], a published work by the author.

relative to the contacts explains the asymmetry in the magnetoresistance.

Using the AMR effect to electrically measure the motion of the vortex in the disk has shown to have much greater resolution compared to the *in situ* MFM. However, both techniques present with conflicting results. While the *in situ* MFM suggests that under applied in-plane field the vortex nucleates before the field direction is changed, the AMR data indicates that the field direction must be changed to nucleate the vortex. This discrepancy may mean that it may be difficult to reliably switch the disks between vortex and collinear magnetic states when they are included in SF hybrid structures.

4.3 L-shape domain wall traps

While the experiments to characterise the magnetic states and vortex state dynamics in the sub micron nickel disks were successful, it was decided that an alternative source of controllable magnetization should be investigated. This was due to both the discrepancy in the dynamics of the vortex measured by *in situ* MFM and magnetoresistance methods, and the evidence that the vortex state is the sole available remnant state in the disks, i.e. it was not possible to switch between vortex and single domain like states at remnance by application of in-plane field. The ideal candidate for this alternative method was that of the L-shape domain wall trap. The L-shape domain wall trap consists of two thin ferromagnetic nanowires that meet at a 90° angle, as demonstrated in figs.4.22 and 4.23. It has been shown [27, 32, 33] that, due to the shape anisotropy of the thin wires, a domain wall can be trapped at the corner by the application of in-plane magnetic field.

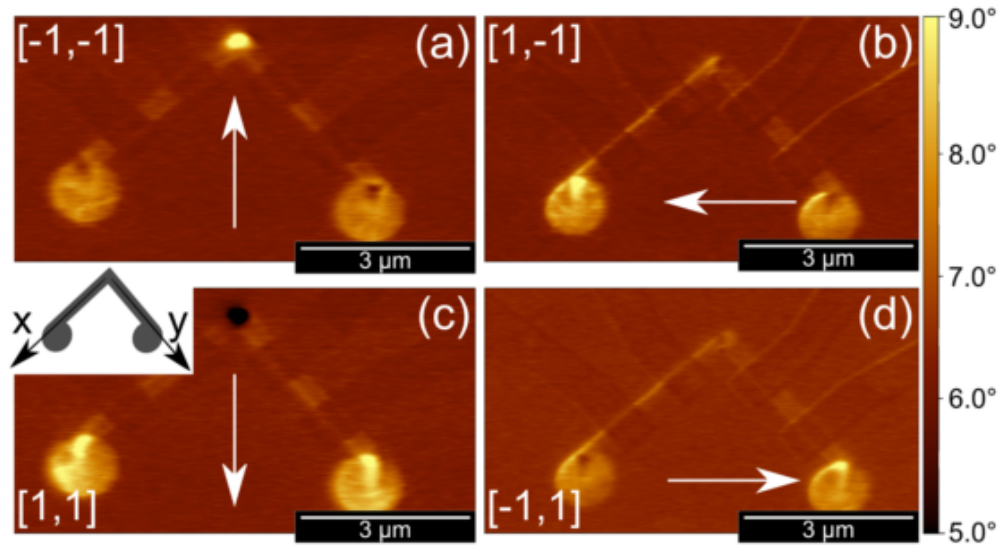


Figure 4.22: MFM images presented by Corte-Leon et al. for a permalloy domain wall trap. In (a) and (c) the field has been applied such that a domain wall is trapped at the corner of the L-shape seen as the bright or dark spot. In (b) and (d) the domain wall has been annihilated by application of the field in the perpendicular direction to (a) and (c). Image adapted from [33]

This is demonstrated in fig. 4.22, which is adapted from the work of Corte-Leon et al. [33]

and shows the MFM phase change response of a permalloy L-shape after an in-plane field of 15 mT has been applied in different directions. When the field is applied in-plane 45° to the arm, as indicated by the white arrows (fig. 4.22a, c), a domain wall can be trapped at the corner, as seen in the MFM images as a bright or dark spot. Equally a state can be achieved where there is no domain wall in the corner (fig. 4.22b, d). Additionally, the nucleation of the domain wall can be easily discerned by electrical measurements of the anisotropic magnetoresistance of the L-shape, i.e. the nucleation of a domain wall manifests in a sudden drop in the magnetoresistance.

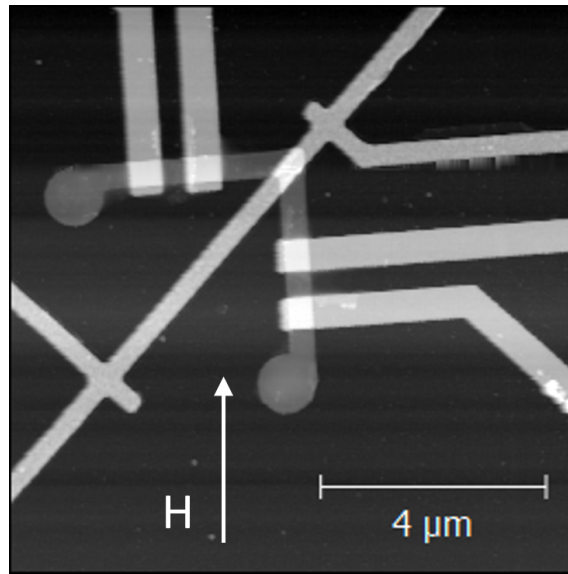


Figure 4.23: Grey scale AFM image of the nickel L-shape hybrid device. The aluminium nanowire lies diagonally across the corner of the L-shape, whilst the gold contacts on the L-shape arms allow for a 4-point resistance measurement of the L-shape magnetoresistance. The contacts used for the amr measurement are annotated. The nucleation of a domain wall should appear as a rapid drop in this magnetoresistance. The sample is mounted in the cryostat with the substrate in-plane with the field, such that the magnetic field is applied perpendicular with one arm as indicated by the white arrow.

The advantage of the L-shape geometry is that it provides a controllable way, by use of in-plane field, to switch between a collinear or domain-wall states at the corner of the device. Furthermore, both the domain wall and collinear states are stable at remnance. Thus, by placing a superconducting element on top of the corner of the L-shape, as demonstrated

in fig. 4.23, the influence of the different magnetization states on the superconductor can be investigated at remnance, without the additional influence of external fields acting upon the superconductor. Furthermore, the magnetic state of the L-shape could be easily measured via AMR with the simple addition of four gold contacts to the arms. This allows a method to know the magnetic state of L-shape used in any SF structure directly, making direct comparison of superconducting and magnetic properties simple. While the same could be performed with the nickel disks, the inclusion of both superconducting elements and additional electrodes on the small area of the disks provides a much greater nanofabrication challenge. The disadvantage of the L-shape geometry is that, for the device to work as intended, the wires that form the corner must be narrow enough to ensure a strong shape anisotropy along the length of the wire. This limits the area of ferromagnetic material available to make an interface with a superconducting film in later SF hybrid devices. The second disadvantage is that the magnetization at the corner will most likely be a complex domain wall structure, rather than the well known vortex structure present in the sub micron disks. This section will discuss the magnetization dynamics of L-shape domain wall traps fabricated using nickel and permalloy. Magnetoresistance and *in situ* MFM data is presented for both L-shape devices. This data is used to describe the nucleation and pinning of a domain wall at the corner of the devices for later use in SF experiments.

4.3.1 Nickel L-shape device

The first L-shape device was made using nickel to replicate the material parameters of the disks, facilitating simpler comparison between later SF structures utilizing the disk geometry. Fig. 4.23 shows an AFM image of the nickel L-shape device, with four gold contacts on the arms for magnetotransport measurements. This device was also used for later SF experiments, thus there is the addition of an aluminium wire overlying the corner of the L-shape. The purpose and geometrical parameters of this wire will be discussed in chapter 5. The L-shape was designed with thickness 25 nm to ensure an in-plane magnetization structure, with arm length 4 μm and width 400 nm. The width of the

arms was a trade off between the requirement of a thinner arms to ensure the desired shape anisotropy for domain wall trapping and area enough to produce an appreciable interface area of aluminium and nickel for SF experiments. The choice of 400 nm wide arms makes the length of interface area between nickel and the aluminium placed diagonally across the L-shape corner ~ 700 nm, close to the dimensions of the nickel disk. The gold contacts used to measure the magnetoresistance of the L-shape were 80 nm thick. The device was fabricated in a three step lithography process, depositing the nickel L-shape first, followed by a second lithography procedure in which an argon etch was performed *in situ* before the deposition of the 80 nm thick aluminium nanowire. A third lithography step was performed to deposit the gold electrodes, in which the argon etch was performed again to ensure good electrical contact between the gold and nickel.

The magnetoresistance of the L-shape measured at room temperature is shown in fig. 4.24, where the resistance has been measured using standard four probe techniques, using the gold contacts. The black curve shows the resistance when the field is swept from negative to positive values, while the red curve shows the opposite sweep direction. The magnetoresistance shows a hysteric behaviour, with a smooth decrease in resistance at ± 12 mT and a minimum in resistance at a field of ± 4 mT followed by a smooth increase beginning at 0 mT and ending at ± 10 mT. The trapping of a domain wall at the corner of the L-shape should manifest in the magnetoresistance as a sharp jump in resistance. This is because, the domain wall should be caused by the rapid change of magnetization direction along the arm parallel to the applied field. The smooth change in magnetoresistance observed instead suggests that the magnetization smoothly rotates with the applied field. Therefore, to investigate the exact behaviour of the magnetization dynamics in the nickel L-shape, an L-shape device was imaged using *in situ* MFM techniques. A test device was required for imaging because the low moment probes required to image the nickel films, as discussed previously, did not produce a large enough contrast to image the magnetic structure of the L-shape that was covered by the Al and Au wires. However, the imaged structure was fabricated on the same substrate and from the same film as the structure measured via transport.

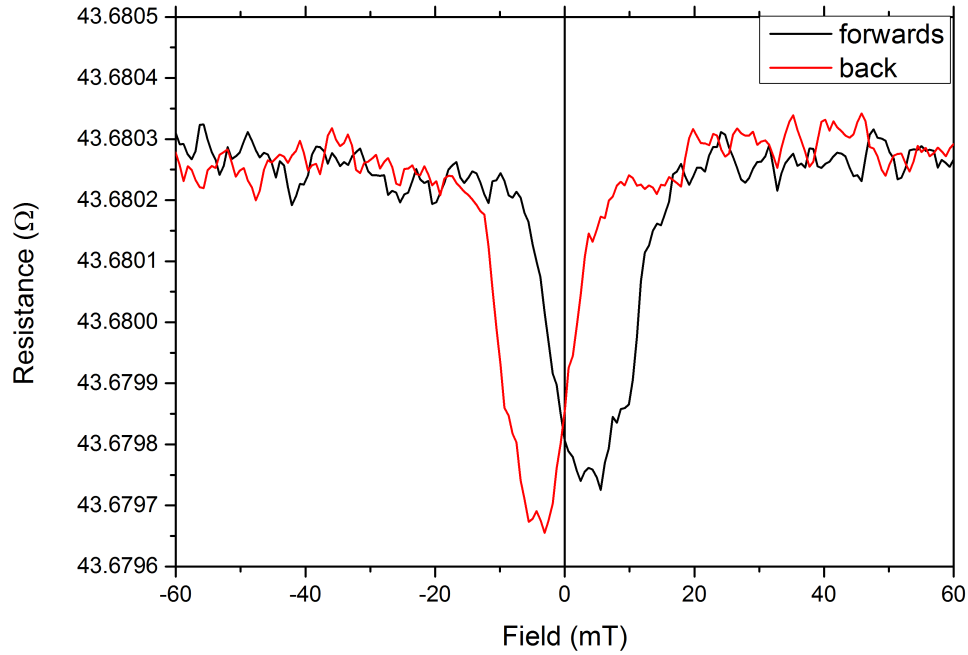


Figure 4.24: The magneto resistance of the nickel L-shape measured at $T = 300$ K with the field applied parallel to one of the arms as in fig. 4.23. The black curve is for the field swept from negative to positive values while the red curve is in the opposite sweep direction.

The MFM images of an L-shape at several magnetic fields are presented in fig. 4.25 a-f. The field directed to the right will be defined as the positive direction. At 50 mT it is observed that the entire L-shape is saturated, as indicated by the dark contrast on the left and bright on the right. As the field is lowered to 20 mT, the domain structure in the vertical arm remains the same, whereas in the horizontal arm several domains are observed to nucleate along the length of the arm. At 10 mT the domain structure in the horizontal arm appears to form a zig-zag like structure, in which the magnetisation alternates pointing across the width of the arm. In the vertical arm, the magnetization is still directed along the field except for the nucleation of a small domain structure near the corner. This behaviour was also observed at zero field. When the field is increased to -10 mT, the zig-zag domains have formed in both arms. An increase in the field to -20 mT causes the zig-zag domains in the horizontal arm to annihilate and align with the

field. In the vertical arm, the zig-zag domains that align with the field grow in size along the arm. Once -50 mT applied field is reached, the entire L-shape is saturated in the field direction. This multi domain behaviour explains the smooth drop in magnetoresistance observed in fig. 4.24.

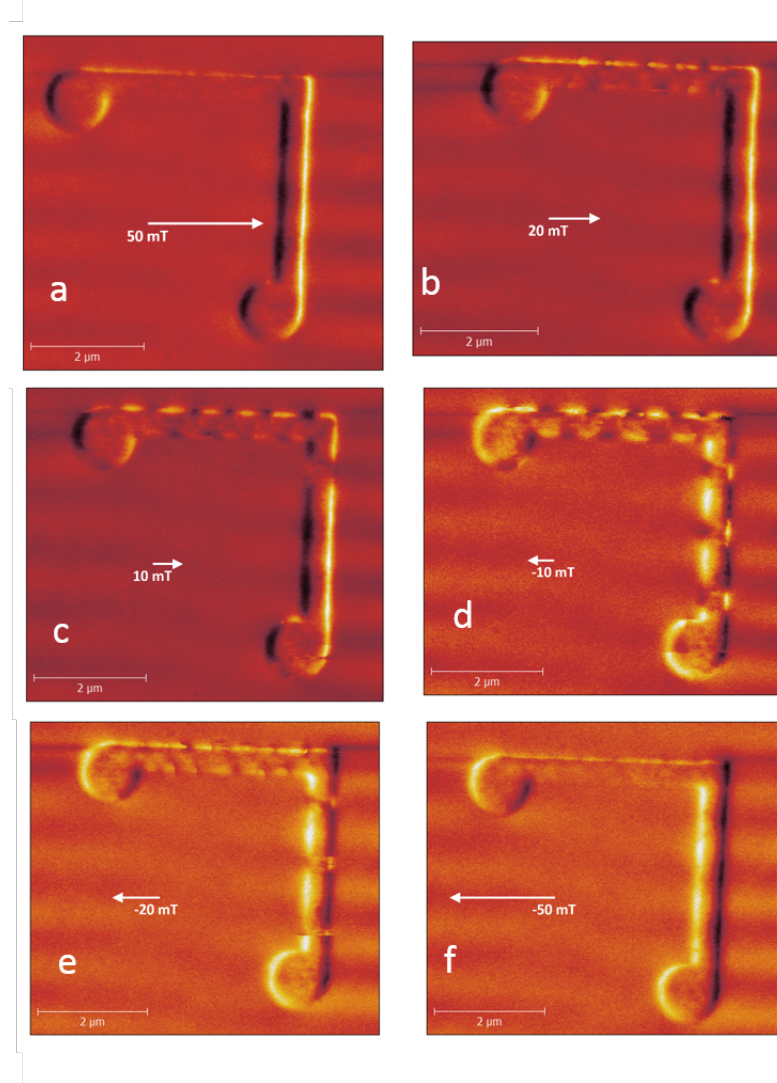


Figure 4.25: *In-situ* MFM images of a nickel L-shape made from the same film as the L-shape that forms the hybrid device measured in fig. 4.24. Images are shown at fields 50, 20, and 10 mT for both field directions, starting at 50 mT and stepping to -50 mT in the order a-f. The MFM images show that the intended shape anisotropy that directs the magnetization along the arms of the L-shape is not strong in the nickel and a complex multi-domain structure forms.

It is likely that the complex behaviour of the nickel L-shape is due to its crystalline anisotropy. It was previously discussed that bulk nickel possess cubic crystalline anisotropy, and that in the thin films presented here it exhibits a thickness dependent effective out-of-plane anisotropy. The MFM images presents in fig. 4.25 indicate that the arms of the L-shape are not narrow enough to create a shape anisotropy large enough to compete with the anisotropy contributions present in nickel. Instead, a complex multi-domain, zig-zag like structure forms that is measured as a smooth decrease and the increase in the magnetoresistance. While the nickel L-shape structure does produce the desired inhomogeneous magnetic state in the corner of the device, it is not a well controlled process or well known magnetic state.

4.3.2 Permalloy L-shape device

Previous experiments that successfully produced L-shape domain wall traps used devices made from permalloy films [27, 32, 33]. This is because permalloy, an alloy of approximately 20 % iron and 80 % nickel, has the magnetic softness of nickel without the magnetocrystalline anisotropy. Therefore, it is an ideal material to use for applications of shape based anisotropy, i.e. in domain wall traps. By fabricating the L-shape using permalloy (Py), the complex domain structure observed in the Nickel L-shape should be avoided and the L-shape should exhibit the intended behaviour.

An SEM image of the permalloy L-shape is shown in fig. 4.26. The magnetoresistance of the L-shape at $T = 0.3\text{ K}$ is presented in fig. 4.27. The black curve shows the resistance when the field is swept from -100 mT to 100 mT and the red curve for the opposite sweep direction. When the field is swept forwards (black curve) there is a smooth monotonic increase in resistance as the field decreases towards zero. As the field is increased beyond zero, a small ($\sim 0.01\ \Omega$) sudden decrease in resistance is observed at 23 mT and at 60 mT . When the field is swept back from 100 mT , a similar small jump in resistance, an increase, is observed at 25 mT . As the field is swept through zero and the direction of field flips, a large decreasing jump in resistance is observed at -12 mT followed by an increasing jump at -16 mT . This large jump in resistance is characteristic of the nucleation of a domain

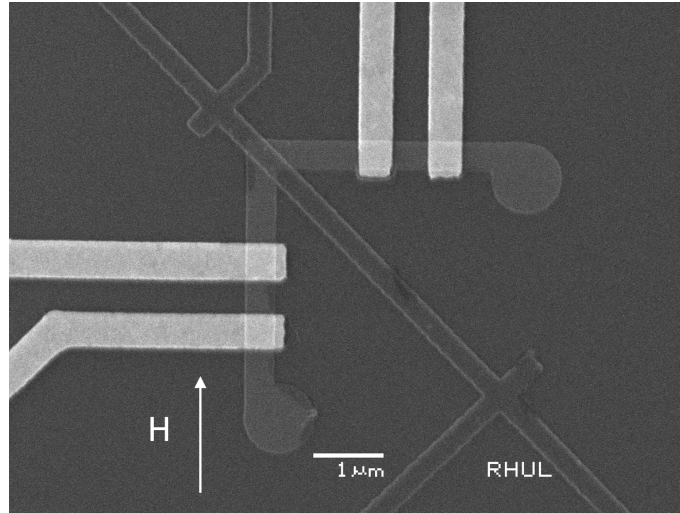


Figure 4.26: SEM image of the Permalloy L-shape hybrid device. The aluminium nanowire lies diagonally across the corner of the L-shape, while the gold contacts on the L-shape arms allow for a 4-point resistance measurement of the L-shape magnetoresistance. The contacts used to measure the magnetoresistance are annotated. The sample is mounted in the cryostat with the substrate in-plane with the field, such that the magnetic field is applied perpendicular with one arm as indicated by the white arrow.

wall at the corner of the L-shape device, therefore at -12 mT a domain wall nucleates in the L-shape ferromagnet which then annihilates at -16 mT.

The asymmetry of the magnetoresistance is unexpected, as one would expect the magnetoresistance to be hysteric and symmetric about the zero field axis. As it is, the magnetoresistance alone suggests a behaviour in which a domain wall can only be nucleated when sweeping the field from positive to negative values. Much like the nickel L-shape, the behaviour of the magnetoresistance was explained by imaging L-shape using *in situ* MFM.

The *in-situ* MFM images of the measured L-shape device are shown in fig. 4.28 with accompanying diagrams of the device magnetization at each field, shown as white arrows. Unlike the nickel device, the permalloy L-shape is not influenced by the field from the standard moment commercial MFM probes. Therefore, the device could be imaged using these probes, with a contrast large enough to be seen through the overlying aluminium wire. The advantage of this is that the exact measured device can be imaged rather

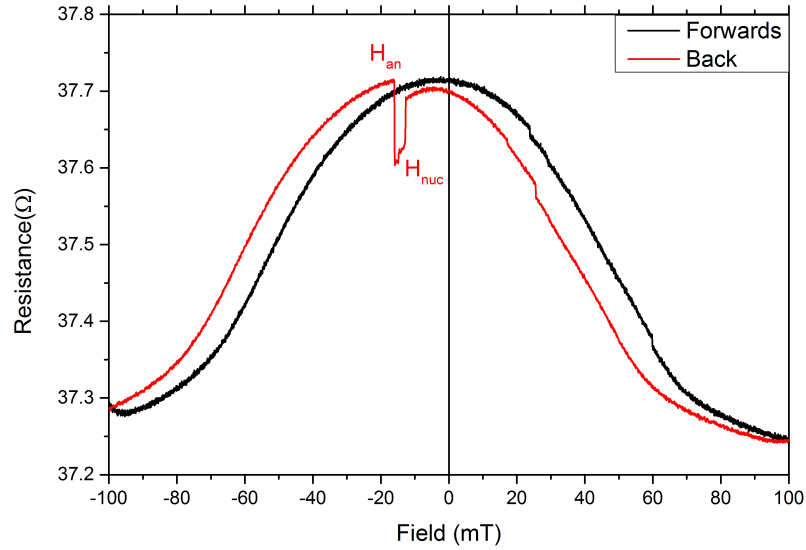


Figure 4.27: The magnetoresistance of the permalloy L-shape measured at $T = 0.3$ K with the field applied parallel to one of the arms as in fig. 4.26. The black curve is for the field swept from negative to positive values while the red curve is in the opposite sweep direction.

than a reference structure. At negative saturation (fig. 4.28a) the entire L-shape device is magnetized along the field direction, including the arm that is perpendicular to the field, which is saturated against its hard axis. As the field is reduced (fig. 4.28b) the magnetization in the perpendicular arm begins to rotate to point downward and a domain wall is smoothly nucleated in the corner seen as a bright contrast (fig. 4.28c). The domain wall is seen to remain in the corner when the field is reduced to zero (fig. 4.28d). The domain wall is annihilated when the field is increased to 10 mT (fig. 4.28e), as the arm parallel to the field rapidly switches direction. The device is then saturated again at 50 mT applied field (fig. 4.28f). When the field is reduced to zero from positive saturation (fig. 4.28g), the magnetization in the perpendicular arm again rotates downward and no domain wall nucleates, suggesting a preferred direction of the magnetization in the perpendicular arm. When a field of -7 mT is applied, the magnetization in the parallel arm rapidly switches direction to align with the field and a domain wall is suddenly nucleated (fig. 4.28h), aligning with the observed sudden drop in the magnetoresistance (fig. 4.27). The

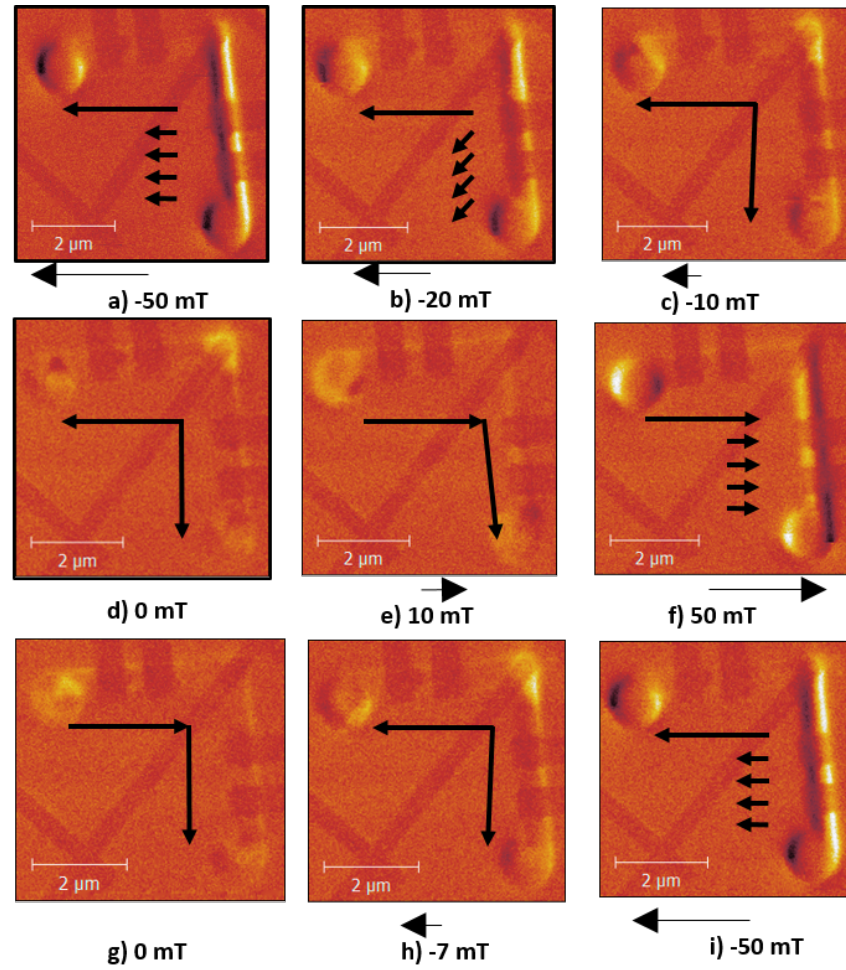


Figure 4.28: *In situ* MFM of permalloy L-shape hybrid junction measured at room temperature. The images a-i are in the order of the applied fields with additional diagrams indicating the magnetization state. All images are set to the same scale, -1 to 1° phase change. At saturation the perpendicular arm is magnetized along its hard axis. As the field is reduced toward zero, a domain wall smoothly nucleates in the corner (bright spot) as the magnetization in the perpendicular arm rotates downward. The domain wall remains as zero field and is then annihilated as the field direction is switched. After being saturated in the opposite direction, the perpendicular arm again rotates downward as the field is reduced back towards zero, showing a preferred direction. There is then no domain wall at zero field. At -7 mT the parallel arm switches direction and the domain wall is suddenly nucleated. It is then smoothly annihilated as the field is increased to saturation.

domain wall is then smoothly annihilated as the field is increased and the magnetization of the perpendicular arm saturates against its hard axis. Therefore, the asymmetry in

the magnetoresistance is due to the preferred downward direction of magnetization in the arm perpendicular to the applied field. A sudden jump in the magnetoresistance is only observed when sweeping from positive to negative fields as this is the only sweep direction in which a domain wall is nucleated by a rapid switching of the parallel arm rather than a smooth rotation of magnetization in the perpendicular arm.

Therefore, as a domain wall can be easily nucleated and annihilated from the corner of the device, and both domain wall state and single domain like state are possible at remanence, the permalloy L-shape provides a controllable method to switch between a collinear and domain wall state when included into SF hybrid structures.

Chapter 5

Hybrid SF junctions

This chapter will discuss the experiments performed to investigate the ferromagnetic proximity effect in a planar geometry. The general design of the sample consists of a superconducting nanowire made of aluminium deposited such that part of the wire passes on top of a ferromagnetic element, in this case the disks or L-shape domain wall traps discussed in chapter 4. The influence of the ferromagnet on the superconductivity in the overlying aluminium creates a new class of SNS-like junction in which the normal and superconducting metals are the same metal, a property not possible in other junctions. The differential resistance and temperature dependence of the critical current transitions in the junction are presented for several samples. It is shown that upon application and removal of an large out-of-plane field, the temperature dependence of the critical current is changed such that the aluminium above the disk is suppressed further. This magnetization dependence is investigated further using the more controllable L-shape domain wall traps presented in chapter 4. These measurements indicate that the suppression of the superconductivity in the aluminium can be reduced by the positioning of a magnetic inhomogeneity beneath the superconductor. The critical current behaviour is compared to the predictions of the theory of critical current in long SNS Junctions by Dubos et al. [91]. The comparison to theory suggests that due to the SN interfaces the junction size is not a constant, but rather the junction is proportional to the temperature. These results encourage a new theoretical treatment of such proximity induced junctions.

It is also observed that by passing current through the planar junction the critical current of an adjacent and otherwise regular superconducting nanowire is limited to that of the critical current of the planar junction at anomalous distances. This long range suppression of critical current is investigated. Two possible sources of the suppression are suggested. Firstly, that it is the injection of spin-polarised quasi-particles with long lifetime into the superconducting aluminium, which suppress superconductivity via pair breaking. Secondly, the suppression is suggested to be due to the induced SNS junction acting as a self heating hotspot. This causes a critical thermal runaway effect forcing the entire superconducting nanowire to transition into the normal state due to the increased electron temperature. Several experiments are presented that attempt to discern which of these effects is the cause of the long range suppression concluding in strong evidence to indicate that local hotspot heating is the cause.

Both the magnetization dependent effects and the long range suppression of critical current are investigated further by use of a hybrid quantum interference design that uses the planar junction as a weak link in a superconducting loop, similar to the experiments in earlier works by the group [20]. These experiments further support that the long range suppression of critical current is due to hotspot heating and that the change in critical current upon application and removal of a large magnetic field is due to the changes in magnetization of the ferromagnet.

5.1 Initial experiments: 800 nm and 1000 nm disks

Hybrid junction behaviour

The first experiments investigating proximity effects in Al-Ni disk hybrids consisted of a simple design of several nickel disks, diameter 800 & 1000 nm and thickness 30 nm (i.e. within the vortex state phase) deposited on to naturally oxidised silicon substrates with an aluminium nanowire, 300 nm wide and 80 nm thick, deposited such that part of the nanowire overlaps the disks. Samples were fabricated in two lithography and deposition steps, one for each layer of material. Before the deposition of aluminium in the second lithography process, twenty seconds of argon etching was performed to clean the nickel surface and ensure little to no oxide at the interface between the nickel and aluminium. This is to create the maximum possible proximity coupling between the ferromagnet and superconductor [20]. An SEM image of an early sample is shown in fig 5.1 along side a 3D AFM topography image of a 1000 nm diameter disk/wire junction. This geometry repeats the earlier experiments of the group [20].

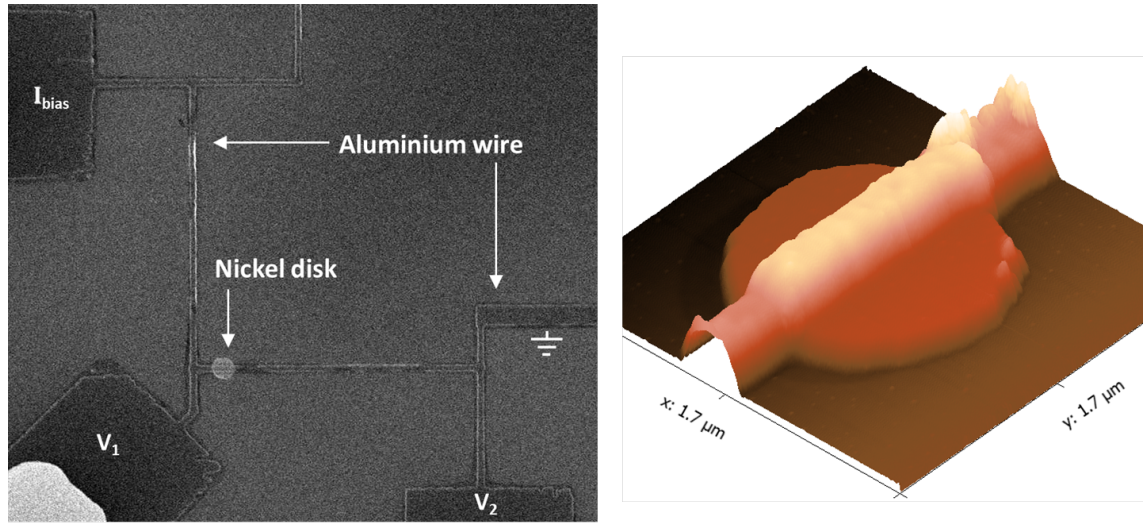


Figure 5.1: Left: SEM image of the first planar junction sample. Right: 3D AFM topography image of a 1000 nm diameter disk/wire junction.

Two samples of the design shown in fig 5.1 were measured, with disk diameters 800 & 1000 nm,

the samples will be referred to as disk samples 1 & 2. The samples were mounted in the ^3He cryostat for electrical measurements. The differential resistance of the samples was measured using the dV/dI method described in chapter 3.

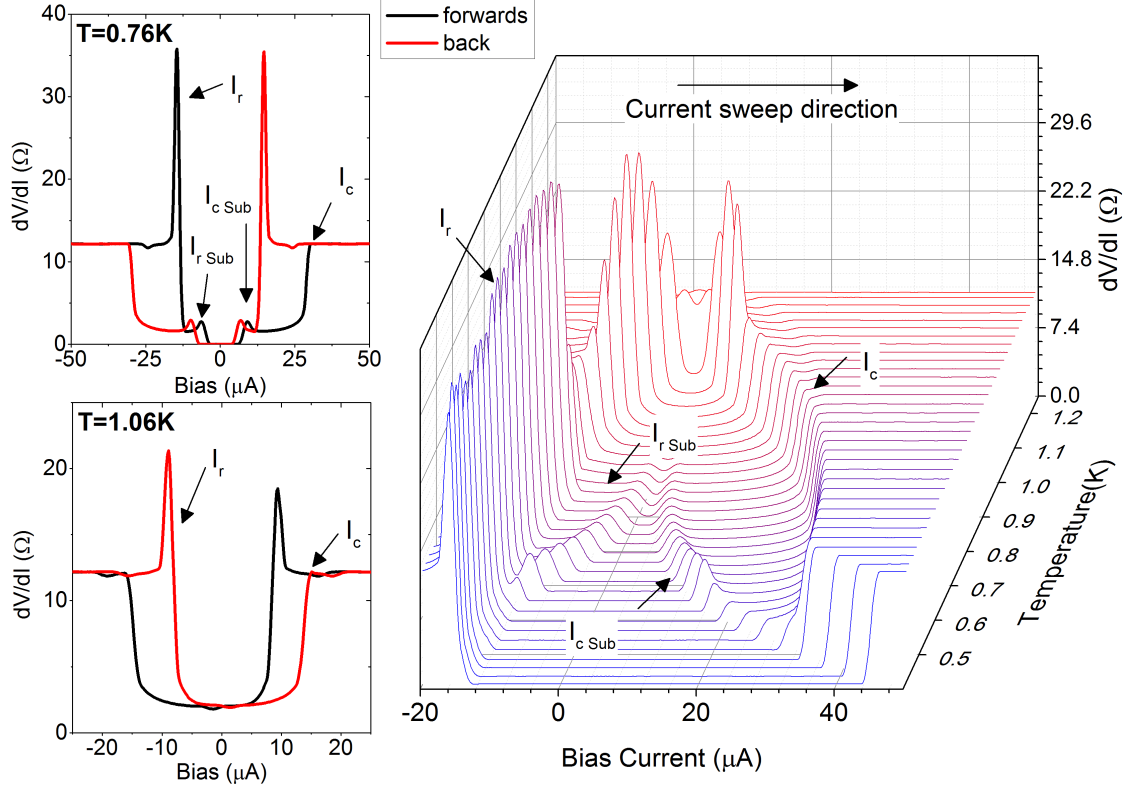


Figure 5.2: Left: The dV/dI of disk sample 1 at 0.76 K (top) and 1.06 K (bottom), the black curve is current swept from negative to positive while the red curve is the opposite sweep direction. The dV/dI is hysteric, a property of superconducting thin films. Right: The temperature dependence of the dV/dI of disk sample 1. The current is swept from negative to positive. Three distinct phases of resistance can be observed: the normal phase where the resistance is $\sim 10\ \Omega$, the SNS phase, where the resistance is $\sim 2\ \Omega$, and the superconducting phase where the resistance is zero. The SNS phase is caused by the aluminium above the nickel transitioning into the normal state before the entire nanowire.

The overall behaviour of the differential resistance of disk sample 1 within the temperature range 0.4 – 1.2 K is illustrated in fig. 5.2 right image. In this figure, the bias current is swept from negative to positive values, while the voltage drop is measured across the sample which is then converted into differential resistance. The current is repeatedly swept

in the manner while the sample is being cooled, obtaining the differential resistance at varying temperature. At temperatures close to $T_c \approx 1.2\text{ K}$ peaks appear in the differential resistance that indicate the aluminium has transitioned into the superconducting state. The position of the second peak, which indicates the transition from superconducting state to the normal state, defines the critical current, I_c , at which the superconducting state is destroyed. The first peak is defined as the re-trapping current, I_r . This transition is at a noticeably reduced current than the critical current. This is due to the well known behaviour of the re-trapping effect. One way of describing the re-trapping effect is by considering that when the aluminium is in the normal state, the Joule heating in the wire raises the electron temperature causing a decrease in the current at which the aluminium will transition into the superconducting state. This causes hysteresis in the measured dV/dI , as illustrated in fig. 5.2 left image, where the black curve is the dV/dI measured while sweeping from negative to positive current and the red curve is the opposite direction. Hysteresis was present in all samples measured, however measurements were completely symmetric about zero bias current. Thus, for the sake of brevity, only the negative to positive sweep data is presented for all samples. Considering the hysteric nature of the dV/dI , the term critical current refers to the transition from superconducting to normal state only. Near T_c at currents less than the re-trapping and critical currents there is still a finite resistance. This indicates that, while the majority of the aluminium nanowire has transitioned into the superconducting state, the aluminium above the nickel is in the normal state. As the temperature is decreased, both the re-trapping and critical currents increase with behaviour like $I_c \propto 1/\sqrt{T}$. At $T \sim 1\text{ K}$ a secondary pair of transitions appear near zero bias current. These transitions indicate that the superconductivity is beginning to nucleate in the aluminium above the nickel and will be referred to as the I_{rSub} and I_{cSub} . As the temperature is reduced further to $T \sim 0.9\text{ K}$, the resistance is zero at currents less than the I_{cSub} and I_{rSub} transitions indicating that the entirety of the aluminium nanowire is now superconducting. As the temperature decreases further, the sub-gap transitions evolve with behaviour similar to $I_{cSub} \propto e^{-T}$. This continues until $T \sim 0.6\text{ K}$ when the I_{rSub} transition reaches the main I_r transition and a single transition

is observed. Similarly at $T \sim 0.5$ K the I_{cSub} approaches the I_c and a single transition appears, except this new critical current transition evolves like the I_{cSub} transition and a discontinuity of the critical current appears.

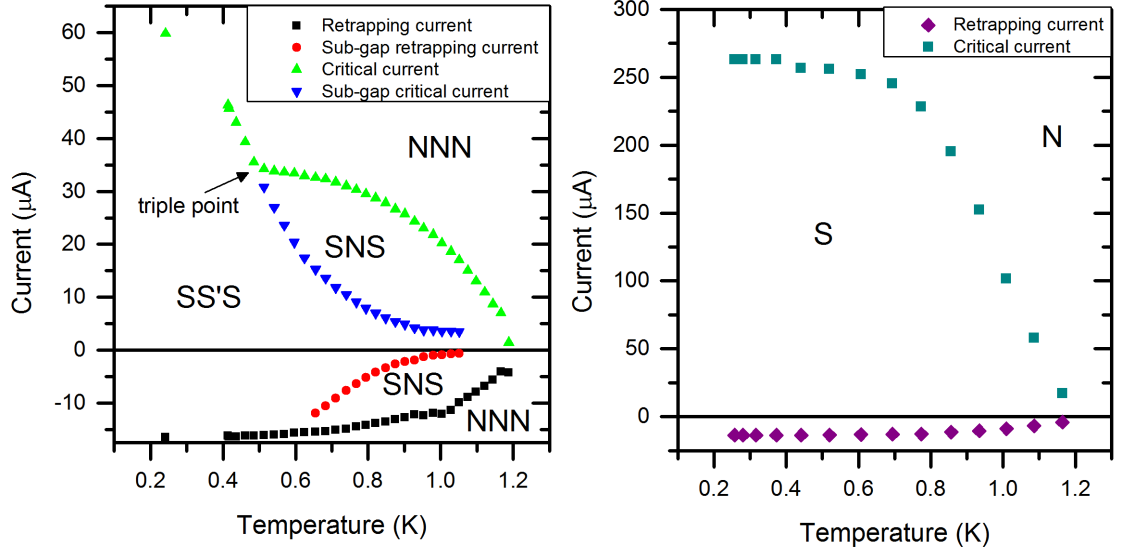


Figure 5.3: Left: The temperature dependence of the four transitions in the 800 nm disk junction of sample 1. The hybrid junction phases have been labelled for clarity. The triple point is defined as the temperature and current where all three phases meet, i.e. in this case at the point $T = 0.485$ K, $I = 35.5$ μ A. Right: The critical current transition for an superconducting aluminium nanowire not under the influence of a nickel disk, but fabricated from the same film as that of the hybrid junction. Without the influence of the hybrid junction, there is only a single transition from superconducting to normal state that evolves with temperature in the expected BCS behaviour.

This behaviour describes an interesting series of events. Concentrating on the positive current (critical current) transitions only, when current is swept from zero current to positive current at temperatures between T_c and $T \sim 0.5$ K, the planar hybrid junction goes through 3 separate phases. First the entire wire is superconducting. Then an SNS phase is observed in which the aluminium above the nickel is normal. The suppression of superconductivity by the disk is not due to the stray field from the disk, but the ferromagnetic proximity of the disk and aluminium. To support this further, control experiments in which the Ni was replaced by a gold disk showed no suppression of superconductivity. It is well known that superconductivity is suppressed by magnetic fields. In thin films, the

critical field is greatly increased for fields applied in the plane with the film as the field penetrates the film uniformly [147]. Therefore, when considering the suppression of the Al film by magnetic field from the nickel, out-of-plane field components should be considered the dominant. In the case of the vortex state, the dominant out of plane field component is that due to the vortex core. The field from the vortex core has been shown to be on the order of $1-2$ mT at a distance of 90 nm [148]. Even if one estimates the vortex core field to be 100 times this at the surface, by assuming the field decays at an approximate rate $1/r^2$, the flux of a 100 nm vortex core penetrating the aluminium would be 7.85×10^{-16} Wb, less than the flux quantum. Furthermore, earlier work in the group [20] showed that by inclusion of a thin oxide barrier between the nickel and aluminium, the suppression effect was almost completely eliminated and the SNS behaviour was only observable very near T_c . Thus, stray field is not the cause of the suppression of the superconductivity in the aluminium. This ferromagnetic suppression of the superconductivity in the aluminium manifests in a reduction of the critical current of the nanowire above the disk and the SNS like phase becomes possible.

This SNS like phase is unique, as the superconducting and normal states coexist in the same metal, with no physical inter-facial boundary separating them, only a boundary between the two electron phases. As the bias current is increased, the remainder of the aluminium transitions to the normal state and the entire wire becomes normal. However, at temperatures lower than $T \sim 0.5$ K only two phases are observed, the superconducting and normal phases. To illustrate this, the positions of the transition peaks in fig 5.2 are shown in fig. 5.3 left and compared with the critical current transitions of an aluminium nanowire of the same dimensions and film as the hybrid junction but without the influence of the nickel disk in fig. 5.3 right. Upon comparison of the two phase diagrams, the SNS phase is absent in the nanowire as is to be expected, with no external influence to weaken the superconductivity along the wire the entire film will transition between the superconducting and normal states in unison. Furthermore, the critical current is far larger in the nanowire, reaching a maximum of $260 \mu\text{A}$ at the base temperature of 0.25 K in comparison with $60 \mu\text{A}$ in the hybrid junction. The evolution of the critical

current with decreasing temperature is also vastly different between the junction and the nanowire. The nanowire exhibits a rapid linear increase of critical current until ~ 0.7 K where it approaches the maximum value. Whereas, on examination of the transition in the hybrid junction, it is clear that the I_{cSub} transition and I_c transition below ~ 0.5 K form a smooth curve that is not linear like that of the nanowire. Therefore, it must be that below ~ 0.5 K the critical current transition of the entire nanowire in contact with hybrid junction is controlled by the critical current of the hybrid junction, such that the transition of the junction either coincides with or induces the transition of the entire nanowire. The temperature and current, at which the superconducting to SNS transition meets the SNS to normal transition, will henceforth be referred to as the triple point temperature or simply triple point, as this is analogous to the triple point in liquid-solid-gas phase diagrams.

Non-local influence

To investigate whether the simultaneous transition of both the hybrid junction and the nanowire at temperatures less than the triple point was coincidental or due to the influence of the hybrid junction upon the adjacent nanowire, the non-local influence of the hybrid junction on the nanowire was measured. Fig. 5.4 b & c show the two measurement arrangements used to measure the critical current of the aluminium wire adjacent to the hybrid junction. In both measurements, only the voltage drop across the wire is measured, as the hybrid junction is not included in the resistance measurement. In fig. Fig. 5.4b the current does not pass through the hybrid junction. whereas in Fig. 5.4c the current does pass through the junction. The comparison of the measured critical current in the two configurations can be seen in fig. Fig. 5.4a. It is immediately obvious that there is a drastic reduction of the critical current of the aluminium nanowire when the current is passed through the hybrid junction. At the base temperature of the cryostat, 0.25 K, when the current bypasses the hybrid junction the critical current is $260 \mu\text{A}$ compared to $60 \mu\text{A}$ when passed through the junction. Furthermore, while no I_{cSub} transition was observed when the current was passed through the hybrid, the line shape of the critical current transition of the wire is identical to that of the critical current transition of the

hybrid including the changing behaviour between the SNS-normal and superconducting to normal state transitions at the triple point temperature $T \sim 0.5$ K. This indicates that the transition from superconducting to normal state of the aluminium nanowire that forms the superconducting elements of the hybrid S-S/F-S junction is dominated completely by the properties of the hybrid junction.

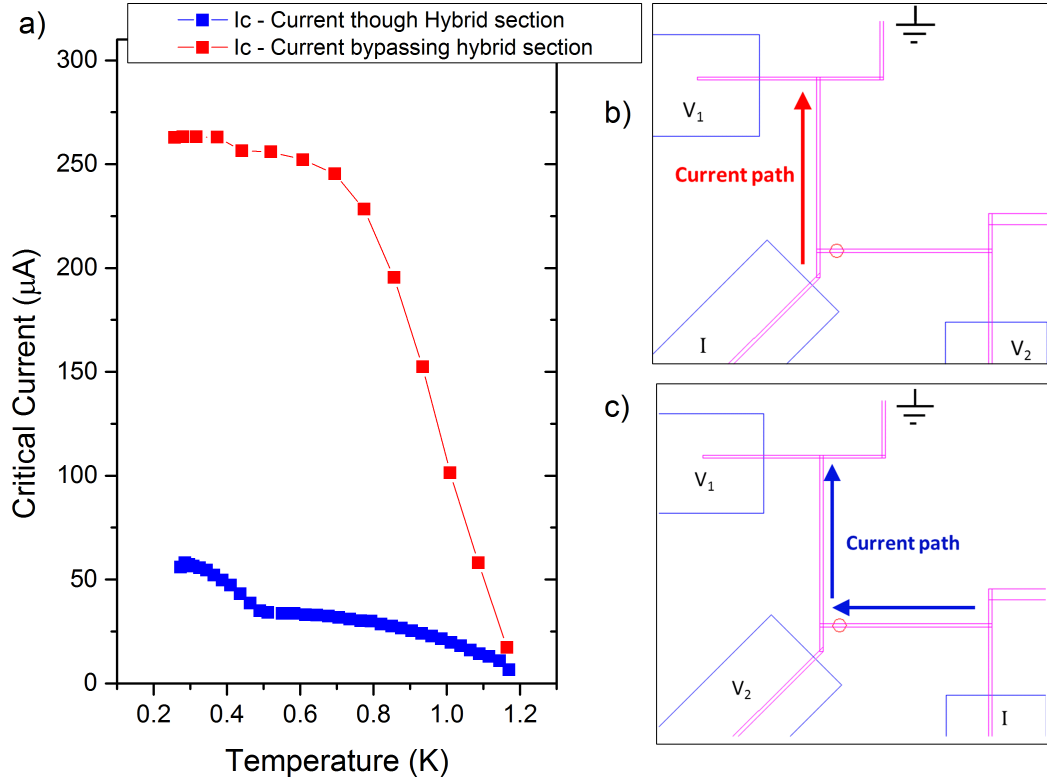


Figure 5.4: The long range influence of the hybrid junction is demonstrated in disk sample 1. The voltage drop is measured across a $10\text{ }\mu\text{m}$ section of superconducting Al nanowire, the electrical configuration does not include the hybrid junction in the measured voltage. Two electrical configurations are used: the current is either passed through the hybrid (c) or bypassing it (b). When the current bypasses the hybrid the critical current of the nanowire is that of the expected BCS like behaviour (a, red line). When the current is passed through the hybrid (a, blue line) the critical current of the nanowire is limited by the critical current of the hybrid junction.

The range of this dominating effect is of great interest. The length of superconducting nanowire affected by the hybrid junction in this experiment is $10\text{ }\mu\text{m}$, on the order of a hun-

dred times larger than the superconducting coherence length in aluminium $\xi_0 \sim 120$ nm. As changes in the superconducting properties of the condensate occur over distances of the order of ξ_0 , it is of great interest to discover the cause of this influence which was the aim of several of the experiments in this project.

Magnetic history dependence

As has been discussed so far, the influence of the nickel disk upon the aluminium wire is such that the ferromagnetic ordering in the nickel suppresses the nanowires superconducting properties. This is evidenced in the greatly reduced critical current of the hybrid junction and nanowire. A new sample was fabricated, disk sample 2, to investigate how this suppression is dependent on the magnetization of the nickel disk. For this investigation a simple procedure was followed. Firstly, the temperature dependence of the differential resistance of the hybrid junction was measured before the application of any magnetic fields. In this measurement it can be said with confidence that the disk is in the vortex state due to its dimensions. Then an out-of-plane field was applied to the sample slowly up to 800 mT and then reduced back to 0 mT, performing effectively a half hysteresis loop. The field was limited to out-of-plane, due to the relative alignment of the cryostat sample mount with the solenoid. The temperature dependence of the differential resistance of the hybrid junction was then remeasured after the field had been removed. The I_c and I_{cSub} transitions for the 800 & 1000 nm disk junctions of disk sample 2 are shown in figure 5.5 before (left) and after (right) the field was applied. Strikingly, after the field has been applied the critical current of both the hybrid junctions is further suppressed. A possible artefact could be related to flux trapping inside the large superconducting magnet. This was eliminated by test measurements of the critical current of the simple aluminium nanowire not influenced by the nickel. This critical current remained unchanged after the application of the field. If there was an external field applied to the entire sample, then the critical current of this wire should also be suppressed. Therefore, it must be that the source of the change the in critical current of the hybrid junctions is related to the magnetization of the nickel disk.

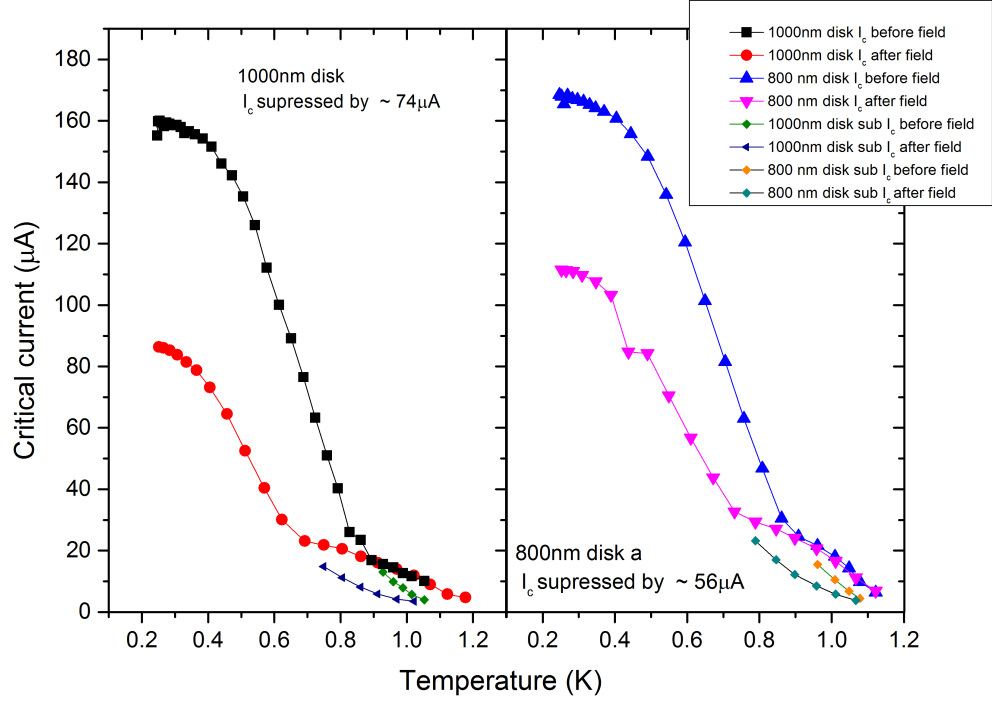


Figure 5.5: The I_c and I_{cSub} transitions for the 1000 nm (left) and 800 nm (right) hybrid junctions with nickel thickness 30 nm before and after the application of 800 mT out-of-plane field. Both junctions reproduce the features of disk sample 1, yet with increased maximum critical current and triple point temperature. After the application and removal of the magnetic field, the critical current of the SNS to normal state transition remains unchanged, however the superconducting to SNS and superconducting to normal transitions have been suppressed, reducing the maximum critical current and triple point temperature.

At $T = 0.25$ K the critical current of the 1000 & 800 nm hybrid junctions has dropped by $74 \mu A$ and $56 \mu A$, respectively. This is a change in critical current of 47 % (1000 nm junction) and 34 % (800 nm junction). Furthermore, the triple point of both junctions has now changed by shifting to a lower temperature, $0.894 \text{ K} \rightarrow 0.692 \text{ K}$ and $0.908 \text{ K} \rightarrow 0.789 \text{ K}$ for the 1000 & 800 nm junctions, respectively. However, at temperatures above the initial triple point ($0.789 \text{ K} / 0.894 \text{ K}$) the critical current behaviour is the same both before and after the field has been applied. As it was not possible to measure the out-of-plane hysteresis of the nickel disks, it is difficult to say with certainty what the magnetization state of the disk is after the field was applied. Before the field is applied, it can be

assumed with good confidence that the disk is in a vortex state as the dimensions of the disk fall within the remnant vortex phase discussed in chapter 4. When considering the theoretical work of Champel and Escrig [18] discussed in section 2.2.2, where it was calculated that the influence of ferromagnet with a collinear magnetization suppresses the singlet superconductivity of an adjacent superconductor more than that of a rotating inhomogeneous magnetization, it could be inferred from the decrease in critical current that the magnetization of the nickel disk is now collinear rather than a vortex. Similarly however, the increase in coercitivity at low temperatures may mean that after the field has been applied the disk is in a state with significantly more out-of-plane components of magnetization, i.e. similar to the canted vortex illustrated in fig. 4.5. Without the ability to image the disks using MFM techniques at low temperature it is difficult to determine exactly what the effect of the field on the disk state is.

These results indicate that, like previously suggested, the superconducting to normal transition below the triple point temperature and the superconducting to SNS transition above the triple point temperature must be due to the same transition, that of the hybrid junction, as these two transitions smoothly merge together at the triple point and both are influenced by changing the magnetic of the disk. Whereas, the SNS -to normal transition above the triple point is not affected by the application of the magnetic field, therefore is likely to be independent of the magnetic properties of the hybrid junction.

These early experiments raised several questions that warranted further investigation. The most fundamental property that required further investigation was the dependence on magnetic state. While the early results showed that the suppression is dependent on the magnetic history, it was inconclusive as to whether the change in critical current could be correlated with a change in magnetic state, specifically a change between inhomogeneous and collinear magnetization, similar to the observations of Kinsey et al. and Rusanov et al. [16, 17]. Further experiments in which the magnetization of the ferromagnetic element was known at all times were required.

The second question raised was, what is the cause of the long range influence of the hybrid junction upon the aluminium nanowire. Two possible explanations arise: the possibility of

suppression of the superconductivity by injection of spin-polarised quasi-particles generated in the hybrid junction, or the suppression of the superconductivity by a local increase in temperature due to Joule heating in the hybrid junction. The possibility of suppression due to the injection of spin polarised quasi-particles was supported by the magnetic history dependence of the superconducting to normal transition below the triple point temperature, where there is no SNS phase and therefore no intermediate Joule heating state exists. It was further supported by the recent observations of spin life times in superconducting aluminium - MgO tunnelling junctions on the order of 0.1 ms [149] by Yang et al. and measurements of non-equilibrium spin imbalance over a distance of several microns by Hubler et al. [150]. Moreover, the experiments by Shin et al. [151] on injection of spin polarised quasi particles from cobalt into aluminium indicate that the spin diffusion length in the superconducting aluminium increases with temperature. The results of these publications suggested that spin-polarised quasi-particles injected into the aluminium nanowire from the nickel disk may survive long enough to suppress the superconductivity over the observed distance of 10 μm . This suppression would be due to the increased recombination time of spin polarised quasi-particles. The recombination time, i.e. the time it takes for two quasi-particles in the superconductor to combine to form a Cooper pair, of two spin polarised quasi-particles will be longer due to the need for one particle to undergo a spin-flip scattering event such that the two quasi-particles can now form a anti-parallel spin singlet Cooper pair. The increased number of unpaired quasi-particles in the superconductor would weaken the overall superconductivity. Such suppression by spin polarized current has been investigated before in Co-Al-Co single electron transistors [152] and high T_c perovskite superconductors in contact with ferromagnetic insulators [153], in which both authors observe suppression of superconductivity that is attributed to spin polarised quasi-particle injection. However, experimental observations of suppression by spin polarised current, specifically in high T_c superconductors has been challenged, suggesting that the suppression of superconductivity is due to the the Joule heating of the current injection electrodes [154]. Therefore, it was of importance to investigate which of these two possibilities was the cause of the long-range suppression.

5.2 Long range suppression due to spin polarised current injection: distance dependence

Experiments to investigate both possible causes of the long-range suppression of superconductivity, i.e. by injection of spin-polarised quasi particles or by local heating, were pursued simultaneously. This section will present the used experiment to test the suppression of superconductivity by injection of spin-polarised quasi-particles.

The problem of spin diffusion in superconducting aluminium was discussed previously by Shin et al. [151]. In this work, the authors injected spin polarised electrons into an aluminium film from a cobalt electrode and measured the voltage drop between the cobalt electrode and an aluminium electrode $L = 3\text{ }\mu\text{m}$ away from the injector. The authors observed two peaks in the differential resistance of the aluminium, the lower peak they attributed to the transition of the aluminium suppressed by the injected spin polarised carriers, while the second was the transition of the aluminium beyond the range of the spin diffusion. The authors then extracted the spin diffusion length d_s using the relation $V_{c,supp}/V_c \simeq d_s/L$, where $V_{c,supp}$ and V_c are the voltages at the suppressed and bulk critical currents. This relation was justified under the assumption that over the spin diffusion length the aluminium turned normal by the injected spins would produce the finite voltage $V_{c,supp}$. Using this method the authors extracted a zero temperature limit of the spin diffusion length to be $d_s = 1.6\text{ }\mu\text{m}$ on the order of the distance of suppression observed in the hybrid junction.

Shin et al. developed a model for the spin diffusion length using the suggestion that the spin diffusion time should be [153] $\tau_s \sim \tau_{ex} k_B T_c / \Delta(T)$ where $\Delta(T)$ is the temperature dependent superconducting gap energy which can be assumed to be the empirical formula $\Delta(T) = \Delta(0) \tanh(1.74 \sqrt{T_c/T - 1})$ and τ_{ex} is dependent on the leakage of exchange field, h_{ex} , into the superconductor, such that $\tau_{ex} \sim \hbar/h_{ex}$.

A picture arises in which the spin diffusion length in the aluminium above and adjacent to the nickel in the hybrid junction is large due to both the exchange field leaking into the superconductor and increased local temperature due to heating in the SNS phase.

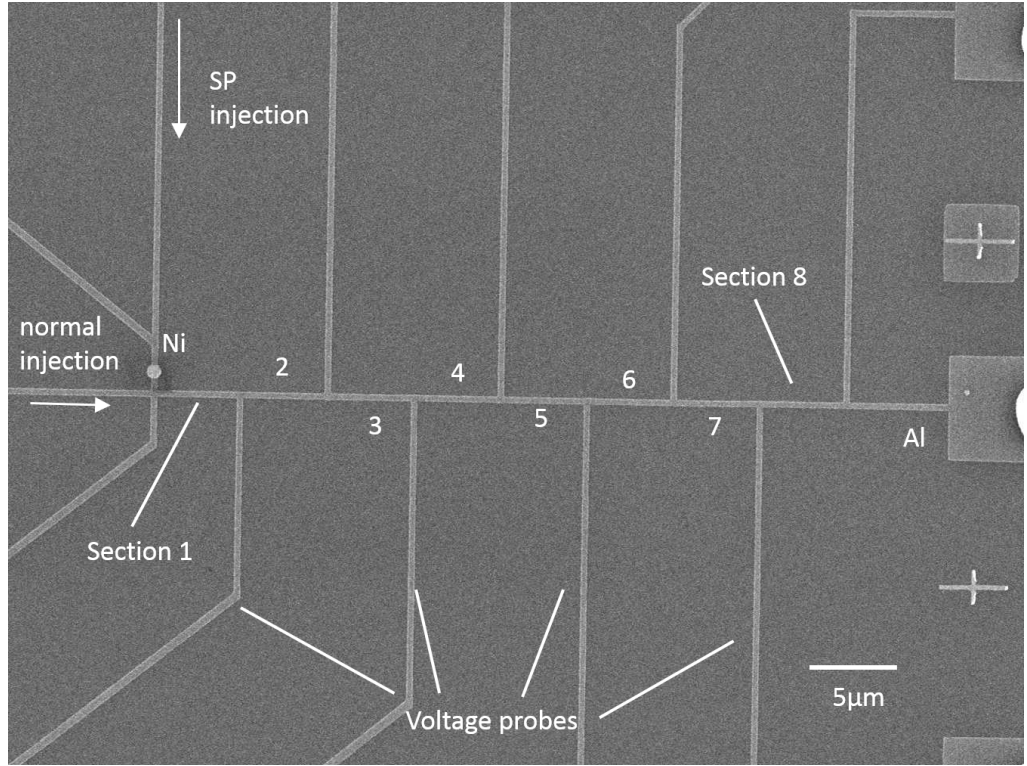


Figure 5.6: SEM image of the device used to investigate the distance dependence of the long range suppression of critical current. A hybrid junction is connected to a 40 μm long aluminium nanowire with an additional electrode to inject current bypassing the hybrid junction. The 40 μm nanowire is separated into eight 5 μm sections with voltage leads for each section such that the critical current of each section can be measured individually.

This creates a large accumulation of spins that are injected into the adjacent aluminium nanowire that suppress the superconductivity and thus critical current. This model does not explain why the SNS phase only exists at temperatures above the triple point however. Nevertheless, this theory should prove simple to test: if the suppression is due to injection of spin polarised electrons, it should be expected that the strength of the suppression effect will diminish over distance with behaviour like e^{-L/d_s} . Therefore, by fabricating a device with a sufficiently long superconducting nanowire and passing current through a hybrid junction, the critical current of the nanowire should increase as the distance from the junction increases.

To this end, the device shown in fig. 5.6 was fabricated. In this device, the hybrid

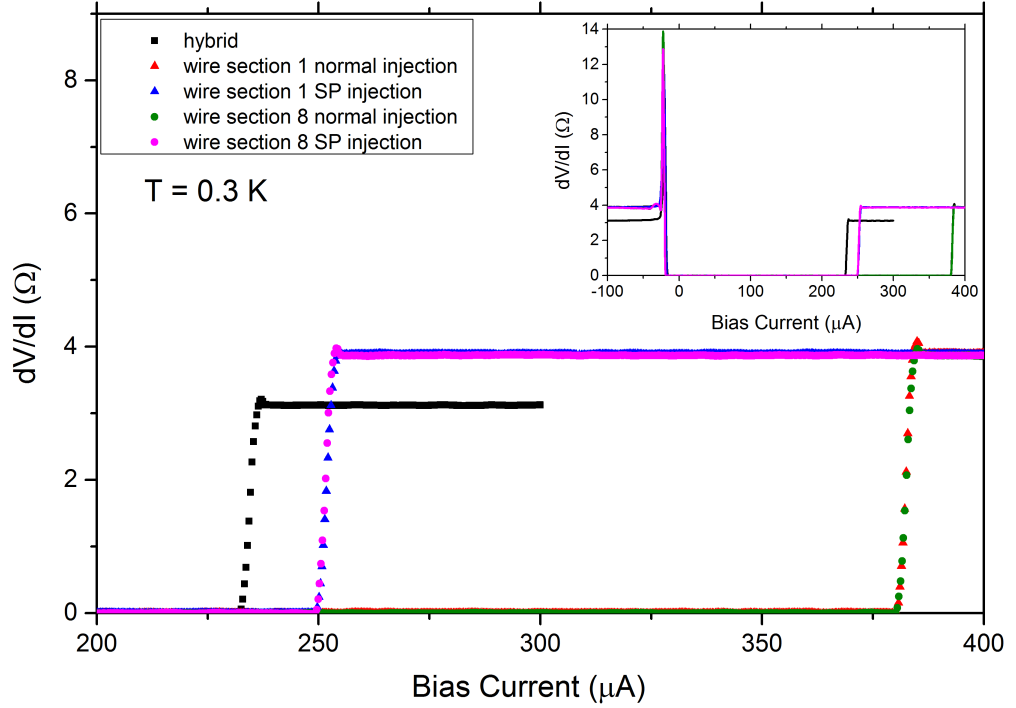


Figure 5.7: The dV/dI zoomed in to the I_c transition of the hybrid junction (black squares) and wire sections 1 and 8 (triangles and circles, respectively), in the normal and spin polarised current injection configurations, at $T = 0.3$ K. The full dV/dI is shown in the inset. Both wire sections 1 and 8 show identical I_c in both injection configurations, with a reduced I_c in the spin polarised configuration, close to that of the hybrid junction.

junction was fabricated using a 800 nm diameter 30 nm diameter nickel disk and the same aluminium nanowire dimensions as previous, 300 nm wide and 80 nm thick. The nanowire connected to the junction was made to be 40 μm long, with voltage leads attached every 5 μm and an additional lead for injection of current bypassing the hybrid junction, named normal injection. This geometry allowed the measurement of the critical current for each wire section separately with injection of current either spin polarised, i.e. through the hybrid, no normal, i.e, bypassing the hybrid. If the long range suppression of critical current is due to injection of spin polarised quasi-particles, the critical current of wire section 8 should be greater than that of wire section 1 in the spin polarised configuration due to the relaxation of the spins over the greater distance, whereas in the normal current injection configuration they should be identical.

The dV/dI , zoomed in to the I_c transition, for the hybrid junction and wire sections 1 and 8 at $T = 0.3$ K is presented in fig. 5.7. The inset in fig. 5.7 shows the full dV/dI . Wire section 1 is shown with diamond symbols whereas section 8 is shown with circles. In the normal injection configuration, with the bias current bypassing the hybrid junction, both wire sections 1 and 8 have identical critical current, $I_c = 385 \mu\text{A}$, as expected. When current is passed through the hybrid junction, the spin polarised configuration, the critical current of both wire sections 1 and 8 is suppressed, as observed in previous samples, but is also identical, at $I_c = 253 \mu\text{A}$, close to the critical current of the hybrid junction, with $I_c = 237 \mu\text{A}$. Furthermore, the measured resistance of the aluminium wire in the both configurations, $\sim 4 \Omega$, is close to the estimated resistance of the entire $5 \mu\text{m}$ wire section, i.e. $R = \rho l/A = 3.5 \Omega$, where $\rho \sim 2 \times 10^{-8} \Omega\text{m}$, $l = 5 \mu\text{m}$ and $A = 2.4 \times 10^4 \text{ nm}^2$. This further indicates that the entire aluminium nanowire has transitioned into the normal state.

The temperature dependences of the critical current of the hybrid junction and wire sections 1 and 8 are shown in fig. 5.8 when the current is injected through the hybrid junction. Like the spin polarised injection dV/dI at $T = 0.3$ K, the critical current behaviour of both wire sections 1 and 8 is identical, and nearly identical to that of the hybrid junction. This indicates either a spin diffusion length much in excess of $40 \mu\text{m}$, which is a very unlikely prospect, or more likely that the suppression is not due to spin injection. Therefore, these results indicate that the long range suppression of critical current cannot be attributed to spin polarised injection.

5.3 Heat sinks sample

The theory of suppression by local heating in the SNS phase could also be simply tested experimentally. The heat generated by Joule losses can be considered by following the theory of Clarke [155], concerning the situation at low temperatures when the electron temperature is driven far out of equilibrium from the phonon temperature such that the temperature, T_e , of the electron gas is:

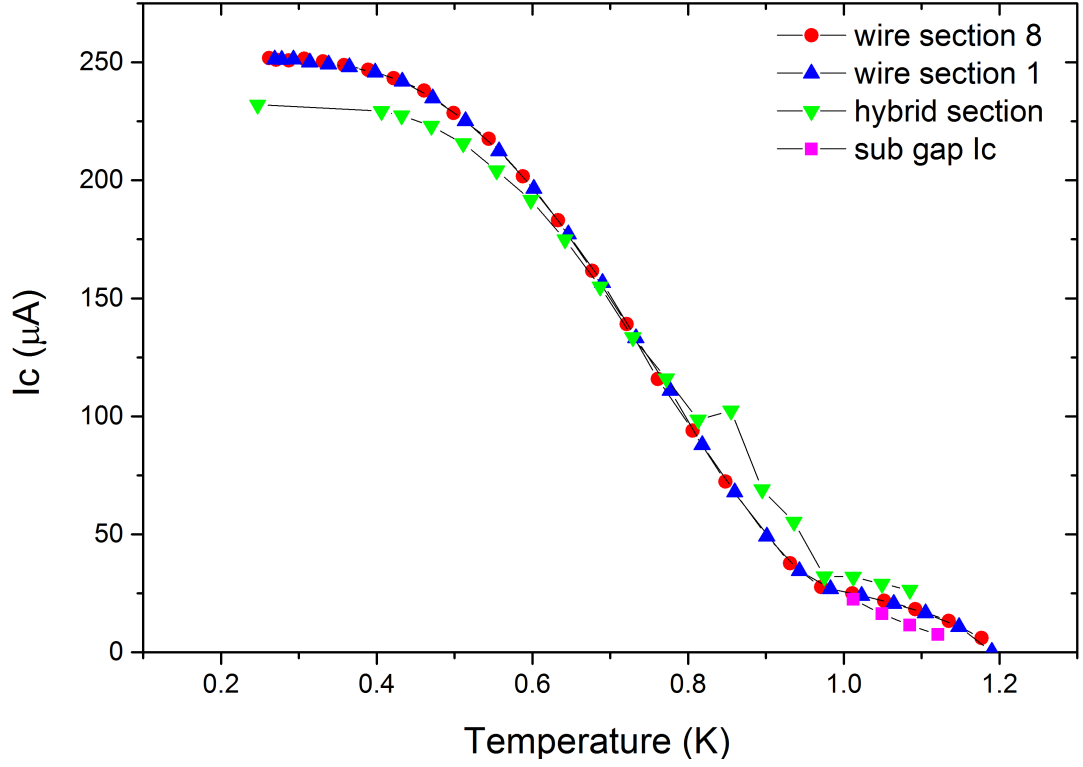


Figure 5.8: The temperature dependence of critical current for the hybrid junction and wire sections 1 and 8 as indicated in fig. 5.6. The critical current behaviour of wire sections 1 and 8 is identical and almost identical to that of the hybrid junction. This suggests that the long range suppression is not due to the injection of spin polarised quasi-particles.

$$T_e = \left(\frac{P}{\Sigma\Omega} + T_p^5 \right)^{1/5} \quad (5.1)$$

where T_p is the temperature of the phonon gas, Ω is the volume in which the power P is uniformly dissipated and Σ is the electron-phonon coupling strength. With an input current, the power supplied is that of Joule heating, therefore $P = \rho j^2 \Omega = \rho I^2 / A \Omega$, where ρ is the resistivity and A is the cross sectional area of the nanowire, j is the current density and I is the total current. In the case of the hybrid junction, a simple approximation can be made that the power dissipates uniformly in the normal aluminium section above the ferromagnet only. The volume dependence of dissipation is then eliminated and the

current required to sustain a given electron temperature is

$$I = \left(\frac{\Sigma}{\rho} (T_e^5 - T_p^5) \right)^{1/2} \quad (5.2)$$

For the superconducting aluminium nanowire adjacent to the normal wire to transition into the normal state, the electron temperature in the normal aluminium at the boundary must be equal to at least T_c . Assuming the electron temperature throughout the normal metal section is uniform and there is no cooling to the adjacent superconducting nanowires, which in reality is an oversimplification, the input current at which the electron temperature in the normal section is equal to T_c is

$$I(T_e = T_c) = \left(\frac{\Sigma}{\rho} (T_c^5 - T_p^5) \right)^{1/2} \quad (5.3)$$

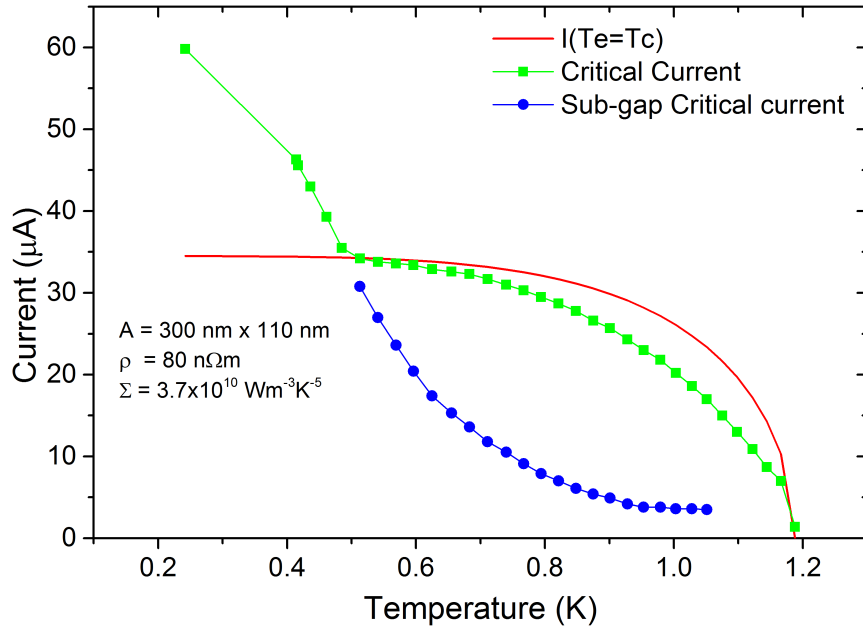


Figure 5.9: The simple hot electron model fit to the 800nm hybrid junction from disk sample 1. The parameters used are $A = 300 \text{ nm} \times 110 \text{ nm}$, $\rho = 80 \text{ n}\Omega\text{m}$, $\Sigma = 3.7 \times 10^{10} \text{ Wm}^{-3}\text{K}^{-5}$. The fit is not ideal, but reproduces relatively well the line shape of the SNS to normal state transition.

This assumption also requires that the phonon temperature is in equilibrium with the bath

temperature. This is true in the case of the thin films used here as the thermal resistance of the interface between the film and the substrate, the Kapitza resistance, is negligible because the film thickness is smaller than the phonon Fermi wavelength [156]. Therefore, by setting the phonon temperature to the bath temperature, a naive approximation for the current $I(T_e = T_c)$ can be made. Fig 5.9 shows eqn. 5.3 fit to the 800 nm disk I_c and I_{cSub} transitions of disk sample 1. In this plot, the resistivity has been calculated using the resistance of the hybrid in the SNS state, $R = 1.945 \Omega$, and the cross sectional of the Al/Ni sandwich, $(80 \text{ nm} + 30 \text{ nm}) \times 300 \text{ nm}$, with the electron phonon constant a free fit parameter equal to $\Sigma = 3.7 \times 10^{10} \text{ W m}^{-3} \text{ K}^{-5}$, which is in good agreement with previous measurements of the electron-phonon coupling in aluminium [156]. While the fit is by no means perfect, this simple model replicates a basic line shape similar to that of the SNS to normal state transition. The deviation from the fit is almost certainly due to the simplicity of the model, which assumes that the heat dissipation is only into the local phonon bath. In reality, the heat will also dissipated into the aluminium nanowires contacting the normal Al/Ni sandwich. The range of suppression of superconductivity can also be understood in this model: if the temperature of the aluminium nanowire adjacent to the Al/Ni sandwich reaches T_c , the superconducting Al in contact with the sandwich will transition to the normal state due to the increased local temperature, this new section of normal Al will now start to dissipate the same power due to Joule heating, raising the local electron temperature to T_c . A run away avalanche effect would occur causing the Al nanowire to rapidly transition to the normal state, as the SN boundary propagates away from the Ni/Al sandwich. At temperatures lower than the triple point temperature, the SNS phase is not accessible, as the critical current of the hybrid junction is greater than that of the critical heating current, thus when the hybrid junction transitions into the normal state, the heating avalanche occurs simultaneously with this transition.

This model of suppression by heating could be easily tested experimentally. This was done by the fabrication of hybrid S-S/F-S junction devices that included the addition of large Ni heat sinks for cooling. The addition of the heat sinks creates a larger volume in which the power can dissipate. By increasing the volume of normal metal, the volume in which the

power is supplied and dissipates is no longer equal. Therefore, the volume term in eqn. 5.1 is no longer cancelled. Again, by a naive approximation that the heat is dissipated evenly throughout the entire Ni volume, inclusive of the heat sinks, the critical heating current should be increased by a factor $\sim \sqrt{\Omega_{sandwich}/\Omega_{heatsinks}}$. This is a simplistic model, as it does not take into account the rate of heat transfer across the Ni. Nevertheless, if the SNS to normal metal transition is due to heating, the inclusion of heat sinks should make a measurable difference to the critical current in the SNS phase.

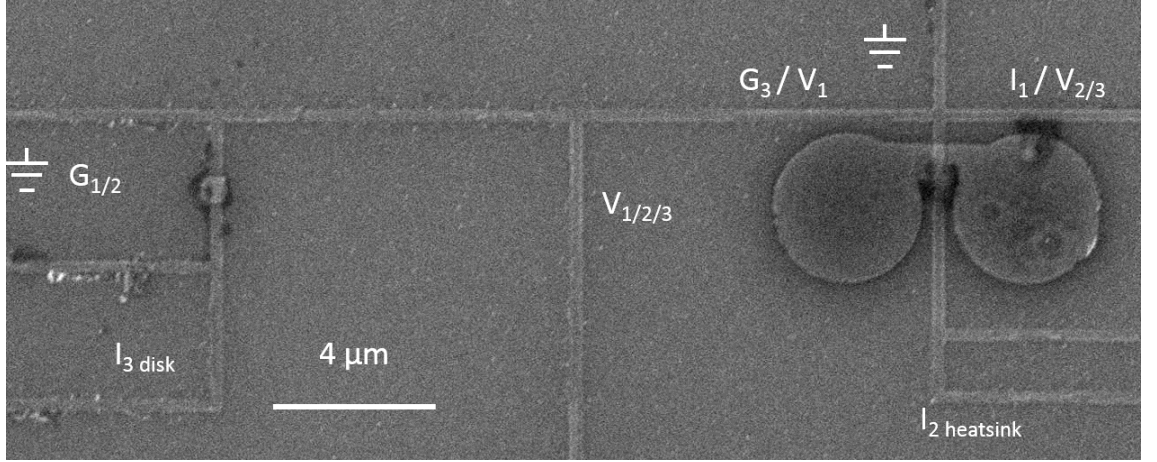


Figure 5.10: SEM image of the device used to test the heating theory, incorporating the circular heat sinks and the 800 nm disk hybrid junction. The electrical configurations, labelled on the image, are designed such that the voltage drop can be measured (V_1 , V_2 , V_3) across the same section of wire when current is supplied through either hybrid junction (I_2 , I_3 , G_2 , G_3), disk or heat sink, or bypassing the junctions (I_1 , G_1). Image was taken several weeks after fabrication and measurement, causing the noticeable degradation

A device was fabricated that reproduced the 800 nm hybrid junction and included a similar hybrid junction with circular heat sinks. An SEM image of the device is shown in fig. 5.10. It should be noted that, as the heat sink junction now uses a different geometry for the nickel element, the magnetization of the nickel beneath the aluminium will be different to that of a vortex state. The electrical measurement configuration has been annotated on the image, showing the variable position of current injection electrodes I_1 , I_2 or I_3 . The voltage was measured across the shared Al nanowire proceeding the hybrid junctions such that the long range influence of injection of current through the hybrid junctions ($I_{2,3}$)

could be investigated and compared to current injection bypassing the hybrid junction (I_1).

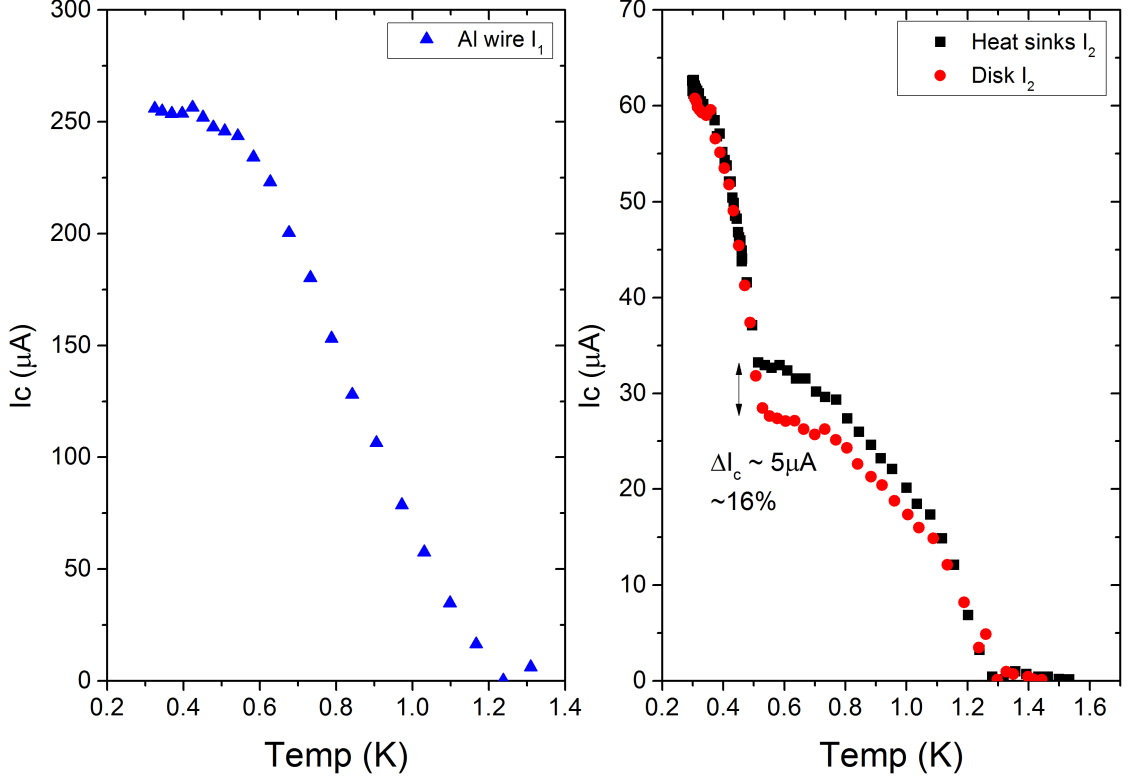


Figure 5.11: The temperature dependence of the adjacent Al nanowire in the heat sink sample for current injection bypassing the junctions, I_1 (left) and through both the disk and heat sink junctions, I_2 and I_3 (right). The I_c behaviour in the I_1 configuration is the same as previous samples. For current injection through hybrid junctions the expected junction behaviour is observed. The heat sink junction shows an increased critical current in this range, 5 μA larger than the disk junction at $T = 0.5$ K

The critical current of the aluminium nanowire in all current configurations is presented in fig 5.11, with the current bypassing the junction presented in the left image and the current through both hybrid junctions presented in the right image. When current is applied to the nanowire bypassing the nickel (fig 5.11 left), the critical current of the wire is as observed to be the same as that of a aluminium nanowire with no ferromagnetic influence. When current is passed through the hybrid junctions (fig 5.11 right), both

junctions show the same behaviour as the initial disk sample and the critical current behaviour at temperatures near T_c is the same for both the disk and heat sink junctions. However, as the temperature decreases the critical current behaviour of the junctions deviate and the heat sink junction shows an increased critical current of 5 μA more than the disk junction at $T = 0.5 \text{ K}$, i.e. just above the triple point temperature. At temperatures below the triple point, both junctions show the same critical current behaviour, due to the similarity in the properties of both hybrid junctions.

The increase in critical current at $T = 0.5 \text{ K}$ equates to an increase of approximately 16 %. By taking the resistance of the junction to be $\approx 2 \Omega$ as observed in earlier samples and calculating the input power of the normal section at I_c as $P_c = I_c^2 R$, the power dissipated at I_c by the normal section at 0.5 K is 1.5 nW and 2.1 nW for the disk and heat sink junctions respectively. This equates to a 40 % increase in power dissipation. This further supports the theory that the reduction in critical current of the nanowire is due to heat generation in the hybrid junction. The addition of the heat sinks increases the current required to input enough heat due to Joule losses into the superconducting nanowire to induce a transition into the normal state by introducing a new path into which the heat can dissipate. This effect is observed most at low temperatures as the electron temperature is more strongly decoupled from the phonon temperature at lower bath temperatures.

As a control experiment to test the influence of heating, SNS junctions were made using gold as the normal metal. Gold was chosen as its good electrical conductivity would translate into good thermal conductivity and the effect should be increased. Furthermore, if the long range suppression were still somehow related to injection of spin polarised quasi-particles, the effect should not be observed in the spin degenerate gold. Three junctions were fabricated, one with no heat sinks, one with heat sinks of the same dimensions as in the hybrid junction sample and one with large heat sinks with area ~ 9 times larger. Each junction had the same dimensions as an equivalent hybrid junction; width 300 nm, thickness 80 nm and length 800 nm. An SEM image of the control devices is presented in fig 5.12.

The differential resistance of each Al/Au SNS sample at $T = 0.3 \text{ K}$ is shown in fig. 5.13, in

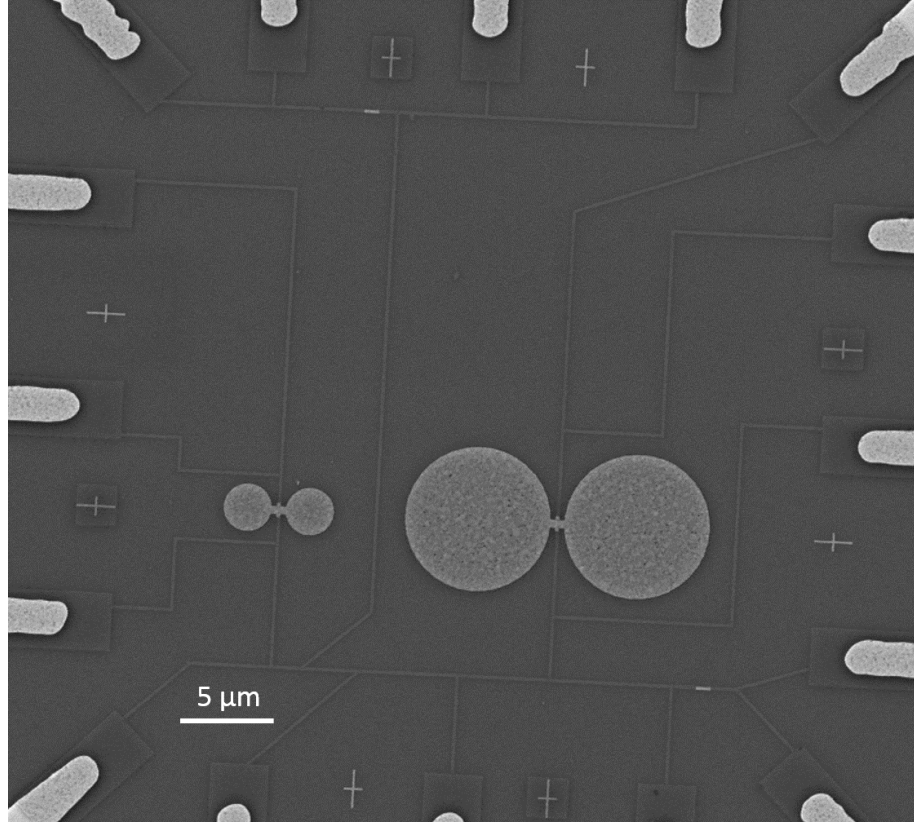


Figure 5.12: SEM image of the Au SNS junctions sample. Three junctions were fabricated, all sharing an adjacent nanowire such that measurements of the wire critical current can be made for current injection through each junction. The three SNS junctions differ in their heat sinks, shown: no heat sinks (bottom right), heat sinks the same size as the hybrid junction samples (left) and heat sinks with ~ 9 times larger area (right).

this figure each dV/dI has been scaled to units of R/R_n where R_n is the normal resistance of each SNS junction. The differential resistance is very similar to that of the hybrid S-S/F-S junctions, giving support to the principle that the hybrid junction can be treated similar to SNS junctions. Each sample shows slightly different sup-gap critical current from the other. Following the theory of Dubos et al. for long SNS junction [91], the junction critical current should be dependent on the normal resistance of the junction (eqn. 2.40), which differs between junctions and thus is likely the cause of their small difference. The critical current (SNS to normal state transition) of all three junctions is vastly different. The values of critical current are $I_c = 16.34, 37.43, 65.42 \mu\text{A}$ for no

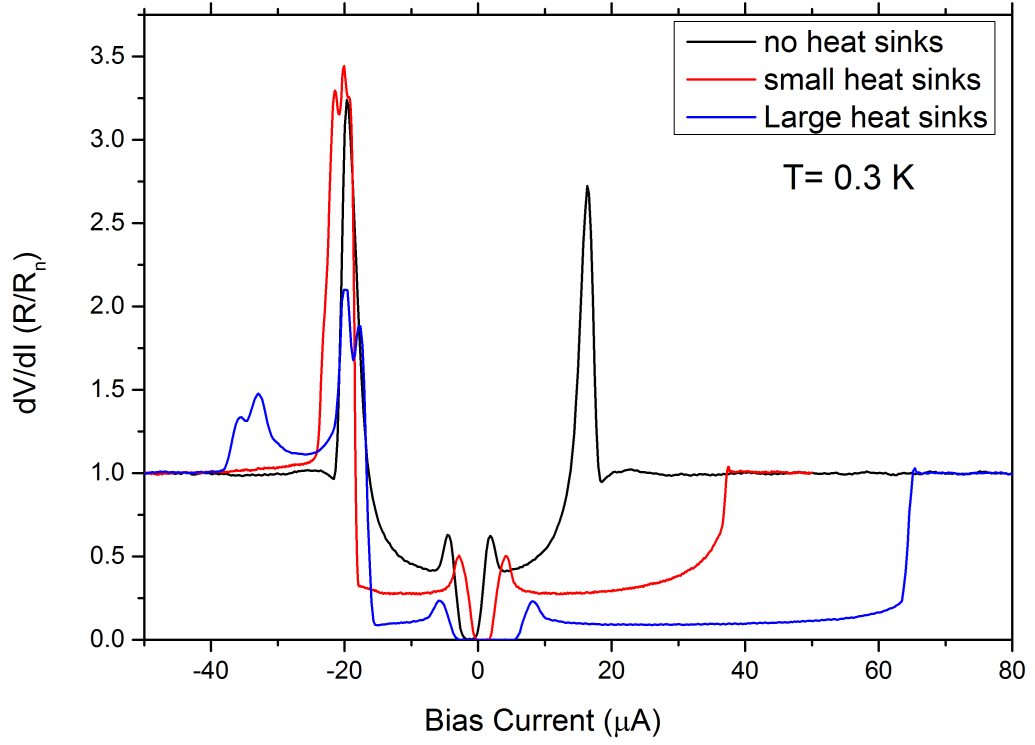


Figure 5.13: The differential resistance of each Au SNS junction at 0.3 K. The resistance of each junction has been normalised to the normal resistance R_n . Each junction shows similar differential resistance to the hybrid junctions, albeit with much reduced I_{cSub} . The Al critical current (SNS to normal state transition) increases rapidly with increasing heat sinks size, i.e. $I_c = 16.34, 37.43, 65.42 \mu\text{A}$ for no heat sinks, small heat sinks, and large heat sinks respectively.

heat sinks, small heat sinks and large heat sinks, respectively. By directly extracting the resistance of each junction in the SNS phase, the power dissipated at I_c for the three junctions at 0.3 K is $P_c = 2.1, 8.2, 61.0 \text{ nW}$ for no heat sinks, small heat sinks, and large heat sinks, respectively. The inclusion of the heat sinks to the gold SNS junction has therefore increased the required input heating power by 419 % and 2904 % for the small and large heat sinks, respectively. Coupled with the similarity in the I_{cSub} for each Au SNS junction, this strongly supports that the cause of the suppression of critical current in the aluminium nanowire is due to heating from the junctions in both the Au/Al SNS junctions and the hybrid Ni/Al junctions.

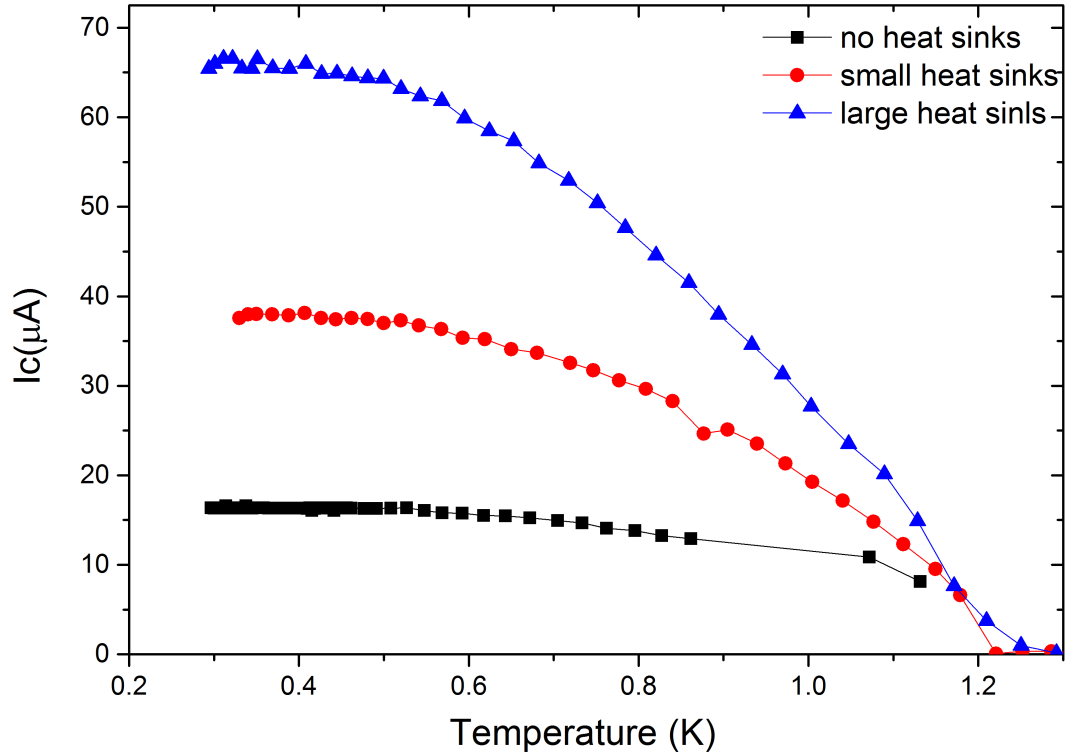


Figure 5.14: The temperature dependence of the critical current for the Al nanowire adjacent to the Al/Au SNS junctions when current is passed through the junctions. The behaviour is again similar to the hybrid Al/Ni junctions. Near T_c all junctions show similar temperature dependence which rapidly deviates as the temperature decreases.

The temperature dependence of the critical current of the adjacent aluminium nanowire for current injection through all three SNS junction is shown in fig 5.14. Similar to the hybrid junction samples, near T_c the critical current behaviour is similar between all three junctions. As the temperature is decreased, their behaviour deviates and the critical current is shown to increase with increasing heat sink size at all temperatures.

The increase of critical current in the SNS phase with the inclusion of the heat sinks strongly suggests that the long-range suppression of critical current in the aluminium nanowire is due to Joule heating in the hybrid junction. The exact mechanism of the suppression by heat will require detailed analysis of the heat flow in the device. This will be discussed in the context of existing theories in section 5.6.2.

5.4 Interferometer devices - Phase coherent oscillations

It was demonstrated by earlier work in the group [20], the hybrid junction is sensitive to phase difference across the junction, as all SNS or indeed generally Josephson junctions are. This was shown by using the junction in the SNS state as a weak link in a superconducting loop and modulating the phase across the weak link by increasing the flux through the loop. However, phase sensitivity was only demonstrated for the superconducting to SNS transition as the strength of the ferromagnetic suppression of superconductivity was strong enough to make the superconducting to normal state transition inaccessible at all available temperatures. If the hypothesis that the SNS to normal state transition and long range suppression of superconductivity are both due to heating within the junction is true, then the superconducting to normal state transition should also be phase sensitive whereas the SNS to normal transition should not be. Furthermore, the effect of changing magnetic history could be further investigated by measurements of the junction phase sensitivity before and after the out-of-plane field was applied.

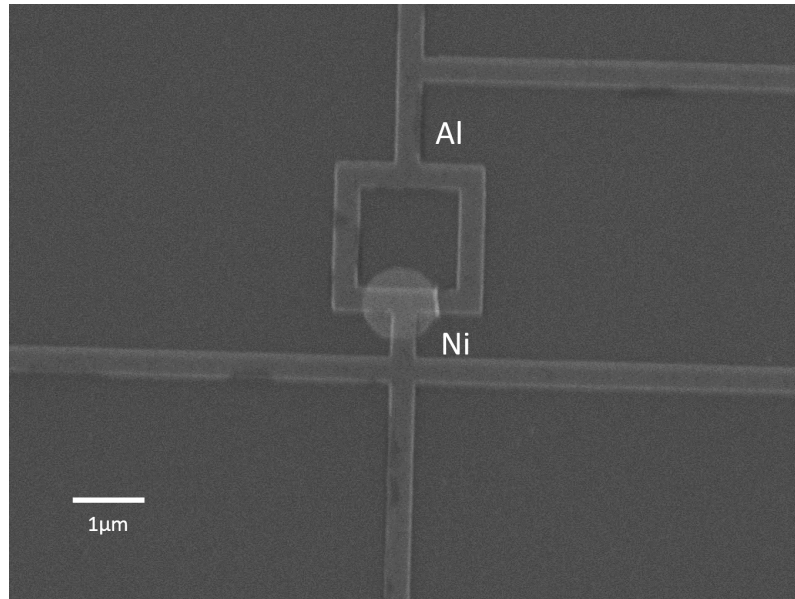


Figure 5.15: SEM image of hybrid junction loop interferometer made using a 1000 nm nickel disk.

Therefore superconducting loop interferometers were fabricated, using the standard fab-

rication procedure, with loop area $1\text{ }\mu\text{m} \times 1\text{ }\mu\text{m}$ and aluminium thickness 80 nm. Two junction sizes were fabricated, 800 and 1000 nm diameter disks with 25 nm nickel thickness, placing the disk dimensions firmly in the remnant vortex state phase. An SEM image of an interferometer device can be seen in fig. 5.15. Measurements were taken of the temperature and magnetic field dependence of the critical current both before and after the application of an 800 mT out-of-plane field, i.e. following the same methodology of previous experiments.

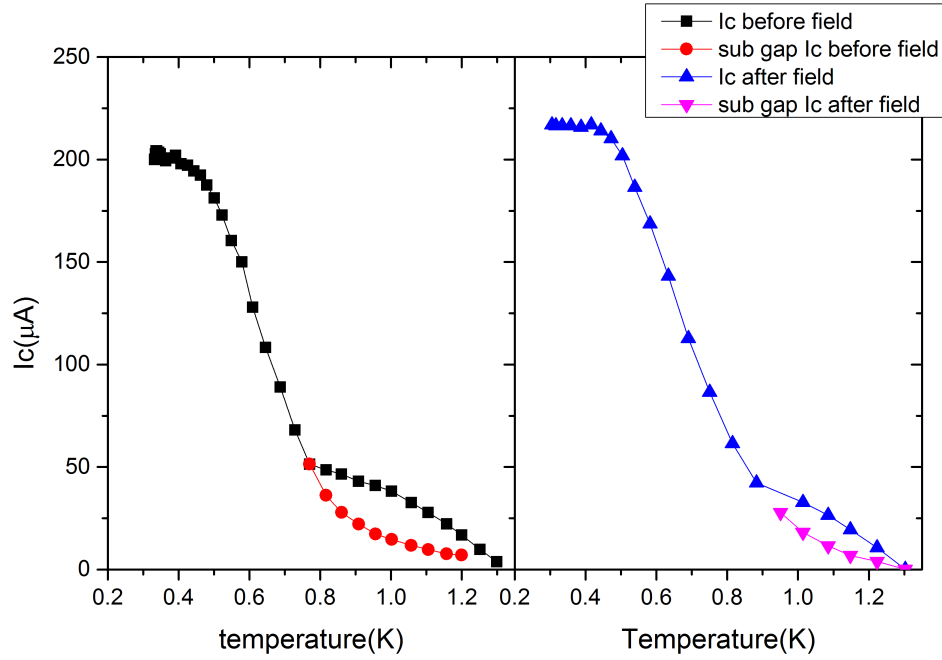


Figure 5.16: The I_c and I_{cSub} dependence on temperature for the 800 nm disk junction before (left) and after (right) the application of 800 mT out-of-plane magnetic field. The behaviour after the application of the field is the opposite to that of previous devices, with the critical current increasing after the field was applied and then removed.

The temperature dependence of the I_{cSub} and I_c for the 800 nm and 1000 nm interferometers before and after field (left and right images respectively) can be seen in figures 5.16 and 5.17 respectively. In the 800 nm disk sample the maximum I_c and triple point temperature change after the field is applied as $202 \rightarrow 216\text{ }\mu\text{A}$ and $0.77 \rightarrow 0.88\text{ K}$, showing an increase in the maximum critical current, opposite to that of the original hybrid

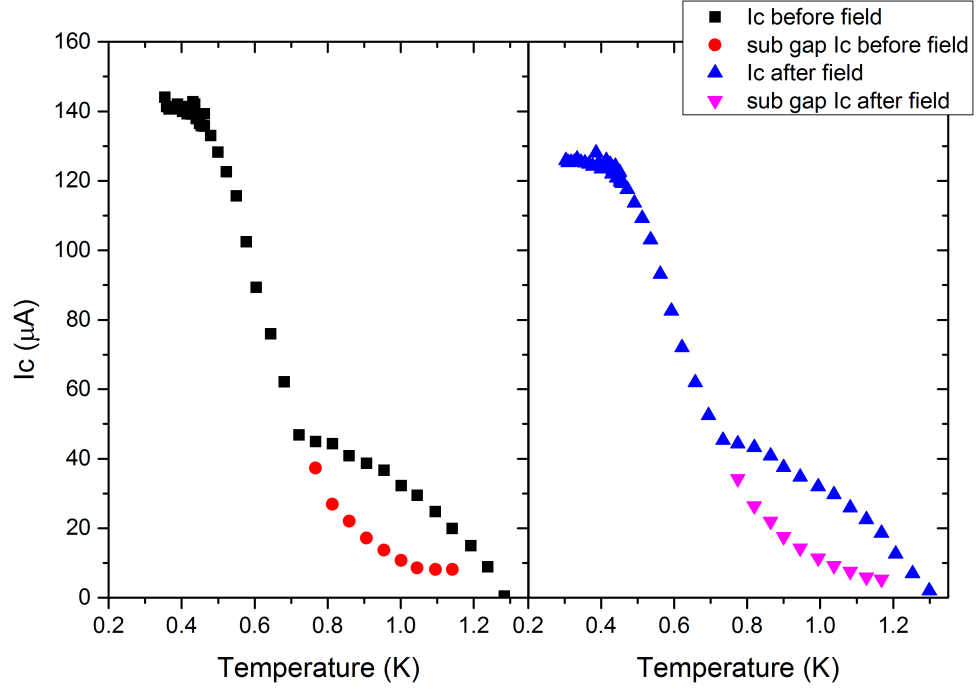


Figure 5.17: The I_c and I_{cSub} dependence on temperature for the 1000 nm disk junction before (left) and after (right) the application of 800 mT out-of-plane magnetic field. In this case the behaviour after the application of the field is the same as previous devices, with the critical current decreasing after the field was applied and then removed.

junction devices. The effect of the magnetic field in the 1000 nm disk interferometer replicates that of the original junction samples in that the maximum critical current and triple point temperature decrease, i.e. $140 \rightarrow 125 \mu\text{A}$ and $0.76 \rightarrow 0.83 \text{ K}$. The discrepancy in the behaviour before and after the field has been applied is strange, but can be explained by observing the dependence of I_c on phase difference across the junction, where the phase difference is controlled by applying a magnetic field perpendicular to the substrate. The magnetic field dependence of the 800 nm disk junction was first measured at 0.85 K such that the junction was in the SNS state, replicating earlier experiments [20]. The magnetic field dependence was measured by first measuring the dV/dI and then stepping the field a small amount ($\sim 80 \mu\text{T}$) and repeating the dV/dI measurement. This is repeated up to $\sim 6 \text{ mT}$. The magnetic field dependence before the large out-of-plane field was applied field, presented in fig. 5.18, shows a re-trapping current of $15 \mu\text{A}$ and oscillations

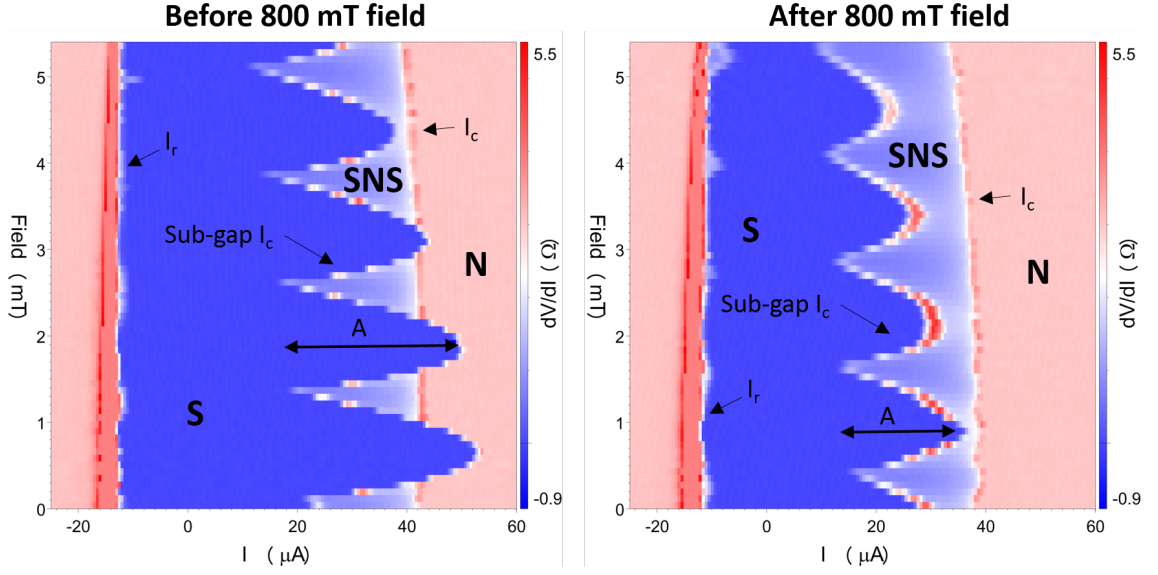


Figure 5.18: The dependence of the differential resistance of the 800 nm disk junction as a function of applied out-of-plane magnetic field before (left) and after (right) the application and removal of an 800 mT magnetic field at 0.85 K. The superconducting (S), normal (N) and SNS states are labelled, as well as the I_{cSub} and I_c transitions and the definition of the amplitude of oscillation A .

in the I_{cSub} with period of 1.22 mT. Taking the fabricated loop area of $1 \mu\text{m} \times 1 \mu\text{m}$ and the magnetic flux quantum, $\Phi_0 = 2.067 \times 10^{-15} \text{ Wb}$, the expected oscillation period is $\sim 2 \text{ mT}$, larger than the observed oscillation. Using the outside perimeter of the loop, $1.3 \mu\text{m} \times 1.3 \mu\text{m}$, to calculate the area gives an expected oscillation period of 1.22 mT, in strong agreement with the observed period of oscillation. The discrepancy in the oscillation period is most likely due to the focusing of flux through the loop due to the meissner effect, such that the actual flux through the loop is slightly greater than the simple approximation $\Phi = B \cdot A$ as the flux expelled by the wire is also passed through the loop area. This creates an effective loop area $1.3 \mu\text{m} \times 1.3 \mu\text{m}$.

In the SNS state, the oscillations in the I_{cSub} before the field was applied (fig. 5.18 left) are so large that the maximum of the oscillation is actually larger than the SNS to normal transition current. It can be seen that when the I_{cSub} becomes greater than the SNS to normal transition, the SNS phase is no longer observed and the entire nanowire transitions

into the normal state at once. This fully supports the long range suppression by heating hypothesis, as once the hybrid junction transitions into the normal state, with critical current larger than the critical heating current, the SNS state should not be observed as the Joule heating in the hybrid junction will immediately be enough input power to heat the entire nanowire. There is also a slow decrease in the I_{cSub} with increasing magnetic field, the oscillations are observed as a modulation to this more general decrease. The decrease in the I_{cSub} is most likely due to the quantization of flux within the normal metal section. This creates a similar phase dependant modulation of the critical current as that of the loop interferometer, with a period of oscillation dependent on the junction area, rather than loop area, that produces a Fraunhofer interference pattern. This decrease in I_c and its relation to the Fraunhofer interference will be discussed in detail towards the end of this section.

By comparison of the magnetic field dependence before (fig. 5.18 left) and after (fig. 5.18) the 800 mT field was applied, the increase in I_c observed in the temperature dependence (fig. 5.16) after the application of the field can be explained. After the field has been applied and removed, a shift in the phase of the oscillation in the I_{cSub} has occurred so that the maximum in I_c is now at 0 mT. In this case the shift approximately -0.66 mT or half a flux quantum. Therefore, when the temperature dependence after the field was applied was measured at 0 mT applied field, the junction was in this maximum state, in comparison to a minimum before the field was applied. However, the critical current is still suppressed after the application of field, with the maximum I_{cSub} changing from $52 \rightarrow 35$ μ A. The amplitude of the oscillation of the I_{cSub} also reduces, from 32 μ A before the field was applied to 16 μ A after the field was applied.

The magnetic field dependence of the 800 nm disk junction dV/dI at 0.3 K is shown in fig. 5.19. Similar to the temperature dependence of I_c below the triple point temperature there is no observed SNS state. The re-trapping current is observed at -15 μ A and the superconducting to normal transition I_c is seen to oscillate with the expected period of 1.22 mT. The observation of the oscillation of this transition further supports the long range suppression by heating hypothesis. At 0.3 K the critical current of the junction is

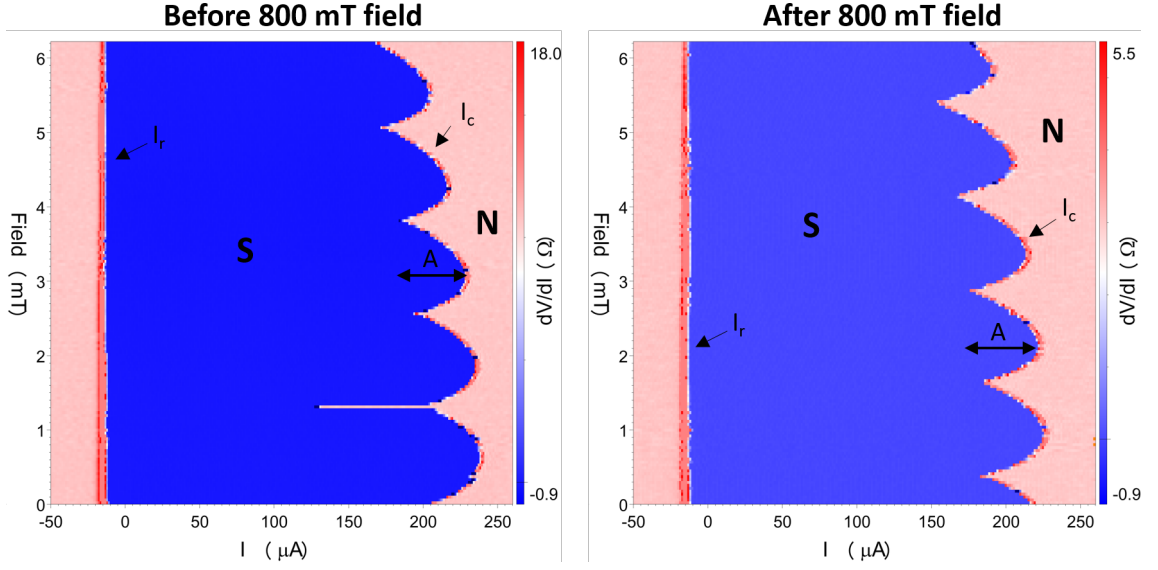


Figure 5.19: The dependence of the differential resistance of the 800 nm disk junction as a function of applied out-of-plane magnetic field before (left) and after(right) the application and removal of an 800 mT magnetic field at 0.3 K. The superconducting (S) and normal (N) states are labelled, as well as the I_c transition and the definition of the amplitude of oscillation A .

always larger than the critical heating current, in the same way as was observed at 0.85 K when the I_{cSub} oscillation became larger than the critical heating current, thus when the junction transitions into the normal state the entire nanowire does also. Therefore, as the junction I_c oscillates with increasing phase difference across the junction, this translates into an apparent phase dependent I_c of the entire nanowire, including the sections of wire without the inverse proximity influence of the ferromagnet. Similar to the measurement at 0.85 K, there is a shift in the phase of the I_c oscillation before and after the field at 0.3 K of 0.27 mT. Like the measurement at 0.85 K the phase shift has masked the reduction of the critical current, as the maximum critical current decreases from 239 μ A before the field to 226 μ A after the field. Whereas, the difference in oscillation amplitude is smaller than measured at 0.85 K, with the amplitude changing from 41 μ A before the field was applied to 40 μ A after the field was applied.

The behaviour at 0.3 K is replicated in the 1000 nm disk interferometer shown in fig. 5.20. Once more, the re-trapping current is observed at -15μ A and the critical current of the

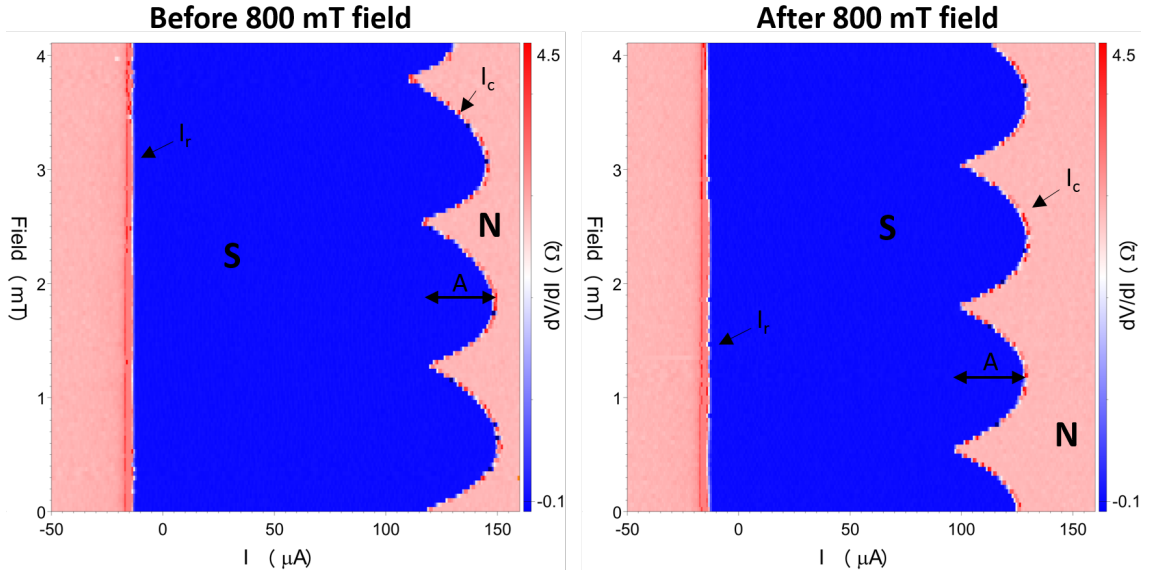


Figure 5.20: The dependence of the differential resistance of the 1000 nm disk junction as a function of applied out-of-plane magnetic field before (left) and after(right) the application and removal of an 800 mT magnetic field at 0.3 K. The superconducting (S) and normal (N) states are labelled, as well as the I_c transition and the definition of the amplitude of oscillation A .

entire nanowire is shown to oscillate with period 1.22 mT. In the same way as the 800 nm disk interferometer the maximum I_c drops from 150 μA before the 800 mT field to 132 μA after the field. Similarly the change in the oscillation amplitude is minimal, changing from 33 μA before the field to 30 μA after the field. In the same way as the 800 nm junction, the phase of the oscillation is observed to shift after the application of the field with a value of 0.5 mT.

The magnetic field dependence of the 1000 nm disk junction at 0.85 K before the field was applied is presented in fig. 5.21. The magnetic field dependence at this temperature could not be measured after the field was applied due to a technical problems with the cryostat. The dV/dI behaviour is again similar to the 800 nm disk junction, showing the expected oscillation in the I_{cSub} with period 1.22 mT, maximum I_{cSub} equal to 26 μA , oscillation amplitude 16 μA , and no oscillation in the SNS to normal state transition.

Both the 800 and 1000 nm diameter disk junctions show that the superconducting to

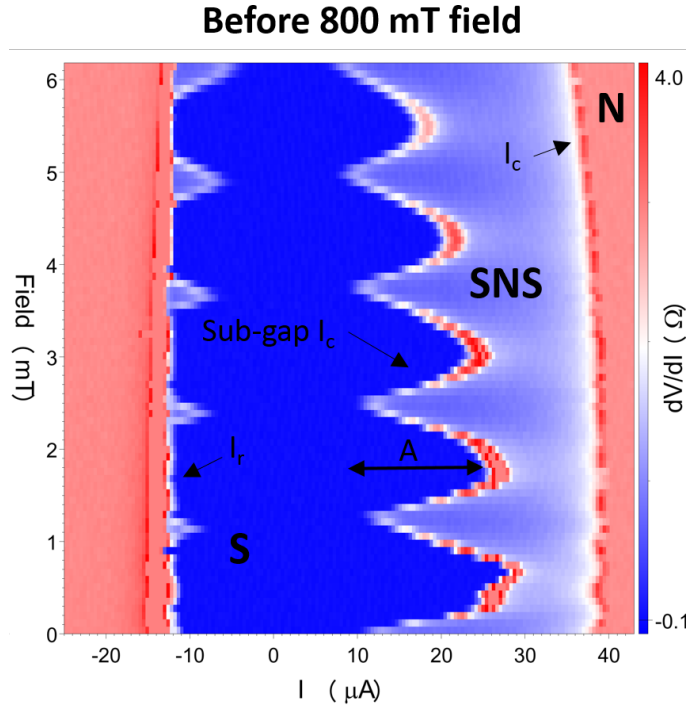


Figure 5.21: The dependence of the differential resistance of the 1000 nm disk junction as a function of applied out-of-plane magnetic field before the application and removal of an 800 mT magnetic field at 0.85 K. The superconducting (S), normal (N) and SNS states are labelled, as well as the I_{cSub} and I_c transitions and the definition of the amplitude of oscillation A .

SNS state transition critical current oscillates as a function of phase difference across the junction, whereas the SNS to normal state transition critical current does not. This strongly supports the hypothesis that the transitions of the hybrid junction consist of two independent effects; the critical current of the hybrid junction itself and the suppression of the superconductivity in the nano-wire due to heat generated by Joule losses in the hybrid junction in the normal state.

The observed phase shift of the oscillation before and after the application of the out-of-plane field is interesting and provides some insight into what has changed in the junction before and after the out of plane field has been applied.

Table 5.1 shows the maximum I_c , oscillation amplitude, and phase shift before and after the field for both devices at 0.3 and 0.85 K, as well as the percentage difference of the

		Max I_c (μA)		ΔMax I_c (%)	I_c Amp. (μA)		ΔI_c Amp. (%)	Phase shift (mT)
		before field	after field		before field	after field		
800 nm	0.85 K	52	35	-32.7	32	16	-50.0	-0.66
	0.3 K	239	226	-5.4	41	40	-2.4	0.27
1000 nm	0.85 K	26	N/A	N/A	16	N/A	N/A	N/A
	0.3 K	150	132	-12.0	33	30	-9.1	0.5

Table 5.1: Table of the I_c properties of 800 and 1000 nm disk interferometer devices before and after the 800 mT field was applied.

change. The phase change observed in both samples is different. The phase change of the oscillation may have been due to trapped external flux from the solenoid, if this were the case the phase change of both junctions would be expected to be the same. Therefore, the phase change could be due to the change in stray field from the ferromagnet upon changing magnetic state after the field was applied. This would explain the difference in the magnitude of the phase shift, as the stray field from each individual disk will be different between samples. This adds support to the hypothesis that an inhomogeneous magnetic state, such as the vortex state, will create a weaker proximity suppression of superconductivity than a single domain like state. This is because, the vortex state will have minimal stray field due to its flux closure domain structure. Whereas, a quasi single domain state that may occur after the application of the out of plane field will have a larger stray field that threads the superconducting loop, inducing the phase change. Conversely however, a magnetic state with increased out of plane components, i.e. a canted vortex state, would also increase the stray flux threading the loop. Therefore, the observed phase shift does suggest that the magnetic state of the disks has changed after the application of the field, it does not allow any conclusions to be made as to what the magnetic state is after the field.

In comparison to the 800 nm junction at 0.85 K, which has a change in maximum I_c of $-32.7 \mu\text{A}$, both the 800 and 1000 nm devices exhibit much less of a decrease in I_c at 0.3 K after the field was applied. Similarly, the change in the oscillation amplitude in the 800 nm junction at 0.85 K is an order of magnitude greater than both junctions at

0.3 K. This suggests that the change in the proximity suppression after the field was applied is most prominent at higher temperatures, closer to T_c . This can be further investigated by considering the general decrease in the maximum I_c of each oscillation. It was discussed earlier that this is most likely the characteristic Fraunhofer interference pattern modulation of critical current in SNS junctions due to the applied perpendicular magnetic field. Such Fraunhofer interference was observed in similar proximity junctions [21, 23, 22]. The Fraunhofer behaviour of the I_c of SNS junctions in a perpendicular field can be described as [157, 23]:

$$I_c = I_c(0) \frac{\Phi_0}{\pi \Phi} \left| \sin\left(\frac{\pi \Phi}{\Phi_0}\right) \right| \quad (5.4)$$

$$\Phi = B \cdot S = BwL \quad (5.5)$$

where $I_c(0)$ is the critical current at 0 applied field, Φ_0 is the magnetic flux quantum, B is the applied field, w is the width of the junction, and L is the length of the junction. Therefore, by fitting the peak I_c of the oscillations in figs. 5.18-5.21 with free fit parameters $I_c(0)$ and L (as $w = 300$ nm, the width of the wire) the size of the junctions at both 0.3 and 0.85 K can be calculated. This will provide an estimate to how much of the the aluminium wire above the ferromagnet is in the normal state due to the proximity suppression.

The fits of equation 5.5 to the peaks of the I_c oscillations of the 800 nm disk junction before (left) and after (right) the field was applied are shown in fig. 5.22. The oscillating I_c (I_{cSub} when at 0.85 K) for each measurement is shown as open symbols whereas the fits to eqn. 5.5 are shown as solid lines with the fit parameters annotated beside each line. All the fits are in very good agreement with the decay in the peak I_c with increasing field. It can be seen that, at 0.3 K the extracted junction length is 373 and 375 nm, before and after the field has been applied, respectively. This is much less than the fabricated junction size of 800 nm. Conversely, at 0.85 K the extracted junction length is 670 and 790 nm before and after the field, respectively. This is much closer to, but still less than, the fabricated junction length. Furthermore, after the field has been applied the junction

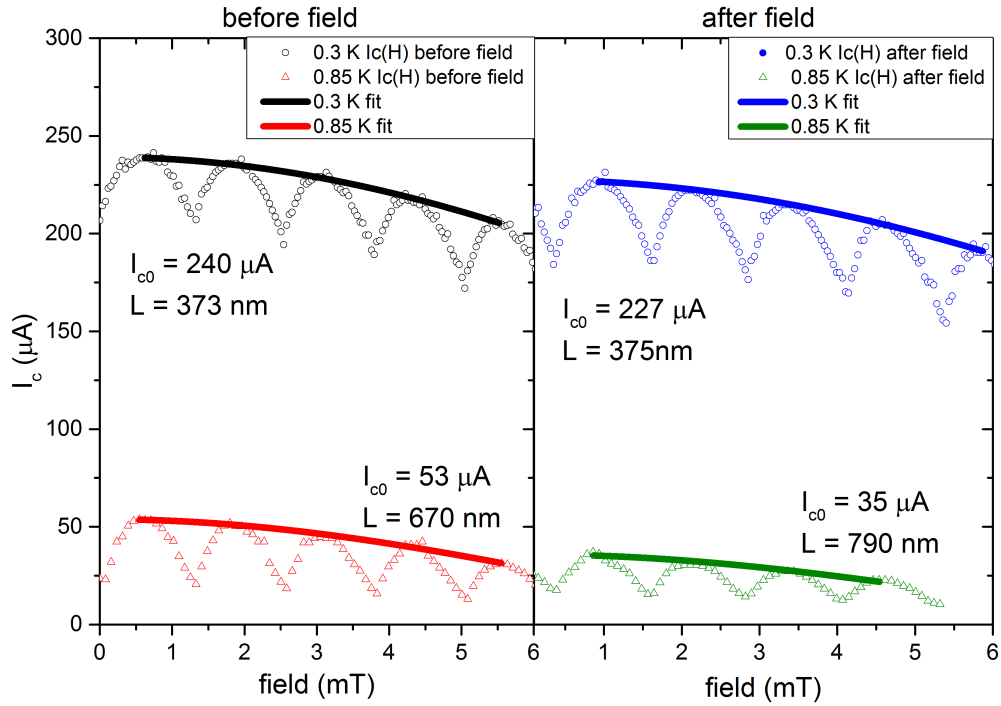


Figure 5.22: Fitting of the peak I_c of the 800 nm disk junction before (left) and after (right) the 800 mT field to the Fraunhofer interference model at 0.3 and 0.85 K. The fits indicate the junction size is proportional to temperature and increases after the application of the magnetic field.

size has increased by only 3 nm at 0.3 K but by 120 nm at 0.85 K. The difference in the extracted junction size at 0.3 and 0.85 K suggests that the junction size is not constant, but proportional to temperature. Furthermore, the increase in junction size after the field has been applied indicates that the application and removal of the 800 mT out of plane field manifests as an increase in junction size.

The same behaviour can be observed in the 1000 nm disk junction, where the fits to eqn. 5.5 before and after field (left and right, respectively) are shown in fig. 5.23. For the 1000 nm junction, the fits before field are again in good agreement with the decay in the peak I_c . At 0.3 K the junction length is 343 nm where as at 0.85 K it is 628 nm. After the field has been applied the fit is only in good agreement with the last four peaks in the oscillation. This is because the first two oscillations show an increase in the peak I_c . This is most likely because of the extra local flux from the change in disk magnetic state,

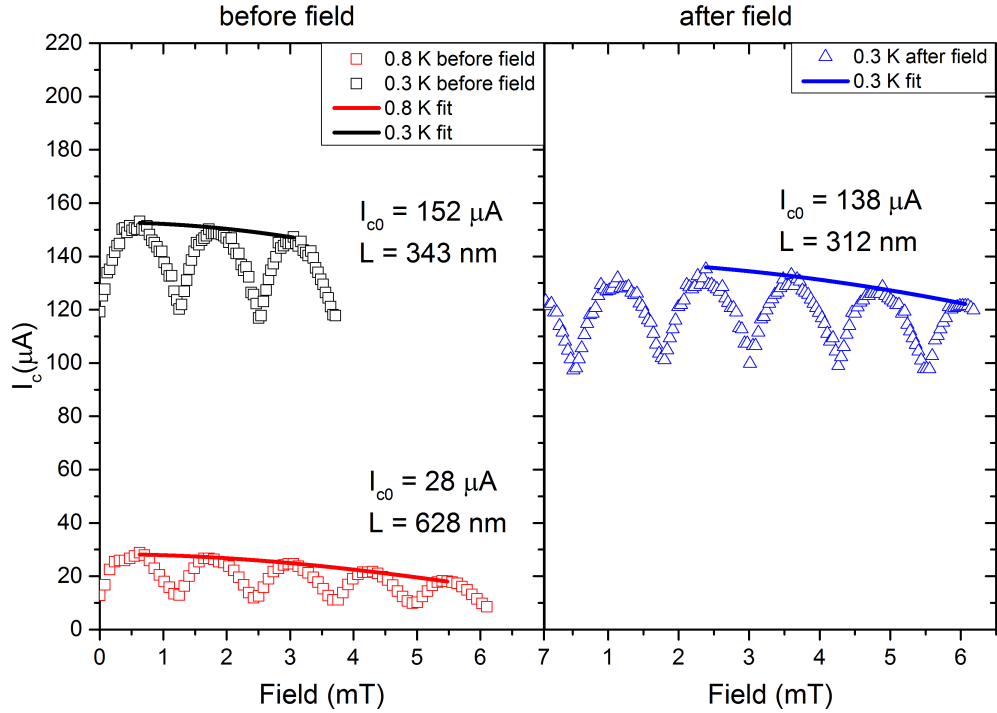


Figure 5.23: Fitting of the peak I_c in the 1000 nm disk junction before (left) and after (right) the 800 mT field to the Fraunhofer interference model at 0.3 and 0.85 K. The fits indicate the junction size is proportional to temperature and increases after the application of the magnetic field.

shifting the position of zero field to ~ 2.5 mT applied field. This supports the earlier theory that the phase shift in the I_c oscillations is due to a change in stray field from the disks.

While the field range is not large enough to conclusively say that the suppression of the I_{cSub} peak is due to Fraunhofer interference, the strong agreement of these fits strongly suggest that this is the case. The fits also indicate that the junction does not have a fixed length, but instead the junction length is proportional to the temperature. The cause and consequences of this temperature dependant junction size will be discussed in detail in section 5.6.1 when comparing the proximity junctions to existing theories of SNS junctions.

5.5 Hybrid junctions using L-shape domain wall traps

The experiments using hybrid junctions made with nickel disks presented so far have indicated that changing the magnetization of the disk alters the critical current of the hybrid junction. However, the method used to change the magnetization is somewhat ambiguous. The efforts to characterise the remnant magnetic states in the disks means that it can be said with confidence that the disks are in a vortex state before the out-of-plane field was applied. However, after the field has been applied the exact magnetic state is not known, instead it is inferred from the suppression of the critical current of the junction that the magnetic state is a more collinear state than the original vortex. This assumption seems valid when considering the earlier results of Kinsey and Rusanov [16, 17] in larger SF bilayer films, in which the critical current was observed to increase at the coercive field of the magnetic film, as well as the theoretical prediction of Champel and Escrig [18] that an inhomogeneous magnetic state in proximity to a superconductor will suppress the superconductivity to a lesser extent than a single domain state. However, the suppression could equally be because the magnetization after the field simply had a larger out-of-plane component and the superconductor was suppressed from the additional stray field.

To account for this ambiguity, the design of the junction was modified in such a way that the magnetic state could be fully controlled. The immediate solution would be to incorporate the measurement of the disk magnetic state via the anisotropic magnetoresistance effect into the hybrid junction measurement. This would require the addition of two gold electrical contacts to the edge of the disk perpendicular to the aluminium nanowire. The fabrication of such devices was attempted, however because the area of the disk not already covered by the aluminium nanowire was very small, it became increasingly difficult to position the additional gold contacts on the disk with enough gold-nickel overlap without also shorting the gold contacts with the aluminium.

Therefore, new hybrid junctions were created in which the ferromagnetic disks were replaced with the L-shape domain wall traps discussed in section 4.3. This section will

present the critical current measurements of first the nickel and then the permalloy L-shape hybrid junctions. Comparison of the critical current measurements is made to the magnetoresistance and MFM images presented in section 4.3.

5.5.1 Nickel L-shape hybrid junction

An AFM image of the nickel L-shape, previously presented in section 5.5, is shown in fig. 5.24 with annotations of the contacts used to measure the L-shape magnetoresistance and the differential resistance of the hybrid junction. The temperature dependence of the differential resistance of the L-shape hybrid junction before the application of any magnetic fields is presented in fig. 5.25. The differential resistance exhibits the same behaviour as the nickel disk junctions; i.e. it is hysteric and the SNS phase is observed at temperatures greater than the triple point temperature 0.74 K with a maximum critical current at 0.4 K of 174 μ A.

To see the effect of changing the magnetization in the corner of the device on the critical current, the field was set to -100 mT and then stepped forwards in 5 mT steps up to 100 mT, measuring the differential resistance at each field point. This was then repeated stepping the field in the opposite direction. The critical current dependence on applied magnetic field is shown in fig 5.26, bottom image.

Black points signify the critical current for the field stepping negative to positive, whereas red points represent the critical current for the opposite step direction. The I_c and I_{cSub} are differentiated by circular symbols for I_c and triangular symbols for the I_{cSub} . The measurement of the anisotropic magnetoresistance measured at room temperature, previously presented in fig. 4.24, is shown in fig 5.26 top image with the applied field aligned with the critical current data.

At -100 mT applied field, the junction is in the SNS phase due to the suppression of superconductivity by applied magnetic field. When the magnetic field is lowered, the triple point field is observed at -60 mT where the I_{cSub} transition becomes larger than the critical heating current. I_c then continues to increase reaching a value of 146 μ A near zero field. Once the magnetic field switches direction however, I_c continues to increase

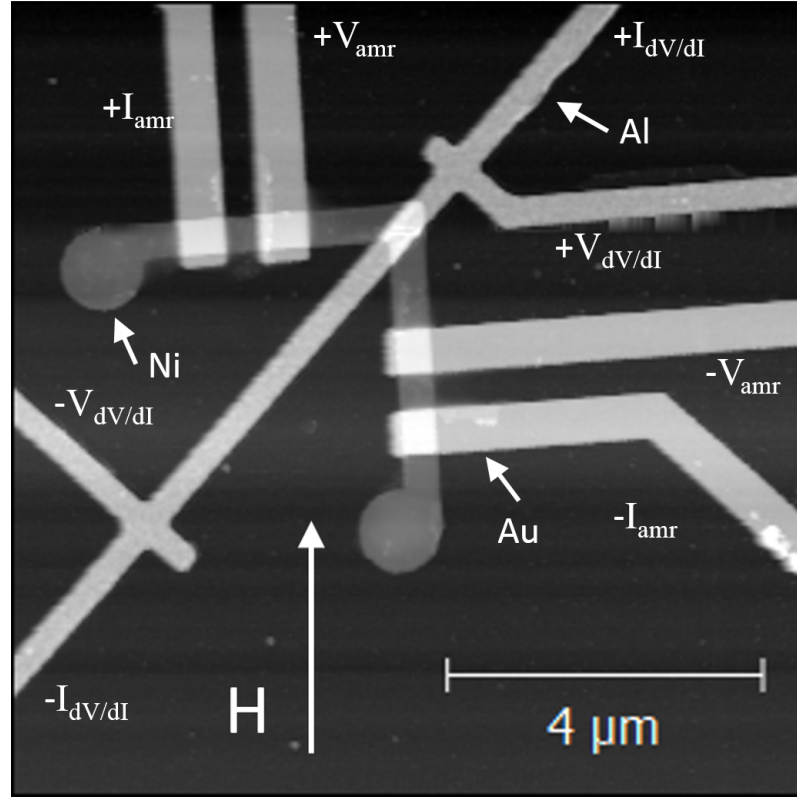


Figure 5.24: Grey scale AFM image of the nickel L-shape hybrid device first presented in section 5.5. The sample is mounted in the cryostat with the substrate in-plane with the field, such that the magnetic field is applied perpendicular with one arm as indicated by the white arrow. The contacts used to measure the magnetoresistance of the L-shape are shown as well as those used to measure the differential resistance of the hybrid junction.

with a maximum of $168 \mu\text{A}$ at 15 mT . Then I_c rapidly drops to $105 \mu\text{A}$ at 25 mT and smoothly decreases. As the field increases, the triple point is observed at 60 mT and the junction re-enters the SNS phase up to 100 mT . As the field is then reduced from 100 mT , the behaviour in the SNS phase is identical to the negative to positive field sweep. Below the triple point, however, I_c is reduced from the up sweep value and again the maximum I_c is observed past zero field at -10 mT . The triple point field is then observed at -60 mT once more and the SNS phase is observed. This behaviour was observed to be reproducible. Comparison of the I_c behaviour with the magnetization dynamics of the nickel L-shape (fig. 4.25) and the magnetoresistance (4.24 top image), shows that the inhomogeneous

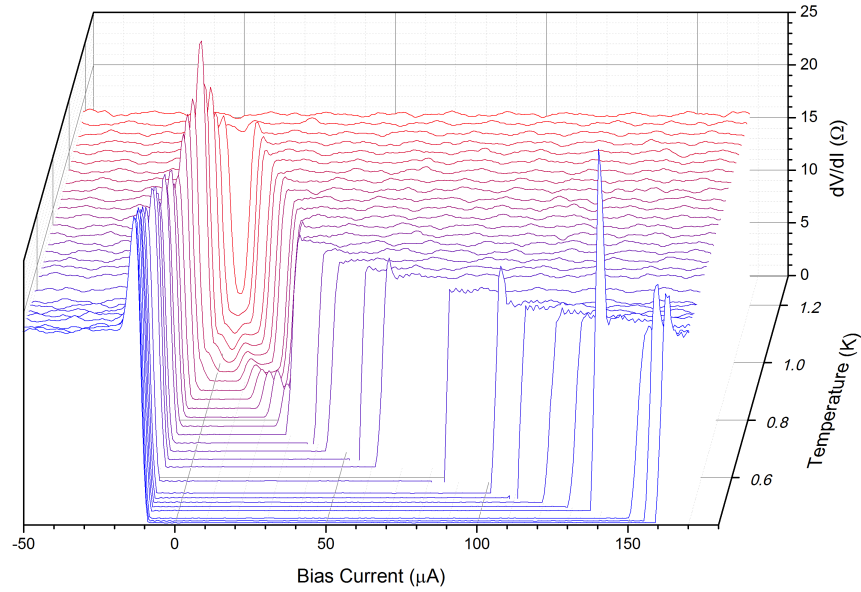


Figure 5.25: The differential resistance of the nickel L-shape hybrid junction. The SNS phase is observed above the triple point temperature 0.74 K and the maximum critical current at 0.4 K is 174 μ A.

magnetization of the multi-domain structure observed at the corner of the L-shape, which nucleates at ± 10 mT coincides with the hysteric maximum in I_c observed in the hybrid junction. This supports the hypothesis that an inhomogeneous magnetization state creates a reduction in the ferromagnetic suppression of the superconductivity in the aluminium above the ferromagnet. However, the complicated multi-domain state that was shown to exist in the L-shape corner makes it difficult to conclusively say that the hysteric nature in I_c is directly linked to the hysteresis of the L-shape.

5.5.2 Permalloy L-shape hybrid junction

To improve upon the L-shape hybrid junction design further, the permalloy L-shape was fabricated. The magnetization dynamics of the permalloy L-shape were presented in section 4.3.2. An SEM image of the permalloy L-shape hybrid junction is shown in fig. 5.27

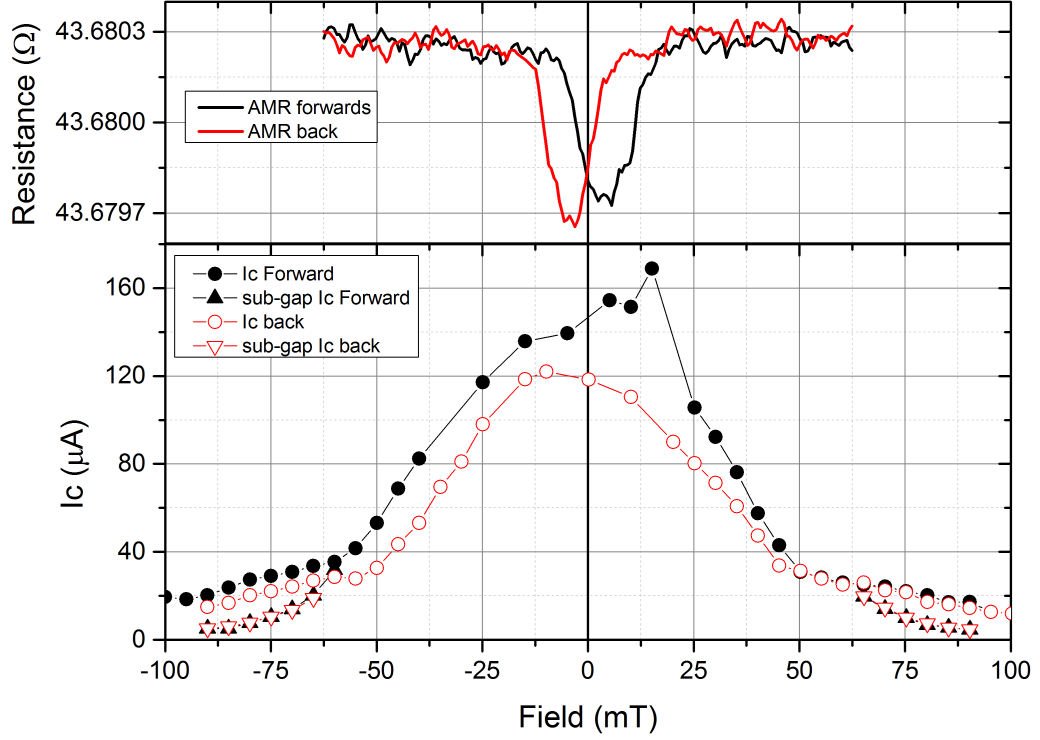


Figure 5.26: Top image: the room temperature magnetoresistance of the nickel L-shape, as was previously presented in fig. 4.24. No sudden drops in resistance characteristic of domain wall nucleation are observed, instead a hysteric smooth drop in resistance is measured. Bottom: The magnetic field dependence of I_c and the I_{cSub} of the L-shape hybrid junction at 0.3 K. Red points denote the I_c when the field is stepped from negative to positive and black points in the opposite direction. I_c is shown by circular symbols while the I_{cSub} is shown by triangular symbols. A hysteric maximum in I_c is seen at 15 mT and -10 mT

with annotations of the contacts used to measure both the L-shape magnetoresistance and the differential resistance of the hybrid junction. Because of the reduced crystalline anisotropy of permalloy relative to nickel, the Py L-shape was shown to successfully nucleate a domain wall, first smoothly when sweeping the field from negative to positive fields and then annihilating at ~ 10 mT. When sweeping from positive to negative fields, it was observed that no domain wall existed at remnance until the field was swept to ~ 7 mT and the domain wall was nucleated in the corner.

The temperature dependence of the differential resistance as well as I_c and I_{cSub} of the

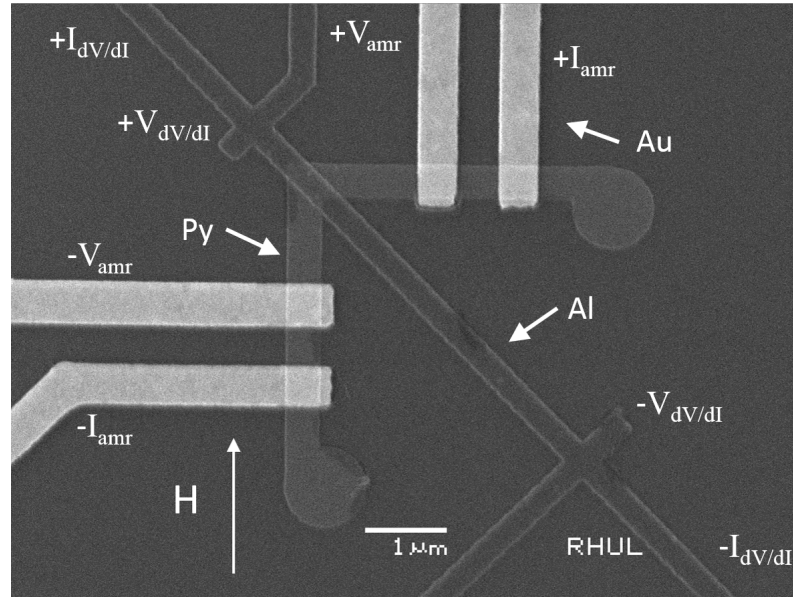


Figure 5.27: SEM image of the Permalloy L-shape hybrid device. The aluminium nanowire lies diagonally across the corner of the L-shape, while the gold contacts on the L-shape arms allow for a 4-point resistance measurement of the L-shape magnetoresistance. The contacts used to measure the magnetoresistance are annotated. The sample is mounted in the cryostat with the substrate in-plane with the field, such that the magnetic field is applied perpendicular with one arm as indicated by the white arrow.

permalloy L-shape hybrid junction are shown in figs. 5.28 and 5.29, respectively. The permalloy L-shape junction behaves in the same way as the nickel junctions, exhibiting the SNS phase at temperatures above the triple point temperature of 0.47 K. The SNS to normal transition in the Py L-shape junction shows some noise in comparison to the junctions made with nickel as well as a more linear dependence on temperature. As this transition has been shown to be due to heating in the junction, the difference in the temperature dependence is possibly due to the differing thermal conductivity and temperature distribution when using permalloy instead of nickel. The maximum critical current at 0.37 K is observed to be $68 \mu\text{A}$.

The magnetic field dependence of I_c and I_{cSub} in the hybrid permalloy L-shape junction at 0.3 K is shown in fig. 5.30 bottom image with the accompanying magnetoresistance of the L-shape shown again in fig. 5.30 top image. The black symbols show the magnetic field

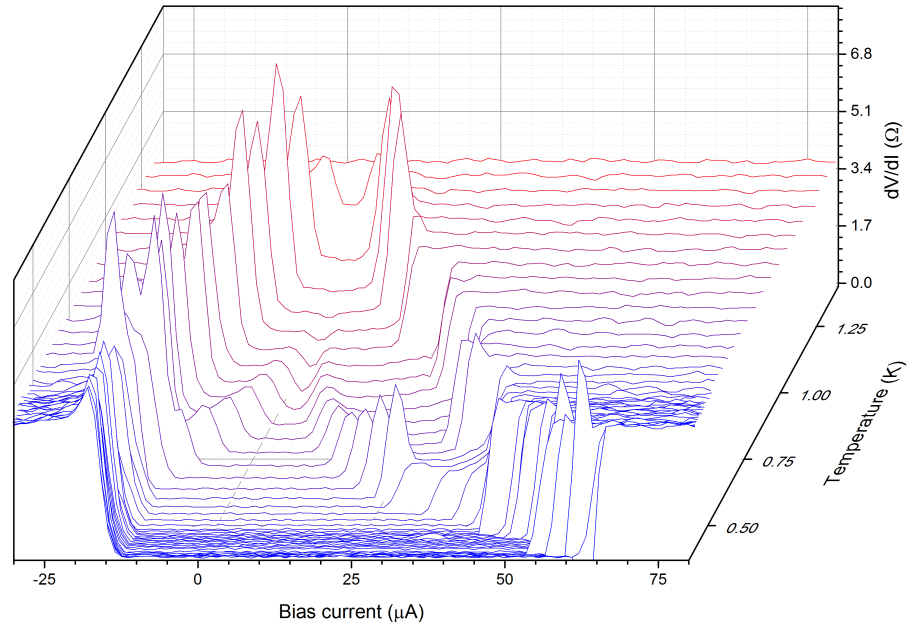


Figure 5.28: The temperature dependence of the differential resistance of the permalloy L-shape hybrid junction. In the permalloy L-shape junction the SNS phase is observed as expected, with the same I_{cSub} behaviour as in the nickel disk junctions

sweep from negative to positive while the red symbols show the field sweep in the opposite direction. The I_c is shown by circular symbols and the I_{cSub} is shown by triangular symbols. At -100 mT the junction is in the SNS phase (black symbols). The I_{cSub} increases smoothly with decreasing field and the triple point field is observed to be -34 mT. I_c then increases with a maximum at zero field of $293 \mu\text{A}$, i.e. much greater than the maximum I_c measured before the field was applied. As the field is increased into positive values, the I_c slowly decreases until 15 mT when the I_c drops and the junction rapidly returns into the SNS phase. The I_{cSub} then shows a peak of $15 \mu\text{A}$ at 45 mT and decreases with increasing field up to 100 mT. As the field is decreased from 100 mT (red symbols), the junction remains in the SNS phase again showing a peak in the I_{cSub} now at 30 mT. As the field is decreased towards zero, the junction remains in the SNS phase until the field changes direction and a sudden increase in I_c is observed at -15 mT. The critical

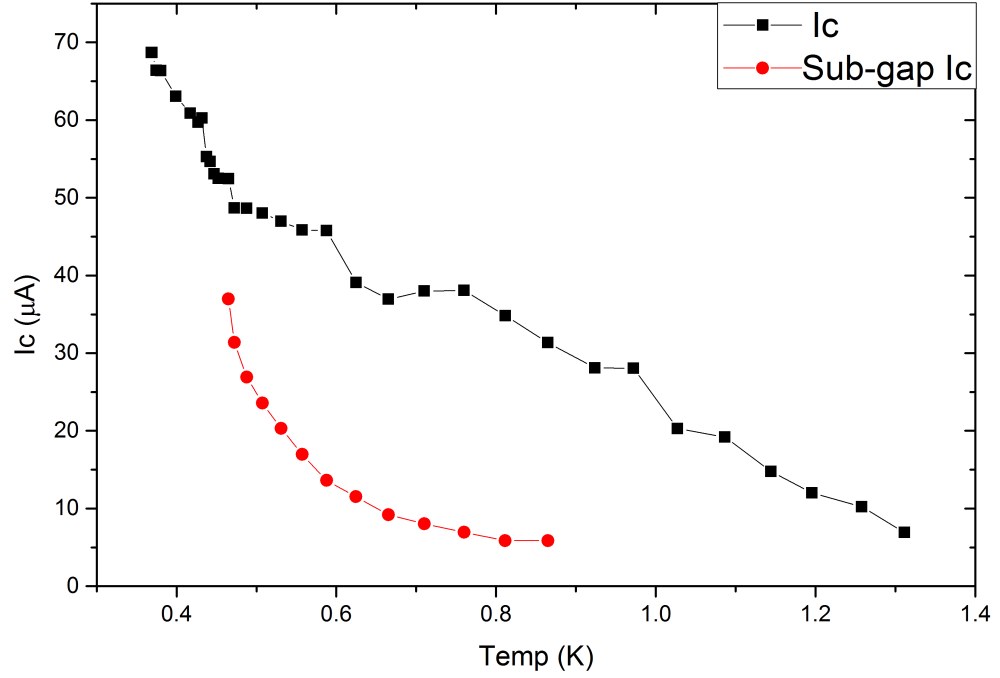


Figure 5.29: The temperature dependence of the critical current of the L-shape hybrid junction before any fields were applied. The I_{cSub} and I_c below the triple point temperature both behave identically to the nickel hybrid junctions, with triple point temperature 0.47 K and maximum critical current 68 μA . The SNS to N transition shows some noise in comparison to the nickel disk junctions and exhibits a more linear dependence on temperature.

current then slowly decreases with the same behaviour as the negative to positive field sweep.

The asymmetry of the magnetic field dependence of I_c mimics that of the asymmetry of the L-shape magnetoresistance. Furthermore, the sudden increase in I_c at -12 mT aligns with the nucleation of the domain wall in the corner observed in the magnetoresistance. Furthermore, by comparison of the *in situ* MFM images presented in section 4.3.2 and accounting for the increase in coercivity due to reduced temperature, for all fields in which the I_c is observed to be large, a domain wall was observed in the corner of the L-shape device. This strongly suggests that the increase in I_c is due to the nucleation of the domain wall and that the local inhomogeneous magnetization does indeed change the

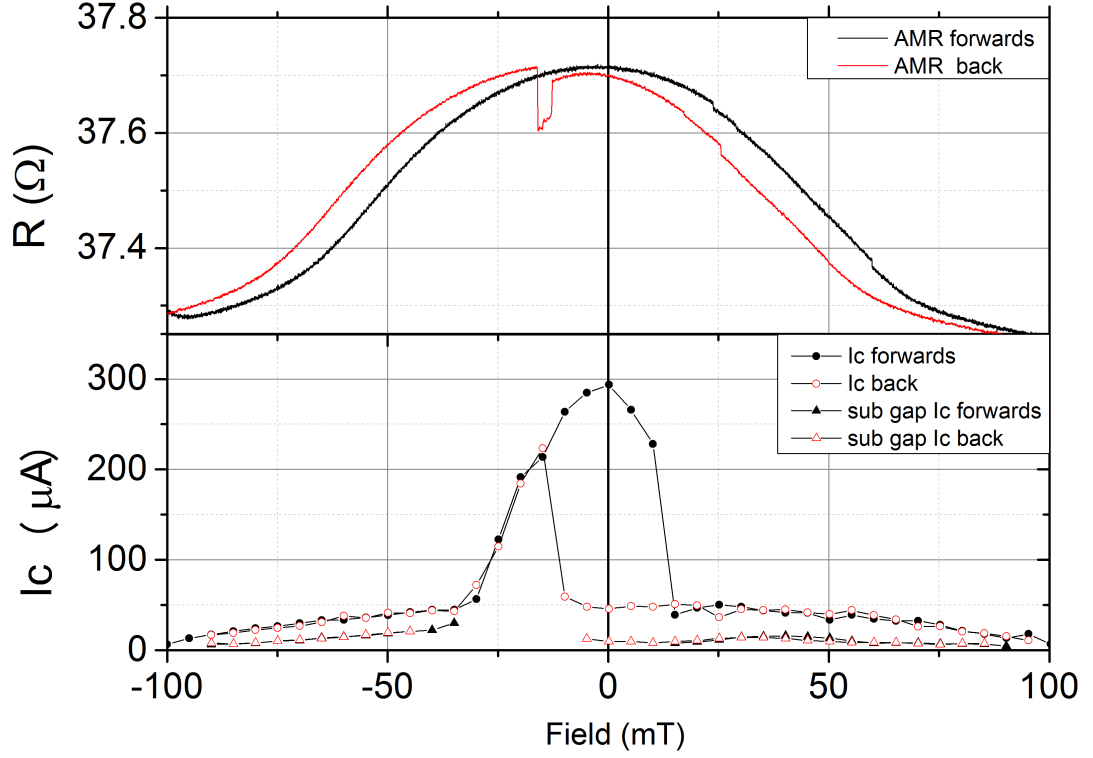


Figure 5.30: Top image: The anisotropic magnetoresistance of the permalloy L-shape at 0.3 K the black curve shows the resistance when the field is swept from negative to positive and the red curve shows the sweep in the opposite direction. No domain wall is observed to nucleate in the negative to positive field sweep. However, in the positive to negative field sweep a domain wall is observed to nucleate at -12 mT and the annihilate at -16 mT. Bottom image: The magnetic field dependence of I_c and I_{cSub} of the permalloy L-shape hybrid junction at 0.3 K. The black symbols show the magnetic field sweep from negative to positive while the red points show the field sweep in the opposite direction. The I_c is shown by circular symbols and the I_{cSub} is shown by triangular symbols. In the forward field sweep I_c increases towards zero field then decreases at 15 mT. In the backwards field sweep I_c does not increase until a sudden jump at -10 mT that aligns with the nucleation of the domain wall in the L-shape domain wall trap.

ferromagnetic suppression of the superconductivity in the aluminium nanowire overlying the permalloy. However, the peaks in the I_{cSub} when in the SNS phase, i.e. at fields greater than ± 30 mT, do not align with any features in the magnetoresistance, as such these features cannot be described in the context of magnetization changes.

The influence of the domain wall upon the critical current of the junction was tested further

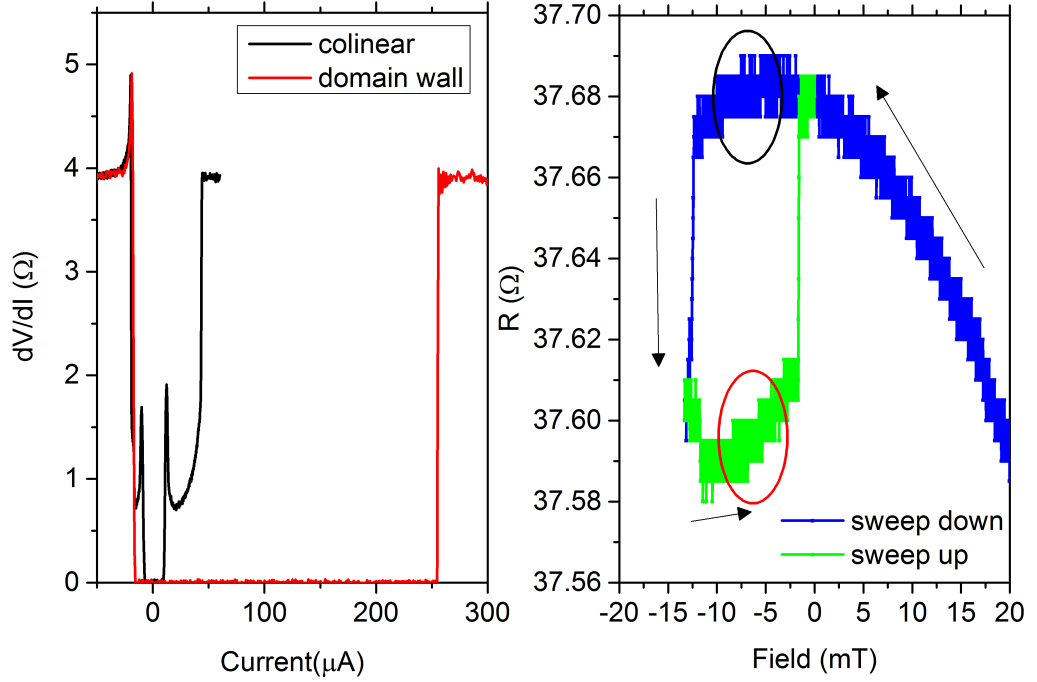


Figure 5.31: Left: the magnetoresistance of the L-shape device during the domain wall trapping procedure. The blue curve shows the resistance when sweeping the field from 100 mT to -13 mT where a domain wall is nucleated and the resistance drops. The green curve then shows the resistance of the L-shape device as the field is swept from -13 mT up to 0 mT where the domain wall is annihilated. The black and red circles indicate where the dV/dI was measured in the collinear and domain wall states respectively. Right: The differential resistance of the hybrid junction measured in the single domain magnetisation (black curve) and domain wall (red curve) states. In the domain wall state I_c is hugely increased in comparison to the single domain magnetisation state.

by measuring the differential resistance of the junction at the same field when the L-shape device was in the single domain or domain wall state. This was done by setting the field to 100 mT, sweeping the field down to -7 mT and measuring the differential resistance at this applied field. The field was then swept to -13 mT to nucleate the domain wall and then swept back to -7 mT to replicate the parameters of the first dV/dI measurement. The differential measurement was then performed again with the domain wall present at the junction. The differential resistance in the single domain and domain wall states are shown in fig. 5.31 left image and the magnetoresistance of the L-shape device for the applied

minor loop is shown in fig. 5.31 right image. At -7 mT in the domain wall magnetization state, the junction is in the SNS phase, with I_{cSub} of $12\text{ }\mu\text{A}$ and I_c of $44\text{ }\mu\text{A}$. When the field is increased to -13 mT, the magnetoresistance of the L-shape device decreases as before and the domain wall is nucleated. As the field is reduced back to -7 mT, the resistance remains approximately the same indicating that the domain wall remains in the corner of the L-shape. The differential resistance measured in this state shows the hybrid junction to be in the fully superconducting state with $I_c = 256\text{ }\mu\text{A}$.

In summary, it can be seen that both the magnetization dynamics and I_c of the hybrid junction are correlated. When sweeping from negative to positive fields a domain wall smoothly nucleates beneath the aluminium and the I_c also smoothly increases. As the field is increased the domain wall is annihilated at small positive field, which aligns with a rapid decrease in I_c . The domain wall remains absent from the corner as the field is swept to positive saturation and back to zero while the I_c remains small in the collinear magnetization state. The domain wall then nucleates at small negative field and the I_c rapidly increases. As the domain wall is then smoothly annihilated the I_c also smoothly decreases. As the magnetization dynamics were observed to behave in this manner at room temperature, via *in situ* MFM, and at low temperatures below the aluminium T_c , via magnetoresistance, it can be concluded that the domain state of the ferromagnet is independent of the superconductor and that the magnetic state controls the superconducting properties in such a way that the inhomogeneous magnetization of the domain wall suppresses the adjacent superconductivity less than the collinear magnetization state as hypothesised.

5.6 Comparison of experimental results to existing theoretical models

The results presented on the hybrid planar junction could be explained as following: suppression of superconductivity in the aluminium nanowire by ferromagnetic proximity forces the aluminium above the ferromagnetic element to transition into the normal state at a much reduced critical current. The hybrid junction can be considered to be an SNS like junction, exhibiting an SNS phase at temperatures close to T_c , where the aluminium above the ferromagnet is normal, while the adjacent aluminium nanowire is in the superconducting state. As the current through the junction is increased in the SNS phase, the input heating power due to Joule losses in the normal metal eventually heats the superconducting aluminium nanowire adjacent to the normal metal, such that the nanowire transitions into the normal state due to the increased electron temperature. The critical current of the junction is dependent on the magnetic state of the ferromagnet in the hybrid junction: inhomogeneous, rotating magnetisations induced an increased critical current compared to collinear single domain like states.

This section will discuss the fitting of the hybrid junction to existing theoretical models for both the critical current in SNS junction and for the suppression of superconductivity due to heating, with the aim to explain the junction critical current as well as the critical heat current behaviour. The theory of critical current in long SNS junctions [91] will be used to fit to the critical current behaviour of the junction, discussing the applicability of this theory to the hybrid junction and the results of fitting. Fitting of traditional hot spot heating models to the SNS to normal state critical heating transition will be discussed, showing that these hot spot models underestimate the observed transition current. The reason for this underestimation is discussed and the full problem of heating in the junction is presented.

5.6.1 Theory of critical current in long SNS junctions

The results presented have indicated that the hybrid junction behaves similar to that of an SNS junction, due to the suppression of superconductivity by ferromagnetic proximity of the nickel and permalloy upon the aluminium nanowire forcing the portion of the nanowire above the nickel to transition into the normal state. Therefore, the supercurrent through the junction should be some combination of the intrinsic super current of the aluminium suppressed by ferromagnetic proximity and that of the supercurrent carried by phase coherent electrons that have been reflected from both SN boundaries by the Andreev reflection mechanism. This was observed in the oscillations of I_c in the hybrid junction interferometers, the oscillations are caused by the phase of Andreev reflected electrons at each boundary of the junction switching between constructive and destructive interference. The critical current of long SNS junctions has been theoretically investigated previously by Dubos and Zaiken [91], in which the critical current dependence on temperature for long SNS junctions was solved. The limit of long SNS junctions refers to the case in which the Thouless energy, E_{th} , being the energy at which Andreev reflected electrons will remain phase correlated across the length of the junction, is much smaller than the superconducting gap of the S metal that forms the SNS junction. If the junction lengths, L , are taken to be 800 and 1000 nm as designed, with diffusion constant $D \approx 0.01 \text{ m}^2 \text{ s}^{-1}$ [20], and the superconducting gap in aluminium to be $\approx 220 \text{ } \mu\text{eV}$ [15], the ratio of the superconducting gap to the Thouless energy ($E_{th} = \hbar D/L^2$) is $\Delta/E_{th} \approx 21, 33$ for the 800 and 1000 nm junctions respectively. Therefore as this ratio is large, and the hybrid junctions can be considered in the long junction limit.

The theory of I_c in long SNS junctions can be considered in two limits, the low and high temperature limits. The low temperature limit will be discussed first. In the low temperature limit, I_c is found to converge to a constant value as the temperature approaches zero:

$$I_c(T = 0) = \frac{10.82 E_{th}}{e R_N} \quad (5.6)$$

where E_{th} is the Thouless energy, e the electron charge, and R_N the normal state resistance. Furthermore, the behaviour in the low temperature limit can be approximated by the expression:

$$I_c(T) = \frac{E_{th}}{eR_N} a(1 - be^{-aE_{th}/3.2k_BT}) \quad (5.7)$$

where $a = 10.82$ and $b = 1.3$ are numerically calculated coefficients. Therefore by extracting the critical current measured at low temperature it is possible to extract the Thouless energy and subsequently effective junction length of the hybrid junction at low temperature using eqn. 5.6 and compare this to the numerical fit of the behaviour of I_c at low temperature using eqn. 5.7. This fitting procedure has been performed on the data presented in fig. 5.5, the 800 nm hybrid nickel disk junction from disk sample 2 before and after the application of the 800 mT out-of-plane field.

The fits of eqn. 5.7 to I_c before and after the field have been applied can be seen in fig. 5.32. These fits are shown by the blue and green lines, respectively. At higher temperatures where the fit is not valid, approximately $T > 0.3T_c$ in this case, the solid lines are replaced with dashed lines. The annotations in fig. 5.32 show the values of E_{th} extracted using eqn. 5.6, where $R_n = 2.3 \Omega$ is taken from the dV/dI data in the SNS phase. Before the field is applied $E_{th} \approx 35 \mu\text{eV}$, indicating an effective junction length of 428 nm. After the field is applied $E_{th} \approx 25 \mu\text{eV}$, and the effective junction length is 514 nm. Both before and after the field has been applied the effective junction length is much smaller than the fabricated junction length of 800 nm. After the field has been applied, the reduction in I_c translates into an increase in the effective junction size. This is in agreement with the junction lengths extracted from fitting the decay of the maximum I_c of the loop interferometers presented in section 5.4, in which the extracted junction lengths ($L \sim 370 \text{ nm}$) at 0.3 K, were also found to be much less than the diameter of the disk.

This can be explained by considering the way in which the SNS junction is created. In traditional SNS junctions, the length of the junction is an unchanging quantity defined by the physical size of the normal metal section and restrained by the interface between

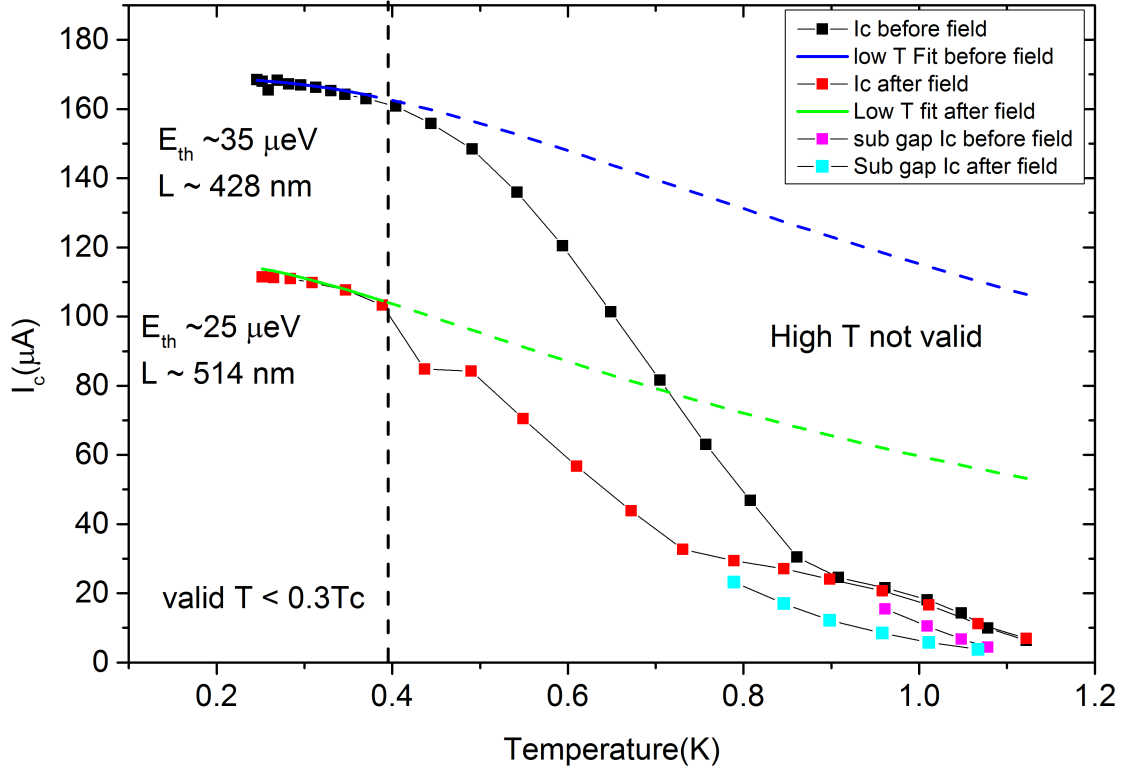


Figure 5.32: Fitting to the data presented in fig. 5.5 for the low temperature limit of the long SNS junction theory defined by eqns. 5.6 and 5.7. The blue solid line is the fit before the 800 mT out-of-plane field was applied and the green line after the field. The dashed sections show where the low temperature numerical approximation (eqn. 5.7) is no longer valid. The low temperature limit calculates the junction length to be 428 nm and 515 nm before and after the field was applied respectively.

the normal and superconducting metals. In the hybrid junctions presented here, the SN boundary is not restrained to any interface between two metals, but rather it is only the boundary between the two phases of the electron gas, i.e. the superconducting condensate and the normal electron gas. The position of this boundary is controlled only by the suppression of superconductivity by proximity to the ferromagnetic element beneath. An equilibrium position of the boundary must form, in which the suppressive effect of the ferromagnet is in equilibrium with the formation of the superconducting condensate in the aluminium directly above the ferromagnet as well as the leakage of Cooper pairs from the non-suppressed condensate in the adjacent nanowire, which will support the

superconductivity in the nanowire above the ferromagnet against the suppression due to proximity to the ferromagnet. This is a complex problem to solve, and would require solution of the condensate wave function across the entire nanowire, including the nickel disk. One can consider however, that the equilibrium position of the boundary should be highly dependent on the properties of the superconducting condensate, the most obvious of which is the temperature dependence. At low temperatures the condensate is at its strongest as almost all the electrons in the metal form the condensate. At temperatures near T_c more electrons have enough energy to break free of the condensate and exist as quasi-particles, the condensate is now weaker because of this. Therefore, at higher temperatures the condensate is weaker in the aluminium the proximity leakage of the condensate from the adjacent nanowire into the junction will combat the suppressive effect of the ferromagnetic proximity less. This causes a shift in the equilibrium of the SN boundary changes, making the junction larger. This was observed when extracting the junction lengths from fitting the decay of the maximum I_c of the loop interferometers presented in section 5.4, in which the extracted junction lengths at 0.85 K were 670 and 790 nm before and after the field was applied, respectively, much larger than at 0.3 K. This is also true when the domain state of the ferromagnet changes, a change in the domain state changes the strength of the ferromagnetic suppression effect and thus the position of the SN boundary. This is what is observed after the out of plane magnetic field has been applied and the vortex state in the disk is inferred to be in a more collinear magnetic state as well as the change in I_c observed when a domain wall was seen to nucleate in the permalloy L-shape hybrid junction.

This hypothesis of a moving SN boundary can be tested further by fitting the I_c behaviour at temperatures near T_c in the limit of a very long junction $\Delta/E_{th} \rightarrow \infty$. In this limit, the critical current of the long SNS junction is now described by the expression

$$I_c(T) \propto T^{3/2} e^{\sqrt{(2\pi k_B T)/E_{th}}} \quad (5.8)$$

By fitting this to the I_{cSub} at temperatures above the triple point and to I_c at temper-

atures below the triple point with a cut off at ~ 0.75 K to account for the limit of high temperature, the Thouless energy can be extracted in this limit. Fig. 5.33 shows these fits before and after the field has been applied (blue and green curves respectively), with annotations for the extracted Thouless energy and effective junction size, L . Before the field is applied the Thouless energy is $1.8 \mu\text{eV}$ and effective junction length $1.914 \mu\text{m}$. After the field has been applied the Thouless energy is $1.6 \mu\text{eV}$ and effective junction length $2.009 \mu\text{m}$. As expected, the junction size is much larger than in the low temperature limit, approximately 4 times larger, supporting the principle of a mobile SN boundary.

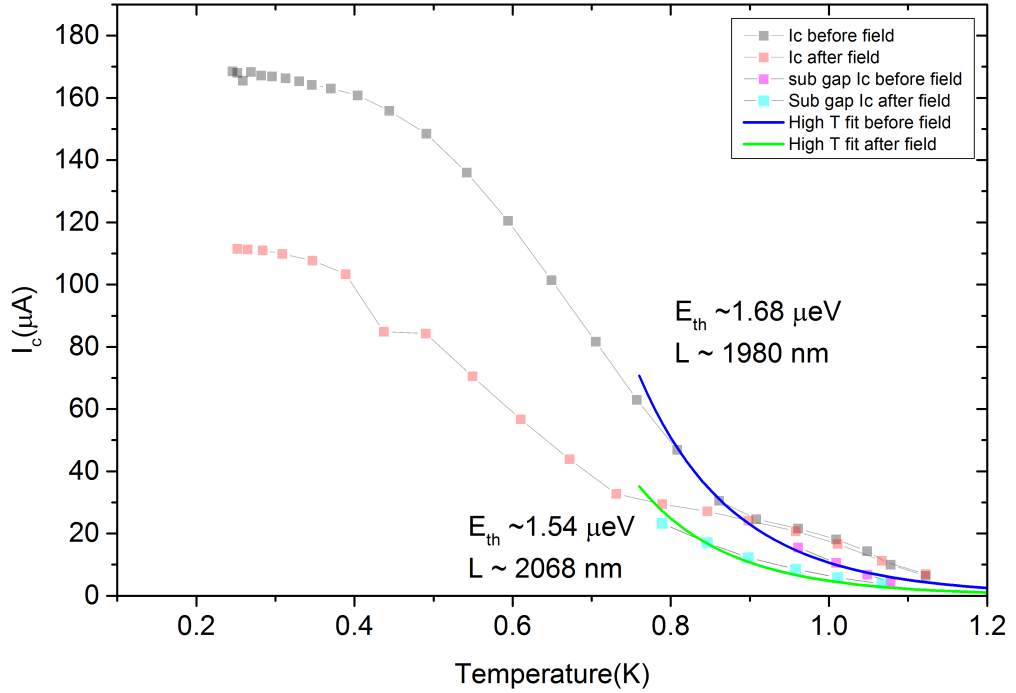


Figure 5.33: Fitting to the data presented in fig. 5.5 for the high temperature limit of the long SNS junction theory defined by eqn. 5.8. The blue solid line is the fit before and the green line the fit after the 800 mT out-of-plane field was applied. In this high temperature limit the junction length is calculated to be 1914 nm and 2009 nm before and after the field was applied respectively.

However, the fits in this limit require an exceptionally large coefficient of proportionality equal to 387.81 and disagree by a factor 2-3 times than the junction lengths extracted in the loop interferometers at 0.85 K. The full equation for the and very long junction limit

near T_c is

$$I_c(T) = \frac{32}{3 + 2\sqrt{2}} \frac{E_{th}}{eRn} \left(\frac{L}{L_T} \right)^3 e^{-L/L_t} \quad (5.9)$$

where the equation is now in terms of, L , the junction length and, $L_T = \sqrt{\hbar D / 2\pi k_B T}$, the thermal coherence length. Using the exacted Thouless energy and junction length from the fits in fig. 5.33, the coefficient of proportionality for junctions of that size would be 0.0224 and 0.0231 before and after the field respectively. These values are much smaller than those used to fit the high temperature limit of I_c in fig. 5.33. This is likely due to the aforementioned change of the boundary position with changing temperature. The boundary will be most unstable near T_c . Over the temperature range in which I_c has been fit, the boundary has move appreciably and the junction size has changed rapidly, moving the junction out of the very long junction limit. The large constant of proportionality in the fit accounts for the effective averaging of Thouless energy in this range. However, in previous work in the group [20] it was shown that the the high temperature limit could be used to fit to the behaviour of the I_{cSub} , with an accurate constant of proportionality. However, the notable difference being that the relative suppression of I_c in samples presented in ref. [20] was much greater than that presented here, with a maximum I_c of only 13 μ A. In those samples, the ferromagnetic suppression was likely to be so dominating that the junction size never moved out of the very long junction limit and eqn. 5.8 was applicable.

Therefore, the high temperature and very long junction limit of the theory of I_c in SNS junctions seem only to be valid when the suppression by ferromagnetic proximity is dominating. It may be possible to fit the observed I_c to the full temperature range using the equation for arbitrary junction length by assuming how the junction size changes. Near T_c the linearised Usadel equations give the I_c for arbitrary junction length to be:

$$eR_N I_c = 64\pi k_B T \sum_{n=0}^{\infty} \frac{L}{L_{\omega_n}} \frac{\Delta^2 \exp(-L/L_{\omega_n})}{(\omega_n + \Omega_n + \sqrt{2(\Omega^2 + \omega_n \Omega_n)})^2} \quad (5.10)$$

where R_N is the resistance of the normal metal, L is the length of the normal metal,

$\omega_n = (2n + 1)\pi k_B T$ is the Matsubara frequency, $\Omega_n = \sqrt{\Delta^2 + \omega_n^2}$ and $L_{\omega_n} = \sqrt{\hbar D / 2\omega_n}$. A simplistic assumption of the changing junction size is that the junction shrinks linearly with temperature such that $L = L_0 T / T_c$ where L_0 is the junction size near T_c . By numerical calculation of eqn. 5.10 for each temperature up to 1000 terms of n it is found that a value of $L_0 = 600$ nm accurately reproduces the I_c of the hybrid junction after the field has been applied for temperatures above 0.42 K. This is in good agreement with the junction size extracted from the interferometer devices at 0.85 K, in with the junction length was $L = 670$ and 790 nm before and after the out of plane field.

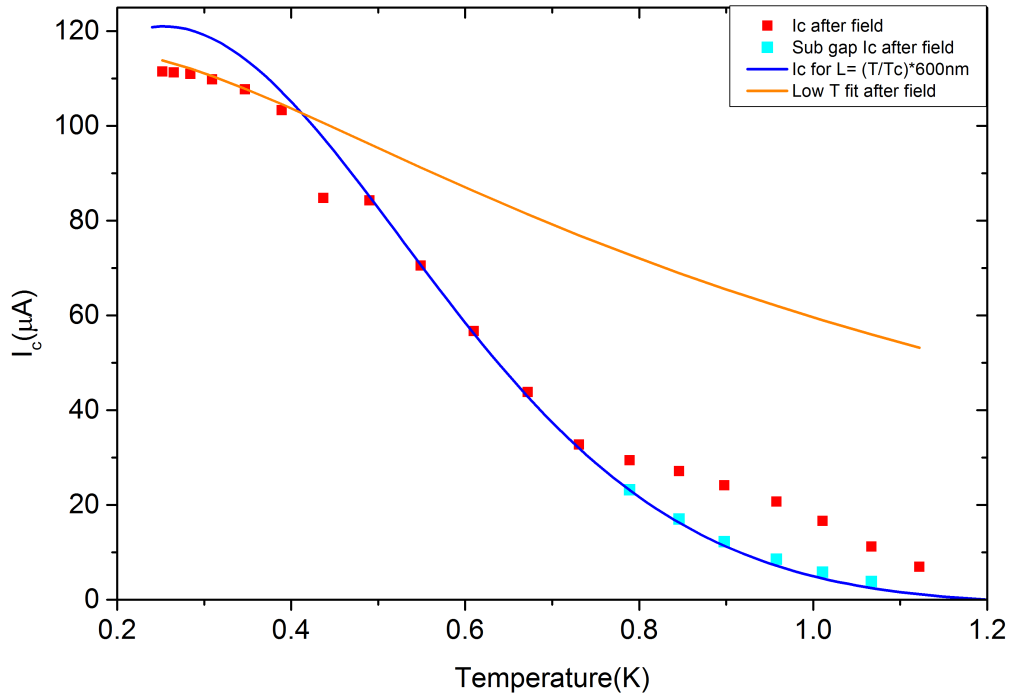


Figure 5.34: Fitting to the data presented in fig. 5.5 for the full calculation of the critical current in long SNS junctions defined by eqn. 5.10, up to $n = 1000$. Only the data after the field has been applied is presented, as no fit was possible for the data before the field was applied. The blue solid line is the fit to the I_c after the field was applied with the simple assumption that the junction length varies linearly with temperature as $L = L_0 T / T_c$ where $L_0 = 600$ nm. The orange line is the fit in the low temperature limit presented again to show how the low temperature behaviour dominates below ~ 0.4 K

The calculated curve is shown as the blue line in fig. 5.34. Below 0.42 K the observed I_c is lower than the predicted value, which now follows the trend as calculated in the

low temperature limit, as shown by the orange line. However, for the I_c measured before the field was applied, no value of L_0 was found to accurately reproduce the observed I_c . In this model, the I_c before the field was applied would require a smaller L_0 . When L_0 was set to smaller values, the line shape of the calculated I_c deviated greatly from the observed I_c . This is understandable, as 600 nm is on the edge of the size that the junction can be considered to be in the long junction limit. In fact, if one extracts the junctions size from the fit in fig. 5.34 at 0.42 K, where the calculated I_c deviates from the observed I_c , the junction size is found to be 210 nm, i.e. not in the long junction limit and not in agreement with the junction lengths extracted in section 5.4 at 0.3 K. Therefore, while this simple approximation of linear decrease in the junction size with temperature can replicate the behaviour of I_c , the resulting modelled junction is not in the long junction limit. Furthermore, eqn. 5.10 is only applicable in the high temperature limit $k_B T \gg E_{th}$. Assuming the empirical dependence of the gap energy on temperature $\Delta(T) = \Delta_0 \tanh(1.74 \sqrt{1 - T/T_c})$ [151], then eqn. 5.10 is only valid above ~ 1 K, and the behaviour below this temperature should not be considered rigorously accurate.

Therefore neither low temperature nor high temperature limits for long junctions appear to fully replicate the junction behaviour. The apparent temperature dependent reduction in junction size indicates that the junction should perhaps be considered in the short junction limit, where $E_{th} \gg \Delta$. In this limit, $I_c(T = 0) \approx 1.326\pi\Delta/2eR_N$ [91]. Therefore, by again extracting the low temperature critical current one can calculate the gap energy ($\Delta = 2eR_N I_c(T = 0)/1.326\pi$) before and after the field to be $\Delta = 185$ and 126 μeV respectively. Both before and after the field the gap is smaller than the gap in aluminium $\Delta_0 = 220$ μeV [158] due to the ferromagnetic suppression. This calculation links the change in I_c upon changing magnetization state to a reduction in gap energy. This would be expected when changing the magnetization from an inhomogeneous to collinear/single domain state. For this calculation to be accurate, however, the junction size at $T = 0$ K must be no larger than 188 and 228 nm before and after the field, respectively, to satisfy the short junction limit $E_{th} \gg \Delta$. Similar to the fitting in fig. 5.34 this junction size is too small to be likely.

It becomes apparent then, while the theory of critical current in long SNS junctions allows some insight into the behaviour of the I_c in the hybrid junctions, it is not in reality applicable to the junctions in a rigorous sense. Fitting to the theory in the long junction limit for both low and high temperature approximations does indicate that the junction size may change with temperature, in agreement with the extracted junction lengths in section 5.4. However, fitting requires that the junction either be in the short limit or use inaccurate parameters. Fitting to the theory for arbitrary junction size in the high temperature limit appears to accurately reproduce the I_c behaviour if a linear dependence of the junction size on temperature is assumed, but again this places the junction to be in the short junction limit and should only be accurate for $T > 1$ K. Assuming the junction to be in the very short limit indicates a change in the magnetic structure manifests in a change of the gap energy of the adjacent aluminium nanowire. However, this requires the junction to be much shorter than seems feasibly possible for these samples. A new theoretically treatment is required to explain the hybrid junctions. The treatment should be a full numerical calculation of the Usadel equations that takes into account the possible motion of the SN barrier and the crossing from the long to short junction limit that the motion of the barrier creates.

5.6.2 Comparison to theory of self heating hotspots

The experiments presented in section 5.2 and 5.3 strongly indicate that both the existence of the SNS to normal state transition and the long range suppression of I_c in the nanowire adjacent to the hybrid junction is due to Joule heating when the junction is in the normal state. The hypothesis is that at a critical input current, the electron temperature in the superconducting nanowire adjacent to the normal aluminium becomes greater than T_c and that section of nanowire then transitions into the normal state. The new section of normal metal now also contributes the the Joule heating and heats the nanowire further away from the junction. This continues and the heating causes an avalanche effect in which the entire nanowire transitions into the normal state.

The effects of a local hot spot in a superconducting nanowire were first considered by Skocpol, Beasley and Tinkham [159], their work is commonly refereed to as the SBT theory. The theory considers the case in which a normal metal section exists in a superconducting thin film bridge on the order of $1\text{ }\mu\text{m}$ wide. The transfer of heat from the film to the cooling bath is considered to be linear and of the form $(\alpha/d)(T(x) - T_b)$, where T_b is the temperature of the cooling bath, $T(x)$ is the temperature distribution along the nanowire, assumed to be one dimensional, d is the thickness of the film and α is the coefficient of heat transfer from the film to the cooling bath per unit area of the film, given in units of $\text{W m}^{-2} \text{K}^{-1}$. The theory solves the full heat equations in the system where a normal section exists across the bridge and defines the minimum applied current for normal section to be sustained in the film as

$$I_h = [\alpha W^2 d (T_c - T_b) / \rho]^{1/2} \quad (5.11)$$

where W is the width of the nanowire and ρ the resistivity in the normal state. This is the input power due to Joule heating which balances the cooling to the coolant bath. The original linear dependence on temperature of the coupling between the film temperature and the bath temperature in the SBT model was found to be accurate only near T_c . The work of Yamasaki and Aomine [160] (Mod SBT) extended the theory to the full

temperature range by replacing the linear approximation with the more accurate $A(T^4 - T_b^4)$ where A is the coefficient of cooling now in units $\text{W m}^{-2} \text{K}^{-4}$. This sets the condition for the minimum current to be:

$$5i_h^2 + 4t^5 = 4(i_h^2 + t^4)^{5/4} \quad (5.12)$$

where t is the dimensionless temperature T/T_c and i_h the dimensionless critical heating current $i_h^2 = I_h^2 \rho / AW^2 dT_c^4$. These theories define the re-trapping current, that is the current at which the superconductor will transition from the normal state to the superconducting state. When reducing the applied current from $I > I_c$, a normal state hot spot will exist as long as $I > I_h$, below I_h the input Joule power is no longer large enough to increase the temperature of the film above T_c and the hot spot disappears. The hybrid junctions presented here have been shown to demonstrate hysteresis and a re-trapping current. To show that this is due to hot spot heating, the re-trapping current can be fitted to eqns. 5.11 and 5.12, with free fit parameters α and A for both fits, respectively. Equation 5.12 was solved numerically using the Newton-Raphson method to find the root at each temperature. The fits of eqns. 5.11 and 5.12 to an 800 nm disk hybrid junction re-trapping current (fig5.3, disk sample 1) are presented in fig. 5.35 as the solid green and blue lines respectively, with the measured the re-trapping current shown as black symbols. At temperatures near T_c , both expressions for the minimum heating current accurately predict the re-trapping current. As the temperature is reduced, the SBT expression deviates from the observed I_r , which is to be expected as this expression is only applicable near T_c . However, the modified SBT theory perfectly predicts the observed re-trapping current. The heat transfer coefficients α and A for these fits are $220 \text{ W m}^{-2} \text{K}^{-1}$ and $540 \text{ W m}^{-2} \text{K}^{-4}$, respectively. The value of $\alpha = 220 \text{ W m}^{-2} \text{K}^{-1}$ is on the order to those reported by Skocpol, Beasley and Tinkham in their original experiment whereas the heating coefficient $A = 540 \text{ W m}^{-2} \text{K}^{-4}$ is ~ 10 times larger than that reported by Yamasaki and Aomine. This is likely due to the differing substrates used, silicon in the results presented here in comparison to sapphire or glass in the original experiments [159, 160]. Further-

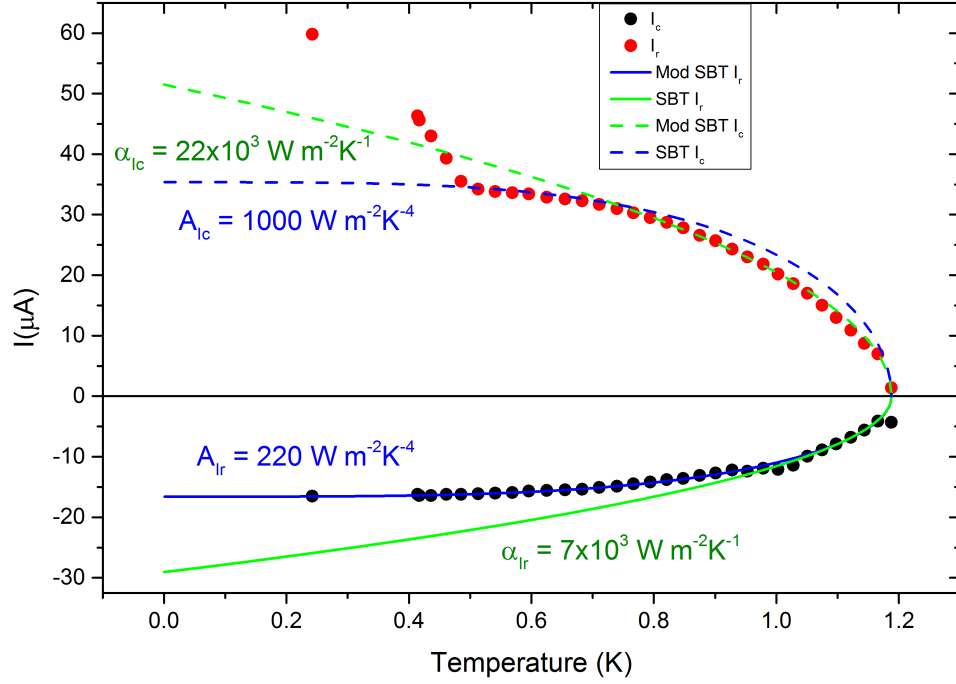


Figure 5.35: Fitting of both the re-trapping current and critical heating current (SNS to normal state transition) for the data presented in fig. 5.3. The solid lines are the calculated re-trapping currents and the dashed lines are the calculated critical heat current. The green lines are the fit using the SBT theory (eqn. 5.11) and blue lines for the modified SBT theory (eqn. 5.12). The re-trapping current is accurately reproduced using both theories near T_c and with the modified SBT theory across the full temperature range, using heat transfer coefficients $\alpha = 220 \text{ W m}^{-2} \text{ K}^{-1}$ and $A = 540 \text{ W m}^{-2} \text{ K}^{-4}$. The critical heating current however is reproduced at high temperature only by the SBT theory and at low temperature only by the modified SBT theory, both requiring much large heat transfer coefficients $\alpha = 22 \times 10^3 \text{ W m}^{-2} \text{ K}^{-1}$ and $A = 1000 \text{ W m}^{-2} \text{ K}^{-4}$.

more, α and A are in reality temperature dependent, thus treating them as temperature independent across a large temperature range will inevitably result in a slightly inaccurate result for α and A . The accuracy of these fits demonstrates that thermal effects play a large role in the behaviour of the hybrid junctions and nanowires presented in this thesis and that the re-trapping current of the nanowire is due to the heat produced by Joule losses in the normal state.

However, the temperature dependence of the I_{rSub} has a line shape like that of the junction I_{cSub} which likely not due to thermal effects but rather the proximity from the adjacent

superconducting nanowire. Furthermore, if one assumes that the I_c of the nanowire when transitioning from either the SNS to normal phase is similarly due to Joule heating, as the experimental observations suggest, then eqns. 5.11 and 5.12 require heat transfer coefficients and order of magnitude larger than those used to fit the re-trapping current. Attempted fits to the I_c using eqns. 5.11 and 5.12 are also shown in fig. 5.35 as the dashed green and blue lines, respectively. Both fits require an order of magnitude increase in the heat transfer coefficient terms α and A , and neither expression accurately reproduces the observed I_c of the SNS to normal transition (red symbols at $T > 0.5$ K). Near T_c the SBT expression replicates the I_c behaviour, while the modified SBT theory overestimates the transition current. As the temperature is reduced to 0.7 K, the SBT expression deviates as in the case of the re-trapping current and the modified SBT expression follows the observed I_c .

The difference in the behaviour of the re-trapping current and the SNS to normal state transition current is because, while they are both phenomena caused by Joule heating, they are in reality two different problems. The re-trapping current calculated in eqns. 5.11 and 5.12 is the minimum current required to heat the thin film in the normal state so that the heat produced equals that which is dissipated to the coolant bath and the temperature of the film remains equal to T_c . In this case the entire film is in the normal state and the heat due to Joule losses is generated everywhere in the film. For the case of heating in the SNS phase, the heat is only produced in the normal metal section that encompasses the aluminium nanowire and the ferromagnetic disk. The heat will then dissipate both into the coolant bath and into each of the adjacent superconducting nanowires. The heating hypothesis is that at some critical input Joule power the temperature within the superconducting nanowire adjacent to the normal section raises above T_c and transitions into the normal state. The normal section thus extends along the wire and continues to heat the adjacent superconducting metal above T_c . A thermal run-away of the NS boundary then occurs and the entire nanowire transitions into the normal state. Therefore, the critical input power or input current for this transition depends on more than simply the heat transfer from the film to the coolant bath, but also on the transfer of heat from

the normal metal to the superconducting metal and then the transfer of heat from the superconducting metal to the coolant bath.

Secondly, the SBT and modified SBT theories consider that the heat transfer is from the film to the substrate and governed by the thermal resistance of the film-substrate interface, the Kapitza resistance, which is due to mismatch of phonons at the boundary. In very thin films, if the thickness of the film is less than the phonon fermi wavelength, then the Kapitza resistance is negligible as no phonon mismatch exists. The films used here are 80 nm whilst the phonon wavelength is approximately 200 nm [156] and the approximation of negligible Kapitza resistance is valid. This means that the temperature of the local phonons can be considered to be equal to the bath temperature and the input Joule power heats the electron gas. The heat dissipation in the film is now from the electrons to the local phonons which has temperature dependence $\Sigma(T_e^5 - T_p^5)$, where Σ is the electron-phonon coupling constant.

Taking these differences into account, the heating caused by the hybrid junction in the SNS phase becomes more complex than the simple hot-spot theories and requires a specific solution to the heat flow equations. The solution to the heat equations for heat transfer $\Sigma(T_e^5 - T_p^5)$ is found to be analytically unsolvable and numerical solutions of the heat equations are outside the scope of this thesis.

Chapter 6

Summary and conclusions

The aim of this project was to investigate the ferromagnetic proximity suppression of superconductivity under the influence of different magnetic states in an effort to prove that collinear magnetization states create a stronger suppression of superconductivity than inhomogeneous states. The ferromagnetic influence was investigated using nickel disks possessing remnant vortex states, and L-shape domain wall traps made of nickel and permalloy, with aluminium nanowires deposited on top of the ferromagnetic element. This created a hybrid SNS junction, in which the superconductivity in the aluminium above the nickel disk was suppressed by proximity to the nickel.

It was imperative to know the magnetic state of the ferromagnetic elements so that any changes in the hybrid junctions could be linked to the magnetization changes in the ferromagnet element. To this end, extensive MFM studies of the magnetic states in nickel disks of diameter 300 – 1000 nm and thickness 15 – 55 nm were performed. It was found that the use of standard moment commercial MFM probes caused a strong interaction between the disks and the probes that pulled the disks magnetization out-of-plane. This interaction obscured the obtained images. MFM measurements using low moment probes avoided this interaction and accurately imaged the magnetic states in the disks.

A phase diagram of magnetic states in the disks was assembled. The smallest disks were found to be in a single domain state, i.e. when the disk diameter was less than 300 – 400 nm and the thickness less than 20 – 25 nm. As the disk size was increased, the vortex state

was observed for diameters greater than 300 – 400 nm and thickness less than 30 – 35 nm. Above 30 – 35 nm thickness the stripe domains were observed to dominate the magnetic states in the disks. The stripe domain state had not been previously observed in nickel disks of this size. By simulation of the magnetic states in the disks using the open source OOMMF code it was found that all the magnetic states imaged by MFM could only be replicated by using a thickness-dependent effective out-of-plane anisotropy.

The magnetization reversal of the nickel vortex state was investigated using both *in situ* MFM and electrical measurement via the anisotropic magnetoresistance effect. *In situ* MFM measurements indicated that the nickel disks in the vortex state dimensional range would always form a vortex state at remnance. Conversely however, measurements of the vortex magnetoresistance showed that the vortex state nucleation occurred after a change in the field direction. Differences in the disk magnetoresistance for different applied field angles were explained by the inhomogeneous current distribution in the disk and the motion of the vortex core relative to the electrical contacts.

In conjunction with the nickel disks, the magnetization dynamics of L-shape domain wall trap devices was investigated, with the aim to use the traps to controllably place a domain wall beneath an overlying superconducting nanowire. Two L-shape devices, one made of nickel and another with permalloy, were measured via magnetotransport methods and *in situ* MFM, with the field applied parallel to one arm. The nickel L-shape device showed a smooth change in magnetoresistance typical of smooth rotation of the magnetization rather than the trapping/un-trapping of a domain wall. The *in situ* MFM measurements confirmed that the nickel L-shape dynamics consisted of a series of complex multi domain nucleations and annihilations, but that a single domain like, and inhomogeneous magnetization state, were possible in the L-shape corner. The multi-domain behaviour of the nickel L-shape was attributed to the cubic magnetocrystalline anisotropy of nickel. Therefore, the L-shape device was fabricated again using permalloy as the magnetic material, as it has negligible magnetocrystalline anisotropy. Magnetotransport measurements of the permalloy L-shape showed an asymmetric behaviour: i.e. rapid changes in the resistance typical of domain wall trapping and de-pinning only when the field was swept from pos-

itive to negative values. *In situ* MFM measurements indicated that the asymmetry was due the combination of a preferred direction of magnetization in the arm perpendicular to the field and the rapid switching of the magnetization in the arm parallel to the field. This meant that when sweeping the field from negative to positive values, a domain wall was smoothly nucleated in the corner and then rapidly annihilated at small positive fields. On the other hand, when sweeping the field from positive to negative values, the domain wall was rapidly nucleated by the switching of the magnetization of the arm parallel to the field, causing the observed jump in the magnetoresistance, and then smoothly annihilated. Disks with dimensions that placed them in the remnant vortex state range were used to create the initial hybrid junctions. The hybrid junctions were observed to exhibit three phases dependent on temperature and applied bias current. Firstly, a phase in which the entire aluminium nanowire is in the superconducting state and a single critical current transition was observed. Secondly, there is an SNS phase in which the nanowire above the ferromagnet transitions into the normal state, while the adjacent nanowire remains superconducting. In this phase two critical current transitions were observed, the I_c when transitioning from the SNS to normal state and the I_{cSub} when transitioning from the superconducting to SNS state. Lastly, a phase in which the entire nanowire is in the normal state was observed. The temperature, at which all three phases meet, was named the triple point. The effect of changing the magnetic state of the disk was investigated by applying and then removing an out-of-plane 800 mT magnetic field in an attempt to alter the disk magnetic state. The I_{cSub} and I_c of the superconducting to normal transition and the triple point temperature were observed to reduced after the application of the field, whilst the SNS to normal transition remained unchanged. This effect was attributed to changing the magnetic state of the disk from the known vortex state to a more collinear state, increasing the ferromagnetic suppression effect.

It was found that, if the current was passed through the hybrid junction, the temperature dependence of the critical current of the adjacent nanowire was the same as the I_c of the hybrid junction. If the temperature dependence of I_c of the nanowire was measured with the current bypassing the hybrid junction, then the I_c was significantly larger, with

different temperature dependence behaviour. This suppression effect, acting over a range larger than the coherence length and thus named the long range suppression effect, was hypothesised to be due to two possible sources: injection of spin polarised quasi-particles from the junction into the adjacent nanowire or increased electron temperature caused by Joule heating in the hybrid junction when in the SNS phase. The inclusion of nickel heat sinks to the hybrid junction increased the critical current of the SNS to normal transition equating to an increased input power of 40 %. A control experiment using Au/Al SNS junctions with and without heat sinks reproduced the observed increase in the required heating power with the inclusion of the heat sinks. Coupled with the lack of any dependence of the long range suppression on distance, it became clear that the long range suppression was most likely to be due to heating.

The treatment of the hybrid junction as an SNS junction was justified by measuring the dependence of the junction critical current on the phase difference across the junction. This was done by fabricating loop interferometers, in which the hybrid junction was the weak link in the loop. The I_{cSub} was observed to oscillate with increasing flux through the loop, with a period of oscillation equal to one flux quantum. Contrarily, the SNS to normal state transition was not observed to oscillate, adding credence to the hypothesis that the superconducting to normal state transition of the nanowire is due to heating. In the superconducting phase, the I_c was also observed to oscillate, corresponding to the transition of the entire nanowire being controlled by the transition of the junction, this further supported the suppression by heat hypothesis. Measurements of the phase dependent oscillations were made after the application of an 800 mT out of plane field, following the method used in the previous experiment. After the field was applied it was observed that the amplitude of the I_c oscillations was reduced at 0.85 K and a phase shift in the oscillation was observed. It was discussed that the observed phase shift may be attributed to the difference in stray field from the disks in different magnetic states before and after the field was applied. By fitting the decay in the peak of the I_{cSub} oscillations to the expected Fraunhofer interference behaviour of SNS junctions in perpendicular magnetic fields, the junction lengths were extracted at 0.3 and 0.85 K before and after the application of the

800 mT out of plane magnetic field. These fits indicated that the junction lengths were smaller than the disk diameter (800 nm), with $L = 370$ nm at 0.3 K. Furthermore, the junction length was proportional to temperature, with $L = 670$ nm at 0.85 K. Using the same fitting procedure for the I_c decay after the 800 mT field was applied indicated that the junction length was now larger than before the field was applied, i.e. 373 and 790 nm at 0.3 and 0.85 K, respectively.

To remove the ambiguity in the magnetic state of the ferromagnetic element of the hybrid junction, the disks were replaced with the L-shape domain wall traps discussed earlier, made using either nickel or permalloy. The nickel device showed a hysteric dependence of critical current on applied in plane field that mimicked that of the hysteresis of the L-shape device magnetoresistance. The I_c behaviour was such that I_c was largest at the fields in which the inhomogeneous multi-domain structure was observed in the nickel L-shape device. The permalloy L-shape hybrid junction showed an asymmetric dependence of I_c on in plane field, that, similar to the nickel device, mimicked the magnetoresistance of the L-shape device. Comparison of the permalloy hybrid junction I_c and the L-shape device magnetoresistance, as well as room temperature *in situ* MFM, showed that all occurrences of increased critical current aligned with field histories, in which a domain wall existed in the corner of the L-shape beneath the hybrid junction. This indicates that in this system, inhomogeneous magnetization states reduce the ferromagnetic proximity suppression of superconductivity.

The theoretical treatment of the critical current in long SNS junctions was used to attempt to describe the behaviour of the hybrid junctions. Fitting of the junction I_c in the long junction, and low and high temperature limits, reflected what was observed by fitting of the Fraunhofer decay of I_c in the interferometer devices, i.e. that the junction length was temperature and magnetic state dependent. This is a sensible conclusion to make, as the SN boundary between the superconducting and normal aluminium has no restraint to any physical position, but is rather an equilibrium between the superconducting and normal electron phases. Alterations to the magnetic state of the ferromagnet also change this equilibrium. This was further indicated by fitting the critical current after the application

of the 800 mT field to the expression for the critical current for arbitrary junction lengths, assuming the junction length decreases linearly with temperature. However, closer attention to the parameters of these fits showed that the solutions were not within the required limits: at low temperature the junction is no longer in the long junction limit, at high temperature an expectationally large constant of proportionality is required to replicate the observed I_c . Treating the junction in the short junction limit indicated that the change of the disk magnetic state could also be linked to a reduction in the superconducting gap energy of the adjacent nanowire. However, the junctions were required to be much shorter than feasible for the measured junctions. For a more robust understanding of the junctions, full calculations of the transport through the junctions should be made, taking into account the mobility of the SN boundary.

The continuation of the research into the magnetic state dependence of the proximity effects should focus on improving the control of the magnetic state of the ferromagnetic element. The ambiguity in the magnetization dynamics of the nickel disks made it difficult to create two distinct remnant states, vortex and collinear/single domain, in which the junction properties could be investigated. The use of the L-shape domain wall traps was a step towards improved magnetic state control. However, the asymmetry in the permalloy L-shape magnetoresistance indicates that these structures can be further improved. Alternative magnetic elements to consider could include notched magnetic nanowires in which a domain wall could be effectively trapped at the notch. The advantage this may have over the L-shape devices would be a clearer distinction between single domain, magnetized along the length of the wire, and domain wall states. A superconducting nanowire could easily be deposited on top of the notch. Another method would be to use an exchange spring, a bilayer ferromagnetic element that allows the fine control of non-collinearity between the two ferromagnetic thin films. Incorporating such an exchange spring into the proximity junction geometry would allow direct comparison of the I_c with the degree of inhomogeneity of the ferromagnetic element. Furthermore, the direction of the inhomogeneity would be perpendicular to the current flow (from the top layer towards the substrate), whereas in the devices presented here, the direction of the magnetic inhomogeneity

geneity has been planar (from one SN boundary to another) in the direction of current flow. Coupled with increased control of the magnetic element, this would be an excellent experiment to test if the type of inhomogeneity is important to the behaviour of the proximity junction. Assuming that these improvements could be made, the hybrid junction stands as a proof of concept for magnetically controlled superconducting junctions. Such a structure may be of great use in superconducting electronics, acting as a switch or memory cell.

Comparison to the theories of local hot spot heating successfully showed that the aluminium films used were sensitive to thermal effects. This was indicated by the exceptional fit of the aluminium nanowire re-trapping current to the theories of Skocpol, Beasley and Tinkham [159], as well as Yamasaki and Aomine [160]. Application of these theories to the SNS to normal state transition, shown to be likely due to local heating, required unrealistically large heat transfer coefficients from the film to the coolant bath. This discrepancy was explained by considering the differences between the cause of the re-trapping effect and the heating of the SNS junction. Whilst the re-trapping current is due to the Joule heating of the entire film, the suppression of superconductivity by heating requires that the heat transfer to the substrate be replaced by the heat transfer of the electron gas to the local phonon system, as well as the inclusion of the heat transfer from the normal aluminium section to the adjacent superconducting nanowires. This complex problem is not analytically solvable, however these results encourage new theoretical work, most likely numerical simulations, to describe the temperature distribution in the proximity junctions.

The suppression of superconductivity by local heating in the SNS phase places a limit on the practical use of the proximity junctions. The heating effect has been shown to cause an avalanche effect, forcing the entire superconducting nanowire in the electrical circuit to transition to the normal state when the junction does. This long range influence would make it difficult to create any memory or switching devices on a single wafer that could be operated independently from one another. However, by measurements of the nickel and gold SNS junctions with heat sinks, it was shown that the suppression of

superconductivity by heating could be alleviated by sufficient cooling. Therefore, the direction of new research into the long range suppression by heating should be towards identification of the critical temperature within the SNS junction and new ways to cool the junction to reduced the suppression by heat. The nature of the heating effect could be investigated further by direct measurements of the electron temperature in the junction. This could be done with the use of normal metal-insulator-superconductor (NIS) tunnel junctions, in which the normal metal would be the junction in the SNS phase. Such NIS junctions have been shown to be useful for local thermometry of the electron temperature in the normal metal [161]. Furthermore, measurement of the electron temperature within the normal aluminium at the critical heating current could provide insight into the thermal conductivity of the unique SN boundary. This experiment could also investigate new ways to cool the SNS junction and alleviate the heating effect. This is because NIS junctions have been shown to cool the electron gas in the N metal [162, 163, 164] by selective tunnelling of high energy electrons into the superconductor. The combinations of the heat sinks used in this work with additional NIS cooling junctions could be used to reduce the heating effect.

In summary, the results of this thesis show many unknown properties of the so called *proximity junctions*, that were previously investigated in the theses of James Wells and Richard Marsh [20, 19] and the published works of Vávra et al. and Lin et al. [21, 22, 23], in which the proximity junctions were shown to indeed be SNS junctions. The results presented in this thesis extend these works by showing that the previously not understood behaviour near T_c is due to local heating in the junction, not due to the relative strength of the condensate as assumed by Vávra et al. and Lin et al. Furthermore, it has been shown that the junction is highly dependent on the magnetic state of the ferromagnetic element. Lastly it has been discussed that, due to the lack of physical restraint on the position of the SN boundary, the junction length is proportional to temperature. This means that, as it is based upon junctions with well defined length, the commonly used theory of critical current in long SNS junctions does not adequately describe the behaviour of these proximity junctions. As such, the results presented in this project encourage new

theoretical work that considers the case of a mobile SN boundary.

The work presented here shows that the class of *proximity junctions* contains a rich breadth of superconducting proximity physics, including the magnetic control of proximity effects. It is my hope that these results encourage further investigation into this new and intriguing system.

Bibliography

- [1] R. Holm and W. Meissner, “Messungen mit hilfe von flüssigem helium. xiii,” *Zeitschrift für Physik*, vol. 74, no. 11, pp. 715–735, 1932.
- [2] P. Fulde and R. A. Ferrell, “Superconductivity in a strong spin-exchange field,” *Physical Review*, vol. 135, pp. A550–A563, aug 1964.
- [3] J. S. Jiang, D. Davidović, D. H. Reich, and C. L. Chien, “Oscillatory superconducting transition temperature in nb/gd multilayers,” *Phys. Rev. Lett.*, vol. 74, pp. 314–317, Jan 1995.
- [4] L. V. Mercaldo, C. Attanasio, C. Coccorese, L. Maritato, S. L. Prischepa, and M. Salvato, “Superconducting-critical-temperature oscillations in nb/cumn multilayers,” *Physical Review B*, vol. 53, no. 21, p. 40, 1996.
- [5] Y. Obi, M. Ikebe, T. Kubo, and H. Fujimori, “Oscillation phenomenon of transition temperatures in nb/co and v/co superconductor/ferromagnet multilayers,” *Physica C: Superconductivity and its Applications*, vol. 317-318, pp. 149–153, 1999.
- [6] F. S. Bergeret, A. F. Volkov, and K. B. Efetov, “Long-range proximity effects in superconductor-ferromagnet structures,” *Physical Review Letters*, vol. 86, no. 18, pp. 4096–4099, 2001.
- [7] A. Kadigrobov, R. I. Shekhter, and M. Jonson, “Quantum spin fluctuations as a source of long-range proximity effects in diffusive ferromagnet-superconductor structures,” *Europhysics Letters*, vol. 54, p. 394, 2001.

- [8] F. Bergeret, A. F. Volkov, and K. Efetov, “Josephson current in superconductor-ferromagnet structures with a nonhomogeneous magnetization,” *Physical Review B*, vol. 64, p. 134506, sep 2001.
- [9] F. S. Bergeret, A. F. Volkov, and K. B. Efetov, “Manifestation of triplet superconductivity in superconductor-ferromagnet structures,” *Physical Review B*, vol. 68, p. 14, mar 2003.
- [10] I. Sosnin, H. Cho, V. T. Petrashov, and A. F. Volkov, “Superconducting phase coherent electron transport in proximity conical ferromagnets,” *Physical review letters*, vol. 96, p. 4, nov 2006.
- [11] R. S. Keizer, S. T. B. Goennenwein, T. M. Klapwijk, G. Miao, G. Xiao, and A. Gupta, “A spin triplet supercurrent through the half-metallic ferromagnet CrO_2 ,” *Nature*, vol. 439, pp. 825–7, feb 2006.
- [12] T. S. Khaire, M. A. Khasawneh, W. P. Pratt, and N. O. Birge, “Observation of spin-triplet superconductivity in Co -based Josephson junctions,” *Physical Review Letters*, vol. 104, p. 137002, mar 2010.
- [13] J. W. a. Robinson, J. D. S. Witt, and M. G. Blamire, “Controlled injection of spin-triplet supercurrents into a strong ferromagnet,” *Science (New York, N.Y.)*, vol. 329, pp. 59–61, jul 2010.
- [14] T. Tokuyasu, J. A. Sauls, and D. Rainer, “Proximity effect of a ferromagnetic insulator in contact with a superconductor,” *Phys. Rev. B*, vol. 38, pp. 8823–8833, Nov 1988.
- [15] M. Sillanpää and T. Heikkilä, “Inverse proximity effect in superconductors near ferromagnetic material,” *EPL (Europhysics ...)*, vol. 56, no. November, pp. 590–595, 2001.

- [16] R. J. Kinsey, G. Burnell, and M. G. Blamire, “Active supercurrent control in superconductor/ferromagnet heterostructures,” *IEEE Transactions on Applied Superconductivity*, vol. 11, no. 1, pp. 904–907, 2001.
- [17] a. Rusanov, M. Hesselberth, J. Aarts, and A. Buzdin, “Enhancement of the superconducting transition temperature in nb/permalloy bilayers by controlling the domain state of the ferromagnet,” *Physical Review Letters*, vol. 93, p. 057002, jul 2004.
- [18] T. Champel and M. Eschrig, “Effect of an inhomogeneous exchange field on the proximity effect in disordered superconductor-ferromagnet hybrid structures,” *Physical Review B*, vol. 72, p. 054523, aug 2005.
- [19] R. Marsh, *Superconducting phase coherent electron transport in nano-engineered ferromagnetic vortices*. PhD thesis, Royal Holloway University of London, 2012.
- [20] J. Wells, *Mutual Proximity Effects in Hybrid Superconducting-Ferromagnetic Nanostructures*. PhD thesis, Royal Holloway University of London, 2013.
- [21] O. Vávra, W. Pfaff, and C. Strunk, “Planar s-(s/f)-s josephson junctions induced by the inverse proximity effect,” *Applied Physics Letters*, vol. 95, no. 2009, pp. 3–6, 2009.
- [22] O. Vávra, W. Pfaff, R. Monaco, M. Aprili, and C. Strunk, “Current-controllable planar s-(s/f)-s josephson junction,” *Applied Physics Letters*, vol. 102, pp. 2013–2016, 2013.
- [23] L. K. Lin, S. Y. Huang, J. H. Huang, and S. F. Lee, “Nb lateral josephson junction induced by inverse proximity effect with nife,” *IEEE Transactions on Magnetics*, vol. 48, pp. 4236–4238, 2012.
- [24] R. E. Dunin-Borkowski, M. R. McCartney, B. Kardynal, and D. J. Smith, “Magnetic interactions within patterned cobalt nanostructures using off-axis electron holography,” *Journal of Applied Physics*, vol. 84, no. 1, pp. 374–378, 1998.

- [25] R. P. Cowburn, D. K. Koltsov, A. O. Adeyeye, and M. E. Welland, "Single-domain circular nanomagnets," *Physical Review Letters*, vol. 83, pp. 1042–1045, aug 1999.
- [26] P. Vavassori, V. Metlushko, B. Ilic, M. Gobbi, M. Donolato, M. Cantoni, and R. Bertacco, "Domain wall displacement in py square ring for single nanometric magnetic bead detection," *Applied Physics Letters*, vol. 93, no. 20, 2008.
- [27] M. Donolato, M. Gobbi, P. Vavassori, M. Leone, M. Cantoni, V. Metlushko, B. Ilic, M. Zhang, S. X. Wang, and R. Bertacco, "Nanosized corners for trapping and detecting magnetic nanoparticles.," *Nanotechnology*, vol. 20, no. 38, p. 385501, 2009.
- [28] K. Nakano, D. Chiba, N. Ohshima, S. Kasai, T. Sato, Y. Nakatani, K. Sekiguchi, K. Kobayashi, and T. Ono, "All-electrical operation of magnetic vortex core memory cell," *Applied Physics Letters*, vol. 99, no. 26, p. 262505, 2011.
- [29] G. Skidmore, A. Kunz, C. Campbell, and E. Dahlberg, "Micromagnetic domain structures in cylindrical nickel dots," *Physical Review B*, vol. 70, p. 012410, jul 2004.
- [30] T. Pokhil, D. Song, and J. Nowak, "Spin vortex states and hysteretic properties of submicron size nife elements," *Journal of Applied Physics*, vol. 87, no. 9, p. 6319, 2000.
- [31] M. Rahm, M. Schneider, J. Biberger, R. Pulwey, J. Zweck, D. Weiss, and V. Uman-sky, "Vortex nucleation in submicrometer ferromagnetic disks," *Applied Physics Let-ters*, vol. 82, no. 23, p. 4110, 2003.
- [32] H. Corte-León, P. Krzysteczko, H. W. Schumacher, A. Manzin, V. Antonov, O. Kaza-kova, I. Nazionale, and T. I, "Tailoring of domain wall devices for sensing applica-tions," *IEEE Transactions on Magnetism*, vol. 50, no. 11, pp. 2–5, 2014.
- [33] H. Corte-León, V. Nabaei, A. Manzin, J. Fletcher, P. Krzysteczko, H. W. Schu-macher, and O. Kazakova, "Anisotropic magnetoresistance state space of permalloy

- nanowires with domain wall pinning geometry,” *Scientific Reports*, vol. 4, pp. 1–10, 2014.
- [34] E. Ising, “Beitrag zur theorie des ferromagnetismus,” *Zeitschrift für Physik*, vol. 31, no. 1, pp. 253–258, 1925.
- [35] E. C. Stoner and E. P. Wohlfarth, “A mechanism of magnetic hysteresis in heterogeneous alloys,” *Philosophical Transactions of the Royal Society of London A: Mathematical, Physical and Engineering Sciences*, vol. 240, no. 826, pp. 599–642, 1948.
- [36] <http://math.nist.gov/oommf/> National Institute of Standards and Technology and National Institute of Standards and Technology, “<http://math.nist.gov/oommf/>,” 2013.
- [37] T. Fischbacher, M. Franchin, G. Bordignon, and H. Fangohr, “A systematic approach to multiphysics extensions of finite-element-based micromagnetic simulations: Nmag,” *Magnetics, IEEE Transactions on*, vol. 43, pp. 2896–2898, June 2007.
- [38] W. Scholz, J. Fidler, T. Schrefl, D. Suess, R. Dittrich, H. Forster, and V. Tsiantos, “Scalable parallel micromagnetic solvers for magnetic nanostructures,” *Comp. Mat. Sci.*, vol. 28, pp. 366–383, 2003. <http://magnet.atp.tuwien.ac.at/scholz/magpar> ¶Parallel Finite Element Micromagnetics Package (magpar).
- [39] A. Morrish, *The physical principles of magnetism*. Wiley series on the science and technology of materials, Wiley, 1965.
- [40] T. Gilbert, “A phenomenological theory of damping in ferromagnetic materials,” *Magnetics, IEEE Transactions on*, vol. 40, pp. 3443–3449, Nov 2004.
- [41] G. S. Abo, Y.-k. Hong, J. Park, J. Lee, W. Lee, and B.-c. Choi, “Definition of magnetic exchange length,” *IEEE Transactions on Magnetics*, vol. 49, pp. 4937–4939, aug 2013.

- [42] A. Hubert and R. Schäfer, *Magnetic domains: the analysis of magnetic microstructures*. Springer Science & Business Media, 2008.
- [43] W. Brown, *Micromagnetics, by w.f. brown*. Interscience, 1963.
- [44] R. P. Cowburn, “Property variation with shape in magnetic nanoelements,” *Journal of Physics D: Applied Physics*, vol. 33, pp. R1–R16, jan 2000.
- [45] T. Shinjo, “Magnetic vortex core observation in circular dots of permalloy,” *Science*, vol. 289, pp. 930–932, aug 2000.
- [46] A. Wachowiak, J. Wiebe, M. Bode, O. Pietzsch, M. Morgenstern, and R. Wiesendanger, “Direct observation of internal spin structure of magnetic vortex cores,” *Science (New York, N.Y.)*, vol. 298, pp. 577–80, oct 2002.
- [47] R. Pulwey, M. Rahm, J. Biberger, and D. Weiss, “Switching behavior of vortex structures in nanodisks,” *IEEE Transactions on Magnetics*, vol. 37, no. 4, pp. 2076–2078, 2001.
- [48] V. Novosad, M. Grimsditch, J. Darrouzet, J. Pearson, S. D. Bader, V. Metlushko, K. Guslienko, Y. Otani, H. Shima, and K. Fukamichi, “Shape effect on magnetization reversal in chains of interacting ferromagnetic elements,” *Applied Physics Letters*, vol. 82, no. 21, pp. 3716–3718, 2003.
- [49] H. Hoffmann and F. Steinbauer, “Single domain and vortex state in ferromagnetic circular nanodots,” *Journal of Applied Physics*, vol. 92, no. 9, p. 5463, 2002.
- [50] J. Ha, R. Hertel, and J. Kirschner, “Micromagnetic study of magnetic configurations in submicron permalloy disks,” *Physical Review B*, vol. 67, p. 224432, jun 2003.
- [51] W. Rave and A. Hubert, “Magnetic ground state of a thin-film element,” *IEEE Transactions on Magnetics*, vol. 36, no. 6, pp. 3886–3899, 2000.
- [52] O. Kazakova, M. Hanson, P. Blomqvist, and R. Wäppling, “Interplay between shape and magnetocrystalline anisotropies in patterned bcc fe/co(001) multilayers,” *Physical Review B*, vol. 69, p. 094408, mar 2004.

- [53] D. Betto and J. M. D. Coey, "Vortex state in ferromagnetic nanoparticles," *Journal of Applied Physics*, vol. 115, p. 17D138, may 2014.
- [54] A. Samardak, E. Sukovatitsina, A. Ognev, M. Stebliy, A. Davydenko, L. Chebotkevich, Y. Keun Kim, F. F. Nasirpouri, S.-M. Janjan, and F. F. Nasirpouri, "Magnetic vortex state and multi-domain pattern in electrodeposited hemispherical nanogranular nickel films," *Journal of Magnetism and Magnetic Materials*, vol. 371, pp. 149–156, dec 2014.
- [55] F. Nasirpouri, A. Nogaret, and S. J. Bending, "Effect of size and configuration on the magnetization of nickel dot arrays," *IEEE Transactions on Magnetics*, vol. 47, pp. 4695–4700, dec 2011.
- [56] K. M. Razeeb, F. M. F. Rhen, and S. Roy, "Magnetic properties of nickel nanowires: Effect of deposition temperature," *Journal of Applied Physics*, vol. 105, no. 8, p. 083922, 2009.
- [57] S. H. Lee, F. Zhu, C. Chien, and N. Marković, "Effect of geometry on magnetic domain structure in ni wires with perpendicular anisotropy: A magnetic force microscopy study," *Physical Review B*, vol. 77, pp. 6–9, 2008.
- [58] T. Y. Chung and S. Y. Hsu, "Detection of the domain structure change using magnetotransport for a series of circular permalloy dots," *Journal of Applied Physics*, vol. 99, no. 8, p. 08B707, 2006.
- [59] C. Y. Kuo, T. Y. Chung, and S. Y. Hsu, "Magnetic vortex structures probed by magnetotransport in sub-micron permalloy disks," *Journal of Physics: Conference Series*, vol. 200, p. 032037, jan 2010.
- [60] P. Vavassori, M. Grimsditch, V. Metlushko, N. Zaluzec, and B. Ilic, "Magnetoresistance of single magnetic vortices," *Applied Physics Letters*, vol. 86, no. 7, p. 072507, 2005.

- [61] M. Goto, H. Hata, A. Yamaguchi, Y. Nakatani, T. Yamaoka, Y. Nozaki, and H. Miyajima, “Electric spectroscopy of vortex states and dynamics in magnetic disks,” *Physical Review B*, vol. 84, p. 064406, aug 2011.
- [62] T. Ishida, T. Kimura, and Y. Otani, “Current-induced vortex displacement and annihilation in a single permalloy disk,” *Physical Review B*, vol. 74, p. 014424, jul 2006.
- [63] S. Kasai, Y. Nakatani, K. Kobayashi, H. Kohno, and T. Ono, “Current-driven resonant excitation of magnetic vortices,” *Physical Review Letters*, vol. 97, p. 107204, sep 2006.
- [64] B. Van Waeyenberge, A. Puzic, H. Stoll, K. W. Chou, T. Tyliczszak, R. Hertel, M. Fähnle, H. Brückl, K. Rott, G. Reiss, I. Neudecker, D. Weiss, C. H. Back, and G. Schütz, “Magnetic vortex core reversal by excitation with short bursts of an alternating field,” *Nature*, vol. 444, pp. 461–4, nov 2006.
- [65] R. Hertel, S. Gliga, M. Fähnle, and C. Schneider, “Ultrafast nanomagnetic toggle switching of vortex cores,” *Physical Review Letters*, vol. 98, p. 117201, mar 2007.
- [66] K. Yamada, S. Kasai, Y. Nakatani, K. Kobayashi, H. Kohno, A. Thiaville, and T. Ono, “Electrical switching of the vortex core in a magnetic disk,” *Nature materials*, vol. 6, pp. 269–3, apr 2007.
- [67] K. Yamada, S. Kasai, Y. Nakatani, K. Kobayashi, and T. Ono, “Switching magnetic vortex core by a single nanosecond current pulse,” *Applied Physics Letters*, vol. 93, no. 15, p. 152502, 2008.
- [68] F. Garcia, H. Westfahl, J. Schoenmaker, E. J. Carvalho, A. D. Santos, M. Pojar, A. C. Seabra, R. Belkhou, A. Bendounan, E. R. P. Novais, and A. P. Guimaraes, “Tailoring magnetic vortices in nanostructures,” *Applied Physics Letters*, vol. 97, no. 2, p. 022501, 2010.

- [69] M. Schneider, H. Hoffmann, and J. Zweck, “Magnetic switching of single vortex permalloy elements,” *Applied Physics Letters*, vol. 79, no. 19, p. 3113, 2001.
- [70] T. Kimura, Y. Otani, H. Masaki, T. Ishida, R. Antos, and J. Shibata, “Vortex motion in chirality-controlled pair of magnetic disks,” *Applied Physics Letters*, vol. 90, no. 13, p. 132501, 2007.
- [71] M.-Y. Im, P. Fischer, K. Yamada, T. Sato, S. Kasai, Y. Nakatani, and T. Ono, “Symmetry breaking in the formation of magnetic vortex states in a permalloy nanodisk,” *Nature communications*, vol. 3, p. 983, jan 2012.
- [72] T. R. McGuire and R. I. Potter, “Anisotropic magnetoresistance,” *IEEE transaction on magnetics*, vol. 11, pp. 1018–1038, 1975.
- [73] W. Meissner and R. Ochsenfeld, “Ein neuer effekt bei eintritt der supraleitfähigkeit,” *Naturwissenschaften*, vol. 21, no. 44, pp. 787–788, 1933.
- [74] M. Tinkham and Physics, *Introduction to Superconductivity: Second Edition (Dover Books on Physics) (Vol i)*. Dover Publications, second edition ed., June 2004.
- [75] J. Bardeen, L. N. Cooper, and J. R. Schrieffer, “Microscopic theory of superconductivity,” *Phys. Rev.*, vol. 106, pp. 162–164, Apr 1957.
- [76] L. N. Cooper, “Bound electron pairs in a degenerate fermi gas,” *Phys. Rev.*, vol. 104, pp. 1189–1190, Nov 1956.
- [77] E. Maxwell, “Isotope effect in the superconductivity of mercury,” *Phys. Rev.*, vol. 78, pp. 477–477, May 1950.
- [78] C. A. Reynolds, B. Serin, W. H. Wright, and L. B. Nesbitt, “Superconductivity of isotopes of mercury,” *Phys. Rev.*, vol. 78, pp. 487–487, May 1950.
- [79] H. Fröhlich, “Theory of the superconducting state. i. the ground state at the absolute zero of temperature,” *Phys. Rev.*, vol. 79, pp. 845–856, Sep 1950.

- [80] J. Bardeen and D. Pines, “Electron-phonon interaction in metals,” *Phys. Rev.*, vol. 99, pp. 1140–1150, Aug 1955.
- [81] D. Pines, “Superconductivity in the periodic system,” *Phys. Rev.*, vol. 109, pp. 280–287, Jan 1958.
- [82] A. Buzdin, “Proximity effects in superconductor-ferromagnet heterostructures,” *Reviews of modern physics*, vol. 77, no. July, pp. 935–976, 2005.
- [83] E. R. A.C. Rose-Innes, *Introduction to superconductivity*. Pergamon, 1994.
- [84] B. Josephson, “Possible new effects in superconductive tunnelling,” *Physics Letters*, vol. 1, no. 7, pp. 251 – 253, 1962.
- [85] R. Parks, *Superconductivity: Part 2 (In Two Parts)*. Superconductivity, Taylor & Francis, 1969.
- [86] M. Eschrig, “Spin-polarized supercurrents for spintronics,” *Physics Today*, vol. 64, no. 1, p. 43, 2011.
- [87] A. F. Andreev, “Thermal conductivity of the intermediate state of superconductors. ii.,” *Soviet Physics JETP*, vol. 20, no. 6, pp. 1490–1493, 1965.
- [88] V. T. Petrashov, V. N. Antonov, P. Delsing, and T. Claeson, “Phase controlled mesoscopic ring interferometer,” *Pis'ma Zh. Eksp. Teor. Fiz.*, vol. 60, no. 8, pp. 589–594, 1994.
- [89] H. le Sueur, P. Joyez, H. Pothier, C. Urbina, and D. Esteve, “Phase controlled superconducting proximity effect probed by tunneling spectroscopy,” *Physical Review Letters*, vol. 100, p. 197002, may 2008.
- [90] P. G. De Gennes, “Boundary effects in superconductors,” *Rev. Mod. Phys.*, vol. 36, pp. 225–237, Jan 1964.

- [91] P. Dubos, H. Courtois, B. Pannetier, F. K. Wilhelm, A. D. Zaikin, and G. Schon, “Josephson critical current in a long mesoscopic s-n-s junction,” *Physical Review B*, vol. 63, no. 6, p. 64502, 2001.
- [92] F. S. Bergeret, A. F. Volkov, and K. B. Efetov, “Odd triplet superconductivity and related phenomena in superconductor-ferromagnet structures,” *Reviews of Modern Physics*, vol. 77, no. 4, pp. 1321–1373, 2005.
- [93] A. I. Buzdin and M. Y. Kupriyanov, “Transition temperature of a superconductor-ferromagnet superlattice,” *Pis'ma Zh. Eksp. Teor. Fiz.*, vol. 52, pp. 1089–1091, 1990.
- [94] Z. Radovic, M. Ledvij, L. Dobrosavljevic-Grujic, A. I. Buzdin, and J. R. Clem, “Transition temperatures of superconductor-ferromagnet superlattices,” *Physical Review B*, vol. 44, no. 2, pp. 759–764, 1991.
- [95] A. S. Sidorenko, V. I. Zdravkov, A. A. Prepelitsa, C. Helbig, Y. Luo, S. Gsell, M. Schreck, S. Klimm, S. Horn, L. Tagirov, and R. Tidecks, “Oscillations of the critical temperature in superconducting nb/ni bilayers,” *Annalen der Physik*, vol. 12, no. 1, p. 37, 2003.
- [96] T. Mühge, N. N. Garif'yanov, Y. V. Goryunov, G. G. Khaliullin, L. R. Tagirov, K. Westerholt, I. A. Garifullin, and H. Zabel, “Possible origin for oscillatory superconducting transition temperature in superconductor/ferromagnet multilayers,” *Phys. Rev. Lett.*, vol. 77, pp. 1857–1860, Aug 1996.
- [97] M. Vélez, M. C. Cyrille, S. Kim, J. L. Vicent, and I. K. Schuller, “Enhancement of superconductivity by decreased magnetic spin-flip scattering: Nonmonotonic T_C dependence with enhanced magnetic ordering,” *Phys. Rev. B*, vol. 59, pp. 14659–14662, Jun 1999.
- [98] L. Lazar, K. Westerholt, H. Zabel, L. R. Tagirov, Y. V. Goryunov, N. N. Garif'yanov, and I. A. Garifullin, “Superconductor/ferromagnet proximity effect in fe/pb/fe trilayers,” *Phys. Rev. B*, vol. 61, pp. 3711–3722, Feb 2000.

- [99] I. A. Garifullin, D. A. Tikhonov, N. N. Garif'yanov, L. Lazar, Y. V. Goryunov, S. Y. Khlebnikov, L. R. Tagirov, K. Westerholt, and H. Zabel, "Re-entrant superconductivity in the superconductor/ferromagnet v/fe layered system," *Phys. Rev. B*, vol. 66, p. 020505, Jul 2002.
- [100] T. Kontos, M. Aprili, J. Lesueur, F. Genêt, B. Stephanidis, and R. Boursier, "Josephson junction through a thin ferromagnetic layer: negative coupling.," *Physical review letters*, vol. 89, no. 13, p. 137007, 2002.
- [101] A. I. Buzdin, L. N. Bulaevskii, and S. V. Panyukov, "Critical-current oscillations as a function of the exchange field and thickness of the ferromagnetic metal (f) in an s-f-s josephson junction," *JETP Letters*, vol. 35, no. 1, p. 178, 1982.
- [102] A. Buzdin and M. Y. Kupriyanov, "Jospehson junction with a ferromagentic layer," *Pis'ma Zh. Eksp. Teor. Fiz.*, vol. 53, no. 6, pp. 308–312, 1991.
- [103] V. V. Ryazanov, V. A. Oboznov, A. Y. Rusanov, A. V. Veretennikov, A. A. Golubov, and J. Aarts, "Coupling of two superconductors through a ferromagnet: Evidence for a π junction," *Physical Review Letters*, vol. 86, pp. 2427–2430, 2001.
- [104] V. V. Ryazanov, V. A. Oboznov, A. S. Prokofiev, V. V. Bolginov, and A. K. Feofanov, "Superconductor-ferromagnet-superconductor 0- π junctions," *Journal of Low Temperature Physics*, vol. 136, no. 5-6, pp. 385–400, 2004.
- [105] H. Sellier, C. Baraduc, F. m. c. Lefloch, and R. Calemczuk, "Temperature-induced crossover between 0 and π states in s/f/s junctions," *Phys. Rev. B*, vol. 68, p. 054531, Aug 2003.
- [106] N. R. A.I. Buzdin, A.V. Vedyayev, "Spin orientation dependent superconductivity in f/s/f structures," *Europhys. Lett.*, vol. 48, pp. 686–691, 1999.
- [107] L. R. Tagirov, "Low-field superconducting spin switch based on a superconductor /ferromagnet multilayer," *Phys. Rev. Lett.*, vol. 83, pp. 2058–2061, Sep 1999.

- [108] I. Baladié, A. Buzdin, N. Ryzhanova, and A. Vedyayev, “Interplay of superconductivity and magnetism in superconductor/ferromagnet structures,” *Phys. Rev. B*, vol. 63, p. 054518, Jan 2001.
- [109] F. S. Bergeret, A. F. Volkov, and K. B. Efetov, “Manifestation of triplet superconductivity in superconductor-ferromagnet structures,” *Phys. Rev. B*, vol. 68, p. 064513, Aug 2003.
- [110] Y. V. Fominov, A. A. Golubov, and M. Y. Kupriyanov, “Triplet proximity effect in fsf trilayers,” *Nuclear Physics*, vol. 77, no. 1, p. 5, 2003.
- [111] J. Y. Gu, C.-Y. You, J. S. Jiang, J. Pearson, Y. B. Bazaliy, and S. D. Bader, “Magnetization-orientation dependence of the superconducting transition temperature in the ferromagnet-superconductor-ferromagnet system: CuNi/Nb/CuNi,” *Phys. Rev. Lett.*, vol. 89, p. 267001, Dec 2002.
- [112] J. Y. Gu, C.-Y. You, J. S. Jiang, and S. D. Bader, “Magnetization-orientation dependence of the superconducting transition temperature and magnetoresistance in the ferromagnet-superconductor-ferromagnet trilayer system,” *Journal of Applied Physics*, vol. 93, no. 10, p. 7696, 2003.
- [113] V. T. Petrashov, V. N. Antonov, S. V. Maksimov, and R. S. Shaikhaidarov, “Conductivity of mesoscopic structures with ferromagnetic and superconducting regions,” *Pis'ma Zh. Eksp. Teor. Fiz.*, vol. 59, no. 8, pp. 523–526, 1994.
- [114] M. Giroud, H. Courtois, K. Hasselbach, D. Mailly, and B. Pannetier, “Superconducting proximity effect in a mesoscopic ferromagnetic wire,” *Phys. Rev. B*, vol. 58, no. 18, p. 4, 1998.
- [115] V. Petrashov, I. Sosnin, I. Cox, A. Parsons, and C. Troadec, “Giant mutual proximity effects in ferromagnetic/superconducting nanostructures,” *Physical Review Letters*, vol. 83, pp. 3281–3284, oct 1999.

- [116] J. Y. Gu, J. Kusnadi, and C.-Y. You, “Proximity effect in a superconductor/exchange-spring-magnet hybrid system,” *Physical Review B*, vol. 81, p. 214435, jun 2010.
- [117] J. W. a. Robinson, F. Chiodi, M. Egilmez, G. B. Halász, and M. G. Blamire, “Supercurrent enhancement in bloch domain walls,” *Scientific reports*, vol. 2, p. 699, jan 2012.
- [118] V. Zdravkov, J. Kehrle, G. Obermeier, D. Lenk, H.-A. Krug von Nidda, C. Müller, M. Kupriyanov, A. S. Sidorenko, S. Horn, R. Tidecks, and L. Tagirov, “Experimental observation of the triplet spin-valve effect in a superconductor-ferromagnet heterostructure,” *Physical Review B*, vol. 87, no. 14, p. 144507, 2013.
- [119] T. E. Baker, A. Richie-Halford, and A. Bill, “Long range triplet josephson current and $0 - \pi$ transitions in tunable domain walls,” *New Journal of Physics*, vol. 16, no. 9, p. 093048, 2014.
- [120] A. Singh, S. Voltan, K. Lahabi, and J. Aarts, “Colossal proximity effect in a superconducting triplet spin valve based on the half-metallic ferromagnet *cro*₂,” *Physical Review X*, vol. 5, no. 2, p. 021019, 2015.
- [121] M. S. Kalenkov, A. D. Zaikin, and V. T. Petrashov, “Triplet superconductivity in a ferromagnetic vortex,” *Physical Review Letters*, vol. 107, p. 4, aug 2011.
- [122] P. M. Tedrow, J. E. Tkaczyk, and A. Kumar, “Spin-polarized electron tunneling study of an artificially layered superconductor with internal magnetic field: Euo-al,” *Phys. Rev. Lett.*, vol. 56, pp. 1746–1749, Apr 1986.
- [123] V. Krivoruchko and E. Koshina, “Inhomogeneous magnetism induced in a superconductor at a superconductor-ferromagnet interface,” *Physical Review B*, vol. 66, p. 014521, jul 2002.

- [124] F. Bergeret, A. F. Volkov, and K. Efetov, “Induced ferromagnetism due to superconductivity in superconductor-ferromagnet structures,” *Physical Review B*, vol. 69, p. 174504, may 2004.
- [125] F. F. Bergeret, A. A. Yeyati, A. Martín-Rodero, and A. Martín-Rodero, “Inverse proximity effect in superconductor-ferromagnet structures: From the ballistic to the diffusive limit,” *Physical Review B*, vol. 72, p. 064524, aug 2005.
- [126] M. Houzet and A. I. Buzdin, “Theory of domain-wall superconductivity in superconductor/ferromagnet bilayers,” *Physical Review B - Condensed Matter and Materials Physics*, vol. 74, no. 21, pp. 1–9, 2006.
- [127] L. Y. Zhu, Y. Liu, F. S. Bergeret, J. E. Pearson, S. G. E. Te Velthuis, S. D. Bader, and J. S. Jiang, “Unanticipated proximity behavior in ferromagnet-superconductor heterostructures with controlled magnetic noncollinearity,” *Physical Review Letters*, vol. 110, no. 17, pp. 1–5, 2013.
- [128] J. Xia, V. Shelukhin, M. Karpovski, A. Kapitulnik, and A. Palevski, “Inverse proximity effect in superconductor-ferromagnet bilayer structures,” *Physical Review Letters*, vol. 102, p. 087004, feb 2009.
- [129] M. G. Flokstra, S. J. Ray, S. J. Lister, J. Aarts, H. Luetkens, T. Prokscha, A. Suter, E. Morenzoni, and S. L. Lee, “Measurement of the spatial extent of inverse proximity in a py/nb/py superconducting trilayer using low-energy muon-spin rotation,” *Physical Review B - Condensed Matter and Materials Physics*, vol. 89, pp. 1–5, 2014.
- [130] D. F. Kyser, “Monte carlo simulation of spatially distributed beams in electron-beam lithography,” *Journal of Vacuum Science and Technology*, vol. 12, no. 6, p. 1305, 1975.
- [131] “Stock image available in clean room at royal holloway. author unknown..”
- [132] “http://spectroscopy.web.psi.ch/rita2/htdocs/auxequip/heliox/helioxman_small.htm.”

- [133] M. McElfresh, *Fundamentals of Magnetism and Magnetic Measurements Featuring Quantum Design's Magnetic Property Measurement system*. Quantum Design, 1994.
- [134] “<http://blog.brukerafmprobes.com/guide-to-spm-and-afm-modes/magnetic-force-microscopy-mfm/>.”
- [135] C. D. Frisbie, *Scanning Probe Microscopy*. 2004.
- [136] T. Wren, B. Gribkov, V. Petrashov, and O. Kazakova, “Phase diagram of magnetic states in nickel submicron disks,” *Journal of Applied Physics*, vol. 118, no. 2, p. 023906, 2015.
- [137] R. P. Boardman, “Micromagnetic simulation of ferromagnetic part-spherical particles,” *Journal of Applied Physics*, vol. 95, no. 11, p. 7037, 2004.
- [138] J. A. Osborn, “Demagnetizing factors of the general ellipsoid,” *Phys. Rev.*, vol. 67, pp. 351–357, Jun 1945.
- [139] P.-O. Jubert and R. Allenspach, “Analytical approach to the single-domain-to-vortex transition in small magnetic disks,” *Phys. Rev. B*, vol. 70, p. 144402, Oct 2004.
- [140] R. I. Joseph, “Ballistic demagnetizing factor in uniformly magnetized cylinders,” *Journal of Applied Physics*, vol. 37, no. 13, pp. 4639–4643, 1966.
- [141] F. Viot, L. Favre, R. Hayn, and M. D. Kuz'min, “Theory of magnetic domains in uniaxial thin films,” *Journal of Physics D: Applied Physics*, vol. 45, no. 40, p. 405003, 2012.
- [142] T. Okuno, K. Shigeto, T. Ono, K. Mibu, and T. Shinjo, “Mfm study of magnetic vortex cores in circular permalloy dots: Behavior in external field,” *Journal of Magnetism and Magnetic Materials*, vol. 240, no. 1-3, pp. 1–6, 2002.
- [143] M. Sawicki, W. Stefanowicz, and A. Ney, “Sensitive squid magnetometry for studying nanomagnetism,” *Semiconductor Science and Technology*, vol. 26, no. 6, p. 064006, 2011.

- [144] T. Wren and O. Kazakova, “Anisotropic magnetoresistance effect in sub-micron nickel disks,” *Journal of Applied Physics*, vol. 117, no. 17, p. 17E134, 2015.
- [145] T. S. Machado, M. Argollo de Menezes, T. G. Rappoport, and L. C. Sampaio, “Magnetotransport in nanostructures: The role of inhomogeneous currents,” *Journal of Applied Physics*, vol. 109, no. 9, p. 093904, 2011.
- [146] M. Goto, H. Hata, A. Yamaguchi, Y. Nakatani, T. Yamaoka, and Y. Nozaki, “Electrical detection of vortex states in a ferromagnetic disk using the rectifying effect,” *Journal of Applied Physics*, vol. 109, no. 7, p. 07D306, 2011.
- [147] R. Meservey and P. Tedrow, “Spin-polarized electron tunneling,” *Physics Reports*, vol. 238, pp. 173–243, mar 1994.
- [148] J.-P. Tetienne, T. Hingant, L. Rondin, S. Rohart, A. Thiaville, J.-F. Roch, and V. Jacques, “Quantitative stray field imaging of a magnetic vortex core,” *Phys. Rev. B*, vol. 88, p. 214408, Dec 2013.
- [149] H. Yang, S.-H. Yang, S. Takahashi, S. Maekawa, and S. S. P. Parkin, “Extremely long quasiparticle spin lifetimes in superconducting aluminium using mgo tunnel spin injectors,” *Nature materials*, vol. 9, pp. 586–93, jul 2010.
- [150] F. Hübler, M. J. Wolf, D. Beckmann, and H. v. Löhneysen, “Long-range spin-polarized quasiparticle transport in mesoscopic al superconductors with a zeeman splitting,” *Physical Review Letters*, vol. 109, p. 207001, nov 2012.
- [151] Y. S. Shin, H. J. Lee, and J. Kim, “Spin diffusion in a superconductor through mesoscopic ferromagnet/superconductor interfaces,” *Physica B: Condensed Matter*, vol. 329-333, no. II, pp. 1411–1412, 2003.
- [152] C. Chen, W. Kuo, D. Chung, J. Shyu, and C. Wu, “Evidence for suppression of superconductivity by spin imbalance in co-al-co single-electron transistors,” *Physical Review Letters*, vol. 88, p. 047004, jan 2002.

- [153] N.-C. Yeh, R. Vasquez, C. Fu, A. Samoilov, Y. Li, and K. Vakili, “Nonequilibrium superconductivity under spin-polarized quasiparticle currents in perovskite ferromagnet-insulator-superconductor heterostructures,” *Physical Review B*, vol. 60, pp. 10522–10526, oct 1999.
- [154] J. Dumont, M. Moragus, B. Leridon, J. Lesueur, and J. P. Contour, “New insight on spin polarized current injection in high- t_c cuprate/manganite devices,” *The European Physical Journal B - Condensed Matter*, vol. 35, pp. 331–337, oct 2003.
- [155] F. C. Wellstood, C. Urbina, and J. Clarke, “Hot-electron effects in metals,” *Physical Review B*, vol. 49, no. 9, pp. 5942–5955, 1994.
- [156] C. D. Shelly, E. A. Matrozova, and V. T. Petrashov, “Resolving thermoelectric paradox in superconductors,” *Science Advances*, vol. 2, no. 2, p. e1501250, 2016.
- [157] F. Chiodi, M. Ferrier, S. Guéron, J. C. Cuevas, G. Montambaux, F. Fortuna, A. Kasumov, and H. Bouchiat, “Geometry-related magnetic interference patterns in long *sns* josephson junctions,” *Phys. Rev. B*, vol. 86, p. 064510, Aug 2012.
- [158] M. Meschke, J. T. Peltonen, J. P. Pekola, and F. Giazotto, “Tunnel spectroscopy of a proximity Josephson junction,” *Physical Review B*, vol. 84, p. 214514, dec 2011.
- [159] W. J. Skocpol, “Self-heating hotspots in superconducting thin-film microbridges,” *Journal of Applied Physics*, vol. 45, no. 9, p. 4054, 1974.
- [160] S. Yamasaki and T. Aomine, “Self-heating effects in long superconducting thin films over a wide temperature range,” *Japanese Journal of Applied Physics*, vol. 18, no. 3, p. 667, 1979.
- [161] H. Courtois, S. Rajauria, P. Gandit, F. W. J. Hekking, and B. Pannetier, “Inherent thermometry in a hybrid superconducting tunnel junction,” *Journal of Low Temperature Physics*, vol. 153, no. 5, pp. 325–338, 2008.

-
- [162] M. Nahum, T. M. Eiles, and J. M. Martinis, “Electronic microrefrigerator based on a normal-insulator-superconductor tunnel junction,” *Applied Physics Letters*, vol. 65, no. 24, pp. 3123–3125, 1994.
- [163] F. Giazotto, T. Heikkilä, A. Luukanen, A. Savin, and J. Pekola, “Opportunities for mesoscopics in thermometry and refrigeration: Physics and applications,” *Reviews of Modern Physics*, vol. 78, pp. 217–274, mar 2006.
- [164] A. V. Timofeev, M. Helle, M. Meschke, M. Möttönen, and J. P. Pekola, “Electronic refrigeration at the quantum limit,” *Physical Review Letters*, vol. 102, no. MAY, pp. 1–5, 2009.